

DEVELOPMENT AND FUNCTIONALIZATION OF SWG
METAMATERIALS IN SI-BASED PICs

DEVELOPMENT AND FUNCTIONALIZATION OF SUBWAVELENGTH
GRATING METAMATERIALS IN SILICON-BASED PHOTONIC
INTEGRATED CIRCUITS

By
CAMERON M. NARAINÉ,
M.A.Sc. (Engineering Physics), B.Sc. (Physics)

A Thesis Submitted to the School of Graduate Studies
in the Partial Fulfillment of the Requirements for the Degree of

Doctor of Philosophy
in
Engineering Physics

McMaster University
Hamilton, Ontario

Doctor of Philosophy (2024)

[Engineering Physics](#)

[McMaster University](#)

Hamilton, Ontario, Canada

TITLE: Development and functionalization of subwavelength grating metamaterials in silicon-based photonic integrated circuits

AUTHOR:

Cameron M. Naraine,

M.A.Sc. (Engineering Physics), B.Sc. (Physics)

SUPERVISORS:

Dr. Jonathan D. B. Bradley

Associate Professor, Department of Engineering Physics,

McMaster University, ON, Canada

Dr. Pavel Cheben

Adjunct Professor, Department of Engineering Physics,

McMaster University, ON, Canada

Principle Research Scientist, Advanced Electronics and Photonics Research Centre,

National Research Council Canada, ON, Canada

SUPERVISORY COMMITTEE MEMBERS:

Dr. Andrew P. Knights

Professor, Department of Engineering Physics,

McMaster University, ON, Canada

NUMBER OF PAGES: [xxv](#), [188](#)

Abstract

Silicon photonics (SiP) has become a cornerstone technology of the modern age by leveraging the mature fabrication processes and infrastructure of the microelectronics industry for the cost-effective and high-volume production of compact and power-efficient photonic integrated circuits (PICs). The impact that silicon (Si)-based PICs have had on data communications, particularly data center interconnection and optical transceiver technologies, has encouraged SiP chip development and their use in other applications such as artificial intelligence, biomedical sensing and engineering, displays for augmented/virtual reality, free-space communications, light detection and ranging, medical diagnostics, optical spectroscopy, and quantum computing and optics. To expand the functionality and improve the performance of SiP circuits for these surging applications, subwavelength grating (SWG) metamaterials have been thoroughly investigated and implemented in various passive integrated photonic components fabricated on the silicon-on-insulator (SOI) platform. SWG metamaterials are periodic structures composed of two materials with different permittivities that exhibit unnatural properties by using a period shorter than the guided wavelength of light propagating through them. The ability to synthesize the constituent SiP materials without any need to alter standard fabrication procedures enables precise, flexible control over the electromagnetic field and sophisticated selectively over anisotropy, dispersion, polarization, and the mode effective index in these metastructures. This provides significant benefits to SOI devices, such as low loss mode conversion and propagation, greater coupling efficiencies and alignment tolerances for fiber-chip interfaces, ultrabroadband operation in on-chip couplers, and improved sensitivities and limits of detection in integrated photonic sensors. Parallel to the rise of SiP technology is the development of other materials compatible with mature PIC fabrication methods both in the foundry (e.g., silicon nitride (Si_3N_4)) and outside the foundry (e.g., high-index oxide glasses such as aluminum oxide (Al_2O_3) and tellurium oxide (TeO_2)). Si_3N_4 offsets the pitfalls of Si as a passive waveguiding material, providing lower scattering and polarization-dependent losses, optical transparency throughout the visible spectrum, increased tolerance to fabrication error, and better handling of high-power optical signals. Meanwhile, Al_2O_3 and TeO_2 both serve as excellent host materials for rare-earth ions, and TeO_2 possesses strong nonlinear optical properties. Using a single-step post-fabrication thin film deposition process, these materials can be monolithically integrated onto Si PICs at a wafer scale, enabling the realization of complementary-metal-oxide-semiconductor (CMOS)-compatible, hybrid SiP devices for

linear, nonlinear, and active functionalities in integrated optics. While SWG metamaterials have widely impacted the design space and applicability of integrated photonic devices in SOI, they have not yet made their mark in other material systems outside of Si. Furthermore, demonstrations of their capabilities in active processes, including optical amplification, are still missing.

In this thesis, we present a process for developing various SWG metamaterial-engineered integrated photonic devices in different material systems both within and beyond SOI. The demonstrations in this thesis emphasize the benefits of SWG metamaterials in these devices and realize their potential for enhancing functionality in applications such as sensing and optical amplification. The objective of the thesis is to highlight the prospects of SWG metamaterial implementation in different media used in integrated optics. This is accomplished by experimentally demonstrating SWG metamaterial waveguides, ring resonators and other components composed of different hybrid core-cladding material systems, including Si-TeO₂ and Si₃N₄-Al₂O₃. Chapter 1 introduces the background and motivation for integrated optics and SWG metamaterials and provides an overview and comparison of the different materials explored in this work. Chapter 2 presents an initial experimental demonstration of TeO₂-coated SOI SWG metamaterial waveguides and mode converters. It also details the design of fishbone-style SWG waveguides aimed at lowering loss and enhancing mode overlap with the active TeO₂ cladding material in the hybrid SiP platform. Chapter 3 details an open-access Canadian foundry process for rapid prototyping of Si₃N₄ PICs, emphasizing the Si₃N₄ material and waveguide fabrication methods, as well as the design and characterization of various integrated photonic components included in a process design kit. The platform is compared against other Si₃N₄ foundries, and plans for further development are also discussed. Chapter 4 reports the first demonstration of SWG metamaterial waveguides and ring resonators fabricated using a Si₃N₄ foundry platform. The measured devices have a propagation loss of ~ 1.5 dB/cm, an internal quality factor of $2.11 \cdot 10^5$, and a bulk sensitivity of ~ 285 nm/RIU in the C-band, showcasing competitive metrics with conventional Si₃N₄ waveguides and SWG ring resonators and sensors reported in SOI. Chapter 5 presents work towards an SWG metamaterial-engineered waveguide amplifier. The fabricated device, based in Si₃N₄ and functionalized by an atomic layer deposited, erbium-doped Al₂O₃ thin film cladding, exhibited a signal enhancement of ~ 8.6 dB, highlighting its potential for on-chip optical amplification. Methods to reduce the loss within the material system are proposed to achieve net gain in future devices. Chapter 6 summarizes the thesis and discusses pathways for optimizing the current devices as well as avenues for exploring new and intriguing materials and devices for future applications in integrated photonics.

Acknowledgements

First and foremost, I want to begin by expressing my sincere gratitude to my supervisors. Dr. Jonathan Bradley recognized my potential prior to pursuing graduate studies (over 6 years ago!) and has since invested much of his time and energy (and, of course, his research funding) into me that have allowed me plentiful opportunities and experiences to grow into the researcher I am today. Thanks to Jon’s guidance, I can confidently say I am an expert in photonics today and aim to make a lasting impact in the field with this work and in my future endeavours. Dr. Pavel Cheben took me under his wing shortly after our first meeting at my first Photonics North conference in 2019. He invited me to work with him at the National Research Council (NRC) Canada in Ottawa on multiple occasions during my Master’s. Through these engagements, he saw something in me that ultimately encouraged me to pursue a PhD, where he volunteered to upgrade as my official PhD co-supervisor. Despite being affiliated with many institutions where he supervises countless students, Pavel always made me feel like I was the most important one, dedicating an abundance of time, energy, patience, and guidance to me, all while reserving a genuine concern for my overall well-being. His attention to detail and pursuit of excellence have been a prime example, compelling me to strive for greatness in my work. His supervision, support and wisdom through the various trials and tribulations I have experienced throughout my academic journey have taught me much about the art of research and about myself. These lessons will serve me in many areas of life for years to come.

This work would not have been possible without Dr. Andy Knights, my original Master’s co-supervisor, who was the first to suggest the marriage of our optically active tellurium oxide thin films with subwavelength grating metamaterials and introduced me to the pioneer of subwavelength integrated photonics, Dr. Pavel Cheben, who ultimately came to be my PhD supervisor. I also wish to extend my gratitude to Dr. Jens Schmid from NRC Canada, who has served as my “pseudo”-supervisor since before my PhD. Jens has provided much insight and delivered important watershed moments throughout our work together that have enhanced my understanding of science and made me a better, well-rounded researcher. We’ve also shared many delightful conversations over Zoom and at conferences, which I look back on very fondly.

I am very grateful to my colleagues in the Bradley Research Group, both past (Dr. Dawson Bonneville, Dr. Hamidu Mbonde, Dr. Henry Frankis, Dr. Jeremy Miller, Dr. Khadijeh Mirarabbas Kiani, Parimal Edke, and Dr. Renjie Wang) and present (Batoul

(Tahoora) Hashemi, Bruno Segat Frare, Manuel (Arthur) Méndez-Rosales, Niloofar Majidian Taleghani, and Pooya Torab Ahmadi). You all taught me a lot, got me excited about the work we do, and provided many needed breaks away from the daily grind of photonics research. Special shout-outs go to Bruno, for being my thesis writing companion and Photonic Devices course TA buddy over the last few months, and to Tahoora, for greatly assisting me with my many projects, particularly in the last year of my PhD.

I am also grateful to the students and alumni from Knights Group (Connor Wong, Dr. David Hagan, Keru Chen, Matt Vukovic, Mohammad Rezaul (Reza) Islam, Dr. Ranjan Das, Dr. Ross Anthony, Yanran Xie, and Dr. Yuxuan (Michael) Gao) and to various members of the Engineering Graduate Society (EGS) and the Engineering Physics department (Aydin Amini, Devon Jones, Dr. Evan Wright, Dr. Liz MacConnachie, Dr. Muhammad Munir, Pedro Oliveira, Dr. D. Paige Wilson, Dr. Samuel Peter, and (who can forget!) Dr. Ramis Arbi) who I've had the pleasure of engaging with over the years, whether enduring the hardships and hurdles of academia, discussing the marvels of science and engineering, playing some casual MTG commander games, or simply enjoying pub fare and each other's company at the Phoenix.

I would like to thank Dr. Jocelyn Westwood-Bachman, Cameron Horvath, and Dr. Mirwais Aktary from Applied Nanotools Inc. (ANT), with whom I worked very closely on our collaborative project to develop ANT's silicon nitride integrated photonics platform since 2020. You all provided endless support, guidance, and kindness throughout our multiple design layouts and fabrication runs together and shared many tips and tricks for streamlining the process that I will certainly use in future roles and projects. I also now understand just how much time and effort goes into building a successful silicon photonics platform and company. The "ANT SiN project" was certainly one of the most fun projects I worked on during my PhD thanks to each of you. Also, thank you to Dr. Nandini Debnath, who joined the ANT team later in my PhD tenure.

Thank you to Nick Hoffman, Dr. Jeffrey Price, and Dr. David Emslie from the Department of Chemistry and Chemical Biology for their time, patience and expertise in helping us develop low loss alumina (and eventually hybrid alumina-erbium) thin films using their custom ALD system. Both Nick and David graciously provided me their time to discuss deposition strategies, deposition scheduling, and detailed explanations of their work that have enhanced my understanding of ALD and given me a greater appreciation for thin film deposition and chemistry overall. I'd like to apologize one last time for driving your reactor to the edge so we could acquire super thick ALD films! Extra thank you to the present and past ORF-RE project managers, Dr. Majeda Al

Hareri and Dr. Blossom Yan, for providing us the opportunity to join the project and participate at the bi-annual ORF-RE Mini Symposiums.

An extended token of my gratitude goes out to the various members and leaders of the Photonics & RF Research Lab at Universidad de Málaga. In November 2023, I was blessed with the opportunity to visit and work at Universidad de Málaga for four weeks. Thank you to Prof. Íñigo Molina-Fernández for accepting me and organizing the logistics that made the exchange possible. Thank you to Prof. Gonzalo Wangüemert-Pérez for leading the project I worked on, and to Dr. José Manuel Luque-González and Alejandro Sánchez Sánchez, with whom I collaborated directly on the project. Thank you to Prof. Robert Halir who provided multiple travel suggestions and brought me cough syrup when I fell ill during the trip, and to Carlos Pérez Armenta who organized a hiking excursion for me and the group to El Torcal National Park. I am also grateful to have met and had various fruitful conversations with other members of the team, including Ana Sánchez Ramírez, Alejandro Fernández Hinestroza, Elio Godoy, Prof. José de-Oliva Rubio, Prof. Laureano Moreno Pozas, Miguel Barona Ruiz, and Victor Gavira Benítez. Finally, thank you to my supervisor, Dr. Pavel Cheben, for introducing me to Íñigo and the group and being the first to propose the collaboration.

Many other institutions and their staff made the work disclosed in this thesis and adjacent projects come to life. Within McMaster University, thank you to:

- Dr. Doris Stevanovic from the Centre for Emerging Device Technologies (CEDT) for giving me 1-on-1 training and access to our state-of-the-art cleanroom,
- Other CEDT staff (Dr. Nebile Isik Goktas) and former and current CEDT directors (Dr. Rafael Kleiman, Dr. Andy Knights, Dr. Ayse Turak, and Dr. Jonathan Bradley) for cultivating a creative and innovative research environment,
- Dr. Zhilin Peng from the Centre for Advanced Nuclear Systems (CANS) for SEM and EDS sample preparation training and access to the CANS electron microscopy suite,
- Various staff from the Canadian Centre for Electron Microscopy (CCEM) for their education on various electron microscopy methods and their services within the CCEM facilities, and
- The current and former administrators of the Engineering Physics department (Robert Laidler, Shu Sum (Samantha) Leung, Linda Ellis, Emma Trueman, and

Nicole MacDonald), whose services made for a much easier and more pleasant graduate student experience.

Outside of McMaster University, thank you to:

- Dr. Lukas Chrostowski from the University of British Columbia, for spearheading the SiEPIC program, which provided much needed training and guidance in the field of silicon photonics in my early years as a graduate student,
- Dr. Jessica Zhang, Dr. Luhua Xu, Sarah Neville, and Dr. Susan Xu from CMC Microsystems, who supplied, and continue to supply, easy access and the corresponding administrative and technical support for important software tools and fabrication technology that is needed for our work, and
- Catriona Scheffer from Ansys, who offered continual administrative and sales support for Lumerical—a requirement for my work that I could not live without and bothered my supervisors about year after year!

I am indebted to the Johnston family (Connor, Gillian, and Owen), who have sheltered and fed me throughout my PhD journey, including the entirety of the COVID-19 pandemic. You allowed me to occupy a whole room (sometimes more than one) in your home so I could manifest the perfect environment to thrive and better myself both as a researcher and as a human being. For this, I am extremely grateful.

I must thank my direct family (mom (Janice), dad (Tony), and Chris Naraine) for providing me endless love and support and countless opportunities to have the life I have today. None of what I have accomplished would have been possible without any of you.

Finally, the ultimate thank you goes to my partner, Courtney Johnston, who has stood by my side throughout my entire academic career with patience, support, and love. You've transformed me into a completely different person, someone I am happy to be, and I am excited to use the experiences and skills I've gained from this journey to build the life we've always dreamed of together. From the bottom of my heart, thank you.

Contents

Abstract	iii
Acknowledgements	v
List of Figures	xii
List of Tables	xx
1 Introduction	1
1.1 Integrated optics	1
1.2 Si and SiN photonics	2
1.3 Subwavelength grating (SWG) metamaterials	4
1.3.1 Overview / state-of-the-art	4
1.3.2 Fundamentals	5
1.3.3 Integrated optics material considerations for SWGs	7
1.4 Thesis overview	13
1.4.1 Thesis objective	13
1.4.2 Statement of thesis work	14
1.4.3 Summary of publications	15
Bibliography	18
2 Silicon subwavelength grating metamaterial waveguides functionalized with tellurium oxide cladding	39
2.1 Introduction	41
2.2 Simulation and design	43
2.2.1 SWG metamaterial waveguides – FDE simulations	44
2.2.2 SWG metamaterial waveguides – FDTD simulations	51
2.2.3 SWG edge couplers – FDE simulations	55
2.2.4 SWG-wire mode transformers – EME simulations	59
2.3 Fabrication and characterization	62

2.3.1	Design #1: SWG waveguide cutback structures	64
2.3.2	Design #2: SWG-wire mode transformers	68
2.3.3	Design #3: FB-SWG waveguides	71
2.4	Conclusion	74
	Bibliography	74
3	A moderate confinement 1.3 and 1.5 μm silicon nitride platform enabled by a rapid prototyping integrated photonics foundry process	82
3.1	Introduction	84
3.2	Fabrication	87
3.2.1	Waveguide fabrication and material properties	87
3.2.2	Post-processing options	88
3.3	SiN PDK components	89
3.3.1	Waveguides	89
3.3.2	Fiber-chip couplers	93
3.3.3	MMI-based 3 dB power splitter	97
3.3.4	All-pass, point-coupled microring resonators	99
3.3.5	SWG metamaterial devices	102
3.4	Discussion	103
3.5	Conclusion	105
	Bibliography	105
4	Subwavelength grating metamaterial waveguides and ring resonators on a silicon nitride platform	116
4.1	Introduction	118
4.2	Design and fabrication	120
4.3	Optical characterization and analysis	123
4.4	Conclusion	129
	Bibliography	130
5	Towards a subwavelength grating metamaterial waveguide amplifier: silicon nitride coated in atomic layer deposited alumina/erbium films	136
5.1	Introduction	139
5.2	Design	142
5.2.1	2D FDE simulations	142
5.2.2	3D FDTD simulations	146
5.3	Fabrication	152

5.3.1	SiN waveguides	152
5.3.2	ALD of undoped and Er-doped Al ₂ O ₃ thin films	153
5.4	Characterization	155
5.4.1	Film characterization	155
5.4.2	Al ₂ O ₃ -coated waveguide characterization	162
5.4.3	Al ₂ O ₃ /Er ₂ O ₃ -coated waveguide characterization	164
5.5	Conclusion	173
	Bibliography	173
6	Conclusion	182
6.1	Summary	182
6.2	Future work	184

List of Figures

1.1	(a) 3D model and (b) dispersion relation diagram for a periodic waveguide.	6
1.2	Fundamental TE mode profiles for Si strip and SWG waveguides with different top claddings.	9
2.1	(a) General cross-sectional diagram of an SOI SWG metamaterial waveguide approximated by EMT in the 2D FDE simulation environment. Inset shows the in-plane cross section (top) and top view (bottom) schematics of conventional (left) and “fishbone” (right) SWG waveguide configurations. Specific in-plane cross-sectional diagrams used for (b) Design #1, (c) Design #2, and (d) Design #3, as specified in Table 2.1.	44
2.2	2D FDE simulated mode effective index (n_{eff}) for EMT-approximated SWG metamaterial waveguide with varying waveguide width (w_{wg}) and TeO ₂ cladding thickness (t_{TeO_2}) and duty cycles (δ) of (a) 0.3, (b) 0.5, (c) 0.7, and (d) 1. Dotted black lines indicate where $n_{\text{eff}} = 1.65$. Designs below these thresholds suffer from significant substrate leakage losses [43].	46
2.3	2D FDE simulated group effective index (n_g) results for EMT-approximated SWG metamaterial waveguides with varying waveguide width (w_{wg}) and TeO ₂ cladding thickness (t_{TeO_2}) and duty cycles (δ) of (a) 0.3, (b) 0.5, (c) 0.7, and (d) 1. Dotted black lines represent thresholds from Fig. 2.2 ($n_{\text{eff}} = 1.65$).	47
2.4	2D FDE simulated TeO ₂ cladding mode overlap (γ_{TeO_2}) for EMT-approximated SWG metamaterial waveguides with varying waveguide width (w_{wg}) and TeO ₂ cladding thickness (t_{TeO_2}) and duty cycles (δ) of (a) 0.3, (b) 0.5, (c) 0.7, and (d) 1. Dotted black lines represent thresholds from Fig. 2.2 ($n_{\text{eff}} = 1.65$).	48

2.5	2D FDE simulated TeO_2 confinement factor (Γ_{TeO_2}) for EMT-approximated SWG metamaterial waveguides with varying waveguide width (w_{wg}) and TeO_2 cladding thickness (t_{TeO_2}) and duty cycles (δ) of (a) 0.3, (b) 0.5, (c) 0.7, and (d) 1. Dotted black lines represent thresholds from Fig. 2.2 ($n_{\text{eff}} = 1.65$).	49
2.6	(a) 3D FDTD simulated photonic bandstructure of proposed device in Design #1. Inset depicts top view index profile at half waveguide height of simulated unit cell with length Λ (black dashed box). Top view Floquet-Bloch mode intensity distribution profile for periodicities and wavenumbers (b) $\Lambda = 300$ nm and $k = 0.33$ and (c) $\Lambda = 360$ nm and $k = 0.47$, at $\lambda = 1480$ nm.	52
2.7	3D FDTD simulated dispersion relation, Floquet-Bloch mode effective index, and group index for the TeO_2 -coated SWG waveguide studied in Design #1.	53
2.8	First order photonic bands of 3D FDTD simulated dispersion relation for various TeO_2 -coated SWG waveguide devices studied in Design #2.	54
2.9	(a) Floquet-Bloch mode propagation and fundamental TE mode profiles (b) across the grating segment and (c) in between adjacent grating segments of the 3D FDTD simulated TeO_2 -coated FB-SWG waveguide device studied in Design #3.	55
2.10	FDE simulated mode effective index for various EMT-approximated SWG waveguides coated with (a) SiO_2 cladding and (b) 100 nm, (c) 200 nm, and (d) 400 nm-thick TeO_2 cladding.	57
2.11	FDE simulated coupling efficiency for an interface between a 2.5 μm MFD lensed fiber and various EMT-approximated SWG waveguides coated with (a) SiO_2 cladding and (b) 100 nm, (c) 200 nm, and (d) 400 nm-thick TeO_2 cladding.	58
2.12	EME simulation of 50 μm -long SWG-wire mode transformers coated in 400 nm-thick TeO_2 cladding. (a) Refractive index and (b) TE-polarized field profiles from a (i) top view ($z = 0.11$ μm) and (ii) side view ($y = 0$ μm). Inset of (a)(i) shows a detailed top view schematic of the original Si waveguide structure in which the simulated EMT-approximated refractive index is based. Lossless mode transformation is achieved from (c) a launched FB-SWG waveguide mode ($x = 5$ μm) to (d) an output wire waveguide mode ($x = 55$ μm).	60

2.13	Simulated transmission obtained from EME (a) propagation sweep at 1.55 μm wavelength and (b) wavelength sweep for SWG-wire mode transformers with various lengths and 400 nm-thick TeO_2 cladding.	62
2.14	(a) Top view schematic of fabricated SWG device with Si wire (solid) and SWG (striped) waveguides sections. Dash lines indicate the locations of the scanning electron microscope (SEM) images of the fabricated b) uncoated and c) 105 nm-thick TeO_2 -coated mode transformer transitions, d) TeO_2 -coated SWG waveguide (side view), and e) uncoated and f) TeO_2 -coated SWG waveguides (angled view). Image in d) was taken 52° to the surface normal while all other images were taken 45° to the surface normal.	64
2.15	(a) Measured insertion loss of SWG waveguides with 3 μm -thick SiO_2 cladding and 100 nm TeO_2 cladding, with $W_{\text{SWG}} = 450$ nm, $\Lambda = 360$ nm and $\delta = 0.5$ and varying SWG waveguide lengths (L_{SWG}) indicated in legend. (b) Measured propagation loss at $\lambda = 1630$ nm and $\lambda = 1480$ nm for the SiO_2 -clad and TeO_2 -clad waveguides, respectively.	66
2.16	Circuit schematic for Design #2 (a) mode transformer test structures and (b) wire waveguide serpentine cutback structures. Inset of (a) shows a detailed diagram of back-to-back mode transformers, which are duplicated across various test structures to extract the loss of a single mode transformer. Structures are not drawn to scale.	69
2.17	Measurement results for Design #2 test circuits. (a) Total measured loss of wire waveguide section in mode transformer test structures based on the results from serpentine cutback structures. (b) Measured insertion loss spectra for each mode transformer test circuit. Only losses from the mode transformers and fiber-chip coupling are included in the data. (c) Linear regression fits of data from b) for specific wavelengths. (d) Loss per mode transformer extracted from fitting method used in (c) for all measured wavelengths.	70
2.18	Mask layout for Design #3, which primarily studies FB-SWG waveguide structures.	72
3.1	(a) Measured refractive index of SiN films with respect to wavelength. Inset shows zoomed-in S-, C-, and L-band regions with error bars reflecting data collected over four fabrication runs. (b) Measured SiN film loss with respect to wavelength across the S-, C- and L-bands. Inset shows measured loss for VIS and additional NIR wavelengths and red-light streak propagating across a planar SiN film sample during characterization.	88

3.2	Simulated mode effective index of 400-nm-thick SiN strip waveguides with air top cladding at wavelengths of (a) 1310 nm and (b) 1550 nm, and with SiO ₂ top cladding at wavelengths of (c) 1310 nm and (d) 1550 nm across various waveguide widths. Insets show fundamental TE (left) and TM (right) mode profiles for designed single mode waveguides, which are marked by yellow and green stars, respectively.	90
3.3	(a) Optical microscope images of fabricated SiN Archimedean spiral waveguide cutback structures, coated in a 3- μ m-thick PECVD SiO ₂ cladding. (b) Measured insertion loss of spiral waveguides with respect to waveguide length and linear regression fits of data for 1310 and 1550 nm wavelengths under TE and TM polarization. Calculated propagation loss using linear regression fitting across wavelengths measured in the (c) O-band and (d) S-, C- and L-bands.	92
3.4	(a) Sideview cross section of simulated SiO ₂ -clad SiN grating coupler in Ansys Lumerical FDTD software. 2D FDTD simulated (b) 1550 nm wavelength TE mode profile and (c) output transmission spectrum for grating coupler. (d) Measured C-band transmission spectrum for the fabricated SiN TE grating coupler. Inset shows SEM image of fabricated fiber-chip SiN grating coupler.	94
3.5	Simulated and measured coupling loss of SiO ₂ -clad SiN inverse nanotaper edge couplers with various tip widths. The couplers are measured for both TE and TM polarizations using LFs at (a) 1310 and (b) 1550 nm wavelength, and SMFs at (c) 1310 and (d) 1550 nm wavelength without and with IMF ($n = 1.46$).	96
3.6	Simulated MMI length (L_{MMI}) as a function of MMI width (W_{MMI}) for 1×2 and 2×2 SiO ₂ -clad SiN MMI couplers at 1550 nm wavelength. The inset shows mask layout schematics of 2×2 (top) and 1×2 (bottom) MMI couplers with the selected parameters of $W_{\text{MMI}} = 5 \mu\text{m}$ and $L_{\text{MMI}} = 20.4 \mu\text{m}$ for the 2×2 coupler and $W_{\text{MMI}} = 3.9 \mu\text{m}$ and $L_{\text{MMI}} = 10 \mu\text{m}$ for the 1×2 coupler (indicated by the stars). (b) Measured excess loss (EL) and imbalance (IMB) of a symmetric 1×2 SiO ₂ -clad MMI power splitter. The insets show the corresponding transmission spectra for two output ports and reference waveguide devices, as well as an SEM image of a fabricated 1×2 MMI power splitter.	98

3.7	Experimental results for SiO ₂ -clad SiN all-pass microring resonators designed for 1310 nm wavelength under (a) TE and (b) TM polarization, and 1550 nm wavelength under (c) TE and (d) TM polarization. Each configuration shows the measured insertion loss spectra (left) and the fitted resonance peaks near the target wavelengths (right) for microring resonators with various coupling gaps highlighting overcoupled (black), critically coupled (red), and undercoupled (blue) resonance behaviours.	100
4.1	Schematic of SiN SWG metamaterial ring resonator. Inset: top view of coupling section between ring resonator and bus waveguide.	120
4.2	Simulated (a) mode effective index, (b) mode overlap with the upper cladding, (c) propagation loss, and (d) minimum bend radius for various TE-polarized SiN SWG metamaterial waveguides, using EMT and a 2D FDE solver.	121
4.3	(a) Top view schematic of SWG-engineered SiN waveguide. 3D FDTD simulated (b) photonic bandstructures and (c) corresponding effective (solid lines) and group (dashed lines) indices of SWG devices with varying grating period Λ . Dashed black lines correspond to a wavelength (λ) of 1550 nm. (d) Floquet-Bloch mode propagating in the SWG SiN waveguide. Transverse mode distributions are shown across the SiN segment (top right) and within the gap between SiN segments (bottom right) for in-plane TE polarization.	122
4.4	(a) Top view scanning electron microscope (SEM) image of SWG edge coupler. (b) Optical microscope image of fabricated SWG ring resonator. (c) Top view SEM image of coupling section of SWG ring resonator circuit with a 1.2 μm gap. (d, e) Detailed magnified views of (a) and (c), as marked.	124
4.5	Measured transmission spectrum for SiN SWG ring resonator with 2 μm gap. Inset: Critically coupled resonances near 1610 nm wavelength with a maximum ER of ~ 14 dB.	125
4.6	Fitted resonances near 1540 nm wavelength for over-coupled (blue), critically coupled (red) and under-coupled (green) SiN SWG ring resonators with 400 μm ring radius and varying gap sizes.	126
4.7	(a) Full measured transmission spectrum, (b) zoomed-in C-band spectrum, and (c) fitted resonance near 1540 nm wavelength for under-coupled SiN SWG ring resonator covered with water.	127

4.8	Measured internal (black triangles) and loaded (red squares) Q factors with the corresponding polynomial fitting curves for SWG ring resonator with 2 μm gap over the C- and L-bands.	129
5.1	(a) Cross sectional diagram of FDE-simulated Al_2O_3 -coated SWG metamaterial waveguide approximated using EMT. (b) Approximated core refractive index of SWG waveguide with SiN core and Al_2O_3 cladding materials as a function of SWG duty cycle based on EMT calculation.	143
5.2	2D FDE simulated (a) mode effective index (n_{eff}), (b) group index (n_g), (c) mode overlap with the Al_2O_3 cladding ($\gamma_{\text{Al}_2\text{O}_3}$), and (d) mode confinement factor in the Al_2O_3 cladding ($\Gamma_{\text{Al}_2\text{O}_3}$) for EMT-approximated SWG metamaterial waveguides with varying waveguide width (w_{wg}) and Al_2O_3 cladding thickness ($t_{\text{Al}_2\text{O}_3}$) and fixed duty cycles (δ) of (i) 0.5, (ii) 0.7, and (iii) 1.	144
5.3	2D FDE simulated TE mode profiles for selected strip waveguide with (a) 100 nm and (b) 500 nm Al_2O_3 cladding thickness, as well as selected SWG metamaterial waveguide with (c) 100 nm and (d) 500 nm Al_2O_3 cladding thickness. The core refractive index of the SWG waveguide with $\delta = 0.5$ is approximated using EMT.	145
5.4	Refractive and group indices of (a) SiN, (b) SiO_2 , and (c) Al_2O_3 materials used in FDTD simulations.	147
5.5	3D model of Al_2O_3 -coated SiN SWG metamaterial waveguide structure simulated in FDTD.	148
5.6	3D FDTD simulated (a) dispersion relation and (b) corresponding effective (top) and group (bottom) refractive indices for Al_2O_3 -coated SiN SWG metamaterial waveguide structure. Legend values in (a) indicate Al_2O_3 cladding thickness ($t_{\text{Al}_2\text{O}_3}$) on left and grating period (Λ) on right, both in units of nm.	149
5.7	3D FDTD simulated Floquet-Bloch mode propagation through the Al_2O_3 -coated SiN SWG metamaterial waveguide (left) and corresponding TE mode profiles across the SiN segments (top right) and within the gap between the SiN segments (bottom right) for waveguides with different simulated $t_{\text{Al}_2\text{O}_3}$ and Λ values.	151
5.8	(a) Mask layout schematic and (b) corresponding optical microscope image of fabricated Al_2O_3 -coated SiN SWG metamaterial waveguides in a spiral configuration with varying lengths.	153

5.9	Custom tALD reactor. (a) 2 ALD reactors with corresponding electronics racks below them in a vented enclosure. (b) Right-side ALD reactor with reaction chamber, attachment points for RT bubblers, and MFCs for gas delivery shown. (c) Open ALD reaction chamber with heated substrate stage and 8 precursor inlets at the top of the reactor shown. (d) Zoomed in image of the reaction chamber. Inset shows inserted stage with clip-mounted waveguide chips and substrate samples receiving ALD films. . . .	154
5.10	(a) J. A. Woollam M-2000 VASE and (b) Metricon 2010/M prism coupler system used for characterizing ALD Al_2O_3 and $\text{Al}_2\text{O}_3/\text{Er}_2\text{O}_3$ films. . . .	156
5.11	ALD Al_2O_3 (A) and $\text{Al}_2\text{O}_3/\text{Er}_2\text{O}_3$ (AE) film characterization results obtained from the VASE. Measured film refractive index (a) as a function of wavelength and (b) with respect to Al:Er cycle ratio for 632.8 nm and 1550 nm wavelengths. . . .	156
5.12	Measured A06 Al_2O_3 film loss with respect to wavelengths in the VIS and NIR spectra. Inset shows green (top) and red (bottom) light propagation through Al_2O_3 film during prism coupling measurements. . . .	158
5.13	ALD $\text{Al}_2\text{O}_3/\text{Er}_2\text{O}_3$ (AE) film characterization results from Metricon prism coupler. (a) Measured film loss with respect to wavelength (points) and corresponding absorption cross section data from literature (lines). (b) Measured film loss with respect to absorption cross section (points) with linear regression fit over data used to extrapolate film background loss and Er ion concentration (lines). . . .	159
5.14	Optical microscope images of (a) normal SiN waveguides and (b) SiN waveguides damaged by flaking during the deposition of ALD $\text{Al}_2\text{O}_3/\text{Er}_2\text{O}_3$ film AE05. . . .	161
5.15	Passive measurement results for fabricated Al_2O_3 -coated SiN SWG metamaterial waveguides. (a) Measured TE-polarized transmission spectra of spiral waveguides with varying length. (b) Measured and fitted insertion loss with respect to SWG waveguide length for various wavelengths across the C- and L-bands. Calculated (c) propagation and (d) coupling loss across all measured wavelengths using linear regression fitting technique from (b). . . .	163

5.16	Passive cutback measurement results for fabricated SiN waveguides coated in hybrid Al ₂ O ₃ /Er ₂ O ₃ ALD films. (a) Measured TE-polarized transmission spectra and (b) fitted insertion loss at 1650 nm wavelength as a function of waveguide length for SiN wire waveguides coated in film AE02. (c) Measured TE-polarized transmission spectra and (d) fitted insertion loss at 1650 nm wavelength as a function of waveguide length for SWG metamaterial waveguides coated in film AE03.	164
5.17	(a) Measured transmission for a 0.64 cm-long SiN (i) wire waveguide coated in film AE02 and (ii) SWG metamaterial waveguide coated in film AE03, broken down into loss contributions from optical fiber transmission (α_{fiber}), fiber-chip coupling (α_{coup}), background loss in the coated SiN waveguide (α_{bg}), and Er absorption (α_{Er}). (b) Isolated Er absorption loss. (c) Calculated effective absorption and emission cross sections based on Eq. 5.7 and 5.8, respectively.	167
5.18	Gain measurements for the fabricated 0.64 cm-long SiN (i) wire waveguide coated in film AE02 and (ii) SWG metamaterial waveguide coated in film AE03. (a) Measured insertion loss across the spectral gain region of interest (1520–1570 nm) for unpumped (black) and pumped (coloured) waveguides. Colour of spectra changes from blue to red as the launched pump power increases. Dotted lines represent power thresholds for surpassing Er absorption loss (dark grey) and achieving internal net gain (light grey). Corresponding measured (b) signal enhancement and (c) internal net gain with respect to launched pump power for 1533 nm (light grey) and 1550 nm (dark grey) wavelengths.	170

List of Tables

1.1	Comparison of Si and SiN photonic materials.	3
1.2	Comparison of fundamental TE mode profiles for SOI strip waveguides and SWG metamaterial waveguides with different top cladding oxide materials.	12
2.1	Summary of Si-TeO ₂ SWG designs studied during this PhD project, with corresponding results from 2D FDE simulations.	50
2.2	Optimal Si SWG edge couplers based on 2D FDE simulations.	59
2.3	Summary of fabricated Si-TeO ₂ SWG designs.	63
2.4	Design #3 mask layout details. Block IDs correspond to Fig. 2.18.	73
3.1	Calculated SMC width for SiN waveguides.	91
3.2	Calculated peak coupling efficiencies for designed SiN edge couplers.	95
3.3	Best measured polarization-independent SiN edge couplers.	97
3.4	Measurement summary of SiO ₂ -clad SiN ring resonators with $R = 250 \mu\text{m}$	102
3.5	Loss comparison of single mode waveguides for commercially available 1.3- and 1.5- μm moderate confinement SiN platforms.	104
4.1	Sensitivity calculations for water-coated SiN waveguides obtained from 3D FDTD simulations.	126
5.1	2D FDE simulation results for selected SiN-Al ₂ O ₃ waveguides designs shown in Fig. 5.3.	146
5.2	3D FDTD results for simulated Al ₂ O ₃ -coated SiN SWG metamaterial waveguide structures.	150
5.3	Summary of variable parameters used for ALD Al ₂ O ₃ /Er ₂ O ₃ film depositions.	155
5.4	Summary of ALD Al ₂ O ₃ /Er ₂ O ₃ film simulation and measurement results.	157
5.5	Summary of passive cutback measurement results for Al ₂ O ₃ /Er ₂ O ₃ -coated SiN waveguides.	166
5.6	Gain measurement results for Al ₂ O ₃ /Er ₂ O ₃ -coated SiN waveguides.	171

List of Acronyms (A-H)

Al_2O_3	aluminum oxide / alumina
$\text{Al}_2\text{O}_3:\text{Er}^{3+}$	erbium-doped aluminum oxide
$\text{Al}_2\text{O}_3/\text{Er}_2\text{O}_3$	alumina/erbia
ALD	atomic layer deposition
AMF	Advanced Micro Foundry
ANT	Applied Nanotools Inc.
ASE	amplified spontaneous emission
BEOL	back-end-of-line
BOX	buried oxide
CAD	computer-aided design
CEDT	Centre for Emerging Device Technologies
CMOS	complementary-metal-oxide-semiconductor
CVD	chemical vapour deposition
DC	directional coupler
DI	de-ionized
DUV	deep-ultraviolet
EBL	electron beam lithography
EM	electromagnetic
EME	eigenmode expansion
EMT	effective medium theory
ER	extinction ratio
Er	erbium
Er_2O_3	erbium oxide / erbia
ETU	energy transfer upconversion
FDE	finite difference eigenmode
FDTD	finite-difference-time-domain
FEM	finite element method
FWM	four-wave mixing
Ge	germanium
HSQ	hydrogen silsesquioxane

List of Acronyms (I-R)

ICP	inductively coupled plasma
IMF	index matching fluid
InGaAs	indium gallium arsenide
InP	indium phosphide
IR	infrared
LF	lensed fiber
LiDAR	light detection and ranging
LPCVD	low pressure chemical vapour deposition
MFD	mode field diameter
MIR	mid-infrared
MFS	minimum feature size
MMI	multimode interference
MPW	multi-project wafer
MZI	Mach-Zehnder interferometer
NIR	near-infrared
PDA	post-deposition annealing
PDK	process design kit
PECVD	plasma enhanced chemical vapour deposition
PIC	photonic integrated circuit
PLC	planar lightwave circuit
PLD	pulsed laser deposition
PML	perfectly matched layer
RBS	Rutherford backscattering spectrometry
RE	rare-earth
RF	radio frequency
RIE	reactive ion etching
RTA	rapid thermal annealing

List of Acronyms (S-Z)

SCG	supercontinuum generation
SEM	scanning electron microscope
SiEPIC	Silicon Electronic & Photonic Integrated Circuit
Si	silicon
SiN	silicon nitride
Si ₃ N ₄	silicon nitride (stoichiometric)
SiO ₂	silicon dioxide
SiP	silicon photonics
SMC	single mode cutoff
SMF	single mode fiber
SOI	silicon-on-insulator
SWG	subwavelength grating
SWGfb	subwavelength grating fishbone
SEM	scanning electron microscope
tALD	thermal atomic layer deposition
TE	transverse electric
TeO ₂	tellurium oxide
TeO ₂ :Er ³⁺	erbium-doped tellurium oxide
TiW	titanium-tungsten
TM	transverse magnetic
TMA	trimethylaluminium
TMAH	tetramethylammonium hydroxide
TPA	two photon absorption
VASE	variable angle spectroscopic ellipsometer
VIS	visible
WDM	wavelength-division-multiplexer
WG	waveguide

Declaration of Academic Achievement

I, Cameron M. Naraine, declare that this thesis titled, “**Development and functionalization of subwavelength grating metamaterials in silicon-based photonic integrated circuits,**” and works presented in it are my own and were led by myself.

Contributions made by others to this work are as listed:

Chapter 2

- AMF fabricated the SOI waveguide chips.
- CMC Microsystems and the SiEPIC program coordinated the MPW run by AMF in which Design #1 was included.
- Jeremy Miller collected and edited all SEM images.
- Henry Frankis and Bruno Segat Frare developed the TeO₂ sputtering recipes and deposited the TeO₂ films for the devices discussed in Design #1 and Design #2, respectively.

Chapter 3

- ANT fabricated all the SiN waveguide chips.
- Jocelyn Westwood-Bachman performed all VASE measurements on the SiN films, and experimentally characterized the grating coupler and some MMI coupler components.
- Cameron Horvath collected all SEM images.
- Bruno Segat Frare assisted with the grating coupler simulations.
- Batoul Hashemi assisted with the edge coupler and some MMI coupler measurements.
- Hamidu Mbonde assisted with the MMI coupler simulations, and many of the designs and mask layouts over multiple fabrication runs.

Chapter 4

- ANT fabricated all the SiN waveguide chips.
- Batoul Hashemi and Niloofar Majidian Taleghani assisted with water-coated device measurements.

Chapter 5

- Nicholas Hoffman deposited all of the Al₂O₃ films.
- Batoul Hashemi performed all prism coupling measurements and some VASE measurements on the Al₂O₃ and Al₂O₃/Er₂O₃ film samples, as well as many of the passive measurements and gain measurements on the Al₂O₃- and Al₂O₃/Er₂O₃-coated SiN waveguide samples.

Chapter 1

Introduction

1.1 Integrated optics

The revolution of photonic integrated circuits (PICs) began with the proposal of integrated optics [1], which involves the miniaturization of complex optical systems onto a single substrate. Many individual components needed for a fully integrated photonic system were developed in the 1970s on various material platforms, including lithium niobate (LiNbO_3), germanium (Ge), and III-V semiconductors [2; 3]. In the mid-1980s, silicon (Si) was proposed and demonstrated as a viable material for PICs, spawning the field of silicon photonics (SiP) [4; 5]. The rise of fiber optical networks and the internet in the 1990s provided a greater need for optical functionality to overcome the limitations of electrical circuits, including huge transmission loss, expensive power consumption, strong heat generation, low bandwidth capacity, and large susceptibility to electromagnetic interference and crosstalk. This led to the development of integrated photonics manufacturing infrastructure [6; 7; 8] and, more recently, to the implementation of optical interconnects within data centers [9], which continue to receive overwhelming amounts of data traffic as we progress into the “Zettabyte Era” [10]. PICs are also being developed for applications such as biomedical sensing [11], quantum optics [12], spectroscopy [13], light detection and range (LiDAR) [14; 15], augmented reality display technology [15], artificial intelligence [16], and free-space wireless communication networks [17]. More applications for integrated photonics devices are expected to arise with technology evolving day by day, so research efforts continue to focus on improving device performance, exploring new functionalities, and expanding the library of integrated photonic components.

Optical circuits have many basic functionalities that are required to realize a fully integrated system on a chip. The basic optical data link circuit [18] includes waveguides for

directing light, optical sources such as lasers, amplifiers for regenerating optical signals deteriorated by loss, optical modulators and switches for on-chip signal modification, and detectors for signal conversion between the optical and electrical domains. Other components that may be required include combiners/splitters, filters, multiplexers, time delay elements, etc.

The primary challenge with integrated optics is finding the proper material or combination of materials that provide optimal performance of all the necessary functions required for an optical circuit and can be fabricated at low cost and with high production yield. Various materials have been used for integrated photonic applications. The ecosystem of photonics has also been shifting towards a ‘fabless’ industry model [19]. This is where foundries first establish a standard, inexpensive, high-quality photonic material platform with a library of verified, high-performance components, i.e., a process design kit (PDK). The PDK and platform are then accessed by third party designers from academia and industry, typically in the form of multi-project wafer (MPW) runs, where multiple designs are manufactured onto a single, shared wafer and then diced into individual chips for distribution to their respective clients [20]. The most appealing photonic materials and devices are those compatible with complementary-metal-oxide-semiconductor (CMOS) fabrication technology, which has formed the backbone of the microelectronics industry. CMOS technology yields high-quality, inexpensive integrated circuits with very high-volume output.

1.2 Si and SiN photonics

The silicon-on-insulator (SOI) platform has become the premium choice for PIC manufacturing primarily due to its compatibility with CMOS processing infrastructure. Following the first demonstration of SOI waveguides in the mid-1980s [4; 5], Si received significant attention as a photonic material [21]. It was recognized as an excellent material for fiber-optic communication applications thanks to its optical transparency in both the second and third telecommunication windows (1.31 and 1.55 μm , respectively). Furthermore, the high-index-contrast of SOI enables high integration density of multiple optical pathways that can manage a high number of data channels per chip [8]. This led to commercialization of various SiP products, including integrated gyroscopes, pressure sensors, interferometers, optical transceivers, and wavelength division multiplexers (WDMs) [8; 22]. Though Si excels at performing the various passive functions required for a PIC, it struggles with performing active functionalities on its own. The centrosymmetric crystal structure of Si causes the Pockels effect to vanish, making switching and

modulation much more difficult compared to III-V semiconductors. Additionally, Si is a poor light emitter due to its indirect bandgap and short non-radiative recombination lifetimes [23; 24].

Silicon nitride (SiN) is another material that is receiving significant interest thanks to its benefits as both a complementary and alternative material to Si. Table 1.1 summarizes the pros and cons of Si and SiN. For starters, SiN, like Si, is CMOS compatible. The index contrast of SiN is much lower than Si yet still relatively high when compared to planar lightwave circuits (PLCs) based on silica glass (e.g., $\Delta n_{\text{Si}} \approx 2$, $\Delta n_{\text{SiN}} \approx 0.5$, $\Delta n_{\text{PLC}} \leq 0.1$). This maintains large integration density and compact footprints in SiN PICs while providing greater design flexibility, lower scattering losses and higher tolerance to fabrication variance over high contrast SOI [25; 26]. SiN exhibits optical transparency throughout the visible (VIS) and near-infrared (NIR) spectra, making it suitable for a wide range of applications, including sensing and biomedical imaging [27]. For active functionality, SiN exhibits negligible two photon absorption (TPA) yet maintains advantageous nonlinear optical properties, such as low third order nonlinear susceptibility, that have been exploited in dispersion engineering, four-wave mixing (FWM), and supercontinuum generation (SCG) [28; 29], helping drive applications such as quantum and nonlinear optics. These attractive properties make SiN a valuable material for PICs [30; 31]. However, like Si, SiN has challenges with active functionalities such as switching, light generation and amplification, modulation, and detection. As a result, intensive research is being conducted towards integration of Si and SiN with each other and with other active photonic materials to realize the full functionality of the sought-after optical superchip [21].

TABLE 1.1: Comparison of Si and SiN photonic materials.

Quality	Si	SiN
CMOS compatible?	Yes	Yes
Refractive index contrast (Δn)	~ 2	~ 0.5
Integration density	High	Moderate
Scattering loss	High	Low
Birefringence	High	Low
Optical transparency	NIR	VIS & NIR
TPA	High	Low

1.3 Subwavelength grating (SWG) metamaterials

1.3.1 Overview / state-of-the-art

SWG metamaterials are structures periodically arranged using two different dielectric media. These metamaterials suppress diffraction effects of light by employing a period smaller than the guided wavelength. Since 2006 [32], SWG metamaterials have been implemented in SOI waveguides to achieve efficient light propagation [33]. They have also been demonstrated in various components and devices [34; 35; 36; 37; 38; 39], leveraging the macroscopic optical properties of the constituent materials and the unique, artificial behaviour of the synthesized composite medium. This has generated enhanced device performance and functionality across a broad array of applications in integrated optics.

Subwavelength structures were first explored by Heinrich Hertz in the late 19th century [40]. Theoretical work on periodically layered media was established soon after by Lord Rayleigh [41], who used an array of parallel dielectric cylinders to predict the birefringence effect that arises from wave propagation through subwavelength structures. In the 1950s, a groundbreaking theoretical study was presented by Rytov [42], who demonstrated that periodically stacked media on a subwavelength scale behave as a homogeneous medium with an effective dielectric permittivity that is dependent not only on the properties of the constituent materials but also on the structural geometry and the polarization of the incident wave. Antireflective subwavelength structures were first discovered in the cornea of night-flying moths in the 1960s [43]. The observed subwavelength array of microscopic pillars serves as camouflage from predators by suppressing residual reflections from the insect's eyes. This inspired the use of subwavelength patterning in anti-reflective lenses in the following years [44]. Since then, optical subwavelength structures have been used in many other applications, including polarizers [45] and free-space optics [46; 47].

Subwavelength metamaterial structures gained significant interest in PICs when they were first suggested and demonstrated by the National Research Council (NRC) Canada for waveguiding in the SOI platform [32; 33]. These waveguides, called SWG metamaterial waveguides, have achieved widespread practical success in SOI as they leverage CMOS manufacturing technology without introducing further fabrication complexity [36]. Like many components in SOI, SWG metamaterial waveguides can be fabricated using a single full-etch step. Furthermore, the lithographic techniques employed by CMOS foundries currently allow feature sizes near or below 100 nm (~ 60 nm for immersion deep-ultraviolet (DUV) lithography), which is small enough for Si

subwavelength structures operating at telecommunication wavelengths. As a result, SWG metamaterial engineering has been implemented in many Si-based components. While many comprehensive review articles have highlighted these devices over the years [36; 34; 35; 37; 38; 39], a few worth mentioning include anti-reflective facets [48], waveguide crossings [49], multiplexers [50], fiber-chip edge couplers [48; 50; 51], surface grating couplers [52; 53; 54; 55; 56; 57; 58; 59; 60; 61; 62], switches [63], filters [64; 65; 66], ring resonators [67; 68; 69; 70], sensors [67; 68; 69; 70; 71; 72; 73; 74], modulators [74; 75], directional couplers [66; 76; 77; 78], nanophotonic beam splitters [79; 80], and devices with managed polarization, anisotropy, and dispersion [81; 82; 83; 84; 85; 86; 87; 88]. SWG-engineered devices are now available in PDKs offered by SiP foundries [89; 90]. Finally, SWG structures are also being explored for mid-infrared wavelength applications, e.g. using suspended Si [91; 92; 93; 94] and Ge [95] platforms.

1.3.2 Fundamentals

SWG metamaterials are a specific category of photonic crystals [96; 97]. Fig. 1.1(a) illustrates an SWG metamaterial waveguide in its most basic form in integrated optics. The waveguide comprises a 1D array of pillars aligned periodically along the propagation axis of the guided mode. Each pillar has a segment length l , width w , and thickness t , is composed of a core material with refractive index n_1 , and is spaced evenly from its adjacent neighbours by a grating period Λ . The waveguide is suspended within a cladding material with refractive index n_2 and sits atop a substrate material with refractive index n_3 . The duty cycle δ of the grating structure is defined as the ratio of the segment length to the period ($\delta = l/\Lambda$). The optical properties of the periodic waveguide are determined by the relationship between Λ , the operating free space wavelength λ , and the waveguide mode effective index n_{eff} . We define three notable operating regions for the periodic waveguide structure, which are individually depicted in the dispersion diagram in Fig. 1.1(b):

- When $\Lambda > \lambda/(2n_{\text{eff}})$, the grating operates within the diffraction regime, where light entering the structure is scattered and radiates into the space above and below the waveguide. Grating couplers primarily operate in this regime. Radiation of the guided mode here contributes significant loss, though lossless propagation is possible under certain configurations, including diffraction-less propagation [98] and Huygens waveguiding [99].
- When $\Lambda \approx \lambda/(2n_{\text{eff}})$, the grating operates within the Bragg regime (or the photonic bandgap), where no propagating optical modes exist. Any light entering

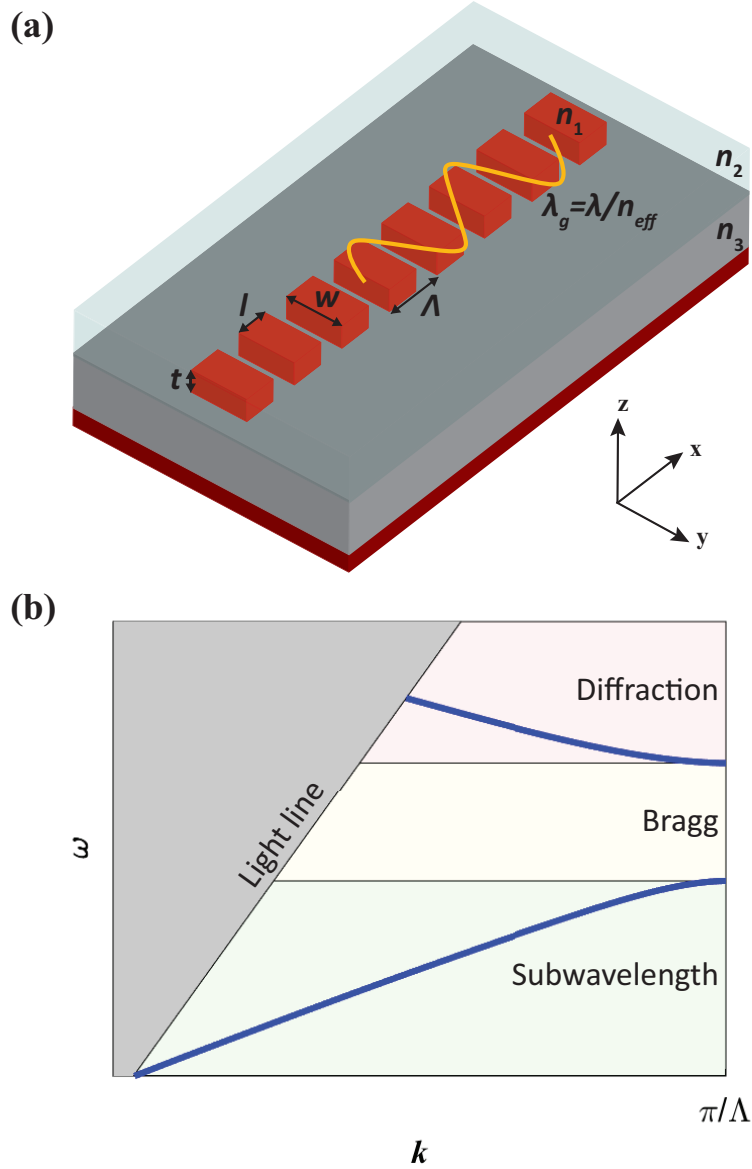


FIGURE 1.1: (a) 3D model and (b) dispersion relation diagram for a periodic waveguide.

the structure is immediately reflected by the grating. Gratings in this regime are appropriately named Bragg gratings, which are heavily incorporated in spectral filters.

- When $\Lambda < \lambda/(2n_{eff})$, the grating operates within the subwavelength regime, where diffraction and reflection effects are suppressed. When the period is substantially

smaller than the guided wavelength, the waveguide supports (theoretically) lossless Floquet-Bloch modes. In this regime, the gratings can be approximated as a homogeneous anisotropic waveguide medium with an equivalent refractive index as described by effective medium theory (EMT) [42]:

$$n_{\parallel}^2 = \delta n_1^2 + (1 - \delta)n_2^2, \quad (1.1)$$

$$\frac{1}{n_{\perp}^2} = \frac{\delta}{n_1^2} + \frac{(1 - \delta)}{n_2^2}, \quad (1.2)$$

where n_1 and n_2 denote the refractive indices of the constituent core and cladding materials, respectively, and n_{\parallel} and n_{\perp} denote the first order approximation of the equivalent refractive indices for the polarization parallel and perpendicular to the grating structure, respectively. For smaller λ/Λ ratios, higher order approximations must be considered for a more accurate calculation of the equivalent refractive indices [100; 101].

For brevity, any device discussed in this thesis that features SWG metamaterials is a lengthwise periodic structure [35] operating along the first order photonic band in the subwavelength regime (e.g., bottom blue line in Fig. 1.1(b)). As a result, any calculations utilizing the EMT approximation will use Eq. 1.1 unless stated otherwise.

1.3.3 Integrated optics material considerations for SWGs

SWG metamaterials are now considered a fundamental building block in integrated photonics as they offer many advantages, including ultrabroadband performance and precise control over polarization, anisotropy, dispersion, and the electromagnetic field distribution [39]. These benefits have been extensively investigated and demonstrated in the SOI platform, where all structures feature an Si waveguide core ($n_1 \approx 3.48$) and typically a cladding composed of silicon dioxide (SiO_2 , $n_2 \approx 1.44$) or air ($n_2 = 1$), depending on the application. From Eq. 1.1, this means the equivalent refractive index of the composite material can be tuned approximately between $\{1.44, 3.48\}$ for the case of SiO_2 cladding, or between $\{1, 3.48\}$ for the case of air cladding, by solely adjusting the duty cycle δ . This refractive index averaging effect shows that SWG waveguides have a lower effective index compared to a conventional strip waveguide (analogous to an SWG waveguide with $\delta = 1$) with an equivalent geometrical cross-section. Fig. 1.2(a,b) compares the fundamental transverse electric (TE) mode profiles ($\lambda = 1550$ nm) of a standard SOI strip waveguide against an SOI SWG metamaterial waveguide with $\delta = 0.5$ approximated by EMT ($n_{\parallel} \approx 2.66$). Both have SiO_2 cladding surrounding

the Si core waveguide, which has 220 nm thickness and 500 nm width. The reduced effective index in the SWG waveguide generates an enlarged optical waveguide mode that experiences greater interaction with the environment outside of the core waveguide material compared to the strip waveguide. This is particularly beneficial for evanescent field sensing applications, where the increased mode overlap with the top cladding sensing medium effectively enhances the sensitivity of the device [71]. This principle holds for any sensing medium with a low refractive index ($n_2 < 1.5$), which is interchangeable depending on the type of sensor (e.g., air for gas sensors [67], de-ionized (DI) water for biosensors requiring microfluidic channels [68; 73]).

1.3.3.1 Functional cladding materials

Other top cladding materials outside of the conventional ones (e.g., SiO₂, water, air) have been proposed and used to improve performance and discover new capabilities in SWG metamaterial waveguides. Some of the first SWG waveguide demonstrations applied SU-8 polymer ($n \approx 1.58$) as the upper cladding material and reported propagation loss as low as 2.1 dB/cm with negligible polarization and wavelength dependent loss [33]. SU-8 polymer was also used to produce athermal SWG waveguides by balancing the large positive thermo-optic coefficient of Si with the polymer's negative thermo-optic coefficient [102]. Chalcogenide glass (As₂₀S₈₀) was proposed and demonstrated as an athermal top cladding for SOI SWG metamaterial waveguides [103]. It also possesses benefits such as high refractive index ($n \approx 2.15$), wide optical transparency, photosensitivity, high non-linearity, and desirable low density for Brillouin photonics. These demonstrations reveal that there is vast potential in the exploration of other cladding materials for SWG metamaterial waveguides that may enhance performance metrics and unlock unique properties for new and exciting applications.

Aluminum oxide (Al₂O₃) is a glass material with many properties that make it attractive for integrated photonic devices. Its relatively high refractive index ($n \approx 1.65$) compared to other oxide materials and low optical loss across a broad spectral range make it an ideal waveguide material for various applications [104]. Furthermore, the fortuitous thermal, chemical, and mechanical properties of Al₂O₃ make it compatible with standard processing techniques, such as lithography, and able to undergo various etching methods, including ion-beam, reactive ion etching (RIE), and acid immersion wet etching [105; 106]. Amorphous Al₂O₃ serves as an excellent host material for rare-earth (RE) dopants, which are widely used for optical amplification and lasing in telecommunications among other applications [107]. Al₂O₃ has been heavily researched for decades, leading to many thin film fabrication methods including pulsed

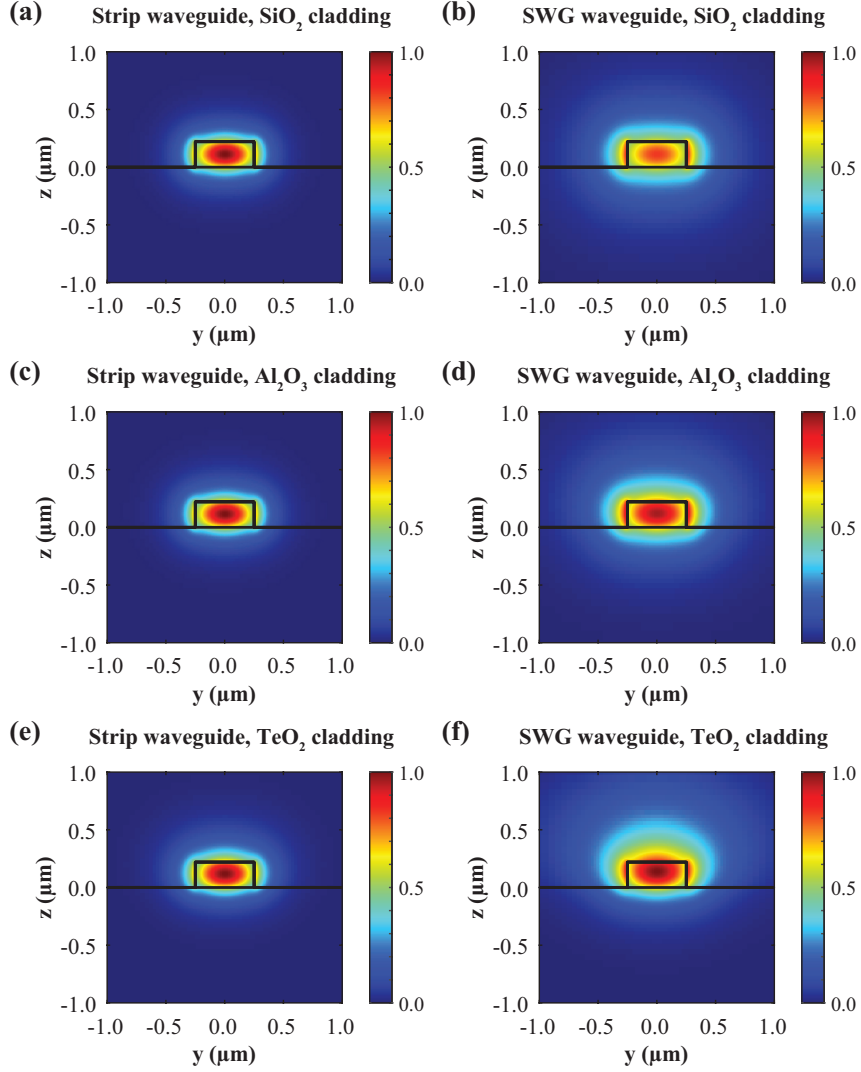


FIGURE 1.2: Fundamental TE mode profiles for Si (a) strip and (b) SWG waveguides with SiO_2 top cladding, (c) strip and (d) SWG waveguides with Al_2O_3 top cladding, and (e) strip and (f) SWG waveguides with TeO_2 top cladding. Each waveguide has 220 nm thickness and 500 nm width.

laser deposition (PLD) [108], chemical vapour deposition (CVD) [109], atomic layer deposition (ALD) [110], the sol-gel method [111], and reactive magnetron sputtering [104; 105; 107; 112; 113; 114]. Of these, reactive magnetron sputtering is a preferred method for thin film applications in integrated optics thanks to its fast, highly uniform, and wafer-scale deposition of low OH^- content material from low-cost precursor targets and its seamless integration with CMOS fabrication technology [114]. In

addition, RE ion incorporation is readily available with the option to simultaneously “co-sputter” high purity Al and RE metallic targets in the same chamber at different rates for films with precisely controlled atomic concentrations [105; 114]. Various Al_2O_3 optical amplifier and laser devices fabricated from reactive co-sputtering have been demonstrated on silicon chips both as etched channel waveguides and as a cladding gain medium on hybrid Si-based waveguide structures with RE ion dopants such as erbium (Er^{3+}) [107; 114; 115; 116; 117; 118; 119; 120; 121; 122; 123; 124; 125; 126; 127], ytterbium (Yb^{3+}) [127], thulium (Tm^{3+}) [128; 129], holmium (Hm^{3+}) [130], and co-doped $\text{Er}^{3+}:\text{Yb}^{3+}$ [131; 132]. ALD is another interesting deposition method for Al_2O_3 films. By sequentially growing Al_2O_3 monolayers under self-limiting conditions, ALD produces excellent quality Al_2O_3 films with ultralow loss and extremely high purity, uniformity and conformality [110; 133; 134; 135]. RE ion incorporation is possible by sequentially growing atomic layers of a RE-based oxide (e.g., erbium oxide Er_2O_3) between cycles of the primary material (e.g., Al_2O_3), which can be adjusted for precise control over the dopant concentration in the resulting RE-doped thin film [136]. ALD $\text{Al}_2\text{O}_3/\text{Er}_2\text{O}_3$ films have been demonstrated as a gain medium for on-chip optical amplifiers, both as the core material in a ridge waveguide configuration [136; 137] and as a cladding material over SiN slot and strip waveguides [138; 139]. The ALD growth process is important for slot waveguides since the deposited material completely fills in the nanoscale gap between the SiN waveguide rails [140; 141]. Such a benefit can be utilized for SWG waveguides, which have nanovoid features between the grating segments. ALD films have many drawbacks compared to sputtering, including very low deposition rates, considerable amounts of organic impurities from leftover precursor materials, small substrate area deposition, and incompatibility with CMOS processing [114]. Nevertheless, ALD serves as a good method for depositing high quality Al_2O_3 films for novel integrated optical devices, such as those discussed throughout this thesis.

Tellurium oxide (TeO_2) is another glass material that shares many similar attributes with Al_2O_3 that make it an appealing waveguide material, including an even higher refractive index ($n \approx 2.1$) than Al_2O_3 [142]. It is less explored than Al_2O_3 and has weaker chemical and thermal stability, making it harder to etch and therefore fabricate for optical waveguides [143; 144]. Nevertheless, like Al_2O_3 , TeO_2 is readily available through reactive magnetron sputtering, so it can be incorporated into a CMOS pilot line and deposited directly onto existing waveguide structures with no patterning required [143; 144; 145; 146]. Furthermore, it possesses various properties that make it an appealing waveguide gain medium and nonlinear optical material, including suitable bonding sites for trivalent rare-earth ion dopants, large emission cross-sections,

wide emission bandwidth, low phonon energies for reduced non-radiative decay, high nonlinear refractive index, low TPA, and large Raman and Brillouin gain coefficients [142; 143; 144; 147; 148]. This has prompted many demonstrations of Si-based PICs with sputtered TeO₂ layers for microring and microcavity resonators [149; 150; 151], sensors [152; 153], non-linear devices [154; 155; 156; 157], and optical amplifiers and lasers utilizing Er³⁺ [158; 159] and Tm³⁺ [160; 161; 162; 163] dopants.

Both Al₂O₃ and TeO₂ have broad potential as cladding materials for SWG waveguides to expand their performance and functionality in various integrated optics applications. Because of their high refractive indices compared to other oxide materials, including SiO₂, SWG waveguides with Al₂O₃ and TeO₂ cladding have a lower core-cladding index contrast, so they experience significantly less loss from sidewall scattering [164]. As attractive host materials for RE ions, Al₂O₃ or TeO₂ can act as monolithically integrated active gain media for waveguide amplifiers constructed using a CMOS foundry process. Fig. 1.2(c-f) show the fundamental TE mode profiles for SOI strip waveguides and EMT-approximated SWG metamaterial waveguides with Al₂O₃ (c,d) and TeO₂ (e,f) top claddings, respectively. Compared to the SWG waveguide with SiO₂ cladding in Fig. 1.2(b), greater modal confinement in the upper cladding is observed for the SWG waveguides with the Al₂O₃ and TeO₂ cladding materials due to their higher refractive indices. This increases the mode overlap with the top cladding material, which is essential for waveguide amplifiers utilizing a RE-doped upper cladding gain medium. Furthermore, because the mode is pulled up towards the high index cladding, substrate leakage loss is significantly reduced. This is a common issue for SWG metamaterial waveguides coated with lower index materials [165]. Regardless of the cladding, its overlap is strengthened in SWG waveguides over strip waveguides since the latter confines the mode more strictly to the waveguide core. This is observed throughout Fig. 1.2, which plots both strip and SWG waveguide modes against one another, and in Table 1.2, which summarizes the waveguide details and mode profile results. The mode overlap with the upper cladding material (γ_{clad}) and the confinement factor in the upper cladding material (Γ_{clad}) are described as [166]:

$$\gamma_{\text{clad}} = \frac{\iint_{\text{clad}} \varepsilon |\mathbf{E}|^2 dydz}{\iint_{\infty} \varepsilon |\mathbf{E}|^2 dydz}, \quad (1.3)$$

$$\Gamma_{\text{clad}} = \frac{n_g}{n_{\text{clad}}} \gamma_{\text{clad}}, \quad (1.4)$$

where ε is the relative permittivity, \mathbf{E} is the electric field, n_g is the group index of the waveguide mode, and n_{clad} is the upper cladding material refractive index. These equations will be used throughout the thesis to quantify the performance of the various

reported devices, which each have different upper cladding materials (e.g., TeO₂, Al₂O₃, SiO₂, water, etc.).

TABLE 1.2: Comparison of fundamental TE mode profiles for 220 nm × 500 nm SOI strip waveguides ($\delta = 1$) and SWG metamaterial waveguides ($\delta = 0.5$) with different top cladding oxide materials from Fig. 1.2.

Cladding	SiO ₂		Al ₂ O ₃		TeO ₂	
n_{clad}	1.44		1.65		2.1	
Waveguide	Strip (a)	SWG (b)	Strip (c)	SWG (d)	Strip (e)	SWG (f)
n_{\parallel}	3.48	2.66	3.48	2.72	3.48	2.87
n_{eff}	2.44	1.70	2.48	1.83	2.58	2.14
n_{g}	4.05	2.66	3.96	2.67	3.74	2.67
A_{eff}	0.19	0.45	0.19	0.43	0.21	0.52
γ_{clad}	0.06	0.23	0.08	0.29	0.15	0.46
Γ_{clad}	0.17	0.42	0.19	0.47	0.27	0.58

1.3.3.2 Alternative SWG metamaterial waveguide materials

While the field of subwavelength integrated photonics has been established and primarily demonstrated in Si [36], there is not much representation of SWG metamaterials in other material platforms in integrated optics. An initial demonstration has already been made for compound indium phosphide (InP)-on-insulator in the form of anti-reflection facets [167]. However, the fabrication of such devices is relatively complex compared to SOI. There is a lot of potential in applying the principles of subwavelength metamaterial engineering in other material platforms compatible with SiP technology. This would introduce the advantages of SWG metamaterials to other scalable waveguide materials with applications that SOI cannot compensate.

As highlighted in Table 1.1, SiN has many enticing properties as a complementary material to Si. The exploration of subwavelength metamaterials in SiN can be considered to follow a similar path to the early research stages of Si SWGs [36]. SiN SWG structures were first discussed in free space optics [168]. Optomechanical systems have used SiN for membrane-type resonators because of its low motional mass and low optical absorption [169]. High-contrast gratings patterned into SiN via electron beam lithography (EBL) can be designed to have zero order diffraction and high reflectivity while exhibiting remarkable mechanical quality factor and finesse [170]. This was demonstrated in a subwavelength high-contrast grating membrane composed of SiN for a membrane-in-the-middle optomechanical cavity system [171]. For integrated nanophotonic devices,

SiN SWG structures have been primarily demonstrated in lens systems and configurations, including low contrast concentrating lenses [172] and silicon-rich SiN metalenses [173]. SWGs consisting of interleaving SiN host and Si inclusion materials were also used to demonstrate a waveguide taper based on the Luneberg lens and a waveguide crossing based on Maxwell’s fisheye lens [174]. Other mentions of SiN SWGs in the literature include the design of layered Si/SiN polarization beam splitters [175] and the demonstration of suspended SWGs for optical beam shaping [176].

While research of SiN-based SWG structures is well underway, the current PIC devices reported in the literature are targeted towards very specific applications and sometimes use SWG material configurations that are complex to fabricate. Considering that SiN is a CMOS compatible material that can be fabricated alongside SOI and is becoming well-established in many SiP foundries, it is appealing to implement SWGs on established SiN platforms within the scope of the fabless industry model, which has not yet been done. Following the footsteps of the successful implementation of SWGs in SOI, it is essential to establish conventional passive SWG building blocks in SiN such as waveguides, couplers, crossings, splitters, and resonators, and then expand the component library towards more advanced structures.

1.4 Thesis overview

1.4.1 Thesis objective

The objective of this thesis is to investigate the design, fabrication, and characterization of novel SWG metamaterial waveguide structures and expand the SWG metamaterial device library for the Si and SiN integrated photonic platforms. The achievement of this objective first required the careful study and design of SWG metamaterial waveguide devices made from CMOS-compatible waveguide materials (Si, SiN) embedded in functional cladding materials (Al_2O_3 , TeO_2) for novel SWG applications, such as on-chip optical amplification. The limitations in the current fabrication technology were also considered. Following design, development of various high-quality thin film fabrication processes as well as experimental characterization and analysis of fabricated test structures and devices were performed. This thesis describes the process of incorporating SWG metamaterial structures into new waveguide platforms, such as SiN, and other unique photonic materials, and uses experimental demonstrations to highlight the potential of these devices for applications in evanescent field sensing and light amplification. The hope for this work is to inspire and motivate other researchers in industry

and academia to contribute to this surging field and expand the component library and application portfolio of SWG metamaterials in integrated photonics.

1.4.2 Statement of thesis work

This thesis represents a collection of research work with the central theme of proposing, developing, and implementing new material configurations in subwavelength integrated photonic devices and applications. The thesis includes 2 published manuscripts and 3 in preparation for submission. The published manuscripts included in the thesis have a preceding statement indicating reproduction with permission and any additions that were made for the purpose of the thesis preparation and presentation.

Chapter 2 presents a published manuscript and subsequent design work on TeO₂-coated SOI SWG metamaterial waveguides. The detailed design process for implementing a new cladding material for SOI SWG metamaterials is presented, along with details for the single-step back-end-of-line (BEOL) deposition process used for the TeO₂ thin films and characterization of the fabricated devices. A proposal and demonstration of other SWG-engineered integrated photonic components for the hybrid Si-TeO₂ material platform are also given.

Chapter 3 presents a manuscript in preparation on a rapid prototyping foundry process for SiN PICs. The SiN waveguide fabrication process is explained, and the additional post-processing options are listed. Essential PDK components, including strip waveguides, fiber-chip couplers, multimode interference (MMI) couplers, and ring resonators are demonstrated and reported. The competitiveness of the platform with other mature SiN foundries is assessed and its highlights are mentioned, including feature size dimensions that are essential for fabricating SWG metamaterial waveguide structures.

Chapter 4 presents a published manuscript on the first demonstration of SWG metamaterial waveguides and ring resonators fabricated using a SiN foundry process. The design, fabrication, and characterization of these devices are investigated. The reported metrics are comparable to equivalent SiN strip waveguides and competitive with SOI SWG devices reported in literature, highlighting the prospects of SWG metamaterials in different material platforms outside of SOI. The resonator's viability as a competitive SiN waveguide sensor for microfluidic applications is also discussed and presented.

Chapter 5 presents a manuscript in preparation on SiN SWG metamaterial waveguides functionalized by hybrid Al₂O₃/Er₂O₃ thin films for optical amplification. Different strip and SWG waveguide designs are compared, and the thermal atomic layer

deposition (tALD) process used for growing undoped and Er-doped Al_2O_3 thin films directly onto the SiN waveguides is explained. Gain measurements revealed signal power enhancement in all measured devices, with the SWG-engineered waveguides exhibiting superior amplification metrics over their strip waveguide counterparts. The discussion of future steps, including methods for reducing background waveguide loss to achieve internal net gain in the devices, concludes the chapter.

Chapter 6 summarizes the work in the thesis, discusses future pathways for building on the presented work, and emphasizes how such endeavours will impact the field of integrated optics.

1.4.3 Summary of publications

The following is a list of journal articles by the author that have contributed to the results presented in this thesis:

- **C. M. Naraine**, J. N. Westwood-Bachman, C. Horvath, M. Aktary, A. P. Knights, J. H. Schmid, P. Cheben, and J. D. B. Bradley, “Subwavelength grating metamaterial waveguides and ring resonators on a silicon nitride platform,” *Laser & Photonics Reviews*, vol. 17, no. 2, p. 2200216, 2023.
- **C. M. Naraine**, J. W. Miller, H. C. Frankis, D. E. Hagan, P. Mascher, J. H. Schmid, P. Cheben, A. P. Knights, and J. D. B. Bradley, “Subwavelength grating metamaterial waveguides functionalized with tellurium oxide cladding,” *Optics Express*, vol. 28, no. 12, pp. 18538–18547, 2020.
- **C. M. Naraine**, B. Hashemi, N. A. Hoffman, A. P. Knights, D. J. H. Emslie, J. H. Schmid, P. Cheben, and J. D. B. Bradley, “Silicon nitride subwavelength grating metamaterial waveguide amplifiers enabled by atomic layer deposited hybrid $\text{Al}_2\text{O}_3/\text{Er}_2\text{O}_3$ cladding,” *manuscript in preparation*.
- **C. M. Naraine**, B. L. Segat Frare, B. Hashemi, A. P. Knights, J. H. Schmid, P. Cheben, and J. D. B. Bradley, “Silicon fishbone subwavelength grating metamaterial waveguides coated in tellurium oxide,” *manuscript in preparation*.
- **C. M. Naraine**, J. N. Westwood-Bachman, C. Horvath, H. M. Mbonde, B. L. Segat Frare, B. Hashemi, P. Torab Ahmadi, K. Setzer, A. McKinlay, K. Mirabbas Kiani, R. Wang, A. P. Knights, P. Mascher, J. H. Schmid, P. Cheben, M. Aktary, and J. D. B. Bradley, “A moderate confinement 1.3 and 1.5 μm silicon nitride

platform enabled by a rapid prototyping integrated photonics foundry process,”
manuscript in preparation.

The author has also contributed to the following conference presentations, posters, and proceedings:

- P. Cheben, J. H. Schmid, J. Zhang, M. Saad Bin-Alam, A. F. Hinestrosa, W. Fraser, R. Korček, J. M. Luque-González, C. P. Armenta, A. Sánchez-Postigo, A. Ortega-Moñux, J. G. Wangüemert-Pérez, I. Molina-Fernández, R. Halir, P. Ginel-Moreno, D. Benedikovič, M. Dado, S. Khajavi, W. N. Ye, Z. Mokeddem, D. Melati, C. Alonso-Ramos, D. González-Andrade, L. Vivien, D. Sirmaci, I. Staude, D.-X. Xu, Y. Grinberg, S. Janz, S. Wang, M. Vachon, R. Cheriton, R. Fernández de Cabo, A. V. Velasco, **C. M. Naraine**, J. D. B. Bradley, and A. P. Knights, “Metamaterial integrated photonics,” *2024 Photonics North (PN)*, Vancouver, BC, Canada, 28-30 May 2024, Keynote.
- J. H. Schmid, P. Cheben, J. Zhang, M. Milanizadeh, S. Bin-Alam, D.-X. Xu, R. Cheriton, M. Vachon, S. Wang, R. Ma, W. Fraser, S. Khajavi, W. N. Ye, P. Ginel Moreno, J. M. Luque-González, A. F. Hinestrosa, A. Sánchez-Postigo, R. Halir, J. G. Wangüemert-Pérez, A. Ortega-Moñux, Í. Molina-Fernández, Z. Mokkedem, D. Melati, C. Alonso-Ramos, L. Vivien, R. Korcek, D. Benedikovic, **C. M. Naraine**, J. D. B. Bradley, Y. D. Sirmaci, and I. Staude, “Recent advances in integrated photonics with subwavelength and resonant metamaterials,” Proc. SPIE PC12889, Integrated Optics: Devices, Materials, and Technologies XXVIII, San Francisco, CA, USA, PC128890M (13 March 2024).
- J. D. B. Bradley, B. L. Segat Frare, B. Hashemi, P. Torab Ahmadi, M. A. Méndez-Rosales, N. Majidian Taleghani, **C. M. Naraine**, K. Mirabbas Kiani, H. C. Frankis, D. B. Bonneville, J. H. Schmid, P. Cheben, P. Ravi Selvaganapathy, P. Mascher, and A. P. Knights, “Prospects and design considerations for hybrid glass-silicon waveguides,” Proc. SPIE PC12891, Silicon Photonics XIX, San Francisco, CA, USA, PC1289107 (13 March 2024).
- **C. M. Naraine**, B. Hashemi, N. A. Hoffman, A. P. Knights, D. J. H. Emslie, J. H. Schmid, P. Cheben, and J. D. B. Bradley, “Silicon nitride subwavelength grating metamaterial waveguides functionalized with atomic layer deposited Al_2O_3 cladding,” *2023 Photonics North (PN)*, Montreal, QC, Canada, 12-15 June 2023, poster PS-63.

- J. D. B. Bradley, H. M. Mbonde, B. L. Segat Frare, N. Singh, M. Sinobad, T. Wildi, **C. M. Naraine**, P. Torab Ahmadi, B. Hashemi, M. A. Méndez-Rosales, H. C. Frankis, D. B. Bonneville, K. Mirabbas Kiani, R. Wang, J. N. Westwood-Bachman, C. Horvath, M. Aktary, R. Mateman, A. Leinse, J. H. Schmid, P. Cheben, P. Mascher, A. P. Knights, T. Herr, and F. Kärtner, “Active, passive and nonlinear integrated photonics in tellurite-coated silicon nitride,” in *Conference on Lasers and Electro-Optics*, San Jose, CA, USA, Technical Digest Series (Optica Publishing Group, 2023), paper JM2O.3.
- C. Horvath, J. N. Westwood-Bachman, K. Setzer, A. McKinlay, **C. M. Naraine**, H. M. Mbonde, B. L. Segat Frare, P. Torab Ahmadi, P. Mascher, J. D. B. Bradley, and M. Aktary, “Prototyping of silicon nitride photonic integrated circuits for visible and near-infrared applications,” *Proc. SPIE 12424, Integrated Optics: Devices, Materials, and Technologies XXVII*, San Francisco, CA, USA, 1242404 (17 March 2023).
- **C. M. Naraine**, J. N. Westwood-Bachman, C. Horvath, M. Aktary, A. P. Knights, J. H. Schmid, P. Cheben, and J. D. B. Bradley, “Silicon nitride ring resonators based on subwavelength grating metamaterials,” *2022 Photonics North (PN)*, Niagara Falls, ON, Canada, 24-26 May 2022, paper 255-s627-282.
- **C. M. Naraine**, J. N. Westwood-Bachman, C. Horvath, M. Aktary, A. P. Knights, J. H. Schmid, P. Cheben, and J. D. B. Bradley, “Silicon nitride waveguides based on subwavelength grating metamaterials,” *2022 Photonics North (PN)*, Niagara Falls, ON, Canada, 24-26 May 2022, paper 255-EABR-282.
- C. Horvath, J. N. Westwood-Bachman, K. Setzer, **C. M. Naraine**, H. M. Mbonde, B. L. Segat Frare, J. D. B. Bradley, and M. Aktary, “Prototyping of silicon nitride photonic integrated circuits using electron beam lithography,” *2022 Photonics North (PN)*, Niagara Falls, ON, Canada, 24-26 May 2022, paper 255-buMq-282.
- **C. M. Naraine**, J. N. Westwood-Bachman, C. Horvath, M. Aktary, A. P. Knights, J. H. Schmid, P. Cheben, and J. D. B. Bradley, “Silicon nitride ring resonators based on subwavelength grating metamaterials,” in *Conference on Lasers and Electro-Optics*, San Jose, CA, USA, Technical Digest Series (Optica Publishing Group, 2022), paper STh2H.3.
- J. D. B. Bradley, K. Mirabbas Kiani, H. C. Frankis, **C. M. Naraine**, D. B. Bonneville, H. M. Mbonde, and A. P. Knights, “Recent progress on rare earth

amplifiers and lasers directly on silicon,” *EPJ Web Conf.*, vol. 267, p. 02041, 2022.

- K. Mirabbas Kiani, H. C. Frankis, **C. M. Naraine**, D. B. Bonneville, A. P. Knights, and J. D. B. Bradley, “A thulium-silicon hybrid microdisk laser,” in *OSA Advanced Photonics Congress 2021*, OSA Technical Digest (Optica Publishing Group, 2021), paper JTh3A.2.
- **C. M. Naraine**, J. W. Miller, H. C. Frankis, P. Mascher, A. P. Knights, J. D. B. Bradley, J. H. Schmid, and P. Cheben, “Optimized design of tellurium oxide coated subwavelength grating metamaterial waveguides,” *2021 Photonics North (PN)*, Virtual Conference, 31 May–2 June 2021, paper 255-Z8me-293.
- **C. M. Naraine**, J. W. Miller, H. C. Frankis, D. E. Hagan, P. Mascher, J. H. Schmid, P. Cheben, A. P. Knights, and J. D. B. Bradley, “Subwavelength grating metamaterial waveguides functionalized with tellurium oxide cladding,” *2020 Photonics North (PN)*, Virtual Conference, 26-28 May 2020, paper PM-3-27-2.
- J. W. Miller, **C. M. Naraine**, H. C. Frankis, D. E. Hagan, A. P. Knights, P. Mascher, and J. D. B. Bradley, “Subwavelength grating waveguides functionalized with tellurium oxide cladding,” *2019 Photonics North (PN)*, Quebec City, QC, Canada, 21-23 May 2019, paper TD-8-23-3.

The author has also contributed as a co-author on the following publications which are not relevant to the thesis:

- N. Majidian Taleghani, **C. M. Naraine**, A. P. Knights, J. H. Schmid, P. Cheben, P. Ravi Selvaganapathy and J. D. B. Bradley, “Comparative analysis of bio-sensitivity in single-mode, polarization-independent silicon nitride microring resonators at telecom wavelengths,” *manuscript in preparation*.
- K. Mirabbas Kiani, H. C. Frankis, **C. M. Naraine**, D. B. Bonneville, A. P. Knights, and J. D. B. Bradley, “Lasing in a hybrid rare-earth silicon microdisk,” *Laser & Photonics Reviews*, vol. 16, no. 1, p. 2100348 (2022).

Bibliography

- [1] S. E. Miller, “Integrated optics: An introduction,” *Bell System Technical Journal*, vol. 48, no. 7, pp. 2059–2069, 1969.

- [2] S. E. Miller, E. A. J. Marcatili, and T. Li, “Research toward optical-fiber transmission systems,” *Proceedings of the IEEE*, vol. 61, no. 12, pp. 1703–1704, 1973.
- [3] H. Kogelnik, “An introduction to integrated optics,” *IEEE Transactions on Microwave Theory and Techniques*, vol. 23, no. 1, pp. 2–16, 1975.
- [4] R. A. Soref and J. P. Lorenzo, “Single-crystal silicon: a new material for 1.3 and 1.6 μm integrated-optical components,” *Electronics Letters*, vol. 21, pp. 953–954, 1985.
- [5] R. A. Soref and J. P. Lorenzo, “All-silicon active and passive guided-wave components for $\lambda = 1.3$ and 1.6 μm ,” *IEEE Journal of Quantum Electronics*, vol. 22, no. 6, pp. 873–879, 1986.
- [6] G. T. Reed, W. R. Headley, and C. E. Jason Png, “Silicon photonics: the early years,” in *Optoelectronic Integration on Silicon II* (J. A. Kubby and G. E. Jabbour, eds.), vol. 5730, pp. 1–18, International Society for Optics and Photonics, SPIE, 2005.
- [7] R. A. Soref, “The past, present, and future of silicon photonics,” *IEEE Journal of Selected Topics in Quantum Electronics*, vol. 12, no. 6, pp. 1678–1687, 2006.
- [8] D. Thomson, A. Zilkie, J. E. Bowers, T. Komljenovic, G. T. Reed, L. Vivien, D. Marris-Morini, E. Cassan, L. Viot, J.-M. Fédéli, J.-M. Hartmann, J. H. Schmid, D.-X. Xu, F. Boeuf, P. O’Brien, G. Z. Mashanovich, and M. Nedeljkovic, “Roadmap on silicon photonics,” *Journal of Optics*, vol. 18, no. 7, p. 073003, 2016.
- [9] Q. Cheng, M. Bahadori, M. Glick, S. Rumley, and K. Bergman, “Recent advances in optical technologies for data centers: a review,” *Optica*, vol. 5, no. 11, pp. 1354–1370, 2018.
- [10] Z.-W. Xu, “Cloud-sea computing systems: Towards thousand-fold improvement in performance per watt for the coming Zettabyte era,” *Journal of Computer Science and Technology*, vol. 29, no. 2, pp. 177–181, 2014.
- [11] M. Iqbal, M. A. Gleeson, B. Spaugh, F. Tybor, W. G. Gunn, M. Hochberg, T. Baehr-Jones, R. C. Bailey, and L. C. Gunn, “Label-free biosensor arrays based on silicon ring resonators and high-speed optical scanning instrumentation,” *IEEE Journal of Selected Topics in Quantum Electronics*, vol. 16, no. 3, pp. 654–661, 2010.

- [12] A. Politi, J. C. Matthews, M. G. Thompson, and J. L. O’Brien, “Integrated quantum photonics,” *IEEE Journal of Selected Topics in Quantum Electronics*, vol. 15, no. 6, pp. 1673–1684, 2009.
- [13] R. Baets, A. Z. Subramanian, A. Dhakal, S. K. Selvaraja, K. Komorowska, F. Peyskens, E. Ryckeboer, N. Yebo, G. Roelkens, and N. Le Thomas, “Spectroscopy-on-chip applications of silicon photonics,” in *Integrated Optics: Devices, Materials, and Technologies XVII* (J. E. Broquin and G. N. Conti, eds.), vol. 8627, p. 86270I, International Society for Optics and Photonics, SPIE, 2013.
- [14] C. V. Poulton, A. Yaacobi, D. B. Cole, M. J. Byrd, M. Raval, D. Vermeulen, and M. R. Watts, “Coherent solid-state LiDAR with silicon photonic optical phased arrays,” *Optics Letters*, vol. 42, no. 20, pp. 4091–4094, 2017.
- [15] J. Notaros, M. Notaros, M. Raval, C. V. Poulton, M. J. Byrd, N. Li, Z. Su, E. S. Magden, E. Timurdogan, T. Dyer, C. Baiocco, T. Kim, P. Bhargava, V. Stojanovic, and M. R. Watts, “Integrated optical phased arrays: LiDAR, augmented reality, and beyond,” in *OSA Advanced Photonics Congress (AP) 2019 (IPR, Networks, NOMA, SPPCom, PVLED)*, p. IM4A.2, Optica Publishing Group, 2019.
- [16] B. J. Shastri, A. N. Tait, T. Ferreira de Lima, W. H. P. Pernice, H. Bhaskaran, C. D. Wright, and P. R. Prucnal, “Photonics for artificial intelligence and neuro-morphic computing,” *Nature Photonics*, vol. 15, no. 2, pp. 102–114, 2021.
- [17] R. Sabella, “Silicon photonics for 5G and future networks,” *IEEE Journal of Selected Topics in Quantum Electronics*, vol. 26, no. 2, pp. 1–11, 2020.
- [18] N. Li, M. Xin, Z. Su, E. S. Magden, N. Singh, J. Notaros, E. Timurdogan, P. Purnawirman, J. D. B. Bradley, and M. R. Watts, “A silicon photonic data link with a monolithic erbium-doped laser,” *Scientific Reports*, vol. 10, p. 1114, 2020.
- [19] M. U. Khan, Y. Xing, Y. Ye, and W. Bogaerts, “Photonic integrated circuit design in a foundry+fabless ecosystem,” *IEEE Journal of Selected Topics in Quantum Electronics*, vol. 25, no. 5, pp. 1–14, 2019.
- [20] C. G. Littlejohns, D. J. Rowe, H. Du, K. Li, W. Zhang, W. Cao, T. Dominguez Bucio, X. Yan, M. Banakar, D. Tran, S. Liu, F. Meng, B. Chen, Y. Qi, X. Chen, M. Nedeljkovic, L. Mastronardi, R. Maharjan, S. Bohora, A. Dhakal, I. Crowe, A. Khurana, K. C. Balram, L. Zagaglia, F. Floris, P. O’Brien, E. Di Gaetano, H. M. Chong, F. Y. Gardes, D. J. Thomson, G. Z. Mashanovich, M. Sorel, and

- G. T. Reed, “CORNERSTONE’s silicon photonics rapid prototyping platforms: Current status and future outlook,” *Applied Sciences*, vol. 10, no. 22, p. 8201, 2020.
- [21] R. A. Soref, “Silicon-based optoelectronics,” *Proceedings of the IEEE*, vol. 81, no. 12, pp. 1687–1706, 1993.
- [22] A. Rickman, “The commercialization of silicon photonics,” *Nature Photonics*, vol. 8, pp. 579–582, 2014.
- [23] G. T. Reed, “The optical age of silicon,” *Nature*, vol. 427, pp. 595–596, 2004.
- [24] M. Lipson, “Guiding, modulating, and emitting light on silicon—Challenges and opportunities,” *Journal of Lightwave Technology*, vol. 23, no. 12, pp. 4222–4238, 2005.
- [25] J. F. Bauters, M. J. R. Heck, D. John, D. Dai, M.-C. Tien, J. S. Barton, A. Leinse, R. G. Heideman, D. J. Blumenthal, and J. E. Bowers, “Ultra-low-loss high-aspect-ratio Si_3N_4 waveguides,” *Optics Express*, vol. 19, no. 4, pp. 3163–3174, 2011.
- [26] R. Baets, A. Z. Subramanian, S. Clemmen, B. Kuyken, P. Bienstman, N. Le Thomas, G. Roelkens, D. Van Thourhout, P. Helin, and S. Severi, “Silicon photonics: Silicon nitride versus silicon-on-insulator,” in *2016 Optical Fiber Communications Conference and Exhibition (OFC)*, pp. 1–3, 2016.
- [27] P. Muñoz, G. Micó, L. A. Bru, D. Pastor, D. Pérez, J. D. Doménech, J. Fernández, R. Baños, B. Gargallo, R. Alemany, A. M. Sánchez, J. M. Cirera, R. Mas, and C. Domínguez, “Silicon nitride photonic integration platforms for visible, near-infrared and mid-infrared applications,” *Sensors*, vol. 17, no. 9, p. 2088, 2017.
- [28] S. Miller, K. Luke, Y. Okawachi, J. Cardenas, A. L. Gaeta, and M. Lipson, “On-chip frequency comb generation at visible wavelengths via simultaneous second- and third-order optical nonlinearities,” *Optics Express*, vol. 22, no. 22, pp. 26517–26525, 2014.
- [29] K. Luke, Y. Okawachi, M. R. E. Lamont, A. L. Gaeta, and M. Lipson, “Broadband mid-infrared frequency comb generation in a Si_3N_4 microresonator,” *Optics Letters*, vol. 40, no. 21, pp. 4823–4826, 2015.
- [30] D. J. Blumenthal, R. Heideman, D. Geuzebroek, A. Leinse, and C. Roeloffzen, “Silicon nitride in silicon photonics,” *Proceedings of the IEEE*, vol. 106, no. 12, pp. 2209–2231, 2018.

- [31] P. Muñoz, P. W. L. van Dijk, D. Geuzebroek, M. Geiselmann, C. Domínguez, A. Stassen, J. D. Doménech, M. Zervas, A. Leinse, C. G. H. Roeloffzen, B. Gargallo, R. Baños, J. Fernández, G. M. Cabanes, L. A. Bru, and D. Pastor, “Foundry developments toward silicon nitride photonics from visible to the mid-infrared,” *IEEE Journal of Selected Topics in Quantum Electronics*, vol. 25, no. 5, pp. 1–13, 2019.
- [32] P. Cheben, D.-X. Xu, S. Janz, and A. Densmore, “Subwavelength waveguide grating for mode conversion and light coupling in integrated optics,” *Optics Express*, vol. 14, no. 11, pp. 4695–4702, 2006.
- [33] P. J. Bock, P. Cheben, J. H. Schmid, J. Lapointe, A. Delâge, S. Janz, G. C. Aers, D.-X. Xu, A. Densmore, and T. J. Hall, “Subwavelength grating periodic structures in silicon-on-insulator: a new type of microphotonic waveguide,” *Optics Express*, vol. 18, no. 19, pp. 20251–20262, 2010.
- [34] J. H. Schmid, P. Cheben, P. J. Bock, R. Halir, J. Lapointe, S. Janz, A. Delâge, A. Densmore, J.-M. Fédéli, T. J. Hall, B. Lamontagne, R. Ma, Í. Molina-Fernández, and D.-X. Xu, “Refractive index engineering with subwavelength gratings in silicon microphotonic waveguides,” *IEEE Photonics Journal*, vol. 3, no. 3, pp. 597–607, 2011.
- [35] R. Halir, P. J. Bock, P. Cheben, A. Ortega-Moñux, C. Alonso-Ramos, J. H. Schmid, J. Lapointe, D.-X. Xu, J. G. Wangüemert-Pérez, Í. Molina-Fernández, and S. Janz, “Waveguide sub-wavelength structures: a review of principles and applications,” *Laser & Photonics Reviews*, vol. 9, no. 1, pp. 25–49, 2015.
- [36] P. Cheben, R. Halir, J. H. Schmid, H. A. Atwater, and D. R. Smith, “Subwavelength integrated photonics,” *Nature*, vol. 560, pp. 565–572, 2018.
- [37] R. Halir, A. Ortega-Moñux, D. Benedikovic, G. Z. Mashanovich, J. G. Wangüemert-Pérez, J. H. Schmid, Í. Molina-Fernández, and P. Cheben, “Subwavelength-grating metamaterial structures for silicon photonic devices,” *Proceedings of the IEEE*, vol. 106, no. 12, pp. 2144–2157, 2018.
- [38] J. M. Luque-González, A. Sánchez-Postigo, A. Hadij-ElHouati, A. Ortega-Moñux, J. G. Wangüemert-Pérez, J. H. Schmid, P. Cheben, Í. Molina-Fernández, and R. Halir, “A review of silicon subwavelength gratings: building break-through devices with anisotropic metamaterials,” *Nanophotonics*, vol. 10, no. 11, pp. 2765–2797, 2021.

- [39] P. Cheben, J. H. Schmid, R. Halir, J. M. Luque-González, J. G. Wangüemert-Pérez, D. Melati, and C. Alonso-Ramos, “Recent advances in metamaterial integrated photonics,” *Advances in Optics and Photonics*, vol. 15, no. 4, pp. 1033–1105, 2023.
- [40] H. Hertz, “Über strahlen elektrischer kraft,” *Wiedemanns Ann.*, vol. 36, p. 769, 1888.
- [41] L. Rayleigh, “LVI. On the influence of obstacles arranged in rectangular order upon the properties of a medium,” *The London, Edinburgh, and Dublin Philosophical Magazine and Journal of Science*, vol. 34, no. 211, pp. 481–502, 1892.
- [42] S. M. Rytov, “Electromagnetic properties of a finely stratified medium,” *Soviet Physics JETP*, vol. 2, no. 3, pp. 466–475, 1956.
- [43] C. G. Bernhard and W. H. Miller, “A corneal nipple pattern in insect compound eyes,” *Acta Physiologica Scandinavica*, vol. 56, no. 3-4, pp. 385–386, 1962.
- [44] P. B. Clapham and M. C. Hutley, “Reduction of lens reflexion by the ‘moth eye’ principle,” *Nature*, vol. 244, no. 5414, pp. 281–282, 1973.
- [45] P. Yeh, “A new optical model for wire grid polarizers,” *Optics Communications*, vol. 26, no. 3, pp. 289–292, 1978.
- [46] J. N. Mait and D. W. Prather in *Selected Papers on Subwavelength Diffractive Optics*, (SPIE Optical Engineering Press, Bellingham, WA, 2001).
- [47] M. W. Farn, “Binary gratings with increased efficiency,” *Applied Optics*, vol. 31, no. 22, pp. 4453–4458, 1992.
- [48] J. H. Schmid, P. Cheben, S. Janz, J. Lapointe, E. Post, A. Delâge, A. Densmore, B. Lamontagne, P. Waldron, and D.-X. Xu, “Subwavelength grating structures in silicon-on-insulator waveguides,” *Advances in Optical Technologies*, p. 685489, 2008.
- [49] P. J. Bock, P. Cheben, J. H. Schmid, J. Lapointe, A. Delâge, D.-X. Xu, S. Janz, A. Densmore, and T. J. Hall, “Subwavelength grating crossings for silicon wire waveguides,” *Optics Express*, vol. 18, no. 15, pp. 16146–16155, 2010.
- [50] P. Cheben, P. J. Bock, J. H. Schmid, J. Lapointe, S. Janz, D.-X. Xu, A. Densmore, A. Delâge, B. Lamontagne, and T. J. Hall, “Refractive index engineering with

- subwavelength gratings for efficient microphotonic couplers and planar waveguide multiplexers,” *Optics Letters*, vol. 35, no. 15, pp. 2526–2528, 2010.
- [51] P. Cheben, J. H. Schmid, S. Wang, D.-X. Xu, M. Vachon, S. Janz, J. Lapointe, Y. Painchaud, and M.-J. Picard, “Broadband polarization independent nanophotonic coupler for silicon waveguides with ultra-high efficiency,” *Optics Express*, vol. 23, no. 17, pp. 22553–22563, 2015.
- [52] R. Halir, P. Cheben, S. Janz, D.-X. Xu, Í. Molina-Fernández, and J. G. Wangüemert-Pérez, “Waveguide grating coupler with subwavelength microstructures,” *Optics Letters*, vol. 34, no. 9, pp. 1408–1410, 2009.
- [53] R. Halir, P. Cheben, J. H. Schmid, R. Ma, D. Bedard, S. Janz, D.-X. Xu, A. Densmore, J. Lapointe, and Í. Molina-Fernández, “Continuously apodized fiber-to-chip surface grating coupler with refractive index engineered subwavelength structure,” *Optics Letters*, vol. 35, no. 19, pp. 3243–3245, 2010.
- [54] R. Halir, L. Zavargo-Peche, D.-X. Xu, P. Cheben, R. Ma, J. H. Schmid, S. Janz, A. Densmore, A. Ortega-Moñux, Í. Molina-Fernández, M. Fournier, and J.-M. Fédeli, “Single etch grating couplers for mass fabrication with DUV lithography,” *Optical and Quantum Electronics*, vol. 44, no. 12, pp. 521–526, 2012.
- [55] D. Benedikovic, P. Cheben, J. H. Schmid, D.-X. Xu, J. Lapointe, S. Wang, R. Halir, A. Ortega-Moñux, S. Janz, and M. Dado, “High-efficiency single etch step apodized surface grating coupler using subwavelength structure,” *Laser & Photonics Reviews*, vol. 8, no. 6, pp. L93–L97, 2014.
- [56] C. Alonso-Ramos, P. Cheben, A. Ortega-Moñux, J. H. Schmid, D.-X. Xu, and Í. Molina-Fernández, “Fiber-chip grating coupler based on interleaved trenches with directionality exceeding 95%,” *Optics Letters*, vol. 39, no. 18, pp. 5351–5354, 2014.
- [57] Y. Wang, X. Wang, J. Flueckiger, H. Yun, W. Shi, R. Bojko, N. A. F. Jaeger, and L. Chrostowski, “Focusing sub-wavelength grating couplers with low back reflections for rapid prototyping of silicon photonic circuits,” *Optics Express*, vol. 22, no. 17, pp. 20652–20662, 2014.
- [58] D. Benedikovic, P. Cheben, J. H. Schmid, D.-X. Xu, B. Lamontagne, S. Wang, J. Lapointe, R. Halir, A. Ortega-Moñux, S. Janz, and M. Dado, “Subwavelength index engineered surface grating coupler with sub-decibel efficiency for 220-nm

- silicon-on-insulator waveguides,” *Optics Express*, vol. 23, no. 17, pp. 22628–22635, 2015.
- [59] D. Benedikovic, C. Alonso-Ramos, P. Cheben, J. H. Schmid, S. Wang, D.-X. Xu, J. Lapointe, S. Janz, R. Halir, A. Ortega-Moñux, J. G. Wangüemert-Pérez, Í. Molina-Fernández, J.-M. Fédéli, L. Vivien, and M. Dado, “High-directionality fiber-chip grating coupler with interleaved trenches and subwavelength index-matching structure,” *Optics Letters*, vol. 40, no. 18, pp. 4190–4193, 2015.
- [60] D. Benedikovic, C. Alonso-Ramos, S. Guerber, X. L. Roux, P. Cheben, C. Dupré, B. Szlag, D. Fowler, E. Cassan, D. Marris-Morini, C. Baudot, F. Boeuf, and L. Vivien, “Sub-decibel silicon grating couplers based on L-shaped waveguides and engineered subwavelength metamaterials,” *Optics Express*, vol. 27, no. 18, pp. 26239–26250, 2019.
- [61] M. Kamandar Dezfouli, Y. Grinberg, D. Melati, P. Cheben, J. H. Schmid, A. Sánchez-Postigo, A. Ortega-Moñux, J. G. Wangüemert-Pérez, R. Cheriton, S. Janz, and D.-X. Xu, “Perfectly vertical surface grating couplers using subwavelength engineering for increased feature sizes,” *Optics Letters*, vol. 45, no. 13, pp. 3701–3704, 2020.
- [62] T. Hao, A. Sánchez-Postigo, P. Cheben, A. Ortega-Moñux, and W. N. Ye, “Dual-band polarization-independent subwavelength grating coupler for wavelength demultiplexing,” *IEEE Photonics Technology Letters*, vol. 32, no. 18, pp. 1163–1166, 2020.
- [63] I. Glesk, P. J. Bock, P. Cheben, J. H. Schmid, J. Lapointe, and S. Janz, “All-optical switching using nonlinear subwavelength Mach-Zehnder on silicon,” *Optics Express*, vol. 19, no. 15, pp. 14031–14039, 2011.
- [64] J. Čtyroký, J. G. Wangüemert-Pérez, P. Kwiecien, I. Richter, J. Litvik, J. H. Schmid, Í. Molina-Fernández, A. Ortega-Moñux, M. Dado, and P. Cheben, “Design of narrowband bragg spectral filters in subwavelength grating metamaterial waveguides,” *Optics Express*, vol. 26, no. 1, pp. 179–194, 2018.
- [65] P. Cheben, J. Čtyroký, J. H. Schmid, S. Wang, J. Lapointe, J. G. Wangüemert-Pérez, Í. Molina-Fernández, A. Ortega-Moñux, R. Halir, D. Melati, D.-X. Xu, S. Janz, and M. Dado, “Bragg filter bandwidth engineering in subwavelength grating metamaterial waveguides,” *Optics Letters*, vol. 44, no. 4, pp. 1043–1046, 2019.

- [66] D. Charron, J. St-Yves, O. Jafari, S. LaRochelle, and W. Shi, “Subwavelength-grating contradirectional couplers for large stopband filters,” *Optics Letters*, vol. 43, no. 4, pp. 895–898, 2018.
- [67] V. Donzella, A. Sherwali, J. Flueckiger, S. M. Grist, S. T. Fard, and L. Chrostowski, “Design and fabrication of SOI micro-ring resonators based on sub-wavelength grating waveguides,” *Optics Express*, vol. 23, no. 4, pp. 4791–4803, 2015.
- [68] J. Flueckiger, S. Schmidt, V. Donzella, A. Sherwali, D. M. Ratner, L. Chrostowski, and K. C. Cheung, “Sub-wavelength grating for enhanced ring resonator biosensor,” *Optics Express*, vol. 24, no. 14, pp. 15672–15686, 2016.
- [69] E. Luan, H. Yun, L. Laplatine, Y. Dattner, D. M. Ratner, K. C. Cheung, and L. Chrostowski, “Enhanced sensitivity of subwavelength multibox waveguide microring resonator label-free biosensors,” *IEEE Journal of Selected Topics in Quantum Electronics*, vol. 25, no. 3, pp. 1–11, 2019.
- [70] H. Yan, L. Huang, X. Xu, S. Chakravarty, N. Tang, H. Tian, and R. T. Chen, “Unique surface sensing property and enhanced sensitivity in microring resonator biosensors based on subwavelength grating waveguides,” *Optics Express*, vol. 24, no. 26, pp. 29724–29733, 2016.
- [71] J. G. Wangüemert-Pérez, P. Cheben, A. Ortega-Moñux, C. Alonso-Ramos, D. Pérez-Galacho, R. Halir, Í. Molina-Fernández, D.-X. Xu, and J. H. Schmid, “Evanescent field waveguide sensing with subwavelength grating structures in silicon-on-insulator,” *Optics Letters*, vol. 39, no. 15, pp. 4442–4445, 2014.
- [72] E. Luan, H. Yun, M. Ma, D. M. Ratner, K. C. Cheung, and L. Chrostowski, “Label-free biosensing with a multi-box sub-wavelength phase-shifted bragg grating waveguide,” *Biomedical Optics Express*, vol. 10, no. 9, pp. 4825–4838, 2019.
- [73] L. Huang, H. Yan, X. Xu, S. Chakravarty, N. Tang, H. Tian, and R. T. Chen, “Improving the detection limit for on-chip photonic sensors based on subwavelength grating racetrack resonators,” *Optics Express*, vol. 25, no. 9, pp. 10527–10535, 2017.
- [74] X. Xu, Z. Pan, C.-J. Chung, C.-W. Chang, H. Yan, and R. T. Chen, “Sub-wavelength grating metamaterial racetrack resonator for sensing and modulation,” *IEEE Journal of Selected Topics in Quantum Electronics*, vol. 25, no. 3, pp. 1–8, 2019.

- [75] Z. Pan, X. Xu, C.-J. Chung, H. Dalir, H. Yan, K. Chen, Y. Wang, B. Jia, and R. T. Chen, “High-speed modulator based on electro-optic polymer infiltrated sub-wavelength grating waveguide ring resonator,” *Laser & Photonics Reviews*, vol. 12, no. 6, p. 1700300, 2018.
- [76] V. Donzella, A. Sherwali, J. Flueckiger, S. T. Fard, S. M. Grist, and L. Chrostowski, “Sub-wavelength grating components for integrated optics applications on SOI chips,” *Optics Express*, vol. 22, no. 17, pp. 21037–21050, 2014.
- [77] R. Halir, A. Maese-Novo, A. Ortega-Moñux, Í. Molina-Fernández, J. G. Wangüemert-Pérez, P. Cheben, D.-X. Xu, J. H. Schmid, and S. Janz, “Colorless directional coupler with dispersion engineered sub-wavelength structure,” *Optics Express*, vol. 20, no. 12, pp. 13470–13477, 2012.
- [78] Y. Wang, Z. Lu, M. Ma, H. Yun, F. Zhang, N. A. F. Jaeger, and L. Chrostowski, “Compact broadband directional couplers using subwavelength gratings,” *IEEE Photonics Journal*, vol. 8, no. 3, pp. 1–8, 2016.
- [79] R. Halir, P. Cheben, J. M. Luque-González, J. D. Sarmiento-Merenguel, J. H. Schmid, J. G. Wangüemert-Pérez, D.-X. Xu, S. Wang, A. Ortega-Moñux, and Í. Molina-Fernández, “Ultra-broadband nanophotonic beamsplitter using an anisotropic sub-wavelength metamaterial,” *Laser & Photonics Reviews*, vol. 10, no. 6, pp. 1039–1046, 2016.
- [80] V. Vakarin, D. Melati, T. T. D. Dinh, X. Le Roux, W. K. K. Kan, C. Dupré, B. Szeglag, S. Monfray, F. Boeuf, P. Cheben, E. Cassan, D. Marris-Morini, L. Vivien, and C. A. Alonso-Ramos, “Metamaterial-engineered silicon beam splitter fabricated with deep UV immersion lithography,” *Nanomaterials*, vol. 11, no. 11, p. 2949, 2021.
- [81] Z. Wang, X. Xu, D. Fan, Y. Wang, H. Subbaraman, and R. T. Chen, “Geometrical tuning art for entirely subwavelength grating waveguide based integrated photonics circuits,” *Scientific Reports*, vol. 6, p. 24106, 2016.
- [82] Z. Wang, X. Xu, D. Fan, Y. Wang, and R. T. Chen, “High quality factor sub-wavelength grating waveguide micro-ring resonator based on trapezoidal silicon pillars,” *Optics Letters*, vol. 41, no. 14, pp. 3375–3378, 2016.
- [83] H. Yun, L. Chrostowski, and N. A. F. Jaeger, “Ultra-broadband 2×2 adiabatic 3 dB coupler using subwavelength-grating-assisted silicon-on-insulator strip waveguides,” *Optics Letters*, vol. 43, no. 8, pp. 1935–1938, 2018.

- [84] D. González-Andrade, J. G. Wangüemert-Pérez, A. V. Velasco, A. Ortega-Moñux, A. Herrero-Bermello, Í. Molina-Fernández, R. Halir, and P. Cheben, “Ultra-broadband mode converter and multiplexer based on sub-wavelength structures,” *IEEE Photonics Journal*, vol. 10, no. 2, pp. 1–10, 2018.
- [85] D. González-Andrade, J. M. Luque-González, J. G. Wangüemert-Pérez, A. Ortega-Moñux, P. Cheben, Í. Molina-Fernández, and A. V. Velasco, “Ultra-broadband nanophotonic phase shifter based on subwavelength metamaterial waveguides,” *Photonics Research*, vol. 8, no. 3, pp. 359–367, 2020.
- [86] J. M. Luque-González, A. Herrero-Bermello, A. Ortega-Moñux, Í. Molina-Fernández, A. V. Velasco, P. Cheben, J. H. Schmid, S. Wang, and R. Halir, “Tilted subwavelength gratings: controlling anisotropy in metamaterial nanophotonic waveguides,” *Optics Letters*, vol. 43, no. 19, pp. 4691–4694, 2018.
- [87] J. M. Luque-González, R. Halir, J. G. Wangüemert-Pérez, J. de Oliva-Rubio, J. H. Schmid, P. Cheben, Í. Molina-Fernández, and A. Ortega-Moñux, “An ultracompact GRIN-lens-based spot size converter using subwavelength grating metamaterials,” *Laser & Photonics Reviews*, vol. 13, no. 11, p. 1900172, 2019.
- [88] J. M. Luque-González, A. Herrero-Bermello, A. Ortega-Moñux, M. Sánchez-Rodríguez, A. V. Velasco, J. H. Schmid, P. Cheben, Í. Molina-Fernández, and R. Halir, “Polarization splitting directional coupler using tilted subwavelength gratings,” *Optics Letters*, vol. 45, no. 13, pp. 3398–3401, 2020.
- [89] L. Chrostowski, H. Shoman, M. Hammood, H. Yun, J. Jhoja, E. Luan, S. Lin, A. Mistry, D. Witt, N. A. F. Jaeger, S. Shekhar, H. Jayatilleka, P. Jean, S. B.-d. Villers, J. Cauchon, W. Shi, C. Horvath, J. N. Westwood-Bachman, K. Setzer, M. Aktary, N. S. Patrick, R. J. Bojko, A. Khavasi, X. Wang, T. Ferreira de Lima, A. N. Tait, P. R. Prucnal, D. E. Hagan, D. Stevanovic, and A. P. Knights, “Silicon photonic circuit design using rapid prototyping foundry process design kits,” *IEEE Journal of Selected Topics in Quantum Electronics*, vol. 25, no. 5, pp. 1–26, 2019.
- [90] S. Y. Siew, B. Li, F. Gao, H. Y. Zheng, W. Zhang, P. Guo, S. W. Xie, A. Song, B. Dong, L. W. Luo, C. Li, X. Luo, and G.-Q. Lo, “Review of silicon photonics technology and platform development,” *Journal of Lightwave Technology*, vol. 39, no. 13, pp. 4374–4389, 2021.
- [91] J. Soler Penadés, C. Alonso-Ramos, A. Z. Khokhar, M. Nedeljkovic, L. A. Boodhoo, A. Ortega-Moñux, Í. Molina-Fernández, P. Cheben, and G. Z. Mashanovich,

- “Suspended SOI waveguide with sub-wavelength grating cladding for mid-infrared,” *Optics Letters*, vol. 39, no. 19, pp. 5661–5664, 2014.
- [92] J. Soler Penadés, A. Ortega-Moñux, M. Nedeljkovic, J. G. Wangüemert-Pérez, R. Halir, A. Z. Khokhar, C. Alonso-Ramos, Z. Qu, Í. Molina-Fernández, P. Cheben, and G. Z. Mashanovich, “Suspended silicon mid-infrared waveguide devices with subwavelength grating metamaterial cladding,” *Optics Express*, vol. 24, no. 20, pp. 22908–22916, 2016.
- [93] J. Soler Penadés, A. Sánchez-Postigo, M. Nedeljkovic, A. Ortega-Moñux, J. G. Wangüemert-Pérez, Y. Xu, R. Halir, Z. Qu, A. Z. Khokhar, A. Osman, W. Cao, C. G. Littlejohns, P. Cheben, Í. Molina-Fernández, and G. Z. Mashanovich, “Suspended silicon waveguides for long-wave infrared wavelengths,” *Optics Letters*, vol. 43, no. 4, pp. 795–798, 2018.
- [94] A. Sánchez-Postigo, J. G. Wangüemert-Pérez, J. Soler Penadés, A. Ortega-Moñux, M. Nedeljkovic, R. Halir, F. El Mokhtari Mimun, Y. Xu Cheng, Z. Qu, A. Z. Khokhar, A. Osman, W. Cao, C. G. Littlejohns, P. Cheben, G. Z. Mashanovich, and Í. Molina-Fernández, “Mid-infrared suspended waveguide platform and building blocks,” *IET Optoelectronics*, vol. 13, no. 2, pp. 55–61, 2019.
- [95] A. Sánchez-Postigo, A. Ortega-Moñux, D. Pereira-Martín, Í. Molina-Fernández, R. Halir, P. Cheben, J. S. Penadés, M. Nedeljkovic, G. Z. Mashanovich, and J. G. Wangüemert-Pérez, “Design of a suspended germanium micro-antenna for efficient fiber-chip coupling in the long-wavelength mid-infrared range,” *Optics Express*, vol. 27, no. 16, pp. 22302–22315, 2019.
- [96] J. D. Joannopoulos, P. R. Villeneuve, and S. Fan, “Photonic crystals: putting a new twist on light,” *Nature*, vol. 386, pp. 143–149, 1997.
- [97] J. D. Joannopoulos, S. G. Johnson, J. N. Winn, and R. D. Meade, *Photonic crystals: molding the flow of light*. Princeton University Press, 2nd ed., 2008.
- [98] C. Alonso-Ramos, X. Le Roux, J. Zhang, D. Benedikovic, V. Vakarín, E. Durán-Valdeiglesias, D. Oser, D. Pérez-Galacho, F. Mazeas, L. Labonté, S. Tanzilli, E. Cassan, D. Marris-Morini, P. Cheben, and L. Vivien, “Diffraction-less propagation beyond the sub-wavelength regime: a new type of nanophotonic waveguide,” *Scientific Reports*, vol. 9, p. 5347, 2019.

- [99] Y. D. Sirmaci, A. Barreda Gomez, T. Pertsch, J. H. Schmid, P. Cheben, and I. Staude, “All-dielectric Huygens’ meta-waveguides for resonant integrated photonics,” *Laser & Photonics Reviews*, vol. 17, no. 6, p. 2200860, 2023.
- [100] P. Lalanne and D. Lemercier-Lalanne, “On the effective medium theory of subwavelength periodic structures,” *Journal of Modern Optics*, vol. 43, no. 10, pp. 2063–2085, 1996.
- [101] P. Lalanne and J.-P. Hugonin, “High-order effective-medium theory of subwavelength gratings in classical mounting: application to volume holograms,” *Journal of the Optical Society of America A*, vol. 15, no. 7, pp. 1843–1851, 1998.
- [102] J. H. Schmid, M. Ibrahim, P. Cheben, J. Lapointe, S. Janz, P. J. Bock, A. Densmore, B. Lamontagne, R. Ma, W. N. Ye, and D.-X. Xu, “Temperature-independent silicon subwavelength grating waveguides,” *Optics Letters*, vol. 36, no. 11, pp. 2110–2112, 2011.
- [103] P. Jean, A. Douaud, S. LaRochelle, Y. Messaddeq, and W. Shi, “Silicon subwavelength grating waveguides with high-index chalcogenide glass cladding,” *Optics Express*, vol. 29, no. 13, pp. 20851–20862, 2021.
- [104] M. K. Smit, G. A. Acket, and C. J. van der Laan, “Al₂O₃ films for integrated optics,” *Thin Solid Films*, vol. 138, no. 2, pp. 171–181, 1986.
- [105] J. D. B. Bradley, F. Ay, K. Wörhoff, and M. Pollnau, “Fabrication of low-loss channel waveguides in Al₂O₃ and Y₂O₃ layers by inductively coupled plasma reactive ion etching,” *Applied Physics B*, vol. 89, no. 2, pp. 311–318, 2007.
- [106] B. Zhou and W. F. Ramirez, “Kinetics and modeling of wet etching of aluminum oxide by warm phosphoric acid,” *Journal of The Electrochemical Society*, vol. 143, no. 2, pp. 619–623, 1996.
- [107] G. N. van den Hoven, E. Snoeks, A. Polman, J. W. M. van Uffelen, Y. S. Oei, and M. K. Smit, “Photoluminescence characterization of Er-implanted Al₂O₃ films,” *Applied Physics Letters*, vol. 62, no. 24, pp. 3065–3067, 1993.
- [108] A. Suárez-García, J. Gonzalo, and C. N. Afonso, “Low-loss Al₂O₃ waveguides produced by pulsed laser deposition at room temperature,” *Applied Physics A*, vol. 77, no. 6, pp. 779–783, 2003.

- [109] Chang Jin Kang, J. S. Chun, and Wong Jong Lee, “Properties of aluminium oxide films prepared by plasma-enhanced metal-organic chemical vapour deposition,” *Thin Solid Films*, vol. 189, no. 1, pp. 161–173, 1990.
- [110] Y. Kim, S. M. Lee, C. S. Park, S. I. Lee, and M. Y. Lee, “Substrate dependence on the optical properties of Al₂O₃ films grown by atomic layer deposition,” *Applied Physics Letters*, vol. 71, no. 25, pp. 3604–3606, 1997.
- [111] M. Benatsou, B. Capoen, M. Bouazaoui, W. Tchana, and J. P. Vilcot, “Preparation and characterization of sol-gel derived Er³⁺:Al₂O₃-SiO₂ planar waveguides,” *Applied Physics Letters*, vol. 71, no. 4, pp. 428–430, 1997.
- [112] G. Este and W. D. Westwood, “Reactive deposition of low loss Al₂O₃ optical waveguides by modified dc planar magnetron sputtering,” *Journal of Vacuum Science & Technology A*, vol. 2, no. 3, pp. 1238–1247, 1984.
- [113] S. M. Arnold and B. E. Cole, “Ion beam sputter deposition of low loss Al₂O₃ films for integrated optics,” *Thin Solid Films*, vol. 165, no. 1, pp. 1–9, 1988.
- [114] K. Wörhoff, J. D. B. Bradley, F. Ay, D. Geskus, T. P. Blauwendraat, and M. Pollnau, “Reliable low-cost fabrication of low-loss Al₂O₃:Er³⁺ waveguides with 5.4-dB optical gain,” *IEEE Journal of Quantum Electronics*, vol. 45, no. 5, pp. 454–461, 2009.
- [115] J. D. B. Bradley, M. Costa e Silva, M. Gay, L. Bramerie, A. Driessen, K. Wörhoff, J.-C. Simon, and M. Pollnau, “170 Gbit/s transmission in an erbium-doped waveguide amplifier on silicon,” *Optics Express*, vol. 17, no. 24, pp. 22201–22208, 2009.
- [116] J. D. B. Bradley, L. Agazzi, D. Geskus, F. Ay, K. Wörhoff, and M. Pollnau, “Gain bandwidth of 80 nm and 2 dB/cm peak gain in Al₂O₃:Er³⁺ optical amplifiers on silicon,” *Journal of the Optical Society of America B*, vol. 27, no. 2, pp. 187–196, 2010.
- [117] J. D. B. Bradley, R. Stoffer, L. Agazzi, F. Ay, K. Wörhoff, and M. Pollnau, “Integrated Al₂O₃:Er³⁺ ring lasers on silicon with wide wavelength selectivity,” *Optics Letters*, vol. 35, no. 1, pp. 73–75, 2010.
- [118] J. D. B. Bradley, R. Stoffer, A. Bakker, L. Agazzi, F. Ay, K. Wörhoff, and M. Pollnau, “Integrated Al₂O₃:Er³⁺ zero-loss optical amplifier and power splitter with 40-nm bandwidth,” *IEEE Photonics Technology Letters*, vol. 22, no. 5, pp. 278–280, 2010.

- [119] S. A. Vázquez-Córdova, M. Dijkstra, E. H. Bernhardt, F. Ay, K. Wörhoff, J. L. Herek, S. M. García-Blanco, and M. Pollnau, “Erbium-doped spiral amplifiers with 20 dB of net gain on silicon,” *Optics Express*, vol. 22, no. 21, pp. 25993–26004, 2014.
- [120] L. Agazzi, J. D. B. Bradley, M. Dijkstra, F. Ay, G. Roelkens, R. Baets, K. Wörhoff, and M. Pollnau, “Monolithic integration of erbium-doped amplifiers with silicon-on-insulator waveguides,” *Optics Express*, vol. 18, no. 26, pp. 27703–27711, 2010.
- [121] M. Belt, T. Huffman, M. L. Davenport, W. Li, J. S. Barton, and D. J. Blumenthal, “Arrayed narrow linewidth erbium-doped waveguide-distributed feedback lasers on an ultra-low-loss silicon-nitride platform,” *Optics Letters*, vol. 38, no. 22, pp. 4825–4828, 2013.
- [122] M. Belt and D. J. Blumenthal, “Erbium-doped waveguide DBR and DFB laser arrays integrated within an ultra-low-loss Si₃N₄ platform,” *Optics Express*, vol. 22, no. 9, pp. 10655–10660, 2014.
- [123] Purnawirman, J. Sun, T. N. Adam, G. Leake, D. Coolbaugh, J. D. B. Bradley, E. S. Hosseini, and M. R. Watts, “C- and L-band erbium-doped waveguide lasers with wafer-scale silicon nitride cavities,” *Optics Letters*, vol. 38, no. 11, pp. 1760–1762, 2013.
- [124] E. S. Hosseini, Purnawirman, J. D. B. Bradley, J. Sun, G. Leake, T. N. Adam, D. D. Coolbaugh, and M. R. Watts, “CMOS-compatible 75 mW erbium-doped distributed feedback laser,” *Optics Letters*, vol. 39, no. 11, pp. 3106–3109, 2014.
- [125] E. S. Magden, N. Li, Purnawirman, J. D. B. Bradley, N. Singh, A. Ruocco, G. S. Petrich, G. Leake, D. D. Coolbaugh, E. P. Ippen, M. R. Watts, and L. A. Kolodziejski, “Monolithically-integrated distributed feedback laser compatible with CMOS processing,” *Optics Express*, vol. 25, no. 15, pp. 18058–18065, 2017.
- [126] D. B. Bonneville, C. E. Osornio-Martinez, M. Dijkstra, and S. M. García-Blanco, “High on-chip gain spiral Al₂O₃:Er³⁺ waveguide amplifiers,” *Optics Express*, vol. 32, no. 9, pp. 15527–15536, 2024.
- [127] J. D. B. Bradley, E. S. Hosseini, Purnawirman, Z. Su, T. N. Adam, G. Leake, D. Coolbaugh, and M. R. Watts, “Monolithic erbium- and ytterbium-doped microring lasers on silicon chips,” *Optics Express*, vol. 22, no. 10, pp. 12226–12237, 2014.

- [128] Z. Su, N. Li, E. S. Magden, M. Byrd, Purnawirman, T. N. Adam, G. Leake, D. Coolbaugh, J. D. B. Bradley, and M. R. Watts, “Ultra-compact and low-threshold thulium microcavity laser monolithically integrated on silicon,” *Optics Letters*, vol. 41, no. 24, pp. 5708–5711, 2016.
- [129] N. Singh, J. Lorenzen, M. Sinobad, K. Wang, A. C. Liapis, H. C. Frankis, S. Haugg, H. Francis, J. Carreira, M. Geiselmann, M. A. Gaafar, T. Herr, J. D. B. Bradley, Z. Sun, S. M. García-Blanco, and F. X. Kärtner, “Silicon photonics-based high-energy passively Q -switched laser,” *Nature Photonics*, vol. 18, no. 5, pp. 485–491, 2024.
- [130] N. Li, E. S. Magden, Z. Su, N. Singh, A. Ruocco, M. Xin, M. Byrd, P. T. Callahan, J. D. B. Bradley, C. Baiocco, D. Vermeulen, and M. R. Watts, “Broadband 2- μm emission on silicon chips: monolithically integrated Holmium lasers,” *Optics Express*, vol. 26, no. 3, pp. 2220–2230, 2018.
- [131] D. B. Bonneville, H. C. Frankis, R. Wang, and J. D. B. Bradley, “Erbium-ytterbium co-doped aluminium oxide waveguide amplifiers fabricated by reactive co-sputtering and wet chemical etching,” *Optics Express*, vol. 28, no. 20, pp. 30130–30140, 2020.
- [132] R. Wang, H. C. Frankis, H. M. Mbonde, D. B. Bonneville, and J. D. B. Bradley, “Erbium-ytterbium co-doped aluminum oxide thin films: Co-sputtering deposition, photoluminescence, luminescent lifetime, energy transfer and quenching fraction,” *Optical Materials*, vol. 111, p. 110692, 2021.
- [133] P. Kumar, M. K. Wiedmann, C. H. Winter, and I. Avrutsky, “Optical properties of Al_2O_3 thin films grown by atomic layer deposition,” *Applied Optics*, vol. 48, no. 28, pp. 5407–5412, 2009.
- [134] M. M. Aslan, N. A. Webster, C. L. Byard, M. B. Pereira, C. M. Hayes, R. S. Wiederkehr, and S. B. Mendes, “Low-loss optical waveguides for the near ultra-violet and visible spectral regions with Al_2O_3 thin films from atomic layer deposition,” *Thin Solid Films*, vol. 518, no. 17, pp. 4935–4940, 2010.
- [135] M. Demirtaş, C. Odacı, N. K. Perkgöz, C. Sevik, and F. Ay, “Low loss atomic layer deposited Al_2O_3 waveguides for applications in on-chip optical amplifiers,” *IEEE Journal of Selected Topics in Quantum Electronics*, vol. 24, no. 4, pp. 1–8, 2018.

- [136] K. Solehmainen, M. Kapulainen, P. Heimala, and K. Polamo, “Erbium-doped waveguides fabricated with atomic layer deposition method,” *IEEE Photonics Technology Letters*, vol. 16, no. 1, pp. 194–196, 2004.
- [137] M. Demirtaş and F. Ay, “High-gain $\text{Er}^{3+}:\text{Al}_2\text{O}_3$ on-chip waveguide amplifiers,” *IEEE Journal of Selected Topics in Quantum Electronics*, vol. 26, no. 5, pp. 1–8, 2020.
- [138] J. Rönn, W. Zhang, A. Autere, X. Leroux, L. Pakarinen, C. Alonso-Ramos, A. Säynätjoki, H. Lipsanen, L. Vivien, E. Cassan, and Z. Sun, “Ultra-high on-chip optical gain in erbium-based hybrid slot waveguides,” *Nature Communications*, vol. 10, p. 432, 2019.
- [139] J. Rönn, J. Zhang, W. Zhang, Z. Tu, A. Matikainen, X. Leroux, E. Durán-Valdeiglesias, N. Vulliet, F. Boeuf, C. Alonso-Ramos, H. Lipsanen, L. Vivien, Z. Sun, and E. Cassan, “Erbium-doped hybrid waveguide amplifiers with net optical gain on a fully industrial 300 mm silicon nitride photonic platform,” *Optics Express*, vol. 28, no. 19, pp. 27919–27926, 2020.
- [140] A. Säynätjoki, L. Karvonen, T. Alasaarela, X. Tu, T. Y. Liow, M. Hiltunen, A. Teronen, G. Q. Lo, and S. Honkanen, “Low-loss silicon slot waveguides and couplers fabricated with optical lithography and atomic layer deposition,” *Optics Express*, vol. 19, no. 27, pp. 26275–26282, 2011.
- [141] L. Karvonen, A. Saynatjoki, Y. Chen, X. Tu, T.-Y. Liow, J. Hiltunen, M. Hiltunen, G.-Q. Lo, and S. Honkanen, “Low-loss multiple-slot waveguides fabricated by optical lithography and atomic layer deposition,” *IEEE Photonics Technology Letters*, vol. 24, no. 22, pp. 2074–2076, 2012.
- [142] R. El-Mallawany, “The optical properties of tellurite glasses,” *Journal of Applied Physics*, vol. 72, no. 5, pp. 1774–1777, 1992.
- [143] S. J. Madden and K. T. Vu, “Very low loss reactively ion etched Tellurium Dioxide planar rib waveguides for linear and non-linear optics,” *Optics Express*, vol. 17, no. 20, pp. 17645–17651, 2009.
- [144] K. Vu and S. Madden, “Tellurium dioxide Erbium doped planar rib waveguide amplifiers with net gain and 2.8dB/cm internal gain,” *Optics Express*, vol. 18, no. 18, pp. 19192–19200, 2010.

- [145] S. M. Pietralunga, M. Lanata, M. Ferè, D. Piccinin, G. Cusmai, M. Torregiani, and M. Martinelli, “High-contrast waveguides in sputtered pure TeO₂ glass thin films,” *Optics Express*, vol. 16, no. 26, pp. 21662–21670, 2008.
- [146] H. C. Frankis, K. Mirabbas Kiani, D. B. Bonneville, C. Zhang, S. Norris, R. Mateman, A. Leinse, N. D. Bassim, A. P. Knights, and J. D. B. Bradley, “Low-loss TeO₂-coated Si₃N₄ waveguides for application in photonic integrated circuits,” *Optics Express*, vol. 27, no. 9, pp. 12529–12540, 2019.
- [147] S. Shen, A. Jha, X. Liu, M. Naftaly, K. Bindra, H. J. Bookey, and A. K. Kar, “Tellurite glasses for broadband amplifiers and integrated optics,” *Journal of the American Ceramic Society*, vol. 85, no. 6, pp. 1391–1395, 2002.
- [148] A. Mori, “Tellurite-based fibers and their applications to optical communication networks,” *Journal of the Ceramic Society of Japan*, vol. 116, no. 1358, pp. 1040–1051, 2008.
- [149] H. C. Frankis, K. Mirabbas Kiani, D. Su, R. Mateman, A. Leinse, and J. D. B. Bradley, “High-*Q* tellurium-oxide-coated silicon nitride microring resonators,” *Optics Letters*, vol. 44, no. 1, pp. 118–121, 2019.
- [150] K. Mirabbas Kiani, D. B. Bonneville, A. P. Knights, and J. D. B. Bradley, “High-*Q* TeO₂-Si hybrid microring resonators,” *Applied Sciences*, vol. 12, no. 3, p. 1363, 2022.
- [151] H. C. Frankis, D. B. Bonneville, and J. D. B. Bradley, “Tellurite glass microcavity resonators integrated on a silicon photonics platform,” *Journal of Optical Microsystems*, vol. 1, no. 2, p. 024002, 2021.
- [152] H. C. Frankis, D. Su, D. B. Bonneville, and J. D. B. Bradley, “A tellurium oxide microcavity resonator sensor integrated on-chip with a silicon waveguide,” *Sensors*, vol. 18, no. 11, p. 4061, 2018.
- [153] D. B. Bonneville, M. Albert, R. Arbi, M. Munir, B. L. Segat Frare, K. Mirabbas Kiani, H. C. Frankis, A. P. Knights, A. Turak, K. N. Sask, and J. D. B. Bradley, “Hybrid silicon-tellurium-dioxide DBR resonators coated in PMMA for biological sensing,” *Biomedical Optics Express*, vol. 14, no. 4, pp. 1545–1561, 2023.
- [154] K. Mirabbas Kiani, H. M. Mbonde, H. C. Frankis, R. Mateman, A. Leinse, A. P. Knights, and J. D. B. Bradley, “Four-wave mixing in high-*Q* tellurium-oxide-coated

- silicon nitride microring resonators,” *OSA Continuum*, vol. 3, no. 12, pp. 3497–3507, 2020.
- [155] H. M. Mbonde, H. C. Frankis, and J. D. B. Bradley, “Enhanced nonlinearity and engineered anomalous dispersion in TeO₂-coated Si₃N₄ waveguides,” *IEEE Photonics Journal*, vol. 12, no. 2, pp. 1–10, 2020.
- [156] N. Singh, H. M. Mbonde, H. C. Frankis, E. Ippen, J. D. B. Bradley, and F. X. Kärtner, “Nonlinear silicon photonics on CMOS-compatible tellurium oxide,” *Photonics Research*, vol. 8, no. 12, pp. 1904–1909, 2020.
- [157] H. M. Mbonde, N. Singh, B. L. Segat Frare, M. Sinobad, P. Torab Ahmadi, B. Hashemi, D. B. Bonneville, P. Mascher, F. X. Kärtner, and J. D. B. Bradley, “Octave-spanning supercontinuum generation in a CMOS-compatible thin Si₃N₄ waveguide coated with highly nonlinear TeO₂,” *Optics Letters*, vol. 49, no. 10, pp. 2725–2728, 2024.
- [158] H. C. Frankis, H. M. Mbonde, D. B. Bonneville, C. Zhang, R. Mateman, A. Leinse, and J. D. B. Bradley, “Erbium-doped TeO₂-coated Si₃N₄ waveguide amplifiers with 5 dB net gain,” *Photonics Research*, vol. 8, no. 2, pp. 127–134, 2020.
- [159] B. L. Segat Frare, P. Torab Ahmadi, B. Hashemi, D. B. Bonneville, H. M. Mbonde, H. C. Frankis, A. P. Knights, P. Mascher, and J. D. B. Bradley, “On-chip hybrid erbium-doped tellurium oxide–silicon nitride distributed Bragg reflector lasers,” *Applied Physics B*, vol. 129, no. 10, p. 158, 2023.
- [160] K. Mirabbas Kiani, H. C. Frankis, H. M. Mbonde, R. Mateman, A. Leinse, A. P. Knights, and J. D. B. Bradley, “Thulium-doped tellurium oxide waveguide amplifier with 7.6 dB net gain on a silicon nitride chip,” *Optics Letters*, vol. 44, no. 23, pp. 5788–5791, 2019.
- [161] K. Mirabbas Kiani, H. C. Frankis, R. Mateman, A. Leinse, A. P. Knights, and J. D. B. Bradley, “Thulium-doped tellurium oxide microring lasers integrated on a low-loss silicon nitride platform,” *Optical Materials Express*, vol. 11, no. 11, pp. 3656–3665, 2021.
- [162] K. Mirabbas Kiani, H. C. Frankis, C. M. Naraine, D. B. Bonneville, A. P. Knights, and J. D. B. Bradley, “Lasing in a hybrid rare-earth silicon microdisk,” *Laser & Photonics Reviews*, vol. 16, no. 1, p. 2100348, 2022.

- [163] K. Mirabbas Kiani, H. C. Frankis, A. P. Knights, and J. D. B. Bradley, “Silicon-thulium hybrid microdisk lasers with low threshold and wide emission wavelength range,” *Optics Express*, vol. 31, no. 12, pp. 20244–20255, 2023.
- [164] J. H. Schmid, A. Delâge, B. Lamontagne, J. Lapointe, S. Janz, P. Cheben, A. Densmore, P. Waldron, D.-X. Xu, and K. P. Yap, “Interference effect in scattering loss of high-index-contrast planar waveguides caused by boundary reflections,” *Optics Letters*, vol. 33, no. 13, pp. 1479–1481, 2008.
- [165] J. D. Sarmiento-Merenguel, A. Ortega-Moñux, J.-M. Fédéli, J. G. Wangüemert-Pérez, C. Alonso-Ramos, E. Durán-Valdeiglesias, P. Cheben, Í. Molina-Fernández, and R. Halir, “Controlling leakage losses in subwavelength grating silicon meta-material waveguides,” *Optics Letters*, vol. 41, no. 15, pp. 3443–3446, 2016.
- [166] J. T. Robinson, K. Preston, O. Painter, and M. Lipson, “First-principle derivation of gain in high-index-contrast waveguides,” *Optics Express*, vol. 16, no. 21, pp. 16659–16669, 2008.
- [167] L. Puts, X. Leijters, P. Cheben, J. Schmid, S. Reniers, and D. Melati, “Anti-reflection subwavelength gratings for InP-based waveguide facets,” *Optics Letters*, vol. 46, no. 15, pp. 3701–3704, 2021.
- [168] S. Astilean, P. Lalanne, P. Chavel, E. Cambril, and H. Launois, “High-efficiency subwavelength diffractive element patterned in a high-refractive-index material for 633 nm,” *Optics Letters*, vol. 23, no. 7, pp. 552–554, 1998.
- [169] C. H. Bui, J. Zheng, S. W. Hoch, L. Y. T. Lee, J. G. E. Harris, and C. Wei Wong, “High-reflectivity, high- Q micromechanical membranes via guided resonances for enhanced optomechanical coupling,” *Applied Physics Letters*, vol. 100, no. 2, p. 021110, 2012.
- [170] U. Kemiktarak, M. Metcalfe, M. Durand, and J. Lawall, “Mechanically compliant grating reflectors for optomechanics,” *Applied Physics Letters*, vol. 100, no. 6, p. 061124, 2012.
- [171] C. Stambaugh, H. Xu, U. Kemiktarak, J. Taylor, and J. Lawall, “From membrane-in-the-middle to mirror-in-the-middle with a high-reflectivity sub-wavelength grating,” *Annalen der Physik*, vol. 527, no. 1–2, pp. 81–88, 2015.
- [172] M. Ye and Y. S. Yi, “Influence of grating thickness in low-contrast subwavelength grating concentrating lenses,” *Optical Engineering*, vol. 55, no. 7, p. 075102, 2016.

- [173] M. Ye, Y. Peng, and Y. S. Yi, “Silicon-rich silicon nitride thin films for subwavelength grating metalens,” *Optical Materials Express*, vol. 9, no. 3, pp. 1200–1207, 2019.
- [174] S. Hadi Badri and M. M. Gilarlue, “Silicon nitride waveguide devices based on gradient-index lenses implemented by subwavelength silicon grating metamaterials,” *Applied Optics*, vol. 59, no. 17, pp. 5269–5275, 2020.
- [175] C.-C. Huang, “Numerical investigations of an ultra-compact polarization beam splitter based on augmented low-index guiding and subwavelength grating structures,” *Scientific Reports*, vol. 8, no. 1, p. 17338, 2018.
- [176] A. Parthenopoulos, A. Akbar Darki, B. R. Jeppesen, and A. Dantan, “Optical spatial differentiation with suspended subwavelength gratings,” *Optics Express*, vol. 29, no. 5, pp. 6481–6494, 2021.

Chapter 2

Silicon subwavelength grating metamaterial waveguides functionalized with tellurium oxide cladding

This chapter describes the design, fabrication, and characterization of tellurium oxide (TeO_2)-coated silicon-on-insulator (SOI) waveguide structures engineered using subwavelength grating (SWG) metamaterials. Silicon photonics (SiP) promises advanced integrated optical chips that leverage well-established, state-of-the-art complementary-metal-oxide-semiconductor (CMOS) manufacturing technology. However, active functionality in silicon (Si) is fundamentally limited because of its low light-emission efficiency, high two photon absorption (TPA) in the near-infrared (NIR) spectrum and short non-radiative recombination lifetime. A promising solution to overcome these limitations is hybridization of Si with functional materials. TeO_2 is a high-index glass material with significant potential in integrated optical devices. It possesses a wide optical transparency range that complements Si and acts as an excellent host for rare-earth (RE) ions, enabling low quenching and large emission bandwidth with high gain potential. TeO_2 can be readily deposited onto SOI chips fabricated at CMOS foundries using a post-process reactive magnetron sputtering system, such as the one at the Centre for Emerging Device Technologies (CEDT) at McMaster University. The system

provides a straightforward, room-temperature process to monolithically integrate both undoped and RE-doped TeO₂ with SOI waveguides. SWG metamaterial structures are fundamental building blocks in integrated photonics thanks to their design flexibility, seamless adoption with existing CMOS fabrication methods, and precise lithographic control over the mode field distribution. Incorporation of SWG metamaterials in Si waveguides enables tunability over the mode effective index such that modal confinement in the waveguide is reduced and interaction with the surrounding cladding material is increased. The devices discussed in this chapter leverage SWG metamaterial engineering to combine Si and TeO₂ materials into a new type of hybrid nanophotonic waveguide. Hybrid Si-TeO₂ metamaterial waveguides are designed to maximize the mode overlap and increase light-matter interaction with the TeO₂ material, which is a key requirement in active devices. Furthermore, our strategy allows efficient control over the photonic bandstructure of the waveguide by modifying the device geometry. The presented work shows that the hybrid Si-TeO₂ SWG metamaterial waveguide is a promising step in the development of new host structures for compact on-chip active devices in SOI photonic integrated circuits (PICs).

The contents of this chapter that discuss the finite-difference-time-domain (FDTD) simulation and design procedure, fabrication, characterization, and analysis of the devices under the label “Design #1” are reprinted in part with open access permission from the published manuscript under the following citation:

Cameron M. Naraine, Jeremy W. Miller, Henry C. Frankis, David E. Hagan, Peter Mascher, Jens H. Schmid, Pavel Cheben, Andrew P. Knights, and Jonathan D. B. Bradley, “Subwavelength grating metamaterial waveguides functionalized with tellurium oxide cladding,” *Optics Express*, vol. 28, no. 12, pp. 18538–18547, 2020. DOI: [10.1364/OE.393729](https://doi.org/10.1364/OE.393729).

All other work presented in the chapter outlines waveguide designs produced after this initial publication and their corresponding measurements (where applicable), and is included in a separate manuscript in preparation. Section 2.1 provides an introduction and motivation for leveraging metamaterial engineering to implement optically active TeO₂ material on the SOI platform. Section 2.2 discusses the design process for various components under investigation on the hybrid Si-TeO₂ platform, including SWG waveguides, edge couplers and mode transformers based on a “fishbone” SWG (FB-SWG) topology. Details of how SWG metamaterial engineering is incorporated in the modelling procedure are highlighted here. Section 2.3 presents the fabrication and characterization procedures and experimental results of the physical devices based on three

separate mask layouts. Each design iteration achieves a separate goal that establishes SWG metamaterial waveguides on the hybrid Si-TeO₂ platform as next generation devices for active applications in integrated photonics. Section 2.4 concludes the findings of this project and outlines future prospects and applications.

Abstract

We report on the design, fabrication, and characterization of SWG metamaterial waveguides and other integrated optical components coated with TeO₂. The structures are first fabricated using a standard CMOS-compatible process on an SOI platform. Amorphous TeO₂ top cladding material is then deposited via post-process radio frequency (RF) magnetron sputtering. The photonic bandstructure is controlled by adjustment of the device geometry, opening a wide range of operating regimes, including subwavelength propagation, slow light and the photonic bandgap, for various wavelength bands within the 1550 nm telecommunications window. The distribution of the mode field is also carefully tuned to reduce loss in the waveguide circuit while sufficiently interacting with the TeO₂ material, which can be optically activated when doped with RE ions using the same deposition procedure. A propagation loss of 1.0 ± 0.1 dB/mm is reported for the first set of TeO₂-clad SWG devices, which is lower than the 1.5 ± 0.1 dB/mm loss reported for the silicon dioxide (SiO₂)-clad reference structure. Mode transformers that smoothly connect SWG and wire waveguides are also characterized and present 0.12 dB loss for a 50 μm coupler length. This is the first time that a high-index ($n > 2$) oxide cladding has been demonstrated for SWG metamaterial waveguides, thus introducing a new material platform for on-chip integrated optics. These results provide encouraging insights for developing and exploring other SWG-based waveguide devices in the Si-TeO₂ integrated optics platform.

2.1 Introduction

SiP has been a subject of immense research interest over the last few decades due to its promise in realizing low-cost, integrated optical chips that leverage well-established, state-of-the-art CMOS manufacturing technology [1; 2; 3; 4]. However, Si still faces several challenges as a photonic material – particularly low light-emission efficiency due to its indirect band gap, short non-radiative recombination lifetime and strong TPA at telecommunication wavelengths [4; 5; 6]. Rather than doping Si with optically active materials to alter its intrinsic properties and overcome these challenges, hybridization of Si with functional cladding materials provides a comparatively simple approach with

less fabrication complexity. Various on-chip devices have utilized this process, including Si wire waveguides [7; 8], slot waveguides [9; 10], nanophotonic beam splitters [11] and microring resonators [12; 13; 14].

SWG metamaterials on the SOI platform are attractive photonic structures due to their simple fabrication process and adjustable waveguide core effective index. Periodic structures have been implemented in Si waveguides to manipulate light in various ways, including diffraction, Bragg reflections, slow light propagation, and low loss Floquet-Bloch mode propagation [15]. The behaviour of the light depends on the location of the operating point of the device within the dispersion diagram [16]. SWG metamaterial waveguides operate well below the photonic bandgap where diffraction effects are suppressed, and the gratings behave as a homogeneous anisotropic medium where light propagation is permitted in the form of Floquet-Bloch modes [16]. The cladding material surrounding the SWG waveguide core plays an important role in determining the core effective index due to the index averaging effect, according to effective medium theory (EMT) [17]. Thus far, SWG devices have been implemented with air, water, SiO₂ and various polymers as cladding materials, yielding a plethora of Si-based integrated optical devices [18], including fiber-to-chip couplers [19; 20; 21; 22; 23; 24], waveguide crossings [25], sensors [26; 27], modulators [28], and multiplexers [29], to name a few. However, the refractive indices of these materials are relatively low, limiting the achievable overlap of an SWG waveguide mode with the cladding material.

TeO₂ has significant potential as a high index cladding ($n \approx 2.1$) for integrated optical devices. Various on-chip thin film waveguides [30; 31; 32], lasers [33; 34], optical amplifiers [34; 35; 36; 37], microring resonators [38; 39], sensors [40] and non-linear devices [41] have incorporated TeO₂ due to its wide optical transparency and promising prospects as a host material for RE ions [42]. TeO₂ employed as a cladding material for SWG waveguides would provide a useful guiding mechanism for the expanded mode caused by the relatively lower SWG waveguide core index. Its high refractive index also attracts the mode upwards and away from the Si substrate, which significantly alleviates substrate leakage loss that often affects SWG metamaterial waveguides [43]. This significantly increases the modal overlap with the top cladding material, which is beneficial for amplification and sensing, and can reduce light interaction with the Si waveguide sidewalls that contributes to waveguide propagation loss caused by scattering. Scattering loss is also reduced due to the lower index contrast between the waveguide core and cladding materials. Furthermore, different TeO₂ film thicknesses, from tens of nanometers to a few microns, can be applied to enable fine control of the Bragg

condition for applications such as slow light devices [44]. This new design parameter can also be exploited to scale down the waveguide geometry while maintaining a relatively high mode effective index, thus increasing design flexibility for SWG waveguides across a wide array of wavelengths that extend beyond the standard telecommunication bands. This advantage is paralleled with the wide optical transparency window of TeO₂ that allows light propagation up to the mid-infrared (MIR) wavelength range, making it a versatile material across multiple platforms.

In this work, we present a new waveguide platform consisting of TeO₂ cladding on Si SWG waveguides. The photonic bandstructure and mode field distribution of the periodic SWG waveguides were engineered by tuning the device geometry within the guidelines of the foundry process. The fabrication processes of both the waveguides and the TeO₂ film are discussed and were considered during the design phase, which involved multiple electromagnetic solvers used to enhance the performance of different components, including waveguides, edge couplers and mode transformers. Modal guidance was demonstrated in the TeO₂-clad SWG waveguide structure with a propagation loss of 1.0 ± 0.1 dB/mm reported above the bandgap. Similar losses can be achieved across other regimes of the device bandstructure, which can be tuned accordingly over a wide range of wavelengths used in telecommunications. Mode transformers that seamlessly transition between wire and SWG metamaterial waveguides were also measured and exhibited a loss of 0.12 dB for a 50 μm coupler length. These devices show promise for this new hybrid material platform, which demonstrates potential for developing active waveguide structures that are compatible with established integrated photonic fabrication technologies.

2.2 Simulation and design

This section highlights the design process for various waveguides and components utilizing SWG metamaterials on the Si-TeO₂ integrated photonics platform. All simulations were performed using the photonic device suite available from Ansys Lumerical. SWG metamaterial waveguide design is first described from a generalized assessment of structures approximated using EMT in a 2D finite difference eigenmode (FDE) solver, and then by calculating the Floquet-Bloch modes and dispersion relations of more specific devices using an accurate and rigorous 3D FDTD solver. The design of both conventional SWG and FB-SWG metamaterial waveguides is discussed. Next, the design of specific SWG-based components, including edge couplers and mode transformers, is explained. FDE simulations were used to obtain the optimal mode field results for the

approximated devices, and a fully vectorial, bi-directional eigenmode expansion (EME) solver was implemented to calculate propagation characteristics and determine the appropriate coupler lengths. These simulation results provided guidance and insight for the fabricated waveguide devices discussed in Section 2.3 and lay the groundwork for future SWG-based components to be investigated in the Si-TeO₂ material platform.

2.2.1 SWG metamaterial waveguides – FDE simulations

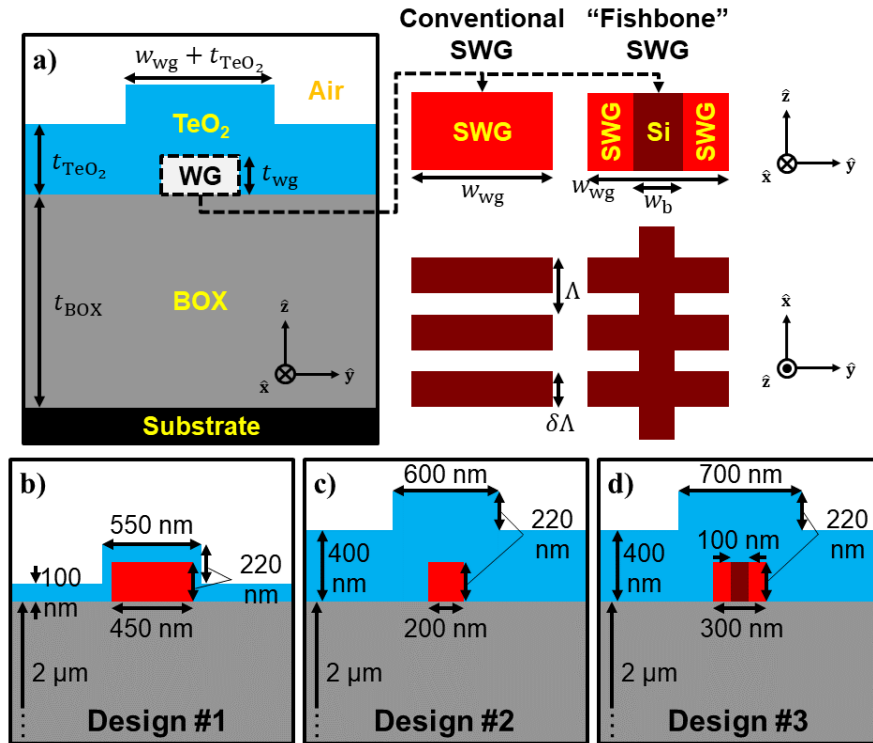


FIGURE 2.1: (a) General cross-sectional diagram of an SOI SWG metamaterial waveguide approximated by EMT in the 2D FDE simulation environment. Inset shows the in-plane cross section (top) and top view (bottom) schematics of conventional (left) and “fishbone” (right) SWG waveguide configurations. Specific in-plane cross-sectional diagrams used for (b) Design #1, (c) Design #2, and (d) Design #3, as specified in Table 2.1.

An FDE solver was used to approximately evaluate the modal properties of SWG metamaterial waveguides with varying geometric parameters. Fig. 2.1(a) shows a cross-section of the waveguide device under investigation using the 2D FDE solver from Ansys Lumerical. The Si substrate, SiO₂ buried oxide (BOX), Si waveguide, averaged SWG waveguide, TeO₂ top cladding and air materials are indicated in black, grey, brown, red,

blue, and white, respectively. With a wavelength of 1550 nm, the corresponding material refractive indices are $n_{\text{Si}} = 3.476$ [45], $n_{\text{TeO}_2} = 2.067$ [46], $n_{\text{SiO}_2} = 1.444$ [45], and $n_{\text{Air}} = 1$. The 3D SWG waveguide is decomposed into a 2D homogenous material with a refractive index determined by the EMT approximation [17]. This core refractive index (n_{SWG}) depends only on the refractive indices of the constituent materials of the original SWG waveguide (i.e., $n_1 = n_{\text{Si}}$ and $n_2 = n_{\text{TeO}_2}$) and the SWG duty cycle, which is defined as waveguide-cladding ratio within one grating period. The geometric dimensions of the TeO_2 layer are based on previous studies that have implemented TeO_2 films from the same deposition system [38; 47]. Fixed parameters in the simulation include the BOX thickness ($t_{\text{BOX}} = 2 \mu\text{m}$) and waveguide thickness ($t_{\text{wg}} = 0.22 \mu\text{m}$), which are determined by the SiP foundries being used for device fabrication. The remaining parameters to be determined are the waveguide width (w_{wg}), SWG duty cycle (δ), and TeO_2 cladding thickness (t_{TeO_2}), which are calibrated during or after fabrication. The waveguide bridge width (w_{b}) is also adjustable for devices utilizing a FB-SWG topology.

An overview of the modal attributes of conventional SWG waveguides coated in TeO_2 cladding was obtained by running a sweep of FDE calculations where δ was fixed and both w_{wg} and t_{TeO_2} were varied between 100 nm and 500 nm. This process was repeated for δ values of 0.3, 0.5, 0.7, and 1, which, according to EMT, correspond to n_{SWG} values of 2.572, 2.860, 3.121, 3.476, respectively. $\delta = 1$ is analogous to a conventional Si wire (i.e., strip) waveguide. The simulation results are summarized as colour maps in the following figures. Fig. 2.2, 2.3, 2.4, and 2.5 show the mode effective index (n_{eff}), group effective index (n_{g}), mode overlap with the TeO_2 top cladding (γ_{TeO_2}), and confinement factor in the TeO_2 top cladding (Γ_{TeO_2}), respectively. The n_{eff} and n_{g} results were collected directly from the FDE solver. γ_{TeO_2} and Γ_{TeO_2} were calculated using Eq. 1.3 and 1.4, respectively, where TeO_2 is the active upper cladding medium.

Overall, the adjustable parameters represent the volume of the high-index materials in the simulation. Specifically, w_{wg} , t_{TeO_2} , and δ control the Si volume, the TeO_2 volume, and the ratio between the two, respectively. As each parameter is increased, n_{eff} increases because the higher-index materials have a greater capability of confining the light. This trend is observed in each colour map of Fig. 2.2. n_{SWG} , and therefore δ , dictates the upper limit of n_{eff} . The group index, n_{g} , represents the rate of change in n_{eff} with respect to wavelength. As expected, n_{g} follows a similar trend to n_{eff} . Changes in the Si volume (i.e., the width) inflict the greatest change on n_{g} because Si has a greater refractive index and material dispersion than TeO_2 and SiO_2 . Therefore, more light confinement in the Si material generates higher n_{g} . Fig. 2.3 demonstrates this with the greatest n_{g}

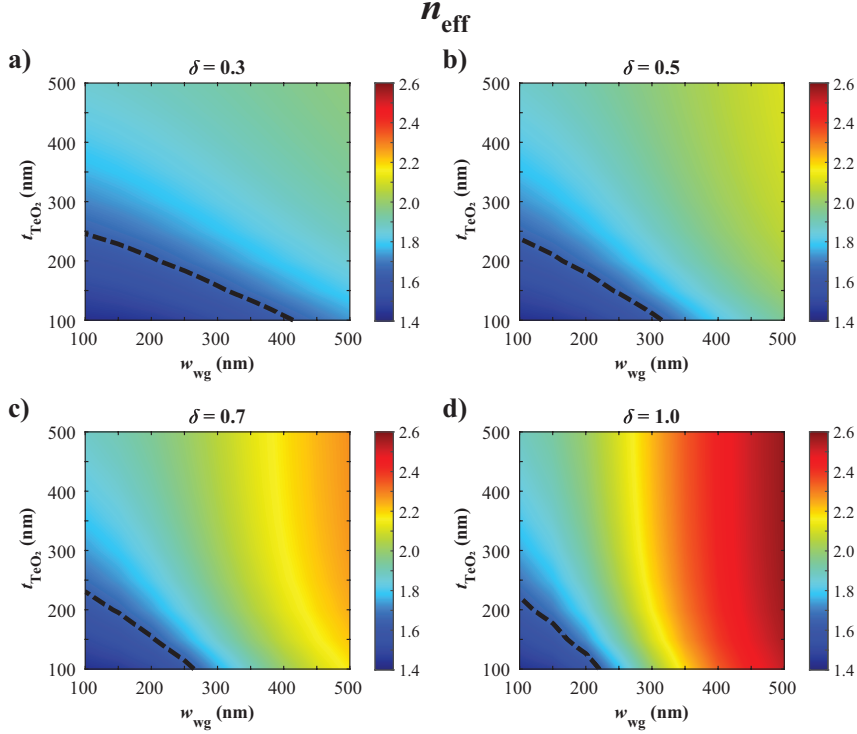


FIGURE 2.2: 2D FDE simulated mode effective index (n_{eff}) for EMT-approximated SWG metamaterial waveguide with varying waveguide width (w_{wg}) and TeO₂ cladding thickness (t_{TeO_2}) and duty cycles (δ) of (a) 0.3, (b) 0.5, (c) 0.7, and (d) 1. Dotted black lines indicate where $n_{\text{eff}} = 1.65$. Designs below these thresholds suffer from significant substrate leakage losses [43].

value of 4.24 observed in a wire waveguide ($\delta = 1$) with moderately high w_{wg} (350 nm) and low t_{TeO_2} (100 nm).

Fig. 2.4 shows that γ_{TeO_2} remains constant for all δ when w_{wg} is minimized. As t_{TeO_2} increases, γ_{TeO_2} is maximized since the mode confinement within the Si core relaxes and expands to the next highest index material (i.e., the TeO₂ cladding). Increasing w_{wg} causes the mode to increasingly concentrate in the waveguide core, thus decreasing γ_{TeO_2} . Wire waveguides are substantially affected by the change in w_{wg} regardless of t_{TeO_2} . On the other hand, SWG waveguides, particularly those with lower δ , alleviate the modal influence of w_{wg} , allowing moderate to high γ_{TeO_2} to be maintained, even in wider waveguides. For example, in waveguides where both w_{wg} and t_{TeO_2} are 500 nm, γ_{TeO_2} is 0.59, 0.39, 0.25, and 0.14 for δ values of 0.3, 0.5, 0.7, and 1, respectively. This is what makes SWG metamaterial waveguides desirable for on-chip optical amplification

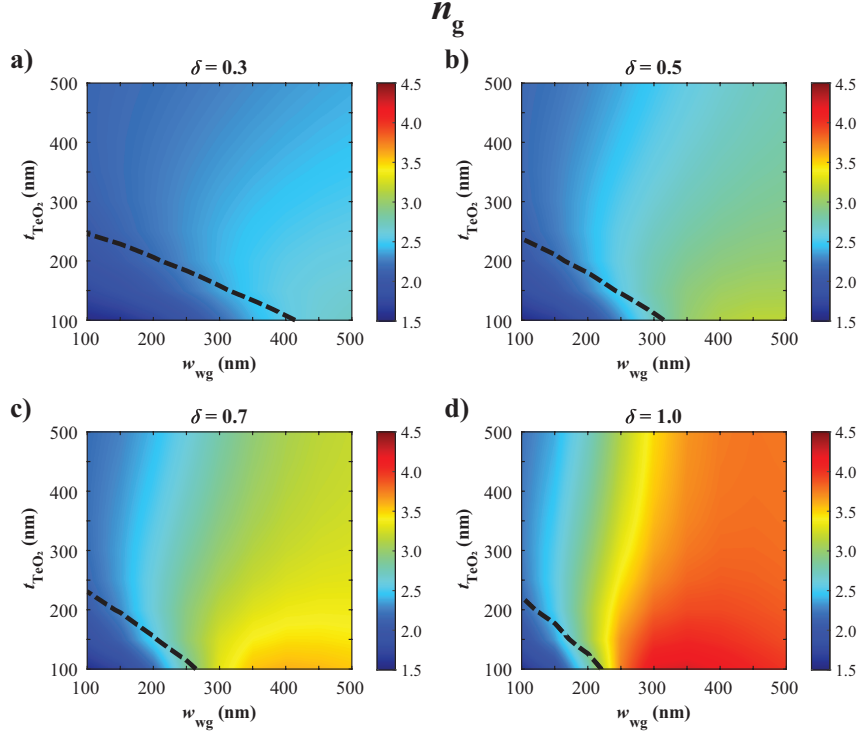


FIGURE 2.3: 2D FDE simulated group effective index (n_g) results for EMT-approximated SWG metamaterial waveguides with varying waveguide width (w_{wg}) and TeO₂ cladding thickness (t_{TeO_2}) and duty cycles (δ) of (a) 0.3, (b) 0.5, (c) 0.7, and (d) 1. Dotted black lines represent thresholds from Fig. 2.2 ($n_{eff} = 1.65$).

using a heterogeneously integrated active gain medium.

The confinement factor in the TeO₂ cladding, Γ_{TeO_2} , has a proportional relationship with n_g and γ_{TeO_2} (see Eq. 1.4). However, the trend of Γ_{TeO_2} shown in Fig. 2.5 closely resembles the plots of γ_{TeO_2} in Fig. 2.4, which validates that Γ_{TeO_2} has a greater dependence on γ_{TeO_2} than n_g . To develop on-chip waveguide amplifiers based on an active gain medium (e.g., erbium (Er)-doped TeO₂) surrounding the core waveguide, a design with high γ_{TeO_2} is desired to maximize Γ_{TeO_2} . However, there is a significant tradeoff between γ_{TeO_2} and n_{eff} . The latter must be carefully optimized for minimizing substrate leakage and bend radiation losses. Loss caused by substrate leakage is considered negligible when $n_{eff} > 1.65$ for SWG metamaterial waveguides atop a 2 μ m thick BOX layer [43]. The dotted black lines in Fig. 2.2 indicate the threshold where $n_{eff} = 1.65$. Waveguides below these lines are assumed to exhibit substantial loss and are not considered for our designs. It is noted that this n_{eff} threshold is much more restrictive for lower δ

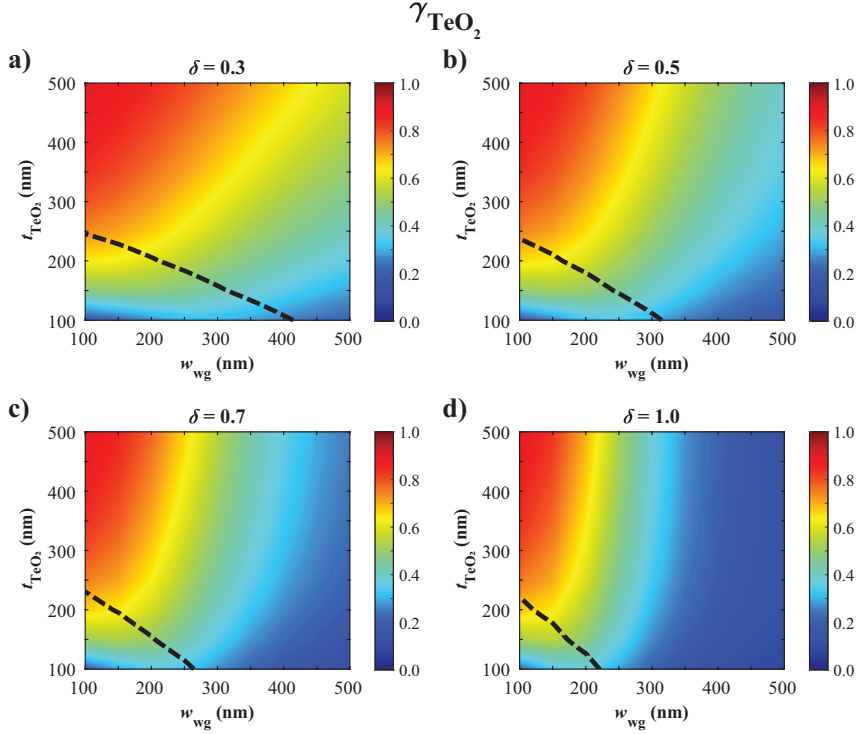


FIGURE 2.4: 2D FDE simulated TeO₂ cladding mode overlap (γ_{TeO_2}) for EMT-approximated SWG metamaterial waveguides with varying waveguide width (w_{wg}) and TeO₂ cladding thickness (t_{TeO_2}) and duty cycles (δ) of (a) 0.3, (b) 0.5, (c) 0.7, and (d) 1. Dotted black lines represent thresholds from Fig. 2.2 ($n_{\text{eff}} = 1.65$).

waveguides. Furthermore, loosely confined modes with low n_{eff} and large mode effective areas are more susceptible to bend radiation loss. To alleviate this problem, either the bend radius of the waveguide must be increased, or the waveguide mode must be converted to increase confinement and leverage tighter bend specifications. Both solutions come at the expense of device compactness. While the latter solution suffers smaller consequences with respect to footprint, it requires additional design steps for efficient mode transformation, which will be discussed later in Section 2.2.4.

Throughout the research conducted within this project, various designs for Si-TeO₂ SWG metamaterial waveguides were selected, fabricated, and characterized. These designs are highlighted in Table 2.1 and their cross-sectional schematics are depicted in Fig. 2.1(b-d). Each design was simulated, fabricated and characterized separately over the span of years. Therefore, the goals of the later designs are based on the successes of their predecessors. “Design #1” was a proof-of-concept design for the Si-TeO₂ platform that

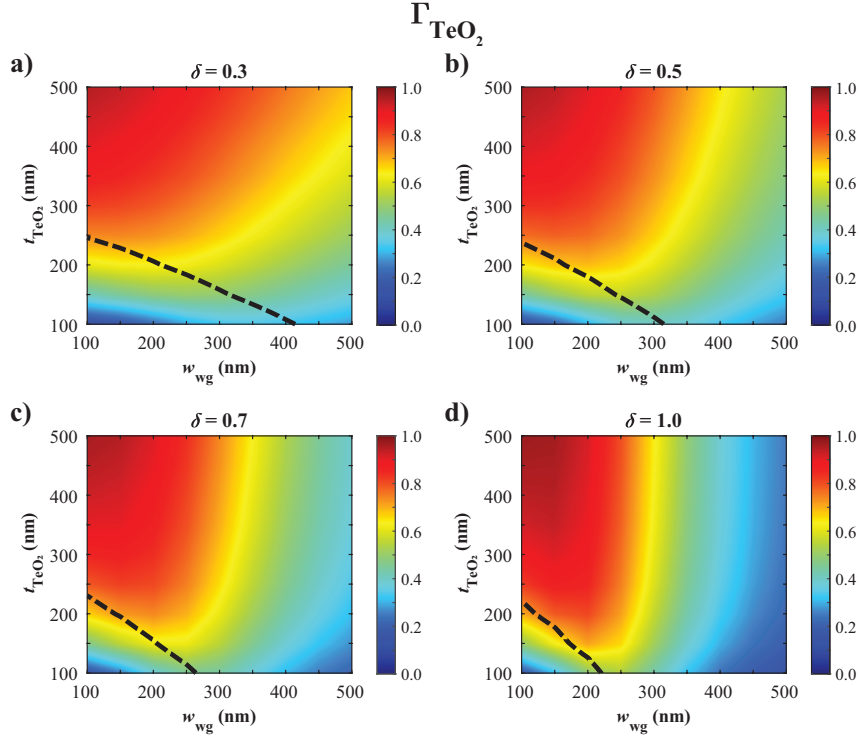


FIGURE 2.5: 2D FDE simulated TeO₂ confinement factor (Γ_{TeO_2}) for EMT-approximated SWG metamaterial waveguides with varying waveguide width (w_{wg}) and TeO₂ cladding thickness (t_{TeO_2}) and duty cycles (δ) of (a) 0.3, (b) 0.5, (c) 0.7, and (d) 1. Dotted black lines represent thresholds from Fig. 2.2 ($n_{\text{eff}} = 1.65$).

was included on a large-scale multi-project wafer (MPW) run. It was also the first design layout I made during my PhD. The goal of the design was to show an initial experimental demonstration of our novel Si waveguide, so we proposed an Si SWG waveguide with a high n_{eff} and disregarded the mode overlap with the TeO₂ cladding (γ_{TeO_2}) for the meantime. The parameters of “Design #1” were $\delta = 0.5$, $w_{\text{wg}} = 450$ nm, and $t_{\text{TeO}_2} = 100$ nm. A grating period (Λ) of 360 nm and 0.5 SWG duty cycle (δ) were used to adhere to the fabrication minimum feature size (MFS) of 180 nm. To avoid the photonic bandgap at 1550 nm wavelength, a thin TeO₂ layer had to be implemented (details discussed later in Section 2.2.2). Following a successful experimental demonstration of the Design #1 SWG metamaterial waveguides on the Si-TeO₂ integrated photonics platform, “Design #2” was proposed to maximize γ_{TeO_2} so that high gain could be achieved in a potential SWG waveguide amplifier device. Parameters of $\delta \sim 0.3$, $w_{\text{wg}} = 200$ nm, and $t_{\text{TeO}_2} = 400$ nm were used. This moderate t_{TeO_2} value provided a safe and versatile range of

TABLE 2.1: Summary of Si-TeO₂ SWG designs studied during this PhD project, with corresponding results from 2D FDE simulations.

Design #	1	2	3
Design goal / description	Proof-of-concept, low γ_{TeO_2} .	High γ_{TeO_2} , high gain design.	First FB-SWG design, moderately high γ_{TeO_2} .
t_{TeO_2} (nm)	100	400	400
w_{wg} (nm)	450	200	300
w_{b} (nm)	N/A	N/A	100
δ	0.5	0.3	0.3
n_{eff}	1.88	1.84	1.95
n_{g}	3.16	2.24	2.57
γ_{TeO_2}	0.19	0.79	0.61
Γ_{TeO_2}	0.29	0.86	0.76

n_{eff} values, as well as substantial γ_{TeO_2} and Γ_{TeO_2} metrics that are much higher than Design #1 and comparable with other Er-doped waveguide lasers on Si [48; 49; 50]. The increased t_{TeO_2} from Design #1 also prevents mode energy from concentrating along the TeO₂-air material boundary above the waveguide, where additional scattering losses are introduced and hinder the device performance. Low δ and w_{wg} also served to boost γ_{TeO_2} . While the fabricated SWG waveguides did not produce viable experimental results, SWG-wire mode transformer components based on FB-SWG waveguide structures were also designed and characterized at this time. Specific design details of these components are discussed in Section 2.2.4 and experimental results of the fabricated structures are shared in Section 2.3.2. Following a successful experimental demonstration of low loss SWG-wire mode transformers, the final design (“Design #3”) proposed and studied FB-SWG waveguides for the Si-TeO₂ platform. These waveguides feature a thin wire waveguide “bridge” section that connects adjacent grating segments together. The bridge provides structural support for the isolated grating segments that still act as a homogeneous medium permitting Floquet-Bloch mode propagation. The results for this design in Table 2.1 used the same FDE simulation procedure described above for the conventional SWG waveguides. The only difference is the addition of an extra Si waveguide piece with width w_{b} ($< w_{\text{wg}}$) in the center of the homogeneous waveguide medium, as illustrated by the brown blocks in the in-plane cross-sectional diagrams of Fig. 2.1. Fabrication and characterization details for Designs #1, #2, and #3 are discussed in Sections 2.3.1, 2.3.2, and 2.3.3 of this thesis, respectively.

2.2.2 SWG metamaterial waveguides – FDTD simulations

Following the initial design stage using the FDE solver, 3D FDTD simulations were conducted to model the photonic bandstructures and calculate the Floquet-Bloch mode effective and group indices of the Si-TeO₂ SWG metamaterial waveguide designs selected from the FDE simulation step (see Table 2.1). In FDTD, the simulation window surrounds a single grating unit cell, as shown in the inset of Fig. 2.6(a) with Si (red), TeO₂ (blue) and air (white) media indicated. Periodic boundary conditions were used along the propagation direction to reduce simulation time, while perfectly matched layer (PML) boundaries were used in the transverse directions of the simulation window. The bandstructure of our SWG device used for Design #1 with a 360 nm grating period (Λ) is depicted in Fig. 2.6(a). The dispersion diagram shows the flattening of the first-order band (in red) as the band edge ($k = \pi/\Lambda$) is approached, and the bandgap region (shaded in yellow) begins. The grey shaded area located above the (black) lightline of SiO₂ ($n \approx 1.444$) corresponds to a continuum of leaky modes. Various mode profiles along the first-order band are shown in Fig. 2.6(b-c) to demonstrate the different Floquet-Bloch mode behaviours that can be exploited in TeO₂-coated Si SWG structures. Fig. 2.6(c) shows the mode profile near the band-edge where the mode intensity is mostly concentrated in and around the high-index Si grating. The mode is more delocalized in Fig. 2.6(b), far from the band-edge, and the smaller period-to-wavelength ratio results in effective homogenization of index contrast.

The Bragg condition states that $n_{\text{eff}} = \lambda_{\text{Bragg}}/(2\Lambda)$, where n_{eff} is the Floquet-Bloch mode effective index, λ_{Bragg} is the Bragg wavelength that marks the boundary between subwavelength regime and photonic bandgap, and Λ is the period (pitch) of the waveguide gratings. For a grating with a period of 360 nm, a Floquet-Bloch mode effective index of ~ 2.06 is achieved at a Bragg wavelength of 1480 nm, as indicated in Fig. 2.7(b) (in black). Conformal cladding materials with lower refractive index, such as SiO₂, and micron-scale thickness cannot achieve a Floquet-Bloch mode effective index this high without having to increase volume fraction of the Si in the waveguide core, which would yield a multimode waveguide and reduce light-matter interaction with the cladding material essential for our aimed application, i.e., light amplification. In contrast to conformal SiO₂ cladding, high-index TeO₂ cladding only a few tens of nanometers thick is sufficient to reach this Floquet-Bloch mode effective index value. Figure 2.7 shows the dispersion relation, Floquet-Bloch mode effective index, and group index with respect to free space wavelength for our SWG device with the same parameters as in Fig. 2.6 but with varying cladding thicknesses of 90 nm (red), 100 nm (green) and 110 nm (blue).

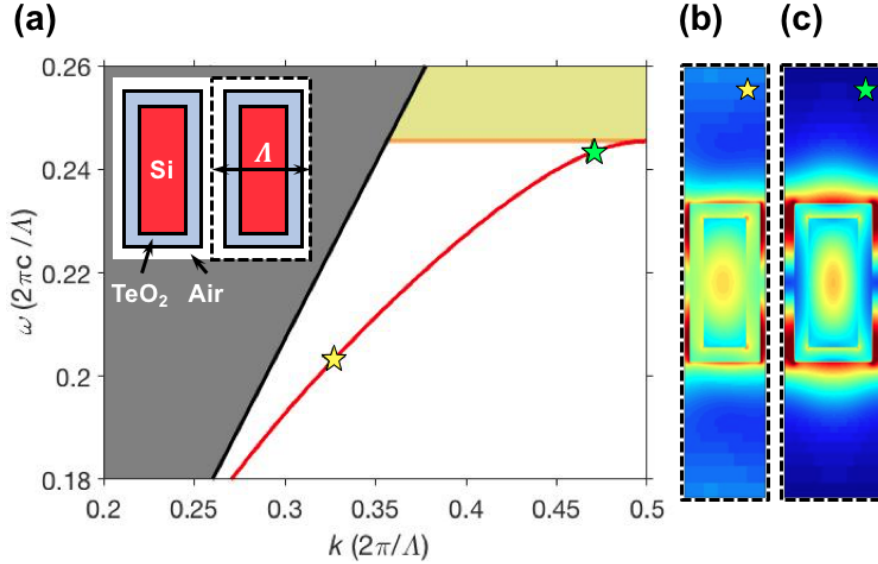


FIGURE 2.6: (a) 3D FDTD simulated photonic bandstructure of proposed device in Design #1. Grey and yellow shaded areas correspond to a continuum of unguided modes above the SiO₂ lightline (in black) and the photonic bandgap, respectively. Inset depicts top view index profile at half waveguide height of simulated unit cell with length Λ (black dashed box). Top view Floquet-Bloch mode intensity distribution profile for periodicities and wavenumbers (b) $\Lambda = 300$ nm and $k = 0.33$ and (c) $\Lambda = 360$ nm and $k = 0.47$, at $\lambda = 1480$ nm. Yellow and green star on the first order band in (a) show the location of (b) and (c), respectively.

The corresponding Bragg wavelengths for these cladding thicknesses are 1444 nm, 1465 nm and 1481 nm, respectively, yielding a 15–20 nm shift in Bragg wavelength with only a 10 nm variation in TeO₂ cladding thickness. This is a significant Bragg wavelength shift, especially compared to equivalent variations in low-index cladding thickness, indicating that TeO₂ provides a useful design parameter for bandgap tunability of SWG waveguides.

Designs #2 and #3 implemented a greater TeO₂ thickness to substantially increase the mode overlap with the TeO₂ cladding material. Furthermore, they used a Si foundry process with a MFS of ~ 60 nm, making the design space for the grating segments more flexible. The same FDTD procedure described above was used for these designs. The simulation setup is equivalent to the schematic displayed in the inset of Fig. 2.6(a), except there is no air gap between the gratings due to the increased TeO₂ cladding thickness. Fig. 2.8(a) displays the first photonic bands of various simulated SWG

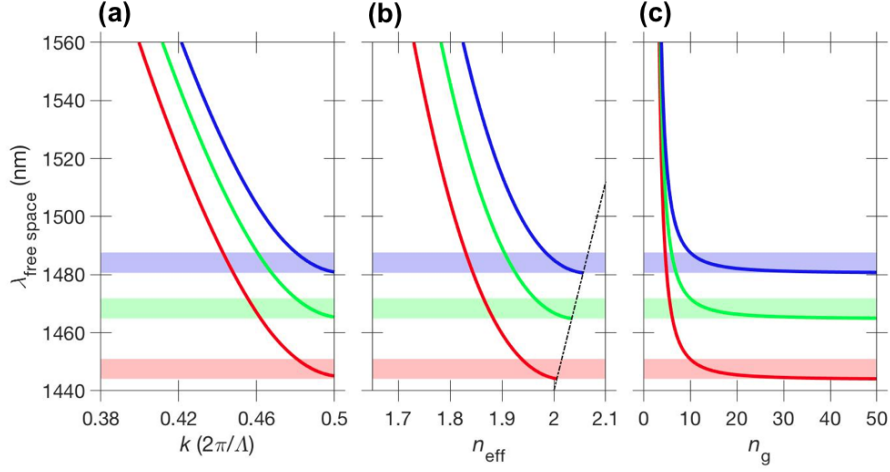


FIGURE 2.7: 3D FDTD simulated (a) dispersion relation, (b) Floquet-Bloch mode effective index, and (c) group index for the TeO₂-coated SWG waveguide with $w_{\text{wg}} = 450$ nm, $\Lambda = 360$ nm and $\delta = 0.5$ studied in Design #1. The red, green and blue curves correspond to TeO₂ cladding thicknesses of 90 nm, 100 nm and 110 nm, respectively. The black dotted line in (b) corresponds to the Bragg condition at $\Lambda = 360$ nm. Shaded areas represent slow light regions where $n_g > 10$ for each case.

waveguide devices for Design #2. The grating segment length ($\delta\Lambda$), depicted in Fig. 2.1, and TeO₂ cladding thickness (t_{TeO_2}) are fixed at 100 nm and 400 nm, respectively, but the waveguide width (w_{wg}) and grating period (Λ) are varied. This bandstructure diagram is expressed with respect to free space wavelength λ rather than frequency ω for clearer visualization. The band edge wavelength (λ_{BE}) for each device is the wavelength where wavevector $k_x = \pi/\Lambda$, which represents the boundary between wavelengths along the band operating in the subwavelength regime ($\lambda > \lambda_{\text{BE}}$), where Floquet-Bloch mode propagation is permitted, and the photonic bandgap ($\lambda < \lambda_{\text{BE}}$), where Bragg reflections occur and prohibit light propagation. As dictated by the Bragg condition, λ_{BE} is significantly redshifted as the period increases. Greater waveguide widths generate the same effect since the waveguide mode effective index increases. However, this change is less significant in comparison to variations in Λ . These two waveguide parameters enable full tunability of the modal properties of the SWG device and its operating wavelengths. Our Er-doped amplifiers utilize 1550 nm and 1480 nm light as the signal and pump sources, respectively, so these are required to be within the subwavelength regime. From Fig. 2.8, these conditions are met when the $\Lambda < 390$ nm for an SWG waveguide with 200 nm width. Like in Fig. 2.6(b-c), three Floquet-Bloch mode profiles in Fig. 2.8 show

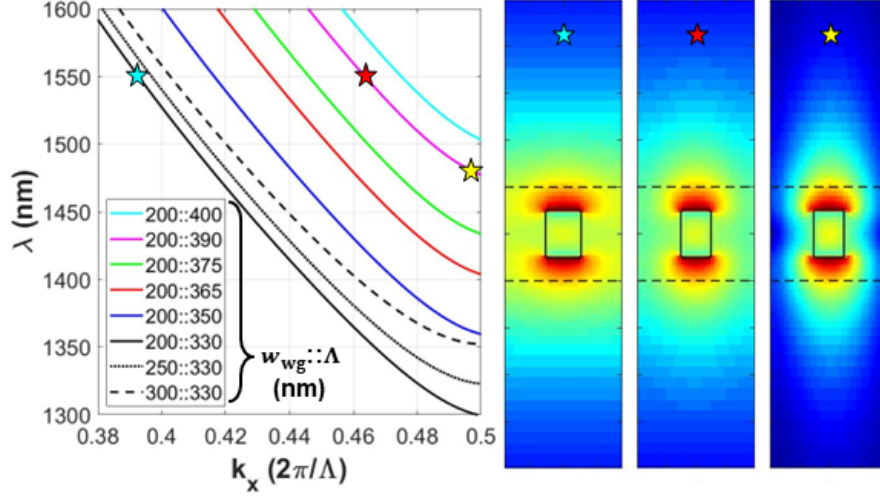


FIGURE 2.8: First order photonic bands of 3D FDTD simulated dispersion relation for various TeO_2 -coated SWG waveguide devices with $\delta\Lambda = 100$ nm and $t_{\text{TeO}_2} = 400$ nm studied in Design #2. Stars on dispersion relation correspond to Floquet-Bloch mode profiles of 200 nm width ($w_{\text{wg}} = 200$ nm) SWG waveguide device with $\Lambda = 330$ nm at 1550 nm wavelength (blue), as well as $\Lambda = 390$ nm at 1550 nm (red) and 1480 nm (yellow) wavelength.

how the band location on the dispersion diagram affects the field distribution through the SWG waveguide. From left to right, the mode evolves from the deep subwavelength regime, where strong modal homogenization and field continuity along the longitudinal axis persists, to photonic bandgap edge, where the electric field concentrates on the grating as the Bragg condition is fulfilled. The slow light regime exists just above λ_{BE} where the band flattens near the band edge and causes the group velocity to approach zero ($v_g \rightarrow 0$, $n_g \rightarrow \infty$). Utilizing the slow light effect on the pump source may provide benefits for increasing the light-matter interaction necessary for higher modal gain output [51]. Using Eq. 1.3, and expanding it to three dimensions with a mode volume overlap integral [28], the calculated mode overlap between the left Floquet-Bloch mode (blue star) and the TeO_2 cladding is 85.2%. This shows slight improvement over the 79.4% overlap calculated in the approximated SWG structure in the 2D FDE simulation (see Table 2.1) because of the inclusion of the TeO_2 region between the gratings that is not considered in the 2D calculation.

Design #3 targeted FB-SWG waveguides featuring a thin wire waveguide bridge with width w_b interconnecting the SWG segments (Fig. 2.9(a)). This increases robustness of the SWGs and reduces the potential for air gap formation between the gratings during

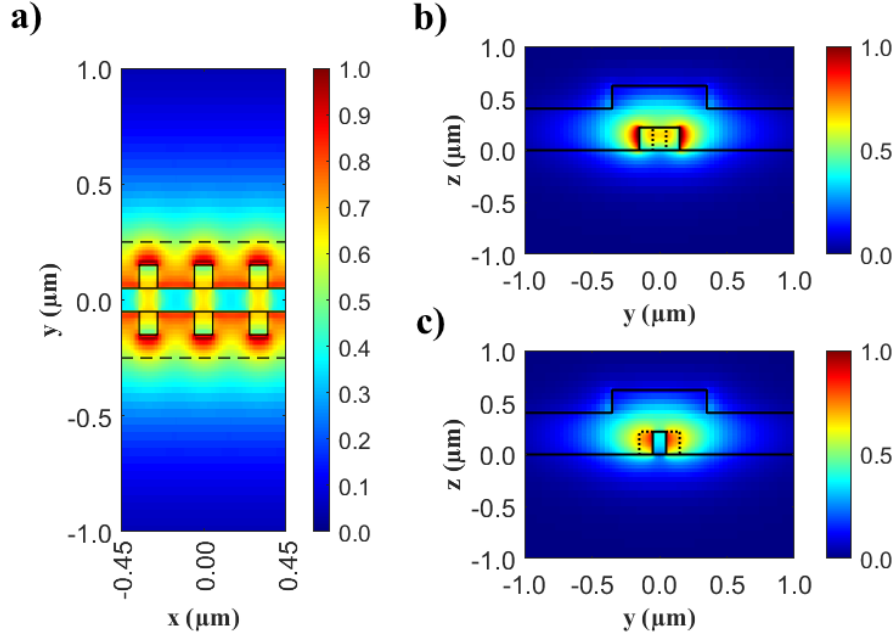


FIGURE 2.9: (a) Floquet-Bloch mode propagation and fundamental TE mode profiles (b) across the grating segment and (c) in between adjacent grating segments of the 3D FDTD simulated TeO₂-coated FB-SWG waveguide device studied in Design #3.

deposition of the TeO₂ thin film. Fig. 2.9 shows the Floquet-Bloch mode profile obtained by 3D FDTD simulations for the Design #3 structure described in Table 2.1 with a 300 nm grating period. Fig. 2.9(a) show the top-view of the Floquet-Bloch mode profile as the field propagates through the waveguide, while Fig. 2.9(b) and (c) show the transverse cross-sections on and between the segments, respectively. The mode effective and group indices are 1.95 and 2.67, respectively. While n_{eff} is in good agreement with the 2D FDE result from Table 2.1, n_g is about 0.1 greater in the 3D simulation. This is due to proper consideration of the material dispersion in the 3D simulation which was neglected in the 2D simulation. The calculated mode overlap with the TeO₂ cladding is 73.2%. Similar to Design #2, this value is larger than the 60.7% calculated from the 2D simulation because the TeO₂ cladding between the gratings is included in the numerator of the integration.

2.2.3 SWG edge couplers – FDE simulations

Edge couplers are used to efficiently couple light between the optical fiber and the chip. Unlike surface grating couplers, edge couplers have lower polarization dependence as well

as broadband operation which is beneficial for coupling pump and signal sources together onto the same waveguide amplifier. A common edge coupler design for Si waveguides involves lateral tapering of the waveguide width near the edge facet that connects to the adjacent fiber [52]. This releases the mode confinement from the waveguide core, generating greater overlap, and therefore lower coupling loss, with the large fiber mode. Edge couplers leveraging SWG metamaterial engineering have been successfully demonstrated with superior performance, as the duty cycle can be tuned to further delocalize the mode from the waveguide and generate polarization-independent mode overlap with the fiber mode and increased tolerance to feature size variations [15; 19; 21].

The FDE solver was used to calculate the fundamental transverse electric (TE) modes of various TeO₂-clad wire and SWG waveguide structures. The calculated waveguide modes were then compared to a fiber mode approximated by a Gaussian beam profile using the integrated overlap analysis tool, which calculated the mode overlap and power coupling between the waveguide and fiber modes. We compared our edge couplers against a lensed fiber with a 2.5 ± 0.5 μm mode field diameter (MFD), which is used in our experimental setup.

Fig. 2.10 and 2.11 show the effective index of SWG waveguide modes for various waveguide widths and duty cycles, and the coupling efficiency of each of these modes with respect to a lensed fiber with 2.5 μm MFD, respectively. Different TeO₂ cladding thicknesses are compared, as well as SiO₂-clad reference structures. The coupling efficiency (CE) of each edge coupler is determined by the power coupling result outputted by the overlap analysis tool in the FDE solver, which accounts for both the overlap and the effective index mismatch between the waveguide and fiber modes. Table 2.2 highlights the optimal edge coupler geometries where the coupling efficiency is at its peak for each waveguide configuration. The SiO₂-clad waveguides experience the best coupling efficiencies (between -0.27 and -0.24 dB) across a variety of waveguide parameters. Each of the optimal SiO₂-clad edge couplers have mode effective indices of ~ 1.45 , which are approximately equal to the fiber mode effective index. Waveguide widths above the optimal point on each data series in Fig. 2.11(a) generate mismatch by over-confining the mode in the waveguide and increasing the effective index. On the other hand, waveguide widths to the left of the peaks lack confinement and generate mode sizes greater than the fiber mode, which also decreases the coupling efficiency. These modes would be more suitable if the fiber MFD was increased. The optimal edge couplers with 100 nm TeO₂ cladding thickness are within the simulated waveguide width range and have a coupling efficiency near -0.95 dB for all duty cycles. This coupling efficiency is less than

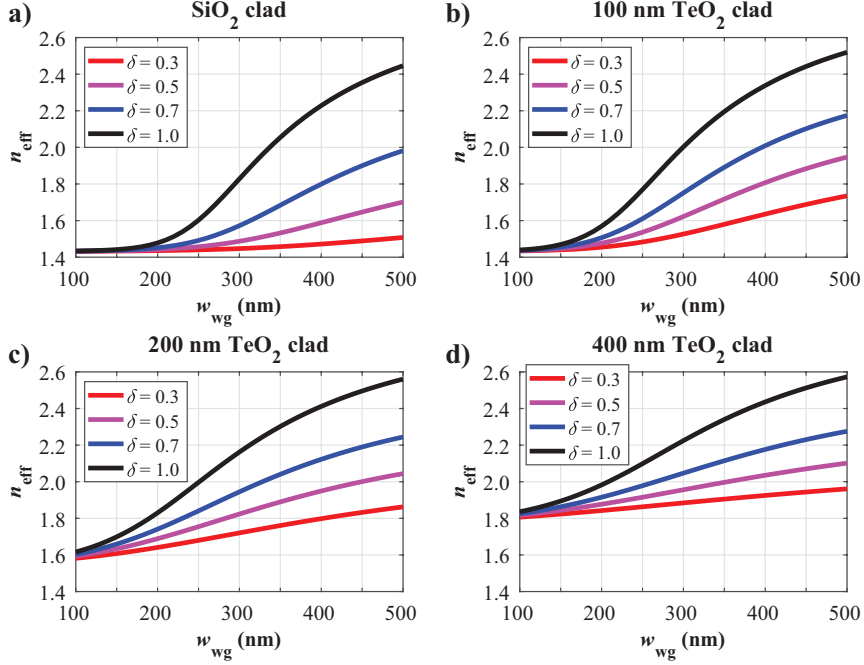


FIGURE 2.10: FDE simulated mode effective index for various EMT-approximated SWG waveguides coated with (a) SiO₂ cladding and (b) 100 nm, (c) 200 nm, and (d) 400 nm-thick TeO₂ cladding.

that of the SiO₂-clad edge couplers because the mode shape of the narrow TeO₂-coated Si waveguide is less representative of a Gaussian profile that the fiber mode resembles. Regardless, this yields the highest coupling efficiency of all the simulated TeO₂-clad waveguides. The optimal edge couplers for waveguides with 200 nm and 400 nm TeO₂ cladding thickness are those with 100 nm waveguide width (i.e., the smallest simulated width), regardless of duty cycle. This is because the mode effective index converges to a specific value called the slab mode effective index ($n_{\text{eff}}^{\text{slab}}$), as $w_{\text{wg}} \rightarrow 0$. $n_{\text{eff}}^{\text{slab}}$ increases with, and is dictated by, the TeO₂ cladding thickness, and was determined to be 1.551 and 1.775 for 200 nm and 400 nm TeO₂ cladding thickness, respectively. For both these thicknesses, the optimal edge coupler has a 0.3 duty cycle and 100 nm waveguide width, which provides coupling efficiencies of -2.161 and -2.861 dB for 200 nm and 400 nm TeO₂ cladding thicknesses, respectively. Increasing the cladding thickness any further will only raise the slab mode effective index and generate greater modal discrepancy from the fiber mode, resulting in lower coupling efficiency. Therefore, the best edge couplers with TeO₂ cladding are those with thinner TeO₂ films. To achieve the highest overall coupling efficiency and still leverage TeO₂ for functionalizing SWG waveguides,

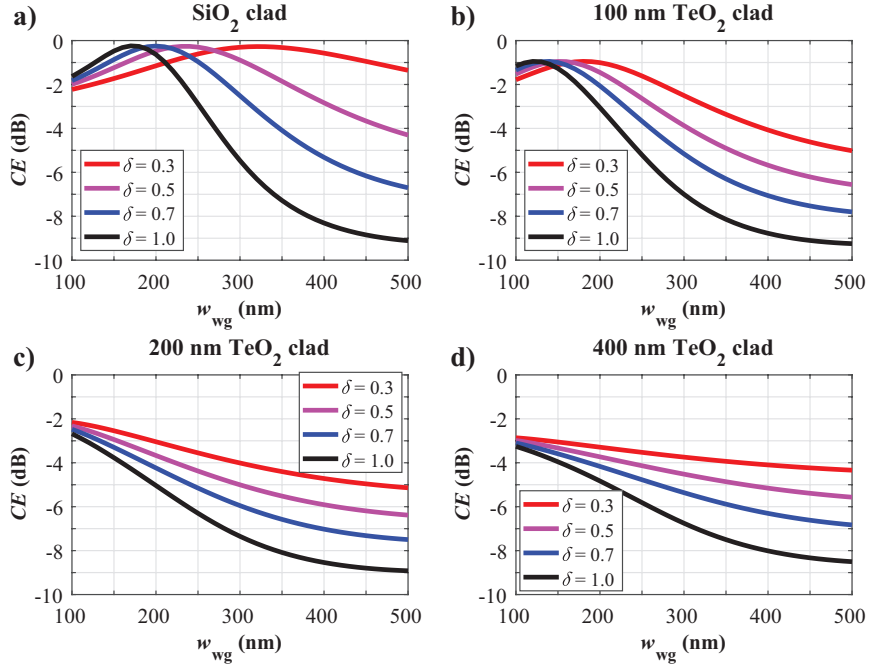


FIGURE 2.11: FDE simulated coupling efficiency for an interface between a 2.5 μm MFD lensed fiber and various EMT-approximated SWG waveguides coated with (a) SiO₂ cladding and (b) 100 nm, (c) 200 nm, and (d) 400 nm-thick TeO₂ cladding.

the designer may coat the edge facets in foundry SiO₂ cladding and include oxide open windows around the areas of interest away from the facets so that the TeO₂ film may be deposited directly onto the inner waveguides after fabrication. However, this option is not offered by all foundries, and it introduces further design challenges, such as mode transition regions between SiO₂-clad and TeO₂-clad waveguide sections.

The foundry used for Design #1 had an MFS of 180 nm. Because of the circuit design considerations, which will be discussed in Section 2.3.1, solid core edge couplers (i.e., duty cycle $\delta = 1$) were used for all devices. A tip width of 180 nm was used to respect the MFS, which provided a coupling efficiency of -2.24 dB for edge couplers coated in 100 nm thick TeO₂. Both Design #2 and #3 targeted 400 nm thick TeO₂ for increased mode interaction with the TeO₂ gain medium. The foundry did not offer oxide open windows, so the edge couplers had to have TeO₂ cladding. Design #2 used both solid core ($\delta = 1$) and SWG ($\delta = 0.3$) edge couplers for various designs with 100 nm waveguide width, yielding coupling efficiencies of -3.256 and -2.861 dB, respectively. Fabrication issues arose around the SWG edge couplers regarding fragility, so all waveguide devices

TABLE 2.2: Optimal Si SWG edge couplers based on 2D FDE simulations.

Cladding	δ	w_{wg} (nm)	n_{eff}	CE (dB)
SiO ₂	0.3	320	1.451	-0.274
	0.5	240	1.453	-0.265
	0.7	200	1.452	-0.251
	1	170	1.450	-0.242
100 nm TeO ₂	0.3	180	1.448	-0.948
	0.5	150	1.447	-0.950
	0.7	140	1.449	-0.948
	1	120	1.447	-0.949
200 nm TeO ₂	0.3	100	1.582	-2.161
	0.5	100	1.593	-2.320
	0.7	100	1.603	-2.475
	1	100	1.616	-2.681
400 nm TeO ₂	0.3	100	1.807	-2.861
	0.5	100	1.816	-2.982
	0.7	100	1.825	-3.099
	1	100	1.836	-3.256

in Design #3 only utilized the solid core edge coupler from Design #2 (with -3.256 dB coupling efficiency). Future design iterations for SWG waveguide amplifiers should strongly consider edge couplers with the best coupling efficiency so that the facet loss, which is a prime culprit for limiting pump power efficiency on chip, is alleviated.

2.2.4 SWG-wire mode transformers – EME simulations

Mode transformers are essential components in the design of an integrated optical circuit incorporating SWG metamaterials. They seamlessly convert a loosely confined SWG waveguide mode into a highly confined wire waveguide mode, and vice versa. Designing a mode transformer with low transition loss provides flexibility in the circuit design. Other common components, such as edge couplers, waveguide bends, directional couplers, and multimode interference (MMI) couplers, can be used in various configurations (SWG-based or wire) throughout the photonic device and connected to waveguide routers of either type (i.e., wire or SWG) as required by the application and without sacrificing performance. For example, our waveguide amplifiers use these mode transformers to efficiently switch between straight SWG waveguide gain sections and wire waveguide bends. This method of routing light has many benefits over SWG bends, including greater compactness and reduced bend radiation loss.

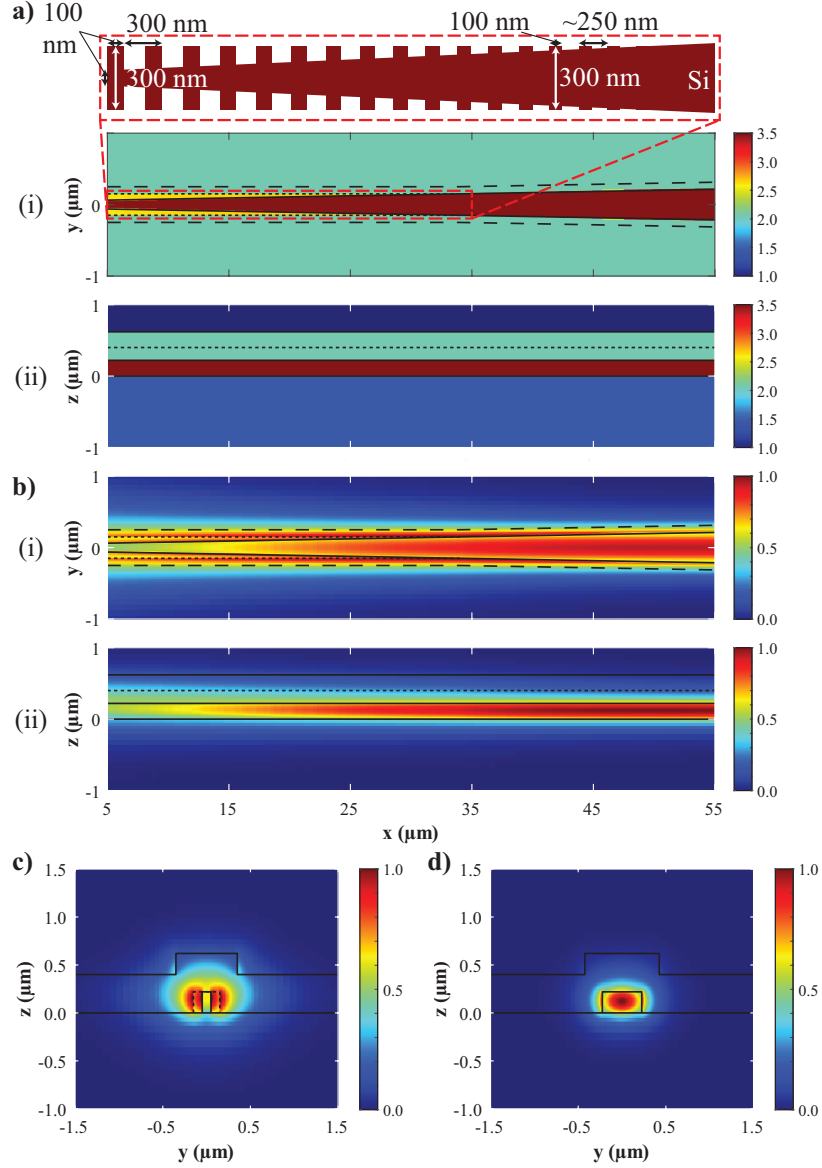


FIGURE 2.12: EME simulation of 50 μm -long SWG-wire mode transformers coated in 400 nm-thick TeO_2 cladding. (a) Refractive index and (b) TE-polarized field profiles from a (i) top view ($z = 0.11 \mu\text{m}$) and (ii) side view ($y = 0 \mu\text{m}$). Inset of (a)(i) shows a detailed top view schematic of the original Si waveguide structure in which the simulated EMT-approximated refractive index is based. Lossless mode transformation is achieved from (c) a launched FB-SWG waveguide mode ($x = 5 \mu\text{m}$) to (d) an output wire waveguide mode ($x = 55 \mu\text{m}$).

A fully vectorial and bi-directional EME solver was used to simulate the efficiency of our TeO₂-coated SWG-wire mode transformers. The EME algorithm uses cells to decompose a device into sets of eigenmodes and then compares the field solutions at adjacent cell boundaries to formulate scattering matrices in each section. Once completed, the S matrix of the entire device can be calculated for any device length without having to repeat the eigenmode computation. This makes the EME method particularly efficient for calculating mode propagation, even over long distances. More rigorous solvers, such as FDTD, scale computational load and time with device length and require full re-calculation when the device parameters are changed. We only used the EME solver to simulate our mode transformers since excellent agreements between 3D-FDTD and 3D-EME simulation results in similar Si photonic couplers have already been previously demonstrated [53].

Fig. 2.12 shows the index and mode profiles of the simulated SWG-wire mode transformer using the EME method. These mode transformers for Design #2 and #3 feature an SWG waveguide with a constant width of 300 nm and a wire waveguide bridge section with a width that inversely and linearly tapers over the device length from 100 nm to 450 nm. The transformer is designed to enable a near lossless transition between a 450 nm-wide wire waveguide and a FB-SWG waveguide with 100 nm and 300 nm width for the wire bridge and SWG, respectively. To ensure each part of the mode transformer operates in the subwavelength regime, the period is adiabatically chirped through the transformer as the Si bridge width increases. The grating segment length is fixed ($\delta\Lambda = 100$ nm), so the duty cycle changes with the period. The inset of Fig. 2.12(a)(i) shows a detailed top view schematic of the Si structure near the SWG waveguide end of the mode transformer and highlights the change in the SWG parameters as the wire waveguide end is approached. EMT is used to imitate a homogeneous medium for the SWG waveguide portion of the transformer. Fig. 2.12(a) shows a gradually increasing core index for the approximated SWG waveguide from left to right due to the increasing duty cycle within this transition. A mode transformer length (L_{MT}) of 50 μm was selected based on similar devices previously demonstrated [21]. Fig. 2.12(b) shows the mode propagation from both a top and side view. The fundamental FB-SWG waveguide and wire waveguide mode profiles shown in Fig. 2.12(c) and (d), respectively, correspond to the launched mode on the left side ($x = 5$ μm) and resulting mode on the right side ($x = 55$ μm) of the field propagation profiles in Fig. 2.12(b). These modes have effective indices of 1.964 and 2.511, respectively.

Fig. 2.13 displays the transmission results from the S matrix calculations performed

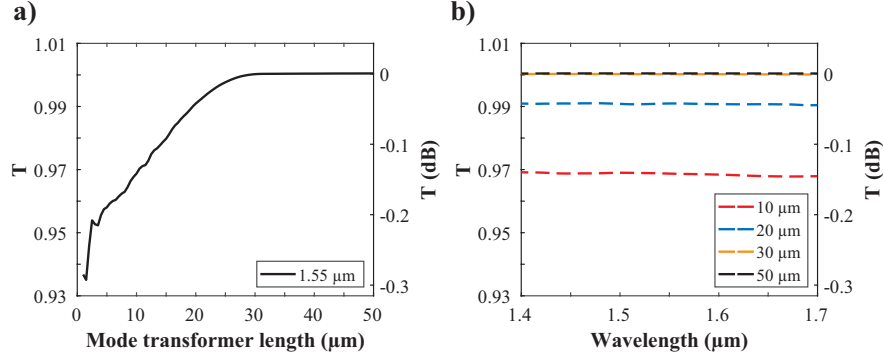


FIGURE 2.13: Simulated transmission obtained from EME (a) propagation sweep at 1.55 μm wavelength and (b) wavelength sweep for SWG-wire mode transformers with various lengths and 400 nm-thick TeO_2 cladding.

by the propagation and wavelength sweeps in the EME analysis. The Si substrate is included in the simulation window, which uses PML boundary conditions on all sides to consider light leakage in the loss calculation. The results from the propagation sweep at 1550 nm wavelength shown in Fig. 2.13(a) present negligible loss for all mode transformers with lengths $> 30 \mu\text{m}$. TeO_2 -coated mode transformers have lower length thresholds for lossless operation because the effective index difference between the modes entering and leaving the transformer is much lower than those coated in lower index claddings, such as SiO_2 or air. This is beneficial for maintaining compactness in mixed SWG/wire waveguide circuits on this integrated photonics platform. Meanwhile, the results from the wavelength sweep for various device lengths shown in Fig. 2.13(b) illustrate wavelength independence across a broad spectrum. SWG-based devices operating in distant telecom bands, such as the O-band or 2- μm window, will require geometric optimization based on the dispersion relation and modal requirements for those wavelengths. Nevertheless, this process shows that SWG-wire mode transformers can be readily designed for the Si- TeO_2 photonics platform regardless of the spectral region.

2.3 Fabrication and characterization

The following section details the fabrication and characterization steps carried out on three distinct layouts for the Si- TeO_2 SWG project in chronological order. The test structures fabricated on each design layout are summarized in Table 2.3. First, conventional SWG metamaterial waveguides coated in TeO_2 were fabricated and measured, showcasing the proof of concept for SWG structures within the heterogeneously integrated

material platform. A thin layer (~ 100 nm) of TeO_2 was applied for this design to respect fabrication specifications set by the foundry while maintaining subwavelength operation, as well as to alleviate the possibility of airgap formation between the grating segments, which increases with deposition time. A propagation loss of 1.0 ± 0.1 dB/mm and a coupling loss of 4.8 ± 0.2 dB/facet were measured in the devices at a wavelength of 1480 nm. Next, an updated design was made to improve the SWG-wire mode transformer performance. A new foundry utilizing electron beam lithography (EBL) technology was used to fabricate these designs and circumvent previous feature size limitations that inflicted Bragg reflections in the spectral region of interest in the initial design. Furthermore, a thicker TeO_2 cladding (~ 400 nm) was applied to increase its modal overlap and reduce the modal density around the material boundaries that inhibit greater loss due to scattering effects. Characterization of cutback-type circuits revealed a loss of 0.12 dB in each mode transformer, which corresponds well with EME simulations given the contribution of imperfections in fabrication. Finally, a third design exploring FB-SWG metamaterial waveguides was generated. This topology provides greater robustness in the grating structures and diminishes the possibility of airgap formation between the grating segments with the addition of the Si bridge through the waveguide. The layout for this design is discussed, but fabrication is still underway, so no experimental results are presented in this thesis.

TABLE 2.3: Summary of fabricated Si- TeO_2 SWG designs.

Design #	1	2*	3
Structures fabricated	Various cutbacks (Wire; SWG)	Various cutbacks (Wire; SWG; MT)	See Table 2.4
Structures measured and reported	Wire cutbacks#; SWG cutbacks	Wire cutbacks#; MT cutbacks	N/A

* MT = mode transformer.

Measured to extract wire waveguide loss from other cutback structures.

For brevity, each of the devices discussed below features an amorphous TeO_2 thin film grown using a RF reactive magnetron sputtering process [38; 47]. This backend deposition procedure enables room temperature deposition at a chip scale, yielding low-loss TeO_2 thin films compatible with active Si photonic devices fabricated in CMOS foundries [54; 55]. Details of the TeO_2 deposition for each chip will be briefly discussed

in the following sections where required.

2.3.1 Design #1: SWG waveguide cutback structures

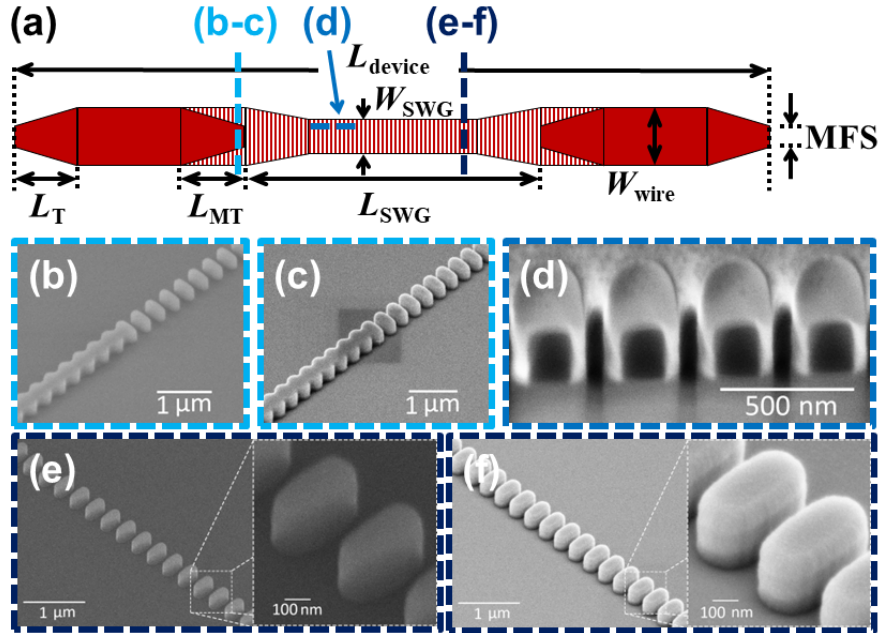


FIGURE 2.14: (a) Top view schematic of fabricated SWG device with Si wire (solid) and SWG (striped) waveguide sections. Dash lines indicate the locations of the scanning electron microscope (SEM) images of the fabricated b) uncoated and c) 105 nm-thick TeO_2 -coated mode transformer transitions, d) TeO_2 -coated SWG waveguide (side view), and e) uncoated and f) TeO_2 -coated SWG waveguides (angled view). Image in d) was taken 52° to the surface normal while all other images were taken 45° to the surface normal.

Our waveguides were fabricated on a 200 mm MPW run on an SOI platform through Advanced Micro Foundry (AMF) in Singapore. A 193 nm deep-ultraviolet (DUV) lithographic process was used with a 220 nm-thick Si waveguide layer on a 2 μm -thick SiO_2 BOX layer. Deep Si trenches were created along the chip edges to facilitate fiber-chip edge coupling. Wafers with and without top oxide cladding deposited by AMF were fabricated, allowing SiO_2 -clad reference structures and exposed waveguide structures for a separate post-process TeO_2 thin film deposition, respectively. It is noted that the DUV lithography process used for our manufacturing has a comparatively large MFS of 180 nm [56]. This MFS allows a minimum grating period of 360 nm with a corresponding 50% duty cycle ($\Lambda = 360$ nm, $\delta = 0.5$), which we used in all our SWG structures. Fig. 2.14(a) shows the overall schematic of our SWG waveguide test structure. A series of

these straight SWG structures were fabricated with different SWG waveguide lengths (L_{SWG}) to measure loss using the cutback method. The SWG waveguide section is connected to two wire waveguide sections that vary in length between devices so that a constant device length of 3 mm ($L_{\text{device}} = 3$ mm) is maintained for all test structures. A standard wire waveguide width of 450 nm ($W_{\text{wire}} = 450$ nm) is used for single mode operation [57]. 50 μm -long mode transformers ($L_{\text{MT}} = 50$ μm) leveraging the SWG waveguide engineering concept first proposed in [21] are used to connect SWG and wire waveguide sections to gradually transform the mode along the device. The Si wire taper in the mode transformer ends with a width of 180 nm, due to MFS restrictions of the fabrication, before joining the SWG region. A series of 450 nm-wide wire waveguides were also fabricated to determine loss of the wire sections. Serpentine structures with 50 μm bend radius were used to obtain different Si-wire waveguide lengths required for loss measurements. All waveguide structures have 75 μm -long tapers ($L_{\text{T}} = 75$ μm) from the wire waveguide sections up to the chip edge where the waveguide width is reduced to 180 nm (MFS limit), to enhance the fiber-chip coupling efficiency.

The wafer was diced into chips following wafer-scale fabrication. We deposited a 101 ± 5 nm-thick TeO_2 film onto chips without SiO_2 top cladding from the foundry. Fig. 2.14(b) and (e) show SEM images of the uncladded mode transformer and SWG waveguide structures on the chip, respectively. Fig. 2.14(c) and (f) show the same structures following the TeO_2 thin film deposition. Given the pitch and duty cycle available for our SWG device, a thin layer of approximately 100 nm is required to ensure an appropriate Floquet-Bloch mode effective index. This also helps minimize air gap formation between the Si segments caused by nucleation of the film on top of the gratings. This is particularly evident in gratings with increased duty cycles or reduced pitches.

We measured the optical propagation loss of the fabricated structures by fiber edge coupling to a set of test structures with different propagation lengths. A tunable laser source was coupled into the chip via lensed fiber with a 2.5 ± 0.5 μm MFD. The input polarization was controlled using polarization paddles at the input of the chip and the transmitted signal at the output was measured using an indium gallium arsenide (InGaAs) photodetector. Figure 2.15(a) shows the measured insertion loss of the waveguide with 3 μm -thick SiO_2 cladding and 100 nm-thick TeO_2 cladding over a 1460–1640 nm wavelength range. Measurements were referenced to a 450 nm-wide wire waveguide structure equivalent to the wire waveguide sections on the SWG device to account only for the loss of the SWG waveguides of varying lengths (L_{SWG}) and the two 50 μm -long mode transformers connecting them to the wire waveguide sections. A Savitsky-Golay

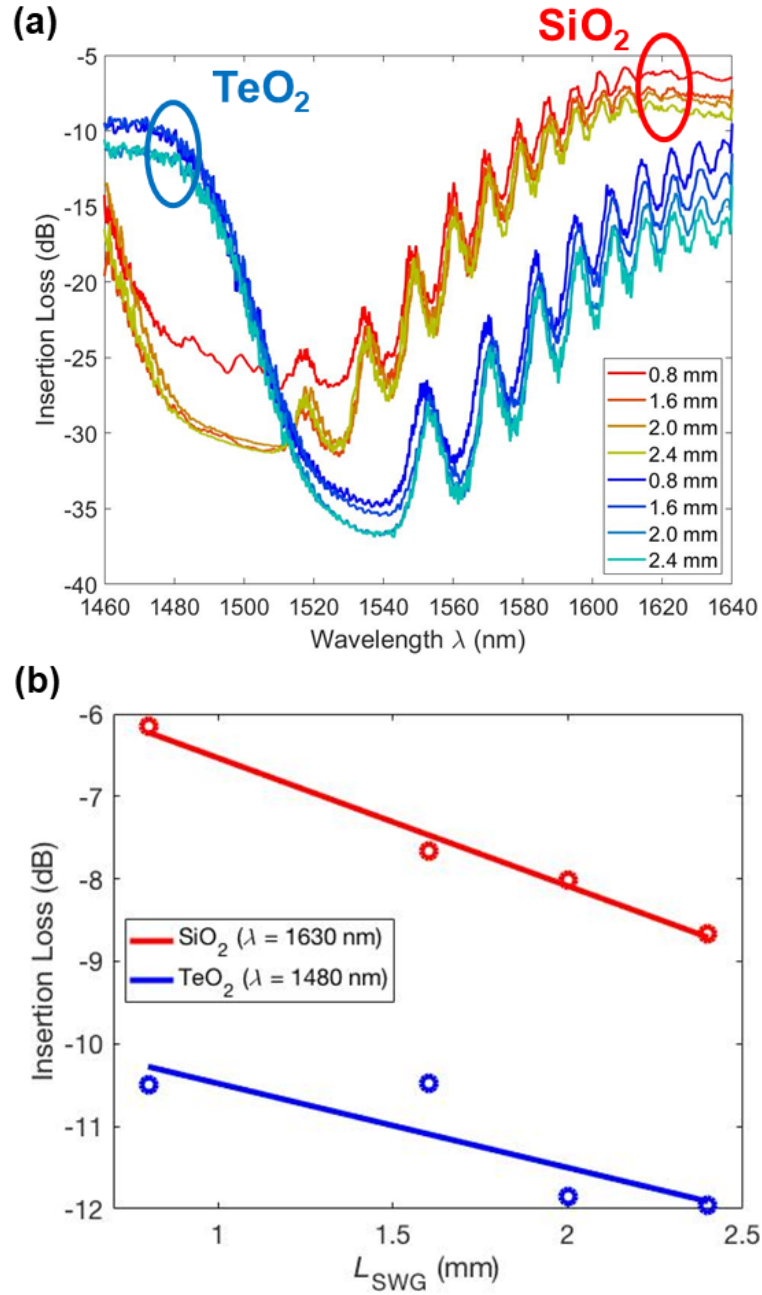


FIGURE 2.15: (a) Measured insertion loss of SWG waveguides with 3 μm -thick SiO_2 cladding and 100 nm TeO_2 cladding, with $W_{\text{SWG}} = 450$ nm, $\Lambda = 360$ nm and $\delta = 0.5$ and varying SWG waveguide lengths (L_{SWG}) indicated in legend. (b) Measured propagation loss at $\lambda = 1630$ nm and $\lambda = 1480$ nm for the SiO_2 -clad and TeO_2 -clad waveguides, respectively.

smoothing filter was applied to the overall spectral data to reduce Fabry-Perot ripple caused by facet reflectivity. Each spectrum displays a bandgap with high reflectivity surrounded by regions of high transmission. The misalignment of the spectra between the different claddings is caused by differences in Floquet-Bloch mode effective index, where the SiO₂-clad spectra have a lower wavelength bandgap than the TeO₂-clad spectra, i.e. a lower Bragg wavelength, as expected. The position of the TeO₂-clad waveguide spectra is significantly redshifted in comparison to the simulation results with a Bragg wavelength of ~ 1530 nm instead of 1465 nm. From the SEM images in Fig. 2.14, we observe rounded waveguide grating structures that result from limited resolution of the DUV lithographic patterning. The round shapes are emphasized following the deposition of the TeO₂ film, which displays excellent uniformity.

The areas of high transmission correspond to the second- and first-order bands below 1480 nm and above 1600 nm, respectively. Fabry-Perot resonance patterns starting at a wavelength of 1540 nm are noted with a gradual ascent in transmission towards higher wavelengths, making it difficult to determine the exact location of the band edge. These oscillations likely arise from the mode transformers approaching Bragg resonance near the junction with the Si wire waveguide. The Floquet-Bloch mode effective index is significantly increased near the Si wire taper and any rounding of the described structures caused by the lithographic patterning might leave behind excess Si, thus contributing to the large redshift in the Bragg resonance wavelength and overall dispersion relation. Bragg wavelengths of 1560 nm and 1670 nm are estimated in the mode transformer at the SWG end, depicted in Fig. 2.14(c), and the wire waveguide end, respectively. This shift affects the transmission spectrum over the wavelength range up to 1670 nm, decreasing transmission and introducing Fabry-Perot fringes. This effect can be readily mitigated by chirping the period along the mode transformer to reduce the Floquet-Bloch mode effective index near the SWG-wire junctions. However, we could not use this technique in our current design due to the comparatively large MFS of the DUV patterning process.

We analyzed losses in the S-band for the TeO₂-clad waveguide and the far end of the L-band for the SiO₂-clad waveguide since Fabry-Perot fringes are minimal in these regions. The propagation losses were fitted using the cutback method and linear regression, as seen in Fig. 2.15(b), and were reported to be 1.0 ± 0.1 dB/mm at $\lambda = 1480$ nm for the TeO₂-clad SWG waveguide and 1.5 ± 0.1 dB/mm at $\lambda = 1630$ nm for the SiO₂-clad SWG waveguide. We attribute the loss primarily to the scattering in the Si waveguide structure due to limited resolution of the lithographic process used. The TeO₂ coating

has been shown to have low planar waveguide propagation loss on the order of 0.1 dB/cm [47]. According to waveguide scattering theory [58], loss scales with a factor of $(n_1^2 - n_2^2)^2$, where n_1 and n_2 are the material indices of the waveguide core and cladding, respectively. Based on this factor, the reduced index contrast of Si-TeO₂ compared to Si-SiO₂ is expected to reduce the scattering losses by approximately 40% for equal mode overlap with the core-cladding interface, which is in good agreement with the observed loss reduction. The fiber-chip coupling loss was also extracted from these measurements, with 4.8 ± 0.2 dB/facet at $\lambda = 1480$ nm for the TeO₂-clad waveguide and 2.5 ± 0.1 dB/facet at $\lambda = 1630$ nm for the SiO₂-clad waveguide. Higher coupling losses are expected for the TeO₂-clad devices due to the higher modal index of the waveguide at the chip edge lowering the overlap with the fiber mode.

2.3.2 Design #2: SWG-wire mode transformers

Waveguides for Design #2 were fabricated on an MPW run using the NanoSOI platform from Applied Nanotools Inc. (ANT) in Edmonton, Alberta, Canada. The wafers have a 220 nm-thick Si device layer on a 2 μm -thick SiO₂ buffer oxide and a 725 μm -thick Si handle. 100 keV EBL technology and an anisotropic inductively coupled plasma reactive ion etching (ICP-RIE) process are used to fully etch through the Si layer down to the buffer oxide and draw fine Si structures with a MFS and spacing of 60 and 70 nm, respectively. These feature sizes are much lower than those used in Design #1 (i.e., MFS = 180 nm) and are essential for developing low-loss subwavelength photonic structures in SOI. Following the primary etching process, the wafer was then diced into chips. A deep-etch process was used to generate 250 μm -deep trenches around the chip perimeter to enable fiber-chip edge coupling. Chips in the run did not receive any SiO₂ top cladding from the foundry per our request. Upon receiving the chips, 382 ± 20 nm-thick TeO₂ thin films were deposited directly onto the exposed waveguides. A relatively thick layer of TeO₂ is required to increase the mode overlap with the cladding material and reduce light interaction with the air above the chip. Prism coupling measurements revealed a TeO₂ film background loss of 1.47 and 1.29 dB/cm at 638 and 847 nm wavelengths, respectively.

Fig. 2.16 illustrates the different photonic circuits used to determine the total loss that arises from our designed TeO₂-coated SWG-wire mode transformer. For consistency, all circuits shown have a fixed wire waveguide width (w) of 450 nm, an edge coupler length (L_{EC}) of 50 μm , and an edge coupler tip width of 100 nm. The mode transformers are as described in Section 2.2.4 (i.e., $w_{\text{SWG}} = 300$ nm, $w_{\text{tip}} = 100$ nm, with the same period and duty cycle parameters). The circuits shown in Fig. 2.16(a) are analogous to cutback

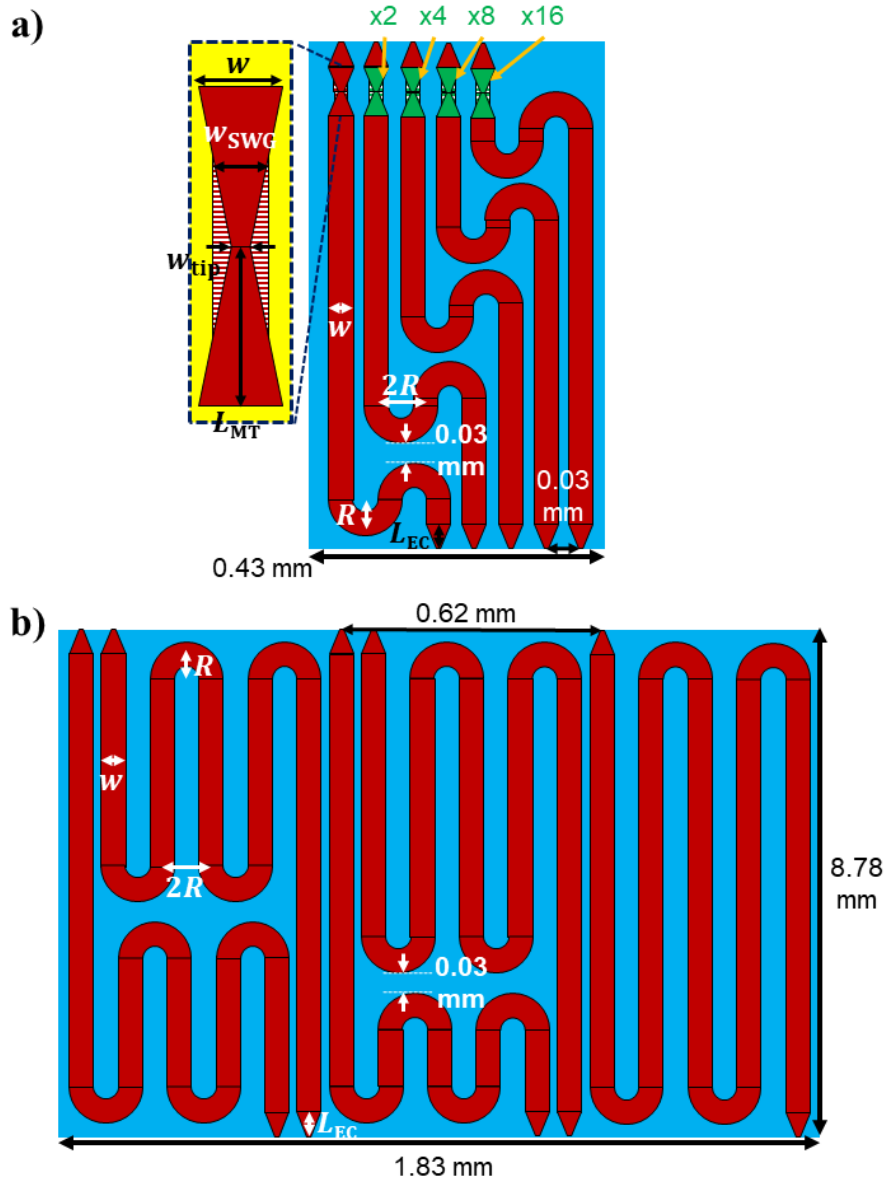


FIGURE 2.16: Circuit schematic for Design #2 (a) mode transformer test structures and (b) wire waveguide serpentine cutback structures. Inset of (a) shows a detailed diagram of back-to-back mode transformers, which are duplicated across various test structures to extract the loss of a single mode transformer. Structures are not drawn to scale.

structures. Each circuit is identical but has a different number of mode transformers. By taking a linear regression fit of the measured power transmission for each circuit

in Fig. 2.16(a) over the total number of mode transformers in each circuit, we can extract the total loss per mode transformer and the associated background loss from the slope and y-intercept of the fit, respectively. The background loss in this case accounts for the fiber-chip coupling loss and the propagation loss of the access wire waveguide section, which is ~ 1 cm long for all mode transformer test circuits. The wire waveguide propagation loss is assessed by performing cutback measurements on the circuits in Fig. 2.16(b). All waveguide bends have a radius (R) of $70 \mu\text{m}$ and are assumed to have negligible radiation loss based on waveguide bend calculations from FDE simulations for our specific geometry.

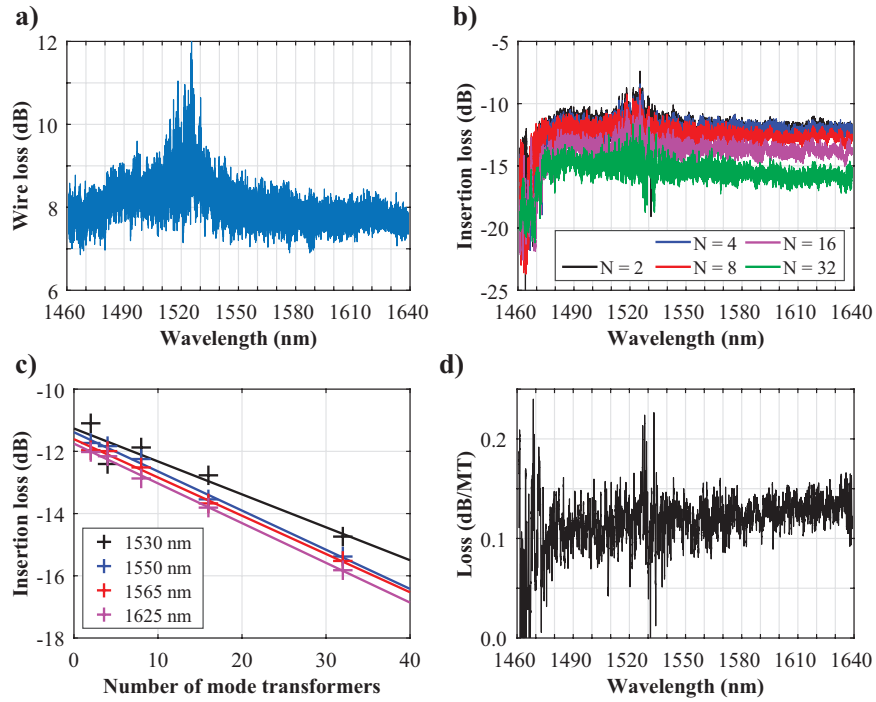


FIGURE 2.17: Measurement results for Design #2 test circuits. (a) Total measured loss of wire waveguide section in mode transformer test structures based on the results from serpentine cutback structures. (b) Measured insertion loss spectra for each mode transformer test circuit. Only losses from the mode transformers and fiber-chip coupling are included in the data. (c) Linear regression fits of data from b) for specific wavelengths. (d) Loss per mode transformer extracted from fitting method used in (c) for all measured wavelengths.

The devices were characterized using the setup described in Section 2.3.1. The cutback measurement procedure used for the SWG waveguides from Design #1 was applied

to the wire waveguide serpentine structures here. These waveguides exhibited a propagation and coupling loss of 7.9 ± 0.4 dB/cm and 3.6 ± 0.44 dB/coupler at a 1550 nm wavelength, respectively. The coupling loss is slightly higher than the simulated loss of 3.26 dB/coupler (Table 2.2). The small discrepancy may be caused by the propagation loss over the 50 μm edge coupler length, which was not accounted for in simulation. The total loss of the wire waveguide section in the mode transformer circuit is obtained by multiplying its length by the measured propagation loss from the wire serpentines and is displayed in Fig. 2.17(a) across the measured spectrum. Fig. 2.17(b) shows the measured transmission spectra of each mode transformer test circuit. Losses from the optical system off-chip and the wire waveguide interconnectors on-chip (i.e., from Fig. 2.17(a)) are excluded, so only losses related to the mode transformers and the fiber-chip coupling are reflected in the depicted data. Linear regression fits were performed over the number of mode transformers included in each circuit for specific wavelengths. These results are shown in Fig. 2.17(c). The loss per mode transformer is determined from the slope of the fit, which is 0.12 dB for each analyzed wavelength. The same procedure is performed over the entire spectrum and the mode transformer loss is depicted in Fig. 2.17(d) for all measured wavelengths. The large drop in transmission for wavelengths below 1480 nm in Fig. 2.17(b) is assumed to be associated with the photonic bandgap caused by the grating portion of the mode transformer, so the mode transformer loss results here are considered unreliable. The large discrepancies near 1530 nm are caused by the loss measured from the wire waveguides, as seen from the spectra in Fig. 2.17(a). As a result, the uncertainty for the mode transformer loss in this region is high. Regardless, for all wavelengths above 1480 nm, the mode transformer loss is quite consistent and determined to be 0.12 ± 0.02 dB. The transformer thus provides an efficient way to transition between TeO₂-clad SWG and wire waveguide modes over a broad band without consuming much real estate on the chip. Various parameters may be adjusted to alleviate bandgap behaviour and accommodate operation in other spectral ranges of interest.

2.3.3 Design #3: FB-SWG waveguides

We re-used the NanoSOI platform offered by ANT, described in Section 2.3.2, for the fabrication of Design #3 to leverage its small feature size specifications, which are necessary for constructing reliable SWG metamaterial waveguide structures. The mask layout used for Design #3, shown in Fig. 2.18, features various photonic circuits for testing the performance of TeO₂-clad waveguides and mode transformers based on the FB-SWG topology. These waveguides are more robust than conventional SWGs with the addition

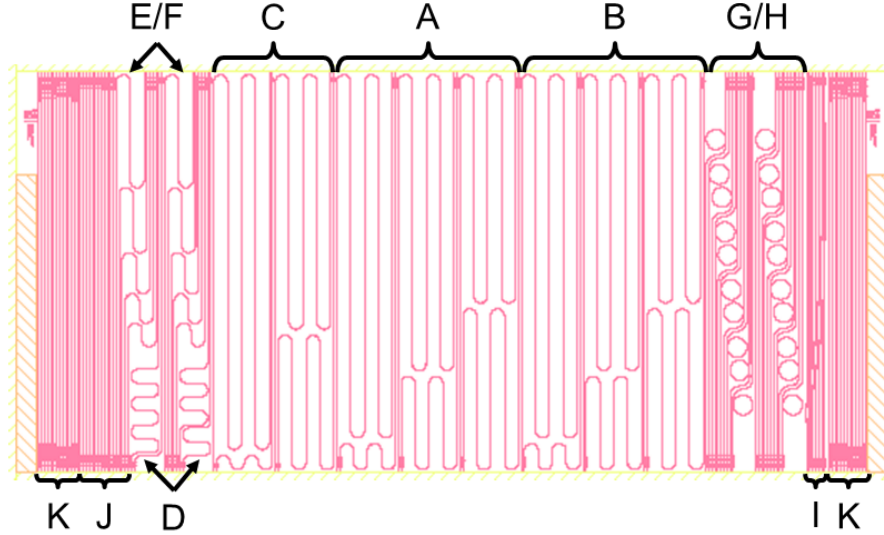


FIGURE 2.18: Mask layout for Design #3, which primarily studies FB-SWG waveguide structures.

of a thin Si support beam that permeates through the gratings and possess a moderate mode overlap factor with the TeO_2 cladding that is greater than that of an equivalent wire waveguide [59]. By combining the benefits of both wire and SWG waveguides, the FB-SWG architecture provides an interesting alternative approach to enhancing gain in waveguide amplifiers. At the time of writing this thesis, this layout was currently under fabrication. As a result, this section provides greater detail on the mask layout and the fabricated test structures for this design in lieu of experimental results.

Table 2.4 summarizes the different blocks shown on the mask layout of Fig. 2.18. The main test structures are the FB-SWG and wire waveguide serpentine (blocks A–C). These circuits use the cutback method to determine the propagation loss of the waveguide in question—in this case, two FB-SWG waveguides ($\Lambda = 300$ nm, $\delta\Lambda = 100$ nm, $w_b = 100$ nm, and $w_{wg} = 300$ and 450 nm for block A and B, respectively), and one wire waveguide ($w_{wg} = 450$ nm). Each serpentine has four 180° wire waveguide bends with 70 μm radius, which were used on the serpentine cutbacks from Design #2. The circuits in block D are bend test structures used to verify any radiation loss related to these bend structures. The FB-SWG serpentine also feature mode transformers that provide smooth transitions between the FB-SWG gain sections and wire waveguide bends. Like block D, the block E and F circuits use back-to-back mode transformers to determine the propagation loss per mode transformation. These are equivalent to the mode transformer “cutback” circuits experimentally demonstrated in Section 2.3.2 for

TABLE 2.4: Design #3 mask layout details. Block IDs correspond to Fig. 2.18.

Block	Devices	Metric	Variable [units]	Variable values
A	FB-SWG serpentines ¹	Propagation loss	FB-SWG length [cm]	[0.39, 0.66, 0.93, 1.20, 1.47, 1.74]
B	FB-SWG serpentines ²	”	”	”
C	Wire serpentines	Propagation loss	Wire length [cm]	[0.39, 0.87, 1.36, 1.84]
D	Wire bends	Loss per 180° bend	# of 90° bends	[2, 6, 10, 14]
E	Mode transformers ¹	Loss per transformer	# of mode transformers	[2, 4, 8, 16, 32]
F	Mode transformers ²	”	”	”
G	FB-SWG ring resonators ¹	Q factor, potential lasers	Coupling gap [μm]	[0.2, 0.3, 0.4, 0.5, 0.6, 0.7, 0.8, 0.9, 1.0, 1.1]
H	FB-SWG ring resonators ²	”	”	”
I	FB-SWG MZIs	FB-SWG group index	Signal arm length [μm]	[10, 25, 50, 100, 250, 500, 1000]
J	Wire edge couplers	Coupling loss	Coupler length / tip width	Various
K	FB-SWG straights	Coupling loss	Various	Various

¹ $w_{\text{wg}} = 300$ nm in Fig. 2.1 diagram.

² $w_{\text{wg}} = 450$ nm in Fig. 2.1 diagram.

Design #2. The parameters in blocks E and F correspond to the parameters in blocks A and B, respectively. Ring resonators in blocks G and H have corresponding FB-SWG geometry to blocks A and B, respectively, and are used to determine the quality (Q) factor of each waveguide. When coated in a RE-doped TeO_2 film, these rings could act as potential on-chip laser cavities [60]. Block I contains Mach-Zehnder interferometer (MZI) test structures with a particular wire and FB-SWG geometry in the reference and signal arms, respectively. Each circuit has a different signal arm length and can be used to determine the group index of the FB-SWG waveguide [61]. Finally, blocks J and K contain straight waveguide test structures of both the wire and FB-SWG variety. The wire waveguides each have different edge coupler parameters, while the FB-SWG waveguides explore different fishbone shape sizes, which may reveal intriguing properties

for future designs.

2.4 Conclusion

In conclusion, we have demonstrated a new type of SWG waveguide on an SOI platform coated with TeO₂. A measured propagation loss of 1.0 ± 0.1 dB/mm and fiber-chip coupling loss of 4.8 ± 0.2 dB/facet were reported for conventional SWG metamaterial waveguides fabricated on a standard foundry process using 193 nm DUV lithography and then coated in a 105 nm-thick TeO₂ thin film deposited using RF reactive magnetron sputtering. Following this initial demonstration, a subsequent SOI SWG waveguide design was proposed, using a thicker TeO₂ cladding layer to reduce the propagation loss. SWG-wire mode transformers based on this new design were fabricated using a different SOI foundry process based on EBL. The measured devices, coated in a 382 nm-thick TeO₂ film, exhibited a 0.12 dB loss over a 50 μ m length across the C- and L-bands, highlighting low loss and broadband mode transformation that can be tuned to accommodate other waveguide geometries and operate in different spectral windows. TeO₂-clad Si FB-SWG waveguides, with greater structural integrity and potentially lower propagation loss compared to conventional SWG waveguides, as well as a greater TeO₂ mode overlap factor over trivial wire waveguides, are currently under investigation and awaiting fabrication. Together, the benefits of both Si SWG waveguides and a high index cladding, such as TeO₂, that can serve as an effective host for active elements, such as Er³⁺, opens new avenues for development of compact on-chip light-emitting devices in SOI PICs.

Bibliography

- [1] G. T. Reed, “The optical age of silicon,” *Nature*, vol. 427, pp. 595–596, 2004.
- [2] G. T. Reed, W. R. Headley, and C. E. Jason Png, “Silicon photonics: the early years,” in *Optoelectronic Integration on Silicon II* (J. A. Kubby and G. E. Jabbour, eds.), vol. 5730, pp. 1–18, International Society for Optics and Photonics, SPIE, 2005.
- [3] R. A. Soref, “The past, present, and future of silicon photonics,” *IEEE Journal of Selected Topics in Quantum Electronics*, vol. 12, no. 6, pp. 1678–1687, 2006.
- [4] D. Thomson, A. Zilkie, J. E. Bowers, T. Komljenovic, G. T. Reed, L. Vivien, D. Marris-Morini, E. Cassan, L. Viot, J.-M. Fédéli, J.-M. Hartmann, J. H. Schmid,

- D.-X. Xu, F. Boeuf, P. O'Brien, G. Z. Mashanovich, and M. Nedeljkovic, "Roadmap on silicon photonics," *Journal of Optics*, vol. 18, no. 7, p. 073003, 2016.
- [5] M. Lipson, "Guiding, modulating, and emitting light on silicon—Challenges and opportunities," *Journal of Lightwave Technology*, vol. 23, no. 12, pp. 4222–4238, 2005.
- [6] A. J. Kenyon, "Erbium in silicon," *Semiconductor Science and Technology*, vol. 20, no. 12, p. R65, 2005.
- [7] L. Agazzi, J. D. B. Bradley, M. Dijkstra, F. Ay, G. Roelkens, R. Baets, K. Wörhoff, and M. Pollnau, "Monolithic integration of erbium-doped amplifiers with silicon-on-insulator waveguides," *Optics Express*, vol. 18, no. 26, pp. 27703–27711, 2010.
- [8] D. Duchense, P. Cheben, R. A. Morandotti, B. Lamontagne, D.-X. Xu, S. Janz, and D. N. Christodoulides, "Group-index birefringence and loss measurements in silicon-on-insulator photonic wire waveguides," *Optical Engineering*, vol. 46, no. 10, p. 104602, 2007.
- [9] A. Tengattini, D. Gandolfi, N. Prtljaga, A. Anopchenko, J. M. Ramirez, F. F. Lupi, Y. Berencen, D. Navarro-Urrios, P. Rivallin, K. Surana, B. Garrido, J.-M. Fedeli, and L. Pavesi, "Toward a 1.54 μm electrically driven erbium-doped silicon slot waveguide and optical amplifier," *Journal of Lightwave Technology*, vol. 31, no. 3, pp. 391–397, 2013.
- [10] D. M. Kita, J. Michon, S. G. Johnson, and J. Hu, "Are slot and sub-wavelength grating waveguides better than strip waveguides for sensing?," *Optica*, vol. 5, no. 9, pp. 1046–1054, 2018.
- [11] D. González-Andrade, C. Lafforgue, E. Durán-Valdeiglesias, X. Le Roux, M. Berciano, E. Cassan, D. Marris-Morini, A. V. Velasco, P. Cheben, L. Vivien, and C. Alonso-Ramos, "Polarization- and wavelength-agnostic nanophotonic beam splitter," *Scientific Reports*, vol. 9, no. 1, p. 3604, 2019.
- [12] J. D. B. Bradley, E. S. Hosseini, Purnawirman, Z. Su, T. N. Adam, G. Leake, D. Coolbaugh, and M. R. Watts, "Monolithic erbium- and ytterbium-doped microring lasers on silicon chips," *Optics Express*, vol. 22, no. 10, pp. 12226–12237, 2014.

- [13] Z. Su, N. Li, E. S. Magden, M. Byrd, Purnawirman, T. N. Adam, G. Leake, D. Coolbaugh, J. D. B. Bradley, and M. R. Watts, “Ultra-compact and low-threshold thulium microcavity laser monolithically integrated on silicon,” *Optics Letters*, vol. 41, no. 24, pp. 5708–5711, 2016.
- [14] P. F. Jarschel, M. C. M. M. Souza, R. B. Merlo, and N. C. Frateschi, “Loss compensation in microring-based Si photonics devices via Er^{3+} doped claddings,” *IEEE Photonics Journal*, vol. 10, no. 4, pp. 1–12, 2018.
- [15] P. Cheben, J. H. Schmid, R. Halir, J. M. Luque-González, J. G. Wangüemert-Pérez, D. Melati, and C. Alonso-Ramos, “Recent advances in metamaterial integrated photonics,” *Advances in Optics and Photonics*, vol. 15, no. 4, pp. 1033–1105, 2023.
- [16] P. Cheben, R. Halir, J. H. Schmid, H. A. Atwater, and D. R. Smith, “Subwavelength integrated photonics,” *Nature*, vol. 560, pp. 565–572, 2018.
- [17] S. M. Rytov, “Electromagnetic properties of a finely stratified medium,” *Soviet Physics JETP*, vol. 2, no. 3, pp. 466–475, 1956.
- [18] R. Halir, P. J. Bock, P. Cheben, A. Ortega-Moñux, C. Alonso-Ramos, J. H. Schmid, J. Lapointe, D.-X. Xu, J. G. Wangüemert-Pérez, Í. Molina-Fernández, and S. Janz, “Waveguide sub-wavelength structures: a review of principles and applications,” *Laser & Photonics Reviews*, vol. 9, no. 1, pp. 25–49, 2015.
- [19] P. Cheben, D.-X. Xu, S. Janz, and A. Densmore, “Subwavelength waveguide grating for mode conversion and light coupling in integrated optics,” *Optics Express*, vol. 14, no. 11, pp. 4695–4702, 2006.
- [20] P. J. Bock, P. Cheben, J. H. Schmid, J. Lapointe, A. Delâge, S. Janz, G. C. Aers, D.-X. Xu, A. Densmore, and T. J. Hall, “Subwavelength grating periodic structures in silicon-on-insulator: a new type of microphotonic waveguide,” *Optics Express*, vol. 18, no. 19, pp. 20251–20262, 2010.
- [21] P. Cheben, J. H. Schmid, S. Wang, D.-X. Xu, M. Vachon, S. Janz, J. Lapointe, Y. Painchaud, and M.-J. Picard, “Broadband polarization independent nanophotonic coupler for silicon waveguides with ultra-high efficiency,” *Optics Express*, vol. 23, no. 17, pp. 22553–22563, 2015.
- [22] R. Halir, P. Cheben, S. Janz, D.-X. Xu, Í. Molina-Fernández, and J. G. Wangüemert-Pérez, “Waveguide grating coupler with subwavelength microstructures,” *Optics Letters*, vol. 34, no. 9, pp. 1408–1410, 2009.

- [23] C. Alonso-Ramos, P. Cheben, A. Ortega-Moñux, J. H. Schmid, D.-X. Xu, and Í. Molina-Fernández, “Fiber-chip grating coupler based on interleaved trenches with directionality exceeding 95%,” *Optics Letters*, vol. 39, no. 18, pp. 5351–5354, 2014.
- [24] D. Benedikovic, P. Cheben, J. H. Schmid, D.-X. Xu, B. Lamontagne, S. Wang, J. Lapointe, R. Halir, A. Ortega-Moñux, S. Janz, and M. Dado, “Subwavelength index engineered surface grating coupler with sub-decibel efficiency for 220-nm silicon-on-insulator waveguides,” *Optics Express*, vol. 23, no. 17, pp. 22628–22635, 2015.
- [25] P. J. Bock, P. Cheben, J. H. Schmid, J. Lapointe, A. Delâge, D.-X. Xu, S. Janz, A. Densmore, and T. J. Hall, “Subwavelength grating crossings for silicon wire waveguides,” *Optics Express*, vol. 18, no. 15, pp. 16146–16155, 2010.
- [26] J. G. Wangüemert-Pérez, P. Cheben, A. Ortega-Moñux, C. Alonso-Ramos, D. Pérez-Galacho, R. Halir, Í. Molina-Fernández, D.-X. Xu, and J. H. Schmid, “Evanescent field waveguide sensing with subwavelength grating structures in silicon-on-insulator,” *Optics Letters*, vol. 39, no. 15, pp. 4442–4445, 2014.
- [27] J. Flueckiger, S. Schmidt, V. Donzella, A. Sherwali, D. M. Ratner, L. Chrostowski, and K. C. Cheung, “Sub-wavelength grating for enhanced ring resonator biosensor,” *Optics Express*, vol. 24, no. 14, pp. 15672–15686, 2016.
- [28] Z. Pan, X. Xu, C.-J. Chung, H. Dalir, H. Yan, K. Chen, Y. Wang, B. Jia, and R. T. Chen, “High-speed modulator based on electro-optic polymer infiltrated sub-wavelength grating waveguide ring resonator,” *Laser & Photonics Reviews*, vol. 12, no. 6, p. 1700300, 2018.
- [29] P. Cheben, P. J. Bock, J. H. Schmid, J. Lapointe, S. Janz, D.-X. Xu, A. Densmore, A. Delâge, B. Lamontagne, and T. J. Hall, “Refractive index engineering with subwavelength gratings for efficient microphotonic couplers and planar waveguide multiplexers,” *Optics Letters*, vol. 35, no. 15, pp. 2526–2528, 2010.
- [30] R. Nayak, V. Gupta, A. L. Dawar, and K. Sreenivas, “Optical waveguiding in amorphous tellurium oxide thin films,” *Thin Solid Films*, vol. 445, no. 1, pp. 118–126, 2003.
- [31] S. M. Pietralunga, M. Lanata, M. Ferè, D. Piccinin, G. Cusmai, M. Torregiani, and M. Martinelli, “High-contrast waveguides in sputtered pure TeO₂ glass thin films,” *Optics Express*, vol. 16, no. 26, pp. 21662–21670, 2008.

- [32] S. J. Madden and K. T. Vu, “Very low loss reactively ion etched Tellurium Dioxide planar rib waveguides for linear and non-linear optics,” *Optics Express*, vol. 17, no. 20, pp. 17645–17651, 2009.
- [33] K. Mirabbas Kiani, H. C. Frankis, C. M. Naraine, D. B. Bonneville, A. P. Knights, and J. D. B. Bradley, “Lasing in a hybrid rare-earth silicon microdisk,” *Laser & Photonics Reviews*, vol. 16, no. 1, p. 2100348, 2022.
- [34] K. Vu, S. Farahani, and S. Madden, “980 nm pumped erbium doped tellurium oxide planar rib waveguide laser and amplifier with gain in S, C and L band,” *Optics Express*, vol. 23, no. 2, pp. 747–755, 2015.
- [35] K. Vu and S. Madden, “Tellurium dioxide Erbium doped planar rib waveguide amplifiers with net gain and 2.8dB/cm internal gain,” *Optics Express*, vol. 18, no. 18, pp. 19192–19200, 2010.
- [36] K. Mirabbas Kiani, H. C. Frankis, H. M. Mbonde, R. Mateman, A. Leinse, A. P. Knights, and J. D. B. Bradley, “Thulium-doped tellurium oxide waveguide amplifier with 7.6 dB net gain on a silicon nitride chip,” *Optics Letters*, vol. 44, no. 23, pp. 5788–5791, 2019.
- [37] H. C. Frankis, H. M. Mbonde, D. B. Bonneville, C. Zhang, R. Mateman, A. Leinse, and J. D. B. Bradley, “Erbium-doped TeO₂-coated Si₃N₄ waveguide amplifiers with 5 dB net gain,” *Photonics Research*, vol. 8, no. 2, pp. 127–134, 2020.
- [38] H. C. Frankis, K. Mirabbas Kiani, D. Su, R. Mateman, A. Leinse, and J. D. B. Bradley, “High-*Q* tellurium-oxide-coated silicon nitride microring resonators,” *Optics Letters*, vol. 44, no. 1, pp. 118–121, 2019.
- [39] K. Mirabbas Kiani, D. B. Bonneville, A. P. Knights, and J. D. B. Bradley, “High-*Q* TeO₂-Si hybrid microring resonators,” *Applied Sciences*, vol. 12, no. 3, p. 1363, 2022.
- [40] H. C. Frankis, D. Su, D. B. Bonneville, and J. D. B. Bradley, “A tellurium oxide microcavity resonator sensor integrated on-chip with a silicon waveguide,” *Sensors*, vol. 18, no. 11, p. 4061, 2018.
- [41] N. Singh, H. M. Mbonde, H. C. Frankis, E. Ippen, J. D. B. Bradley, and F. X. Kärtner, “Nonlinear silicon photonics on CMOS-compatible tellurium oxide,” *Photonics Research*, vol. 8, no. 12, pp. 1904–1909, 2020.

- [42] A. J. Kenyon, “Recent developments in rare-earth doped materials for optoelectronics,” *Progress in Quantum Electronics*, vol. 26, no. 4, pp. 225–284, 2002.
- [43] J. D. Sarmiento-Merenguel, A. Ortega-Moñux, J.-M. Fédéli, J. G. Wangüemert-Pérez, C. Alonso-Ramos, E. Durán-Valdeiglesias, P. Cheben, Í. Molina-Fernández, and R. Halir, “Controlling leakage losses in subwavelength grating silicon metamaterial waveguides,” *Optics Letters*, vol. 41, no. 15, pp. 3443–3446, 2016.
- [44] P. Jean, A. Gervais, S. LaRochelle, and W. Shi, “Slow light in subwavelength grating waveguides,” *IEEE Journal of Selected Topics in Quantum Electronics*, vol. 26, no. 2, pp. 1–8, 2020.
- [45] J. M. Luque-González, A. Sánchez-Postigo, A. Hadij-ElHouati, A. Ortega-Moñux, J. G. Wangüemert-Pérez, J. H. Schmid, P. Cheben, Í. Molina-Fernández, and R. Halir, “A review of silicon subwavelength gratings: building break-through devices with anisotropic metamaterials,” *Nanophotonics*, vol. 10, no. 11, pp. 2765–2797, 2021.
- [46] H. M. Mbonde, H. C. Frankis, and J. D. B. Bradley, “Enhanced nonlinearity and engineered anomalous dispersion in TeO₂-coated Si₃N₄ waveguides,” *IEEE Photonics Journal*, vol. 12, no. 2, pp. 1–10, 2020.
- [47] H. C. Frankis, K. Mirabbas Kiani, D. B. Bonneville, C. Zhang, S. Norris, R. Mateman, A. Leinse, N. D. Bassim, A. P. Knights, and J. D. B. Bradley, “Low-loss TeO₂-coated Si₃N₄ waveguides for application in photonic integrated circuits,” *Optics Express*, vol. 27, no. 9, pp. 12529–12540, 2019.
- [48] M. Belt, T. Huffman, M. L. Davenport, W. Li, J. S. Barton, and D. J. Blumenthal, “Arrayed narrow linewidth erbium-doped waveguide-distributed feedback lasers on an ultra-low-loss silicon-nitride platform,” *Optics Letters*, vol. 38, no. 22, pp. 4825–4828, 2013.
- [49] E. S. Hosseini, Purnawirman, J. D. B. Bradley, J. Sun, G. Leake, T. N. Adam, D. D. Coolbaugh, and M. R. Watts, “CMOS-compatible 75 mW erbium-doped distributed feedback laser,” *Optics Letters*, vol. 39, no. 11, pp. 3106–3109, 2014.
- [50] Purnawirman, N. Li, E. S. Magden, G. Singh, N. Singh, A. Baldycheva, E. S. Hosseini, J. Sun, M. Moresco, T. N. Adam, G. Leake, D. Coolbaugh, J. D. B. Bradley, and M. R. Watts, “Ultra-narrow-linewidth al₂o₃:er³⁺ lasers with a wavelength-insensitive waveguide design on a wafer-scale silicon nitride platform,” *Optics Express*, vol. 25, no. 12, pp. 13705–13713, 2017.

- [51] S. Ek, P. Lunnemann, Y. Chen, E. Semenova, K. Yvind, and J. Mork, “Slow-light-enhanced gain in active photonic crystal waveguides,” *Nature Communications*, vol. 5, no. 1, p. 5039, 2014.
- [52] V. R. Almeida, R. R. Panepucci, and M. Lipson, “Nanotaper for compact mode conversion,” *Optics Letters*, vol. 28, no. 15, pp. 1302–1304, 2003.
- [53] M. Papes, P. Cheben, D. Benedikovic, J. H. Schmid, J. Pond, R. Halir, A. Ortega-Moñux, G. Wangüemert-Pérez, W. N. Ye, D.-X. Xu, S. Janz, M. Dado, and V. Vainek, “Fiber-chip edge coupler with large mode size for silicon photonic wire waveguides,” *Optics Express*, vol. 24, no. 5, pp. 5026–5038, 2016.
- [54] N. Li, M. Xin, Z. Su, E. S. Magden, N. Singh, J. Notaros, E. Timurdogan, P. Purnawirman, J. D. B. Bradley, and M. R. Watts, “A silicon photonic data link with a monolithic erbium-doped laser,” *Scientific Reports*, vol. 10, p. 1114, 2020.
- [55] E. S. Magden, N. Li, Purnawirman, J. D. B. Bradley, N. Singh, A. Ruocco, G. S. Petrich, G. Leake, D. D. Coolbaugh, E. P. Ippen, M. R. Watts, and L. A. Kolodziejski, “Monolithically-integrated distributed feedback laser compatible with CMOS processing,” *Optics Express*, vol. 25, no. 15, pp. 18058–18065, 2017.
- [56] R. J. Bojko, J. Li, L. He, T. Baehr-Jones, M. Hochberg, and Y. Aida, “Electron beam lithography writing strategies for low loss, high confinement silicon optical waveguides,” *Journal of Vacuum Science Technology B*, vol. 29, no. 6, p. 06F309, 2011.
- [57] L. Chrostowski and M. Hochberg, *Silicon Photonics Design: From Devices to Systems*. Cambridge University Press, 2015.
- [58] J. H. Schmid, A. Delâge, B. Lamontagne, J. Lapointe, S. Janz, P. Cheben, A. Densmore, P. Waldron, D.-X. Xu, and K. P. Yap, “Interference effect in scattering loss of high-index-contrast planar waveguides caused by boundary reflections,” *Optics Letters*, vol. 33, no. 13, pp. 1479–1481, 2008.
- [59] L. S. Puumala, S. M. Grist, K. Wickremasinghe, M. A. Al-Qadasi, S. J. Chowdhury, Y. Liu, M. Mitchell, L. Chrostowski, S. Shekhar, and K. C. Cheung, “An optimization framework for silicon photonic evanescent-field biosensors using sub-wavelength gratings,” *Biosensors*, vol. 12, no. 10, p. 840, 2022.
- [60] K. Mirabbas Kiani, H. C. Frankis, R. Mateman, A. Leinse, A. P. Knights, and J. D. B. Bradley, “Thulium-doped tellurium oxide microring lasers integrated on

a low-loss silicon nitride platform,” *Optical Materials Express*, vol. 11, no. 11, pp. 3656–3665, 2021.

- [61] I. Glesk, P. J. Bock, P. Cheben, J. H. Schmid, J. Lapointe, and S. Janz, “All-optical switching using nonlinear subwavelength Mach-Zehnder on silicon,” *Optics Express*, vol. 19, no. 15, pp. 14031–14039, 2011.

Chapter 3

A moderate confinement 1.3 and 1.5 μm silicon nitride platform enabled by a rapid prototyping integrated photonics foundry process

This chapter outlines an integrated photonics foundry process for rapid prototyping silicon nitride (SiN) waveguides designed for operation in the second and third telecommunication windows (1.31 and 1.55 μm wavelengths, respectively). SiN is a desirable material for silicon photonics (SiP) applications due to its compatibility with complementary-metal-oxide-semiconductor (CMOS) fabrication technologies and various benefits over silicon (Si), including low scattering and polarization-dependent loss, greater tolerance to fabrication error, optical transparency through the visible (VIS) spectrum, and negligible two photon absorption (TPA) at telecom wavelengths. Many integrated photonics foundries have already incorporated SiN material into their product lines, whether as the primary waveguide layer or as an additional medium to boost functionality and applicability in their current high-performance photonic integrated circuits (PICs). However, many of these SiN waveguides and their processes are developed to accommodate specific applications with definitive metrics, which introduces some restrictions on their use.

Furthermore, most industrial fabs offering these products and services produce chips at relatively high volumes, which results in a high price point and design/fabrication cycles that span many months. This is deterring for novice designers, academic researchers and start-up companies with low budgets and tight timelines hoping to explore and experiment with SiN PICs in their own scientific and research and development work.

Here, we present our progress on the moderate confinement SiN platform developed with the integrated photonics foundry Applied Nanotools Inc. (ANT). The waveguides, grown via low pressure chemical vapour deposition (LPCVD), feature a moderate thickness of 400 nm, which enables single mode operation and design flexibility over various wavelength ranges for different applications. Direct-write electron beam lithography (EBL) is used to pattern the SiN layer and generate waveguide feature sizes down to ~ 100 nm, which are essential for fabricating metamaterial structures. The measured SiN waveguide loss is between 0.6-1.3 dB/cm for the O-band and between 0.4-1.8 dB/cm across the S-, C- and L-bands for both transverse electric (TE) and transverse magnetic (TM) polarizations, which is comparable to many other moderate confinement SiN waveguide platforms. Important integrated photonics components are also reported for wavelengths near 1.31 μm and 1.55 μm , including fiber-chip couplers, multimode interference (MMI)-based power splitters, and ring resonators. These building blocks were developed over four designs and fabrication verification runs and have been compiled into a process design kit (PDK), which is commercially available directly through the foundry or through multi-project wafer (MPW) aggregate services such as CMC Microsystems. The foundry performs five MPW runs a year with turnaround times of around 8 weeks, providing a quick, low-cost method for fabricating SiN chips with passive and thermo-optic active photonics devices. As the SiN photonics ecosystem continues to grow and new applications emerge daily, this rapid prototyping service provides a convenient system to access SiN PIC technology that is necessary for encouraging its exploration and advancing the field of integrated photonics.

The contents of this chapter represent a manuscript in preparation by the authors. This work has been included in the thesis to highlight the initial and ongoing development of the integrated photonics platform that forms the underlying foundation of the SiN-based subwavelength grating (SWG) metamaterial waveguide devices discussed in the subsequent chapters. Section 3.1 introduces the motivation for exploring SiN as a photonic material and provides a comprehensive background on the global effort in SiN photonics research and infrastructure. Section 3.2 presents details of the SiN film and waveguide fabrication, and highlights additional post-processing options available

to platform users. Section 3.3 shares the design process and characterization results for various integrated photonic components, all of which are included in the platform PDK. The results are thoroughly examined for each reported component. Section 3.4 discusses how ANT’s SiN platform fits into the current SiN photonics ecosystem and suggests areas for further development of the platform. Finally, Section 3.5 summarizes the platform’s key features and reported metrics, and concludes with remarks of its goals towards supporting research and development in SiN PICs and its expanding pool of applications.

Abstract

We describe a rapid prototyping process for SiN PICs operating at wavelengths around 1.3 and 1.5 μm . Moderate confinement SiN waveguides and other essential integrated photonic components, such as fiber-chip couplers, MMI-based 3-dB power splitters, microring resonators, and SWG metamaterial waveguides, were fabricated and characterized and are reported. The prototyping platform features a 400-nm-thick layer of SiN grown via LPCVD and uses direct-write EBL to define single mode waveguide structures that exhibit losses of <1.3 dB/cm across the O-band and <1.8 dB/cm across the S-, C- and L-bands for both TE and TM polarizations. The platform is commercially available through the NanoSOI Design Center operated by ANT with five MPW runs per year that have fast turnaround times on the scale of weeks rather than months. This provides a route toward the rapid fabrication of SiN chip-based passive and thermo-optic active photonic devices with critical resolution down to 100 nm, making it an attractive solution for entry-level designers, device innovators and small companies on tight budgets looking to incorporate integrated SiN circuits into early-stage applications of SiP.

3.1 Introduction

SiP is a disruptive technology that leverages mature microelectronics manufacturing processes for the fabrication of compact, scalable, economic, and high-performance PICs [1; 2]. It has already revolutionized the datacom industry by transforming the optical transceiver market and is being explored in many other application areas such as sensing, quantum photonics, programmable photonics, augmented reality, artificial intelligence, and light detection and ranging (LiDAR) [3]. As a result, many CMOS fabrication facilities have adopted fabless/foundry models for SiP by developing high-performance integrated optical circuits and components and compiling them into a PDK, which is then offered for use to customers on MPW fabrication runs [4; 5]. This model provides

open access of well-established fabrication technologies to small research groups and commercial enterprises for a relatively low cost [6]. While SiP has proven successful in optical telecommunications in the near-infrared (NIR) spectrum, Si has many material limitations that hinder its performance for other application areas, including optical absorption at wavelengths below 1.1 μm (biomedical sensing, spectroscopy), strong TPA below wavelengths of 2.2 μm (nonlinear processes, quantum photonics), and an indirect bandgap (optical amplification) [6; 7]. Solutions to overcome these challenges include the integration of other CMOS-compatible materials with Si, or the replacement of Si altogether with other material systems.

SiN is a CMOS-compatible material which is complementary to Si and has been demonstrated as a versatile alternative for developing PICs with high integration density and compact footprints [7; 8; 9]. SiN's refractive index contrast versus silicon dioxide (SiO_2) is moderate ($\Delta n_{\text{SiN}} \approx 0.5$ @ $\lambda = 1550$ nm) and is much lower than Si ($\Delta n_{\text{Si}} \approx 2$ @ $\lambda = 1550$ nm). This provides higher tolerance to fabrication variance as well as significant reduction in waveguide losses caused by sidewall scattering and birefringence effects [9]. Unlike Si, SiN is transparent across the VIS and NIR spectra, making it a prime candidate for sensing and spectroscopy applications [10]. Furthermore, while its Kerr nonlinear coefficient is smaller than Si, TPA in the NIR spectrum is negligible in SiN due to its large bandgap. This, along with a moderately high third order nonlinear susceptibility relative to other dielectric materials [11], makes SiN an overall more desirable material for developing integrated optical devices for nonlinear processes such as frequency comb generation, four-wave mixing (FWM) and supercontinuum generation (SCG) [7; 12]. These advantages have surged research interest in and led to many demonstrations of SiN-based integrated photonic devices [13], thus encouraging many foundries to incorporate SiN into their product line or completely build a foundation upon it over recent decades [14], including AIM Photonics [15], AMF [16], CEA-LETI [17], CORNERSTONE [18], IMB-CNM [19; 20], IMEC [21], LIGENTEC [22; 23; 24; 25], and LioniX International [26; 27]. Each of these institutions provide open access to their SiN technology to interested designers through MPW runs that are supplied with a complimentary PDK [6; 14].

With such a wide array of applications and corresponding operational wavelengths for SiN PICs, there exists a great variance in SiN thickness across the network of SiP foundries [28]. As a result, SiN waveguide platforms are typically categorized in terms of their modal confinement [19]. Low confinement waveguides feature a very thin SiN film (thickness, $t_{\text{SiN}} < \sim 150$ nm) surrounded by very thick SiO_2 cladding layers (> 6 μm

each). A high-aspect-ratio SiN strip waveguide (width:thickness $> 10:1$) guides the light through the surrounding SiO₂ with minimal sidewall interaction, enabling ultra-low-loss performance below 0.1 dB/m in the NIR wavelength range [29; 30; 31]. The downsides of these waveguides are the extreme polarization dependence and the large device footprint (e.g., bend radius $R > 0.5$ mm) required for maintaining guidance of the loosely confined mode, making compact circuit design difficult. Well-established foundry accessible low confinement waveguides include the single stripe TriPleX waveguides offered by LioniX International [26; 27]. On the other end, high confinement waveguides use thicker SiN films ($t_{\text{SiN}} > 400$ nm) to contain the waveguide mode within the high index SiN core. This significantly reduces device footprint and propagation loss by alleviating modal interaction with the SiN waveguide boundaries [32]. Furthermore, the high mode overlap with the waveguide core also provides greater flexibility in tailoring the waveguide dispersion, which is essential for exploiting nonlinear optical processes in the SiN material [33]. However, fabrication of high confinement waveguides is difficult since SiN films with $t_{\text{SiN}} > 400$ nm can suffer from large tensile stress during deposition, resulting in film cracking which limits optical quality and device yield [32]. Many methods for constructing thick, high-quality SiN films have been proposed and demonstrated, including isolation trench inscription [32], thermal cycling [33; 34], stress engineering with Si-rich films [35], reactive sputtering [36], and additive patterning processes, such as trench-defined waveguides formed by substrate prepatterning [37] and the photonic Damascene process [22; 23; 24]. Moderate confinement waveguides occupy the middle ground with SiN film thicknesses between approximately 150 and 400 nm. Waveguides with these film heights are highly versatile since they can be tuned to support single mode operation for various polarization states across a wide spectral range from the VIS [21] through the NIR [38; 39]. Single mode moderate confinement waveguides have reasonable integration density with bend radii under 500 μm for most wavelengths [19]. Furthermore, SiN film layers in this range are grown in a single large wafer-scale deposition step and patterned using standard subtractive etching processes. This avoids complex fabrication methods required for thicker SiN films and provides flexibility in the fabrication process dependent on the desired application. All these benefits have made moderate confinement SiN waveguides a very appealing option for multilayer integration of SiN with other CMOS foundry platforms to enable 3D PICs with enhanced functionalities [11; 17; 40; 41]. Though best shown in thick SiN waveguides, nonlinear optical processes such as SCG have been demonstrated in moderate confinement SiN waveguides that featured a partial underetch of the SiO₂ substrate [42] and hybrid integration with highly nonlinear glass materials [43; 44]. However, all these advantages come at the expense of

increased propagation loss compared to the other SiN waveguide classifications [19]. The reduced mode confinement, compared to high confinement waveguides, induces greater interaction with the waveguide sidewalls and correspondingly higher losses, which are also much more prominent when compared with low confinement waveguides. Nevertheless, with their broad practicality, moderate confinement SiN waveguides provide a highly versatile starting point for designers looking to incorporate SiN waveguides in their application spaces.

In this paper, we present the most recent developments and findings of the moderate confinement SiN platform offered by integrated photonics foundry ANT [45]. The main platform is composed of 400-nm-thick SiN waveguides grown via LPCVD and patterned using direct-write EBL technology. These waveguides feature NIR losses that are competitive with other commercially available moderate confinement SiN foundry platforms. Importantly, the rapid prototyping process enables affordable, low-volume production of PICs with short turnaround times (< 2 months) that are desirable for entry-level designers, university-level researchers, and companies with tight time budgets looking to explore SiN-based solutions for early-stage applications of SiP [6; 46]. We report on essential components for SiN PICs, including fiber-chip couplers, MMI-based power splitters, ring resonators, and SWG metamaterial waveguide structures, which have been developed and tested on the platform and are available in an open-source PDK. Future insights into the evolution of this platform are also discussed, including the development of thinner SiN films for VIS light applications. With five MPW runs occurring every year, this rapid prototyping service provides easy and consistent access to SiN PIC technology that uses standard features sizes and material properties for potential product scaling to larger industrial fabs, as well as a low barrier to entry in research and development that will stimulate the advancement of high performance integrated photonic devices based in SiN.

3.2 Fabrication

3.2.1 Waveguide fabrication and material properties

The basis for our SiN waveguides is a LPCVD thin film. The SiN film is deposited on a 4-inch Si wafer with a 4.5 μm -thick layer of SiO₂ grown with thermal oxidation. The thermal oxide wafers are purchased from WaferPro. The LPCVD recipe is tuned specifically to reduce propagation loss in the C-band and to mitigate stress in the film. To ensure that the SiN is suitable for waveguides, the refractive index n was measured

using ellipsometry (J.A. Woollam VASE), and the loss of the planar film for the fundamental TE polarized mode was measured using a prism coupling system (Metricon Model 2010/M). Measurements were performed over four LPCVD deposition runs, and the results are shown in Fig. 3.1. The error bars indicate the standard deviation of the measurements. At 1550 nm wavelength, the refractive index is 1.997 ± 0.002 and the slab loss is 0.42 ± 0.24 dB/cm.

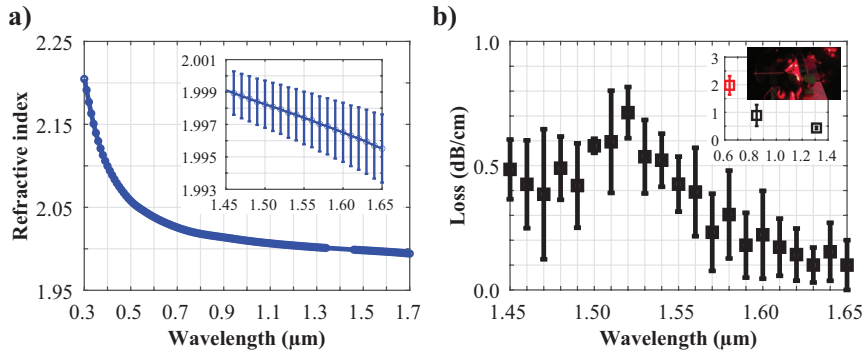


FIGURE 3.1: (a) Measured refractive index of SiN films with respect to wavelength. Inset shows zoomed-in S-, C-, and L-band regions with error bars reflecting data collected over four fabrication runs. (b) Measured SiN film loss with respect to wavelength across the S-, C- and L-bands. Inset shows measured loss for VIS and additional NIR wavelengths and red-light streak propagating across a planar SiN film sample during characterization.

We apply a hard mask based on hydrogen silsesquioxane (HSQ) resist to the top surface of the wafer and pattern and develop it using 100 keV EBL technology and a tetramethylammonium hydroxide (TMAH)-based etchant, respectively. The pattern is then transferred into the SiN film using a reactive ion etching (RIE) process based on a trifluoromethane/oxygen (CHF_3/O_2) chemistry, after which we remove the hard mask with an acidic wet etchant.

3.2.2 Post-processing options

Additional layers can be processed once the SiN waveguide layer has been completed. A 3- μm -thick SiO_2 cladding grown by plasma enhanced chemical vapour deposition (PECVD) can be added onto the chips to protect the waveguides and reduce the index contrast around the waveguide. The thick cladding also serves to isolate the waveguides from metallic micro-heaters that can be patterned near the waveguides for thermo-optic control. For this micro-heater process, a 200 nm-thick titanium-tungsten (TiW)

alloy is deposited and patterned. Electrical bond pads and traces made of 500 nm-thick aluminum are then patterned and etched afterward. To protect the heaters from damage due to oxidation, a 300 nm-thick SiO₂ passivation layer is deposited across the entire wafer, and bond pad openings are etched through the SiO₂ and down to the aluminum. Although the thermo-optic effect is weaker in SiN compared to Si [9; 47], thermal tuning is still widely applicable in SiN PICs.

Edge couplers are important in many applications to couple light in and out of PICs with wide bandwidth and low insertion loss [48]. To fabricate edge couplers, the oxide cladding (if present) and buried oxide (BOX) are etched using an RIE process. The SiN waveguides are etched in the same step, and the etch is designed to create a smooth facet for edge coupling. Subsequently, the Si handle is etched to a depth of 250 μm using a deep RIE process. This depth is sufficient for lensed fibers (LFs) or fiber arrays to be placed near the waveguides to facilitate the lowest insertion loss possible.

Another process option available for our SiN waveguide platform is window openings to the SiN through the SiO₂ top cladding. A hard mask is applied, the windows are etched down to the BOX to expose the SiN waveguides, and then the hard mask is removed. This is useful in sensor applications where the waveguides are selectively directly exposed to an analyte [49].

3.3 SiN PDK components

This section highlights the performance of the various SiN integrated photonic components included in the PDK available from ANT. We report on fundamental building blocks for PICs, such as strip waveguides, fiber-chip grating and edge couplers, 3 dB power splitters based on the MMI topology, and all-pass microring resonators. The subsequent subsections will describe the application, design process, fabrication details and measurement results for each respective component included in the PDK.

3.3.1 Waveguides

Optical waveguides are the most common structures in PICs as they are responsible for guiding light throughout the chip. The two most common waveguide configurations in SiP are strip (fully etched) and rib (partially etched) waveguides. For our SiN circuits, we developed strip waveguides only, since rib waveguides require multiple fabrication etch steps, which is a feature not yet available on our platform.

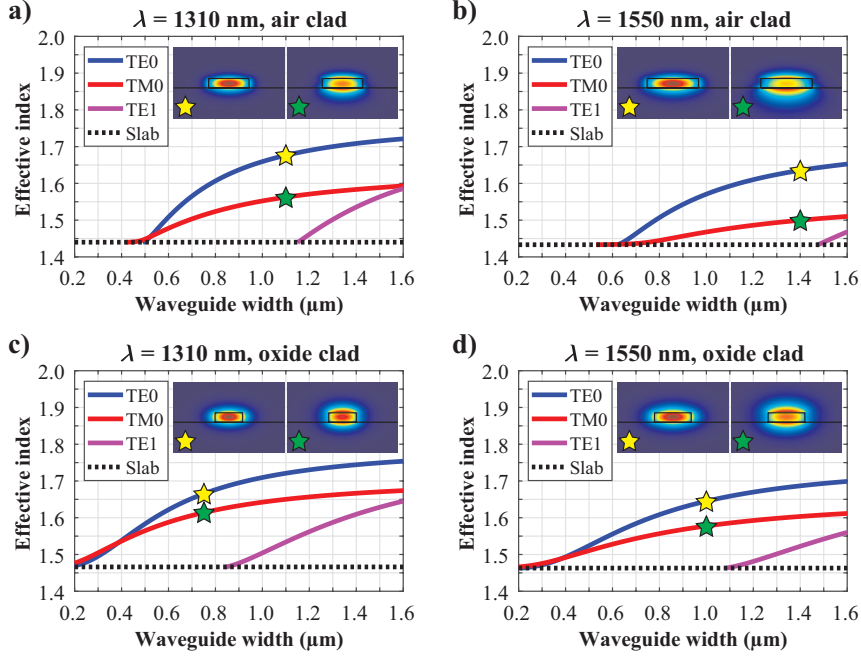


FIGURE 3.2: Simulated mode effective index of 400-nm-thick SiN strip waveguides with air top cladding at wavelengths of (a) 1310 nm and (b) 1550 nm, and with SiO₂ top cladding at wavelengths of (c) 1310 nm and (d) 1550 nm across various waveguide widths. Insets show fundamental TE (left) and TM (right) mode profiles for designed single mode waveguides, which are marked by yellow and green stars, respectively.

We studied the modal properties of our SiN strip waveguides by employing the finite difference eigenmode (FDE) solver from Ansys Lumerical. Fig. 3.2 shows the calculated mode effective indices (n_{eff}) of our 400-nm-thick SiN strip waveguides as a function of waveguide width. The waveguides are simulated at standard telecom wavelengths of 1310 and 1550 nm with two different top claddings: air, and 3- μm thick PECVD SiO₂ (refractive index $n \sim 1.47$ @ $\lambda = 1550$ nm). The slab mode effective index in each waveguide configuration is calculated as the effective index with no SiN waveguide present in the simulation. Modes are only supported by the waveguide when their n_{eff} is greater than the slab mode effective index. As the waveguide width increases, the structure begins to support additional modes as their effective indices surpass the slab mode effective index threshold. We quantify the single mode cutoff (SMC) as the maximum waveguide width in which only the fundamental TE (TE0) and TM (TM0) modes are guided. These results are highlighted in Table 3.1, along with the selected

waveguide widths we used for our designs and fabricated test structures, which function as single mode waveguides below the SMC widths.

Waveguide bends are necessary for directing light within photonic devices and around the chip but can introduce additional loss from increased interaction with sidewall roughness and bend mode radiation. The former cause is primarily dictated by the fabrication process and may be accentuated by the fracturing writing methodology adopted by EBL [50]. Therefore, it is difficult to optimize in the design phase. However, the latter can be alleviated by selecting a bend radius that is large enough to minimize radiation loss, yet small enough to maintain compactness. The bent waveguide option in the FDE solver was used to assess the waveguide bends for the selected designs in each of our SiN waveguide arrangements. A perfectly matched layer (PML) boundary layer was applied on the outer edge of the bend to absorb light leaking from the waveguide bend. The bend radius was then swept from high to low until it was too tight to guide the bend mode, which becomes completely absorbed by the PML boundary due to excessive bend radiation loss. We define the minimum bend radius of our waveguides as the smallest bend radius that supports the fundamental mode with < 0.01 dB/cm bend loss, which is based on the simulated real and imaginary effective indices. These results are also summarized in Table 3.1 for both the TE₀ and TM₀ modes.

TABLE 3.1: Calculated SMC width for SiN waveguides.

Top cladding	Air	Air	SiO ₂	SiO ₂
Wavelength (μm)	1.31	1.55	1.31	1.55
SMC width (μm)	1.14	1.47	0.83	1.07
Selected waveguide width (μm)	1.1	1.4	0.75	1.0
Minimum bend radius, TE₀ (μm)	100	110	110	120
Minimum bend radius, TM₀ (μm)	190	350	150	190

We characterized the fabricated SiN waveguides using a fiber-to-fiber edge coupled setup consisting of a tunable laser, photodetector, a 3-paddle polarization controller (for dictating the polarization of the light in the fiber prior to entering the chip), and 1550 nm LFs with a 2.5 μm spot size to reduce fiber-chip coupling losses. We used the cutback method to determine the propagation loss of SiO₂-clad waveguides fabricated with varying lengths in an Archimedean spiral topology. The waveguide widths for the 1310 and 1550 nm wavelength spirals match the selected waveguide widths listed in Table 3.1 (i.e., 0.75 and 1 μm, respectively) so that the waveguides are single mode in their given spectral windows. The smallest bend radius in each spiral is 250 μm, which is well above the calculated minimum bend radii in Table 3.1 for all waveguide configurations,

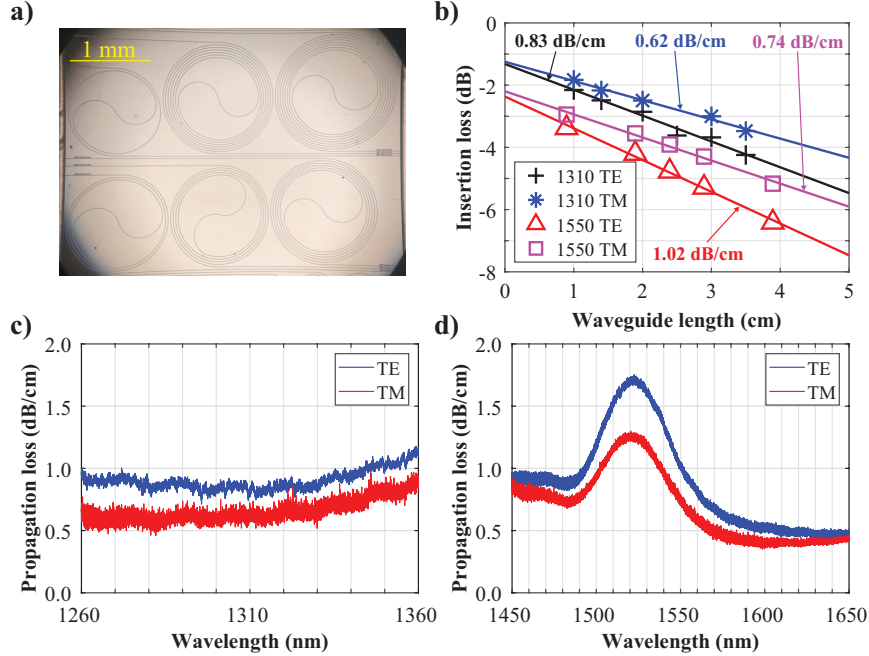


FIGURE 3.3: (a) Optical microscope images of fabricated SiN Archimedean spiral waveguide cutback structures, coated in a 3- μm -thick PECVD SiO_2 cladding. (b) Measured insertion loss of spiral waveguides with respect to waveguide length and linear regression fits of data for 1310 and 1550 nm wavelengths under TE and TM polarization. Calculated propagation loss using linear regression fitting across wavelengths measured in the (c) O-band and (d) S-, C- and L-bands.

so we assume bend radiation loss to be negligible. Fig. 3.3 shows the measurement results for these waveguides. Linear regression fits of the measured insertion loss data shown in Fig. 3.3(b) reveal TE and TM propagation losses of 0.83 ± 0.06 and 0.62 ± 0.07 dB/cm, respectively, at 1310 nm wavelength, and 1.02 ± 0.08 and 0.74 ± 0.07 dB/cm, respectively, at 1550 nm wavelength. Similar fits were also applied across all wavelengths within the spectral window of both tunable laser sources (Keysight Technologies N7778C, options 113 and 216) and plotted in Fig. 3.3(c, d). The loss significantly increases near 1520 nm, which is attributed to absorption caused by vibrational overtones of N-H and Si-H bonds in the SiN film leftover from the deposition process [51]. While prominent in the as-deposited LPCVD SiN film, waveguides fabricated using PECVD typically exhibit much higher losses because of their lower deposition temperature that is less capable of driving out these parasitic impurities [11; 39]. The waveguide loss for TM polarization is considerably lower than the TE polarization waveguide loss within this

absorption window. We attribute this to the smaller TM modal confinement in the SiN waveguide core (34% for TM vs. 59% for TE) reducing the effect of absorption from the hydrogen contaminants. There is also less modal interaction with the waveguide sidewalls for TM modes (e.g., see insets of Fig. 3.2(d)), so the TM loss is notably lower than the TE loss across all measured wavelengths. Finally, we observe that the propagation loss of the two individual polarizations converge around 0.5 dB/cm near 1650 nm wavelength. This insinuates strong polarization independence can be achieved in our moderate confinement waveguides when designed accordingly.

3.3.2 Fiber-chip couplers

Optical couplers are critical components that connect waveguides on the chip to macroscopic optical devices, such as external laser sources and detectors, via an optical fiber. The two most common types of fiber-chip couplers are grating couplers and edge couplers. Grating couplers use periodic grating structures in the core material and the concept of diffraction to direct light from a vertically angled fiber above the chip into the waveguides along the horizontal plane. Generally, these couplers have a good fiber misalignment tolerance and do not require additional complex fabrication steps (though some exceptions are made for enhancing the coupling efficiency and directionality, including multi-step etching of the device layer [52], bottom reflector fabrication via backside substrate engineering [53], and dual-level material configurations [54]). However, grating couplers suffer from various drawbacks, including increased design complexity, large device footprint, smaller bandwidth, and higher loss. Edge couplers interact with the optical fiber at the side (or edge) of the chip. Since they are essentially just extensions of the waveguide, their design is quite simple. The most common edge coupler design is a linear inverse nanotaper from the waveguide to the chip facet [48]. They also offer greater bandwidth than grating couplers. However, edge couplers have inherently greater fabrication complexity, as they require precise deep trench etching around the chip edge that provides optical fibers direct access to the coupler. We designed and fabricated both surface grating couplers and waveguide edge couplers using our SiN platform. The reported results correspond to the standard devices now available in ANT's SiN PDK.

3.3.2.1 Grating couplers

The designed surface grating coupler has the same operating principle as the single/full etch Si grating couplers available in the open-source SiEPIC-EBeam-PDK [46; 55]. The couplers are designed for a center wavelength near 1550 nm and for use with SiO₂ cladding at an input angle of +8° from the incident normal. Our initial design reported

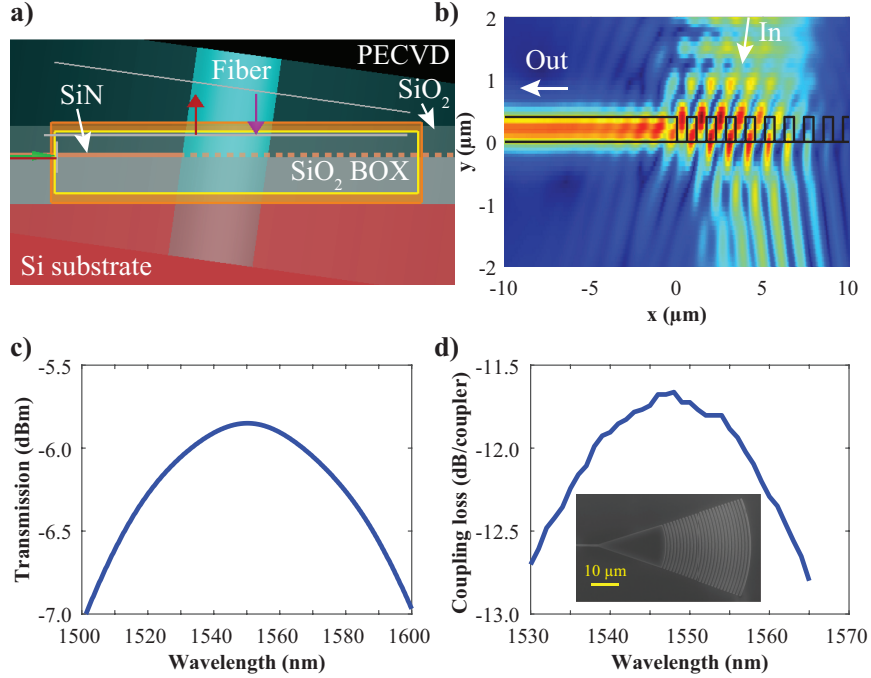


FIGURE 3.4: (a) Sideview cross section of simulated SiO₂-clad SiN grating coupler in Ansys Lumerical FDTD software. 2D FDTD simulated (b) 1550 nm wavelength TE mode profile and (c) output transmission spectrum for grating coupler. (d) Measured C-band transmission spectrum for the fabricated SiN TE grating coupler. Inset shows SEM image of fabricated fiber-chip SiN grating coupler.

here operates under TE polarization only. Future designs will aim to incorporate both TM polarization only and polarization-independent operation. We used analytic equations commonly used in grating coupler design [56] to approximate essential grating coupler parameters, such as grating period, duty cycle, and grating length. The finite-difference-time-domain (FDTD) solver from Ansys Lumerical was employed to optimize the parameters. The simulation features a TE-polarized single mode fiber (SMF) input source above the grating coupler at an angle of +8° from the incident normal and an output waveguide at the end of the grating coupler, where a power monitor is placed to detect the intensity of the light reaching the waveguide. Fig. 3.4(a-c) highlight the simulation setup, side mode profile, and spectral transmission results of a SiN grating coupler with 1.18 μm grating period, 0.5 duty cycle, and 30 μm grating length. The peak power detected at the output waveguide corresponds to a coupling efficiency of -5.85 dB at a center wavelength of 1550 nm. The 1-dB bandwidth is determined to be ~90 nm, which far exceeds the C-band.

We fabricated grating couplers with SiO₂ cladding and measured them on a separate setup consisting of a tunable C-band laser source, a 1×4 vertical fiber array with identical SMF-28 fibers at a pitch of 250 μm, and an indium gallium arsenide (InGaAs) photodetector. The laser source has a step size of 1 nm. We adjusted the fiber array to an input angle of +8° to the incident normal of the chip surface. Fig. 3.4(d) displays the measurement results. The grating coupler exhibits a peak coupling loss of 11.7 dB/coupler at a center wavelength of 1548 nm. The 1-dB bandwidth is 25 nm and nearly covers the entire C-band.

3.3.2.2 Edge couplers

TABLE 3.2: Calculated peak coupling efficiencies for designed SiN edge couplers.

Wavelength (μm)	Fiber MFD (μm)	Pol.	Tip width (nm)	CE (dB)
1.31	2.2	TE	250	-0.32
1.31	2.2	TM	205	-0.34
1.55	2.5	TE	330	-0.29
1.55	2.5	TM	305	-0.29
1.31	9.2	TE	140	-2.32
1.31	9.2	TM	100	-2.29
1.55	10.4	TE	175	-2.36
1.55	10.4	TM	100	-2.11

We designed waveguide edge couplers that are linearly and inversely tapered over a given length until the edge of the chip is reached. With a suitable coupler length, the main source of coupling loss arises from mode mismatch between the fiber and waveguide at the coupler tip. We used the same simulation procedure for the waveguides to calculate the mode profiles of various edge coupler tip widths. The modes were then compared to desired fiber mode profiles using a modal overlap calculation with the built-in overlap analysis tool in the FDE solver. The fiber mode was approximated as a Gaussian mode profile with a beam waist radius equivalent to half the fiber mode field diameter (MFD, i.e., width of the $1/e^2$ field intensity profile). MFDs of 2.2, 2.5, 9.2 and 10.4 μm were used to represent the mode profiles of a tapered LF at 1310 and 1550 nm wavelengths and a SMF at 1310 and 1550 nm wavelengths, respectively. Table 3.2 summarizes the best of the simulated SiO₂-clad SiN edge couplers. The coupling efficiency (*CE*) is the log scale value of the normalized mode overlap between the fiber and waveguide modes

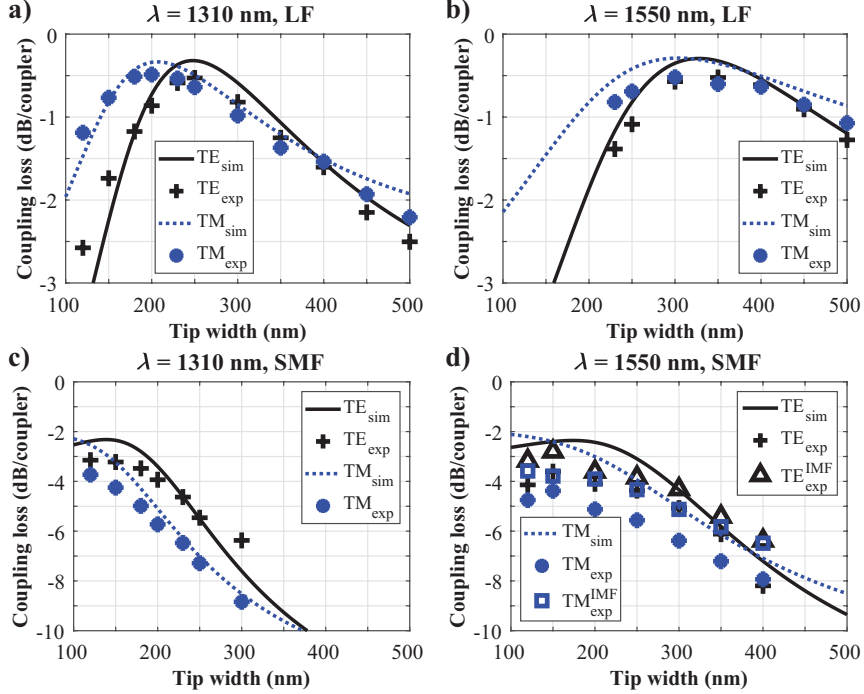


FIGURE 3.5: Simulated and measured coupling loss of SiO₂-clad SiN inverse nanotaper edge couplers with various tip widths. The couplers are measured for both TE and TM polarizations using LFs at (a) 1310 and (b) 1550 nm wavelength, and SMFs at (c) 1310 and (d) 1550 nm wavelength without and with IMF ($n = 1.46$).

calculated by the FDE solver. The lowest simulated tip width was 100 nm due to the minimum feature size (MFS) of the platform.

We fabricated edge coupler test structures consisting of 0.75- μm -wide straight waveguides and 100- μm -long inverse taper edge couplers with varying tip widths. The same experimental setup described in Section 3.3.1 was used to measure the coupling loss of our edge couplers with tapered LFs (OZ optics DTS0080) and SMFs (ThorLabs SMF-28-J9). Fig. 3.5 shows the measurement results compared with the calculated mode-mismatch loss. The optimized edge couplers are summarized in Table 3.3. In each case, the experimental data matches the simulation trend well. Discrepancies between the best simulated and measured edge coupler tip width (i.e., where peak coupling efficiency is achieved) may occur because of the angled sidewall in the fabricated devices not considered in the simulation. The LF data displays a vertical difference of only < 0.3 dB/coupler for experiment versus simulation in all cases. However, there is a greater

TABLE 3.3: Best measured polarization-independent SiN edge couplers.

Wavelength (μm)	Fiber type	Tip width (nm)	Pol.	<i>CE</i> sim. (dB/coupler)	<i>CE</i> exp. (dB/coupler)
1.31	LF	230	TE	-0.37	-0.54
			TM	-0.39	-0.53
1.55	LF	350	TE	-0.32	-0.52
			TM	-0.35	-0.60
1.31	SMF	120	TE	-2.38	-3.15
			TM	-2.54	-3.73
1.55	SMF	150	TE	-2.40	-3.61
			TM	-2.41	-4.38
1.55	SMF*	150	TE	N/A	-2.80
			TM	N/A	-3.79

* IMF applied.

difference for SMF, with the smallest power variation being ~ 0.8 and ~ 1.2 dB/coupler for 1310 and 1550 nm wavelengths, respectively. To minimize additional experimental loss due to reflections at interfaces, we applied index matching fluid (IMF) with a refractive index of 1.46 directly onto both input and output fiber-chip coupling interfaces. For 1550 nm wavelength, the loss was improved by ~ 0.8 and ~ 0.6 dB/coupler for TE and TM polarization, respectively. No measurable coupling loss reduction was observed for 1310 nm wavelength, so no IMF results are shown.

3.3.3 MMI-based 3 dB power splitter

Optical splitters and combiners are fundamental components in PICs and have been demonstrated in various forms, such as directional couplers (DCs), Y-splitters, Mach-Zehnder interferometers (MZIs), and MMI couplers. Among these, DCs are relatively more sensitive to fabrication tolerance, while Y-splitters and MZIs suffer from high insertion loss and large footprint, respectively, making them less desirable for low-loss highly compact devices. MMI couplers, on the other hand, are compact, low loss, and are much more robust with regards to fabrication tolerance and error [57; 58]. We designed 1×2 symmetric and 2×2 paired MMI-based power splitters using the finite element method (FEM) solver in Synopsys RSoft. Multimode waveguides with various widths were simulated. According to the self-imaging principle [59], the beat length is calculated such that:

$$L_{\pi} = \frac{\pi}{\beta_0 - \beta_1} = \frac{\lambda}{2(n_{\text{eff},0} - n_{\text{eff},1})}, \quad (3.1)$$

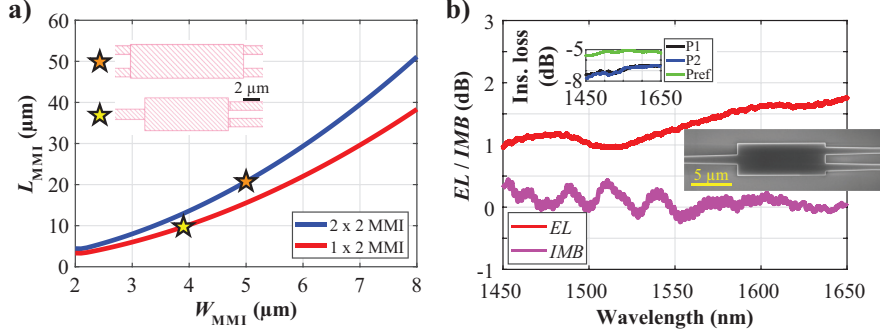


FIGURE 3.6: Simulated MMI length (L_{MMI}) as a function of MMI width (W_{MMI}) for 1×2 and 2×2 SiO_2 -clad SiN MMI couplers at 1550 nm wavelength. The inset shows mask layout schematics of 2×2 (top) and 1×2 (bottom) MMI couplers with the selected parameters of $W_{\text{MMI}} = 5 \mu\text{m}$ and $L_{\text{MMI}} = 20.4 \mu\text{m}$ for the 2×2 coupler and $W_{\text{MMI}} = 3.9 \mu\text{m}$ and $L_{\text{MMI}} = 10 \mu\text{m}$ for the 1×2 coupler (indicated by the stars). (b) Measured excess loss (EL) and imbalance (IMB) of a symmetric 1×2 SiO_2 -clad MMI power splitter. The insets show the corresponding transmission spectra for two output ports and reference waveguide devices, as well as an SEM image of a fabricated 1×2 MMI power splitter.

where β_0 and β_1 are the propagation constants and $n_{\text{eff},0}$ and $n_{\text{eff},1}$ are the calculated effective refractive indices of the two lowest order modes, respectively. The MMI length can then be determined as $L_{\text{MMI}} = (3L_\pi)/8$ for a 1×2 MMI splitter and $L_{\text{MMI}} = L_\pi/2$ for a 2×2 MMI splitter based on the respective interference mechanisms [59; 60; 61]. Fig. 3.6(a) shows the results of the FEM simulations for a SiN MMI splitter at 1550 nm wavelength. We fabricated various MMI power splitters across multiple fabrication runs. Fig. 3.6(b) shows the S-, C- and L-band measurement results for a 1×2 MMI splitter with a width of $3.9 \mu\text{m}$ and length of $10 \mu\text{m}$. The excess loss (EL) and imbalance (IMB) are defined as:

$$EL = 10 \log_{10} \left(\frac{P_1 + P_2}{P_{\text{ref}}} \right), \quad (3.2)$$

$$IMB = 10 \log_{10} \left(\frac{P_1}{P_2} \right), \quad (3.3)$$

where P_{ref} is the measured power transmission from a straight SiN waveguide reference device, and P_1 and P_2 are the measured power transmission from the two MMI output ports, all in units of mW [62]. A Savitzky-Golay finite impulse response smoothing filter with a polynomial order of 2 and frame length of 500 was applied to the data to reduce Fabry-Perot fringes arising from facet reflections. The MMI power splitter exhibits an

excess loss of 1.22 ± 0.16 dB and a power imbalance of 0.04 ± 0.40 dB across the C-band. These metrics can be improved by carefully optimizing the tapers and sine bends joining the MMI coupler to the access waveguides [62].

3.3.4 All-pass, point-coupled microring resonators

Ring resonators are essential building blocks in integrated photonic circuits with a wide range of applications, including filtering, switching, optical delay lines, sensing, modulation, and lasing [63]. An all-pass ring resonator consists of the ring (i.e., a circular optical waveguide looped in on itself) and a single bus waveguide placed near one side of the ring, which enables light coupling to the ring. Two fundamental metrics used to evaluate the performance of ring resonators are the finesse (\mathcal{F}) and the quality factor (Q), which are defined as:

$$\mathcal{F} = \frac{FSR}{FWHM} = \frac{\lambda_0^2}{FWHM \cdot n_g \cdot 2\pi R}. \quad (3.4)$$

$$Q = \frac{\lambda_0}{FWHM}. \quad (3.5)$$

where FSR is the free spectral range, $FWHM$ is the resonance width (or “full width at half maximum”), λ_0 is the resonance wavelength, n_g is the group index, and R is the ring radius. These equations relate to the storage of optical energy within the resonator. More specifically, the finesse represents the number of roundtrips made by light in the ring before its energy is reduced to $1/e$ of its initial value, and the quality factor (or simply, Q) represents the number of oscillations of the field before the circulating energy is depleted to $1/e$ of the initial energy [63]. The quality factor can be defined as unloaded or loaded depending on the arrangement of the resonator. The unloaded Q of a resonator is the quality factor when there are no external coupling mechanisms present. Losses in such a resonator are only affected by the properties of the resonator itself, including absorption and scattering that occur as the light circulates. This component is also referred to as the intrinsic Q (Q_i) and is useful for describing the propagation loss of a resonator. The loaded Q (Q_L) of a resonator is the quality factor in which external coupling mechanisms are present and considered. Losses caused by coupling between the resonator and an external waveguide are represented by the extrinsic Q (Q_e). The loaded Q is calculated such that:

$$\frac{1}{Q_L} = \frac{1}{Q_i} + \frac{1}{Q_e}. \quad (3.6)$$

By this definition, the loaded Q is always smaller than the unloaded Q [63]. When the power coupling to the bus waveguide is equal to the power loss in the resonator (i.e., $Q_i = Q_e = 2Q_L$), the ring is considered critically coupled. The transmission at the resonance wavelength drops to zero and the extinction ratio (ER) is maximized. We will use loaded Q to define the Q -factor in our all-pass ring resonators, since the adjacent bus waveguide acts as an external coupling component that introduces additional losses to the cavity.

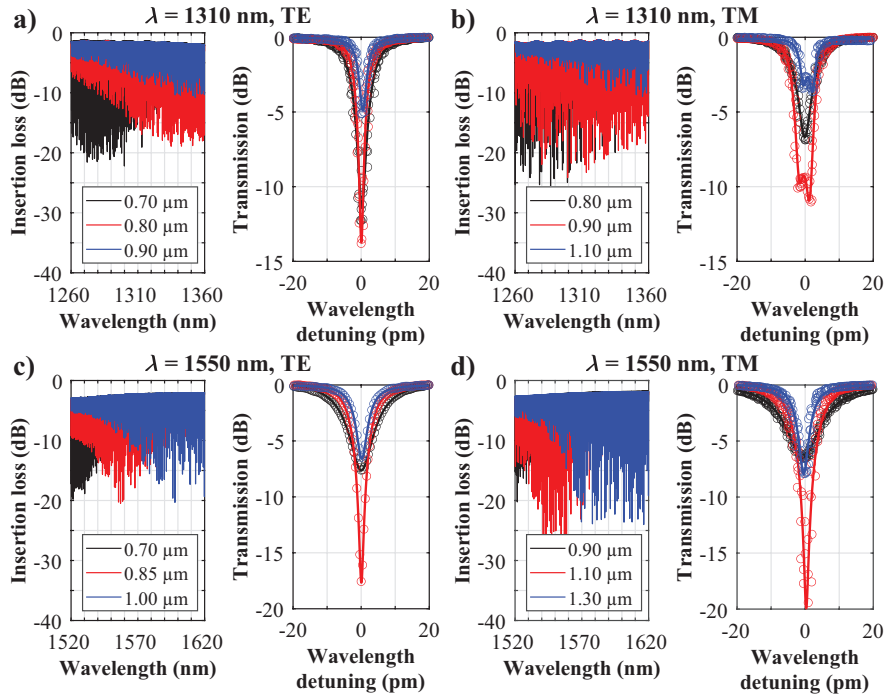


FIGURE 3.7: Experimental results for SiO_2 -clad SiN all-pass microring resonators designed for 1310 nm wavelength under (a) TE and (b) TM polarization, and 1550 nm wavelength under (c) TE and (d) TM polarization. Each configuration shows the measured insertion loss spectra (left) and the fitted resonance peaks near the target wavelengths (right) for microring resonators with various coupling gaps highlighting overcoupled (black), critically coupled (red), and undercoupled (blue) resonance behaviours.

For our component library, we designed point-coupled ring resonators in an all-pass configuration. The circuit design features a ring placed adjacent to a single mode bus waveguide that connects to opposing sides of the chip for fiber interfacing. The nearest distance between the ring and bus waveguide is the coupling gap G . We selected a single-mode ring and bus waveguide width W , which is dependent on the wavelength

range of interest (i.e., $W = 0.75 \mu\text{m}$ for O-band, $W = 1 \mu\text{m}$ for C-band). A ring radius $R = 250 \mu\text{m}$ is selected for all the devices for consistency and to alleviate bend radiation loss for all devices under test regardless of wavelength and polarization. Multiple ring resonator circuits are fabricated with varying G to assess the ring-bus coupling condition across the measured spectra. Our ring resonators were measured using our fiber edge coupling experimental setup and the results are shown in Fig. 3.7. For all wavelengths and polarizations, the spectra exhibit a shift in the critical coupling position (where ER is the greatest) to higher wavelengths as G increases. The exact critical coupling points for 1310 nm wavelength in the O-band ring resonator could not be precisely determined, but the spectra in Fig. 3.7(a-b) suggest that they may be achieved using coupling gaps of ~ 0.75 and $\sim 0.85 \mu\text{m}$ for TE and TM polarization, respectively. From Fig. 3.7(c-d), the critical coupling point for the C-band ring resonator is located at 1550 nm using coupling gaps of 0.85 and 1.1 μm for TE and TM polarization, respectively. Resonances near the wavelengths of interest (i.e., 1310 and 1550 nm) are collected and plotted together in the insets of Fig. 3.7. To assess the quality factors, we approximated and fit the resonances with a Lorentzian lineshape function [64; 65]. Table 3.4 summarizes the results for the resonance fittings. Q_L increases with G since Q_i remains relatively constant with the resonator geometry while Q_e gradually increases as the coupling strength declines. The resonance linewidth becomes narrower as G increases and the behaviour of the ring resonator changes from overcoupled (black, $Q_i > Q_e$) to critically coupled (red, $Q_i \approx Q_e$) to undercoupled (blue, $Q_i < Q_e$). Some resonances exhibit a double resonance dip, or doublet. Two counter-propagating modes in the resonator experience strong modal coupling when their degeneracy is lifted due to scattering from surface roughness along the resonator path [66]. A statistical model that considers these mode splitting effects is incorporated into our fitting algorithm for these specific resonances [67]. The model considers a doublet as two individual peaks each with their own quality factors and the quality factors shown in Table 3.4 for the doublet resonances are simply the averages of the two respective quality factors. The propagation loss can be calculated using the equation:

$$\alpha = \frac{2\pi n_g}{\lambda_0 Q_i} = \frac{\lambda_0}{FSR \cdot Q_i \cdot R}, \quad (3.7)$$

where n_g is the experimental group index, λ_0 is the resonant wavelength, Q_i is the intrinsic quality factor of the undercoupled ring resonator determined by the resonance fitting, and FSR is the free spectral range [68]. Using the data from Table 3.4, the measured propagation losses in the ring resonators are 0.94 and 0.62 dB/cm for 1310 nm wavelength under TE and TM polarization, respectively, and 1.02 and 0.94 dB/cm for 1550 nm wavelength under TE and TM polarization, respectively. These results agree

well with the spiral cutback loss data (within ± 0.1 dB/cm), apart from the 1550 TM result, and show comparable performance to all-pass ring resonators demonstrated on other moderate confinement SiN platforms [39; 69; 70].

TABLE 3.4: Measurement summary of SiO₂-clad SiN ring resonators with $R = 250$ μm .

λ_0 (nm)	Pol.	W (μm)	G (μm)	C.*	ER (dB)	FSR (nm)	n_g	Q_i ($\cdot 10^5$)	Q_L ($\cdot 10^5$)
1308.77	TE	0.75	0.7	OC	11.4	0.53	2.08	4.88	1.80
1308.62	TE	0.75	0.8	UC	13.7	0.53	2.08	4.67	2.81
1309.39	TE	0.75	0.9	UC	4.9	0.53	2.08	4.70	3.69
1310.53	TM	0.75	0.8	OC	6.7	0.54	2.01	6.39	1.73
1310.14	TM	0.75	0.9	UC	10.9	0.54	2.01	6.33 [!]	2.67 [!]
1308.10	TM	0.75	1.1	UC	4.1	0.54	2.01	6.85 [!]	4.95 [!]
1547.23	TE	1.00	0.7	OC	7.6	0.75	2.04	3.58	1.08
1552.51	TE	1.00	0.85	CC	17.7	0.75	2.04	3.48	1.96
1552.60	TE	1.00	1.0	UC	6.6	0.76	2.03	3.48	2.55
1550.40	TM	1.00	0.9	OC	6.5	0.79	1.93	3.20	0.86
1550.54	TM	1.00	1.1	CC	19.9	0.80	1.93	3.25	1.47
1549.55	TM	1.00	1.3	UC	7.9	0.79	1.93	3.60	2.51

* C. = coupling condition; OC = overcoupled; CC = critically coupled; UC = undercoupled.

[!] Averaged between quality factors calculated for split resonance peaks.

3.3.5 SWG metamaterial devices

SWG metamaterials have become fundamental building blocks in SiP thanks to their ability to enhance design flexibility by leveraging precise lithographic control over the waveguide effective index and mode field distribution [71]. SWG metamaterials have been implemented in many on-chip photonic components, such as waveguides, fiber-chip couplers, crossings, filters, switches, multiplexers, and various devices responsible for managing polarization, anisotropy, and dispersion [72; 73; 74]. This has prompted the adoption of SWG metamaterials into more complex optical micro-systems including on-chip biosensors [75], modulators [76] and commercial products such as IBM's fiber-chip coupling interfaces [77]. While SWG metamaterials have primarily benefited the silicon-on-insulator (SOI) platform, their operating principles can be applied in other material platforms in integrated optics [78]. The use of EBL technology enables feature size dimensions suitable for fabricating SWG metamaterial structures on our SiN platform. Therefore, SWG metamaterials can be incorporated into the design space and

applied in the fabricated devices to expand the application and performance profile of the various SiN components already available in the PDK. We recently demonstrated the first SiN-based SWG metamaterial waveguides and ring resonators on our platform [79]. The design, fabrication and results of these devices are disseminated in Chapter 4 and demonstrate metrics that are comparable with SiN strip waveguides on our platform, competitive with other moderate confinement SiN platforms, and superior to SOI SWG ring resonators reported in literature. Such demonstrations are encouraging the incorporation of SWG metamaterials in other essential SiN photonic components, such as couplers with small footprint and wide operational bandwidth [80]. While SWG metamaterials are relatively new in SiN, our rapid prototyping SiN platform provides an excellent foundation in which to explore their design in other fascinating SiN devices.

3.4 Discussion

Table 3.5 summarizes the waveguide losses for our platform and for other commercially available moderate confinement SiN/SiO₂ foundry platforms [19]. Overall, our losses at 1310 and 1550 nm wavelengths are <1.1 dB/cm, which is competitive with many other SiN foundries. There is a notable absence of reported TM polarized waveguides. However, we report loss for both TE and TM polarization in our waveguides and demonstrate superior TM loss metrics across the O- and C-band compared to the TE loss. This is encouraging for platform users exploring SiN PIC applications where TM polarization is desired, such as biosensing, where the strip waveguide TM mode exhibits greater overlap, and therefore greater sensitivity, with the sensing medium over the TE mode [81], and high-speed optical communications, where information signal processing is performed in independent polarization states [82].

Methods for improving the waveguide loss are underway. Reassessment of the hard mask material and quality may help to reduce the line edge roughness, which in turn would decrease sidewall roughness and lower the overall waveguide loss. Post-deposition annealing (PDA) is a straightforward solution for driving out excess hydrogen pollutants from the SiN film [84; 85], which are responsible for the increased waveguide loss in the C-band. These post-processing steps can be avoided by performing the LPCVD run at higher temperatures to drive out hydrogen during the deposition. However, this would require adjustment of the deposition recipe. Overall, any form of SiN film optimization will require careful consideration of film cracking as our selected thickness lies on the threshold in which tensile stress may hinder the film quality [19].

TABLE 3.5: Loss comparison of single mode waveguides for commercially available 1.3- and 1.5- μm moderate confinement SiN platforms.

Platform	SiN dep. method	Pattern. method *	λ (μm)	Pol.	w (μm)	t (μm)	Loss (dB/cm)	Ref.
AIM	PECVD	IL-RIE	1.55				1.0-4.5	[15]
AMF	PECVD		1.31	TE		0.4	<0.2	[16]
	LPCVD	DUV-	1.31	TE		0.4	<0.3	
	PECVD	Dry	1.55	TE		0.4	<3.01	
	LPCVD		1.55	TE		0.4	<0.42	
CEA-LETI	PECVD		0.94	TE	0.6	0.3	1.5	[17]
	LPCVD	DUV-	0.94	TE	0.6	0.3	1.0	
	PECVD	RIE	1.31	TE	0.7	0.6	0.8	
	LPCVD		1.55	TE	0.75	0.75	1.5	
CORNER-STONE	PECVD	EBL	1.31	TE	0.9	0.3	1.0	[18]
			1.55	TE	1.2	0.3	1.5	
IMB-CNM	LPCVD	ILS-RIE	1.55	TE		0.281	0.99	[20]
SIMIT	LPCVD		1.55	TE	1.0	0.4	0.157	[83]
ANT	LPCVD	EBL-RIE	1.31	TE	0.75	0.4	0.83	This work
			1.31	TM	0.75	0.4	0.62	
			1.55	TE	1.0	0.4	1.02	
			1.55	TM	1.0	0.4	0.74	

* DUV = deep-ultraviolet; IL = Immersion lithography; ILS = I-line stepper.

The waveguides, edge couplers and ring resonators presented above were developed over four design/fabricate/test cycles. During this time, we established an exemplary model for verifying the correctness and accuracy between simulation, technological process and experiment. This method will be very useful for the development of other integrated photonic components on the platform. The grating couplers and 3 dB MMI power splitters presented are in their preliminary development stages and require further optimization to strengthen their performance. We believe these components can be improved through judicious design to better match other state-of-the-art SiN devices [80; 86]. Research and development on other important integrated photonic components, including directional couplers, interferometers, Bragg gratings, and various components featuring SWG metamaterials is on-going and the PDK is being continuously updated.

3.5 Conclusion

We have presented the results for a commercially available SiN platform built upon a rapid prototyping foundry process. The moderate confinement single mode waveguides exhibit losses as low as 0.6 and 0.4 dB/cm across the O- and C-bands, respectively, which are competitive with SiN platforms from other foundries. Other necessary components for PICs are demonstrated and included in a complimentary PDK, such as fiber-chip couplers, 3 dB MMI power splitters, and ring resonators. Subwavelength metastructures with critical feature sizes down to 100 nm can also be fabricated on the platform and have been shown in other works (see Chapter 4). These device designs can be modified to accommodate other areas of the VIS and NIR spectra for various applications of SiN photonics. The platform is available to users through multiple MPW runs per year that each have rapid turnaround times of several weeks, providing small research groups and start-up companies easy access to low-cost SiN PICs. As the application space of SiN photonics constantly grows, the SiN technology offered by ANT will continue to expand with improved designs on existing components for various targeted functions and operations. The platform demonstrated here enables users to rapidly design and test high quality PICs in SiN to cultivate their solutions in various SiP applications.

Bibliography

- [1] B. Jalali and S. Fathpour, “Silicon photonics,” *Journal of Lightwave Technology*, vol. 24, no. 12, pp. 4600–4615, 2006.
- [2] R. A. Soref, “The past, present, and future of silicon photonics,” *IEEE Journal of Selected Topics in Quantum Electronics*, vol. 12, no. 6, pp. 1678–1687, 2006.
- [3] D. Thomson, A. Zilkie, J. E. Bowers, T. Komljenovic, G. T. Reed, L. Vivien, D. Marris-Morini, E. Cassan, L. Viot, J.-M. Fédéli, J.-M. Hartmann, J. H. Schmid, D.-X. Xu, F. Boeuf, P. O’Brien, G. Z. Mashanovich, and M. Nedeljkovic, “Roadmap on silicon photonics,” *Journal of Optics*, vol. 18, no. 7, p. 073003, 2016.
- [4] A. E.-J. Lim, J. Song, Q. Fang, C. Li, X. Tu, N. Duan, K. K. Chen, R. P.-C. Tern, and T.-Y. Liow, “Review of silicon photonics foundry efforts,” *IEEE Journal of Selected Topics in Quantum Electronics*, vol. 20, no. 4, pp. 405–416, 2014.
- [5] M. U. Khan, Y. Xing, Y. Ye, and W. Bogaerts, “Photonic integrated circuit design in a foundry+fabless ecosystem,” *IEEE Journal of Selected Topics in Quantum Electronics*, vol. 25, no. 5, pp. 1–14, 2019.

- [6] A. Rahim, T. Spuesens, R. Baets, and W. Bogaerts, “Open-access silicon photonics: Current status and emerging initiatives,” *Proceedings of the IEEE*, vol. 106, no. 12, pp. 2313–2330, 2018.
- [7] R. Baets, A. Z. Subramanian, S. Clemmen, B. Kuyken, P. Bienstman, N. Le Thomas, G. Roelkens, D. Van Thourhout, P. Helin, and S. Severi, “Silicon photonics: Silicon nitride versus silicon-on-insulator,” in *2016 Optical Fiber Communications Conference and Exhibition (OFC)*, pp. 1–3, 2016.
- [8] D. J. Blumenthal, R. Heideman, D. Geuzebroek, A. Leinse, and C. Roeloffzen, “Silicon nitride in silicon photonics,” *Proceedings of the IEEE*, vol. 106, no. 12, pp. 2209–2231, 2018.
- [9] A. Rahim, E. Ryckeboer, A. Z. Subramanian, S. Clemmen, B. Kuyken, A. Dhakal, A. Raza, A. Hermans, M. Muneeb, S. Dhoore, Y. Li, U. Dave, P. Bienstman, N. Le Thomas, G. Roelkens, D. Van Thourhout, P. Helin, S. Severi, X. Rottenberg, and R. Baets, “Expanding the silicon photonics portfolio with silicon nitride photonic integrated circuits,” *Journal of Lightwave Technology*, vol. 35, no. 4, pp. 639–649, 2017.
- [10] S. Romero-García, F. Merget, F. Zhong, H. Finkelstein, and J. Witzens, “Silicon nitride CMOS-compatible platform for integrated photonics applications at visible wavelengths,” *Optics Express*, vol. 21, no. 12, pp. 14036–14046, 2013.
- [11] W. D. Sacher, Y. Huang, G.-Q. Lo, and J. K. S. Poon, “Multilayer silicon nitride-on-silicon integrated photonic platforms and devices,” *Journal of Lightwave Technology*, vol. 33, no. 4, pp. 901–910, 2015.
- [12] D. J. Moss, R. Morandotti, A. L. Gaeta, and M. Lipson, “New CMOS-compatible platforms based on silicon nitride and Hydex for nonlinear optics,” *Nature Photonics*, vol. 7, no. 8, pp. 597–607, 2013.
- [13] C. Xiang, W. Jin, and J. E. Bowers, “Silicon nitride passive and active photonic integrated circuits: trends and prospects,” *Photonics Research*, vol. 10, no. 6, pp. A82–A96, 2022.
- [14] A. Rahim, J. Goyvaerts, B. Szelag, J.-M. Fedeli, P. Absil, T. Aalto, M. Harjanne, C. Littlejohns, G. Reed, G. Winzer, S. Lischke, L. Zimmermann, D. Knoll, D. Geuzebroek, A. Leinse, M. Geiselmann, M. Zervas, H. Jans, A. Stassen, C. Domínguez,

- P. Muñoz, D. Domenech, A. L. Giesecke, M. C. Lemme, and R. Baets, “Open-access silicon photonics platforms in Europe,” *IEEE Journal of Selected Topics in Quantum Electronics*, vol. 25, no. 5, pp. 1–18, 2019.
- [15] N. M. Fahrenkopf, C. McDonough, G. L. Leake, Z. Su, E. Timurdogan, and D. D. Coolbaugh, “The AIM Photonics MPW: A highly accessible cutting edge technology for rapid prototyping of photonic integrated circuits,” *IEEE Journal of Selected Topics in Quantum Electronics*, vol. 25, no. 5, pp. 1–6, 2019.
- [16] S. Y. Siew, B. Li, F. Gao, H. Y. Zheng, W. Zhang, P. Guo, S. W. Xie, A. Song, B. Dong, L. W. Luo, C. Li, X. Luo, and G.-Q. Lo, “Review of silicon photonics technology and platform development,” *Journal of Lightwave Technology*, vol. 39, no. 13, pp. 4374–4389, 2021.
- [17] Q. Wilmart, H. El Dirani, N. Tyler, D. Fowler, S. Malhouitre, S. Garcia, M. Casale, S. Kerdiles, K. Hassan, C. Monat, X. Letartre, A. Kamel, M. Pu, K. Yvind, L. K. Oxenløwe, W. Rabaud, C. Sciancalepore, B. Szelag, and S. Olivier, “A versatile silicon-silicon nitride photonics platform for enhanced functionalities and applications,” *Applied Sciences*, vol. 9, no. 2, p. 255, 2019.
- [18] C. G. Littlejohns, D. J. Rowe, H. Du, K. Li, W. Zhang, W. Cao, T. Dominguez Bucio, X. Yan, M. Banakar, D. Tran, S. Liu, F. Meng, B. Chen, Y. Qi, X. Chen, M. Nedeljkovic, L. Mastronardi, R. Maharjan, S. Bohora, A. Dhakal, I. Crowe, A. Khurana, K. C. Balram, L. Zagaglia, F. Floris, P. O’Brien, E. Di Gaetano, H. M. Chong, F. Y. Gardes, D. J. Thomson, G. Z. Mashanovich, M. Sorel, and G. T. Reed, “CORNERSTONE’s silicon photonics rapid prototyping platforms: Current status and future outlook,” *Applied Sciences*, vol. 10, no. 22, p. 8201, 2020.
- [19] P. Muñoz, G. Micó, L. A. Bru, D. Pastor, D. Pérez, J. D. Doménech, J. Fernández, R. Baños, B. Gargallo, R. Alemany, A. M. Sánchez, J. M. Cirera, R. Mas, and C. Domínguez, “Silicon nitride photonic integration platforms for visible, near-infrared and mid-infrared applications,” *Sensors*, vol. 17, no. 9, p. 2088, 2017.
- [20] G. Micó, L. A. Bru, D. Pastor, D. Doménech, J. Fernández, A. Sánchez, J. M. Cirera, C. Domínguez, and P. Muñoz, “Silicon nitride photonics: from visible to mid-infrared wavelengths,” in *Silicon Photonics XIII* (G. T. Reed and A. P. Knights, eds.), vol. 10537, p. 105370B, International Society for Optics and Photonics, SPIE, 2018.

- [21] A. Z. Subramanian, P. Neutens, A. Dhakal, R. Jansen, T. Claes, X. Rottenberg, F. Peyskens, S. Selvaraja, P. Helin, B. Du Bois, K. Leyssens, S. Severi, P. Deshpande, R. Baets, and P. Van Dorpe, “Low-loss singlemode PECVD silicon nitride photonic wire waveguides for 532–900 nm wavelength window fabricated within a CMOS pilot line,” *IEEE Photonics Journal*, vol. 5, no. 6, p. 2202809, 2013.
- [22] M. H. P. Pfeiffer, A. Kordts, V. Brasch, M. Zervas, M. Geiselmann, J. D. Jost, and T. J. Kippenberg, “Photonic Damascene process for integrated high- Q microresonator based nonlinear photonics,” *Optica*, vol. 3, no. 1, pp. 20–25, 2016.
- [23] M. H. P. Pfeiffer, C. Herkommer, J. Liu, T. Morais, M. Zervas, M. Geiselmann, and T. J. Kippenberg, “Photonic Damascene process for low-loss, high-confinement silicon nitride waveguides,” *IEEE Journal of Selected Topics in Quantum Electronics*, vol. 24, no. 4, pp. 1–11, 2018.
- [24] J. Liu, G. Huang, R. N. Wang, J. He, A. S. Raja, T. Liu, N. J. Engelsen, and T. J. Kippenberg, “High-yield, wafer-scale fabrication of ultralow-loss, dispersion-engineered silicon nitride photonic circuits,” *Nature Communications*, vol. 12, no. 1, p. 2236, 2021.
- [25] J. A. Smith, H. Francis, G. Navickaite, and M. J. Strain, “SiN foundry platform for high performance visible light integrated photonics,” *Optical Materials Express*, vol. 13, no. 2, pp. 458–468, 2023.
- [26] K. Wörhoff, R. G. Heideman, A. Leinse, and M. Hoekman, “TriPleX: a versatile dielectric photonic platform,” *Advanced Optical Technologies*, vol. 4, no. 2, pp. 189–207, 2015.
- [27] C. G. H. Roeloffzen, M. Hoekman, E. J. Klein, L. S. Wevers, R. B. Timens, D. Marchenko, D. Geskus, R. Dekker, A. Alippi, R. Grootjans, A. van Rees, R. M. Oldenbeuving, J. P. Epping, R. G. Heideman, K. Wörhoff, A. Leinse, D. Geuzebroek, E. Schreuder, P. W. L. van Dijk, I. Visscher, C. Taddei, Y. Fan, C. Taballione, Y. Liu, D. Marpaung, L. Zhuang, M. Benelajla, and K.-J. Boller, “Low-loss Si₃N₄ TriPleX optical waveguides: Technology and applications overview,” *IEEE Journal of Selected Topics in Quantum Electronics*, vol. 24, no. 4, pp. 1–21, 2018.
- [28] P. Muñoz, P. W. L. van Dijk, D. Geuzebroek, M. Geiselmann, C. Domínguez, A. Stassen, J. D. Doménech, M. Zervas, A. Leinse, C. G. H. Roeloffzen, B. Gargallo, R. Baños, J. Fernández, G. M. Cabanes, L. A. Bru, and D. Pastor, “Foundry developments toward silicon nitride photonics from visible to the mid-infrared,”

- IEEE Journal of Selected Topics in Quantum Electronics*, vol. 25, no. 5, pp. 1–13, 2019.
- [29] J. F. Bauters, M. J. R. Heck, D. John, D. Dai, M.-C. Tien, J. S. Barton, A. Leinse, R. G. Heideman, D. J. Blumenthal, and J. E. Bowers, “Ultra-low-loss high-aspect-ratio Si_3N_4 waveguides,” *Optics Express*, vol. 19, no. 4, pp. 3163–3174, 2011.
- [30] J. F. Bauters, M. J. R. Heck, D. D. John, M.-C. Tien, W. Li, J. S. Barton, D. J. Blumenthal, J. E. Bowers, A. Leinse, and R. G. Heideman, “Ultra-low-loss single-mode Si_3N_4 waveguides with 0.7 dB/m propagation loss,” in *2011 37th European Conference and Exhibition on Optical Communication*, pp. 1–3, 2011.
- [31] J. F. Bauters, M. J. R. Heck, D. D. John, J. S. Barton, C. M. Bruinink, A. Leinse, R. G. Heideman, D. J. Blumenthal, and J. E. Bowers, “Planar waveguides with less than 0.1 dB/m propagation loss fabricated with wafer bonding,” *Optics Express*, vol. 19, no. 24, pp. 24090–24101, 2011.
- [32] K. Luke, A. Dutt, C. B. Poitras, and M. Lipson, “Overcoming Si_3N_4 film stress limitations for high quality factor ring resonators,” *Optics Express*, vol. 21, pp. 22829–22833, Sep 2013.
- [33] J. S. Levy, A. Gondarenko, M. A. Foster, A. C. Turner-Foster, A. L. Gaeta, and M. Lipson, “CMOS-compatible multiple-wavelength oscillator for on-chip optical interconnects,” *Nature Photonics*, vol. 4, no. 1, pp. 37–40, 2010.
- [34] A. Gondarenko, J. S. Levy, and M. Lipson, “High confinement micron-scale silicon nitride high Q ring resonator,” *Optics Express*, vol. 17, no. 14, pp. 11366–11370, 2009.
- [35] J. P. Epping, M. Hoekman, R. Mateman, A. Leinse, R. G. Heideman, A. van Rees, P. J. van der Slot, C. J. Lee, and K.-J. Boller, “High confinement, high yield Si_3N_4 waveguides for nonlinear optical applications,” *Optics Express*, vol. 23, no. 2, pp. 642–648, 2015.
- [36] S. Zhang, T. Bi, I. Harder, O. Ohletz, F. Gannott, A. Gumann, E. Butzen, Y. Zhang, and P. Del’Haye, “Low-temperature sputtered ultralow-loss silicon nitride for hybrid photonic integration,” *Laser & Photonics Reviews*, vol. 18, no. 4, p. 2300642, 2024.
- [37] C. J. Krückel, A. Fülöp, T. Klintberg, J. Bengtsson, P. A. Andrekson, and V. Torres-Company, “Linear and nonlinear characterization of low-stress high-confinement

- silicon-rich nitride waveguides,” *Optics Express*, vol. 23, no. 20, pp. 25827–25837, 2015.
- [38] P. Muellner, E. Melnik, G. Koppitsch, J. Kraft, F. Schrank, and R. Hainberger, “CMOS-compatible Si_3N_4 waveguides for optical biosensing,” *Procedia Engineering*, vol. 120, pp. 578–581, 2015. Eurosensors 2015.
- [39] Y. Huang, J. Song, X. Luo, T.-Y. Liow, and G.-Q. Lo, “CMOS compatible monolithic multi-layer Si_3N_4 -on-SOI platform for low-loss high performance silicon photonics dense integration,” *Optics Express*, vol. 22, no. 18, pp. 21859–21865, 2014.
- [40] K. Shang, S. Pathak, B. Guan, G. Liu, and S. J. B. Yoo, “Low-loss compact multi-layer silicon nitride platform for 3D photonic integrated circuits,” *Optics Express*, vol. 23, no. 16, pp. 21334–21342, 2015.
- [41] W. D. Sacher, J. C. Mikkelsen, Y. Huang, J. C. C. Mak, Z. Yong, X. Luo, Y. Li, P. Dumais, J. Jiang, D. Goodwill, E. Bernier, P. G.-Q. Lo, and J. K. S. Poon, “Monolithically integrated multilayer silicon nitride-on-silicon waveguide platforms for 3-D photonic circuits and devices,” *Proceedings of the IEEE*, vol. 106, no. 12, pp. 2232–2245, 2018.
- [42] H. Zhao, B. Kuyken, S. Clemmen, F. Leo, A. Subramanian, A. Dhakal, P. Helin, S. Severi, E. Brainis, G. Roelkens, and R. Baets, “Visible-to-near-infrared octave spanning supercontinuum generation in a silicon nitride waveguide,” *Optics Letters*, vol. 40, no. 10, pp. 2177–2180, 2015.
- [43] N. Singh, H. M. Mbonde, H. C. Frankis, E. Ippen, J. D. B. Bradley, and F. X. Kärtner, “Nonlinear silicon photonics on CMOS-compatible tellurium oxide,” *Photonics Research*, vol. 8, no. 12, pp. 1904–1909, 2020.
- [44] H. M. Mbonde, N. Singh, B. L. Segat Frare, M. Sinobad, P. Torab Ahmadi, B. Hashemi, D. B. Bonneville, P. Mascher, F. X. Kärtner, and J. D. B. Bradley, “Octave-spanning supercontinuum generation in a CMOS-compatible thin Si_3N_4 waveguide coated with highly nonlinear TeO_2 ,” *Optics Letters*, vol. 49, no. 10, pp. 2725–2728, 2024.
- [45] C. Horvath, J. N. Westwood-Bachman, K. Setzer, A. McKinlay, C. M. Naraine, H. M. Mbonde, B. L. Segat Frare, P. Torab Ahmadi, P. Mascher, J. D. B. Bradley, and M. Aktary, “Prototyping of silicon nitride photonic integrated circuits for visible

- and near-infrared applications,” in *Integrated Optics: Devices, Materials, and Technologies XXVII* (S. M. García-Blanco and P. Cheben, eds.), vol. 12424, p. 1242404, International Society for Optics and Photonics, SPIE, 2023.
- [46] L. Chrostowski, H. Shoman, M. Hammood, H. Yun, J. Jhoja, E. Luan, S. Lin, A. Mistry, D. Witt, N. A. F. Jaeger, S. Shekhar, H. Jayatileka, P. Jean, S. B.-d. Villers, J. Cauchon, W. Shi, C. Horvath, J. N. Westwood-Bachman, K. Setzer, M. Aktary, N. S. Patrick, R. J. Bojko, A. Khavasi, X. Wang, T. Ferreira de Lima, A. N. Tait, P. R. Prucnal, D. E. Hagan, D. Stevanovic, and A. P. Knights, “Silicon photonic circuit design using rapid prototyping foundry process design kits,” *IEEE Journal of Selected Topics in Quantum Electronics*, vol. 25, no. 5, pp. 1–26, 2019.
- [47] K. Johnson, N. Alshamrani, D. Almutairi, A. Grieco, C. Horvath, J. N. Westwood-Bachman, A. McKinlay, and Y. Fainman, “Determination of the nonlinear thermo-optic coefficient of silicon nitride and oxide using an effective index method,” *Optics Express*, vol. 30, no. 26, pp. 46134–46146, 2022.
- [48] V. R. Almeida, R. R. Panepucci, and M. Lipson, “Nanotaper for compact mode conversion,” *Optics Letters*, vol. 28, no. 15, pp. 1302–1304, 2003.
- [49] A. Densmore, M. Vachon, D.-X. Xu, S. Janz, R. Ma, Y.-H. Li, G. Lopinski, A. Delâge, J. Lapointe, C. C. Luebbert, Q. Y. Liu, P. Cheben, and J. H. Schmid, “Silicon photonic wire biosensor array for multiplexed real-time and label-free molecular detection,” *Optics Letters*, vol. 34, no. 23, pp. 3598–3600, 2009.
- [50] S. Patrick, R. J. Bojko, S. J. H. Stammberger, E. Luan, and L. Chrostowski, “Improvement of silicon waveguide transmission by advanced e-beam lithography data fracturing strategies,” *Journal of Vacuum Science Technology B*, vol. 35, no. 6, p. 06G504, 2017.
- [51] S. C. Mao, S. H. Tao, Y. L. Xu, X. W. Sun, M. B. Yu, G. Q. Lo, and D. L. Kwong, “Low propagation loss sin optical waveguide prepared by optimal low-hydrogen module,” *Optics Express*, vol. 16, no. 25, pp. 20809–20816, 2008.
- [52] Y. Chen, T. Domínguez Bucio, A. Z. Khokhar, M. Banakar, K. Grabska, F. Y. Gardes, R. Halir, Í. Molina-Fernández, P. Cheben, and J.-J. He, “Experimental demonstration of an apodized-imaging chip-fiber grating coupler for Si₃N₄ waveguides,” *Optics Letters*, vol. 42, no. 18, pp. 3566–3569, 2017.

- [53] S. Nambiar, A. Kumar, R. Kallega, P. Ranganath, and S. K. Selvaraja, “High-efficiency grating coupler in 400nm and 500nm PECVD silicon nitride with bottom reflector,” *IEEE Photonics Journal*, vol. 11, no. 5, pp. 1–13, 2019.
- [54] V. Vitali, C. Lacava, T. Domínguez Bucio, F. Y. Gardes, and P. Petropoulos, “Highly efficient dual-level grating couplers for silicon nitride photonics,” *Scientific Reports*, vol. 12, no. 1, p. 15436, 2022.
- [55] Y. Wang, X. Wang, J. Flueckiger, H. Yun, W. Shi, R. Bojko, N. A. F. Jaeger, and L. Chrostowski, “Focusing sub-wavelength grating couplers with low back reflections for rapid prototyping of silicon photonic circuits,” *Optics Express*, vol. 22, no. 17, pp. 20652–20662, 2014.
- [56] X. Chen, Z. Cheng, C. K. Y. Fung, and H. K. Tsang, “Design and applications of silicon waveguide grating couplers,” in *Silicon Photonics VII* (J. Kubby and G. T. Reed, eds.), vol. 8266, p. 82660I, International Society for Optics and Photonics, SPIE, 2012.
- [57] S. Özbayat, K. Kojima, T. Koike-Akino, B. Wang, K. Parsons, S. Singh, S. Nishikawa, and E. Yagyu, “Application of numerical optimization to the design of inp-based wavelength combiners,” *Optics Communications*, vol. 322, pp. 131–136, 2014.
- [58] J. Mu, S. A. Vázquez-Córdova, M. A. Sefunc, Y.-S. Yong, and S. M. García-Blanco, “A low-loss and broadband MMI-based multi/demultiplexer in Si₃N₄/ technology,” *Journal of Lightwave Technology*, vol. 34, no. 15, pp. 3603–3609, 2016.
- [59] L. B. Soldano and E. C. M. Pennings, “Optical multi-mode interference devices based on self-imaging: principles and applications,” *Journal of Lightwave Technology*, vol. 13, no. 4, pp. 615–627, 1995.
- [60] D. Dai and S. He, “Optimization of ultracompact polarization-insensitive multimode interference couplers based on Si nanowire waveguides,” *IEEE Photonics Technology Letters*, vol. 18, no. 19, pp. 2017–2019, 2006.
- [61] A. Maese-Novo, R. Halir, S. Romero-García, D. Pérez-Galacho, L. Zavargo-Peche, A. O.-M. nux, I. Molina-Fernández, J. G. Wangüemert-Pérez, and P. Cheben, “Wavelength independent multimode interference coupler,” *Optics Express*, vol. 21, no. 6, pp. 7033–7040, 2013.

- [62] M. Hill, X. Leijtens, G. Khoe, and M. Smit, “Optimizing imbalance and loss in 2×2 3-dB multimode interference couplers via access waveguide width,” *Journal of Lightwave Technology*, vol. 21, no. 10, pp. 2305–2313, 2003.
- [63] W. Bogaerts, P. De Heyn, T. Van Vaerenbergh, K. De Vos, S. Kumar Selvaraja, T. Claes, P. Dumon, P. Bienstman, D. Van Thourhout, and R. Baets, “Silicon microring resonators,” *Laser & Photonics Reviews*, vol. 6, no. 1, pp. 47–73, 2012.
- [64] B. E. Little, J.-P. Laine, and S. T. Chu, “Surface-roughness-induced contradirectional coupling in ring and disk resonators,” *Optics Letters*, vol. 22, no. 1, pp. 4–6, 1997.
- [65] C. Manolatou, M. J. Khan, S. Fan, P. R. Villeneuve, H. A. Haus, and J. D. Joannopoulos, “Coupling of modes analysis of resonant channel add-drop filters,” *IEEE Journal of Quantum Electronics*, vol. 35, no. 9, pp. 1322–1331, 1999.
- [66] D. S. Weiss, V. Sandoghdar, J. Hare, V. Lefèvre-Seguin, J.-M. Raimond, and S. Haroche, “Splitting of high- Q mie modes induced by light backscattering in silica microspheres,” *Optics Letters*, vol. 20, pp. 1835–1837, Sep 1995.
- [67] M. Borselli, T. J. Johnson, and O. Painter, “Beyond the rayleigh scattering limit in high- Q silicon microdisks: theory and experiment,” *Optics Express*, vol. 13, no. 5, pp. 1515–1530, 2005.
- [68] P. Rabiei, W. H. Steier, C. Zhang, and L. R. Dalton, “Polymer micro-ring filters and modulators,” *Journal of Lightwave Technology*, vol. 20, no. 11, pp. 1968–1975, 2002.
- [69] N. Sherwood-Droz and M. Lipson, “Scalable 3D dense integration of photonics on bulk silicon,” *Optics Express*, vol. 19, no. 18, pp. 17758–17765, 2011.
- [70] A. Frigg, A. Boes, G. Ren, I. Abdo, D.-Y. Choi, S. Gees, and A. Mitchell, “Low loss CMOS-compatible silicon nitride photonics utilizing reactive sputtered thin films,” *Optics Express*, vol. 27, no. 26, pp. 37795–37805, 2019.
- [71] P. Cheben, R. Halir, J. H. Schmid, H. A. Atwater, and D. R. Smith, “Subwavelength integrated photonics,” *Nature*, vol. 560, pp. 565–572, 2018.
- [72] R. Halir, A. Ortega-Moñux, D. Benedikovic, G. Z. Mashanovich, J. G. Wangüemert-Pérez, J. H. Schmid, Í. Molina-Fernández, and P. Cheben, “Subwavelength-grating metamaterial structures for silicon photonic devices,” *Proceedings of the IEEE*, vol. 106, no. 12, pp. 2144–2157, 2018.

- [73] J. M. Luque-González, A. Sánchez-Postigo, A. Hadij-ElHouati, A. Ortega-Moñux, J. G. Wangüemert-Pérez, J. H. Schmid, P. Cheben, Í. Molina-Fernández, and R. Halir, “A review of silicon subwavelength gratings: building break-through devices with anisotropic metamaterials,” *Nanophotonics*, vol. 10, no. 11, pp. 2765–2797, 2021.
- [74] P. Cheben, J. H. Schmid, R. Halir, J. M. Luque-González, J. G. Wangüemert-Pérez, D. Melati, and C. Alonso-Ramos, “Recent advances in metamaterial integrated photonics,” *Advances in Optics and Photonics*, vol. 15, no. 4, pp. 1033–1105, 2023.
- [75] J. G. Wangüemert-Pérez, A. Hadij-ElHouati, A. Sánchez-Postigo, J. Leuermann, D.-X. Xu, P. Cheben, A. Ortega-Moñux, R. Halir, and Í. Molina-Fernández, “Subwavelength structures for silicon photonics biosensing,” *Optics & Laser Technology*, vol. 109, pp. 437–448, 2019.
- [76] Z. Pan, X. Xu, C.-J. Chung, H. Dalir, H. Yan, K. Chen, Y. Wang, B. Jia, and R. T. Chen, “High-speed modulator based on electro-optic polymer infiltrated subwavelength grating waveguide ring resonator,” *Laser & Photonics Reviews*, vol. 12, no. 6, p. 1700300, 2018.
- [77] T. Barwicz, B. Peng, R. Leidy, A. Janta-Polczynski, T. Houghton, M. Khater, S. Kamlapurkar, S. Engelmann, P. Fortier, N. Boyer, and W. M. J. Green, “Integrated metamaterial interfaces for self-aligned fiber-to-chip coupling in volume manufacturing,” *IEEE Journal of Selected Topics in Quantum Electronics*, vol. 25, no. 3, pp. 1–13, 2019.
- [78] P. Cheben, D.-X. Xu, S. Janz, and A. Densmore, “Subwavelength waveguide grating for mode conversion and light coupling in integrated optics,” *Optics Express*, vol. 14, no. 11, pp. 4695–4702, 2006.
- [79] C. M. Naraine, J. N. Westwood-Bachman, C. Horvath, M. Aktary, A. P. Knights, J. H. Schmid, P. Cheben, and J. D. B. Bradley, “Subwavelength grating metamaterial waveguides and ring resonators on a silicon nitride platform,” *Laser & Photonics Reviews*, vol. 17, no. 2, p. 2200216, 2023.
- [80] X. Ai, Y. Zhang, W.-L. Hsu, S. Veilleux, and M. Dagenais, “Broadband 2×2 multimode-interference coupler on the silicon-nitride platform,” *Optics Express*, vol. 32, no. 6, pp. 9405–9419, 2024.

- [81] A. Densmore, D.-X. Xu, S. Janz, P. Waldron, J. Lapointe, T. Mischki, G. Lopinski, A. Delâge, J. H. Schmid, and P. Cheben, “Sensitive label-free biomolecular detection using thin silicon waveguides,” *Advances in Optical Technologies*, vol. 2008, p. 725967, 2008.
- [82] D. Dai and J. E. Bowers, “Silicon-based on-chip multiplexing technologies and devices for Peta-bit optical interconnects,” *Nanophotonics*, vol. 3, no. 4-5, pp. 283–311, 2014.
- [83] Z. Li, Z. Fan, J. Zhou, Q. Cong, X. Zeng, Y. Zhang, and L. Jia, “Process development of low-loss LPCVD silicon nitride waveguides on 8-inch wafer,” *Applied Sciences*, vol. 13, no. 6, p. 3660, 2023.
- [84] H. J. Stein, P. S. Peercy, and R. J. Sokel, “Post-deposition high temperature processing of silicon nitride,” *Thin Solid Films*, vol. 101, no. 4, pp. 291–298, 1983.
- [85] K. N. Andersen, W. E. Svendsen, T. Stimpel-Lindner, T. Sulima, and H. Baumgärtner, “Annealing and deposition effects of the chemical composition of silicon-rich nitride,” *Applied Surface Science*, vol. 243, no. 1, pp. 401–408, 2005.
- [86] R. Korček, D. Medina Quiroz, Q. Wilmart, S. Edmond, P. Cheben, L. Vivien, C. Alonso-Ramos, and D. Benedikovič, “Library of single-etch silicon nitride grating couplers for low-loss and fabrication-robust fiber-chip interconnection,” *Scientific Reports*, vol. 13, no. 1, p. 17467, 2023.

Chapter 4

Subwavelength grating metamaterial waveguides and ring resonators on a silicon nitride platform

This chapter includes the findings presented in a published manuscript on the demonstration of subwavelength grating (SWG) metamaterial waveguides and ring resonators fabricated on a commercially available rapid prototyping silicon nitride (SiN) foundry platform. The developments in silicon photonics (SiP) technology are leading the advances in disciplines as diverse as high-speed optical communications, quantum physics, sensing, and light detection and ranging (LiDAR). SiN has evolved as a promising complementary material to silicon (Si) for integrated photonics. It offers low mode propagation losses, enhanced fabrication tolerance, transparency throughout the visible (VIS) light spectrum, advantageous nonlinear properties, and still leverages the mature fabrication processes of the microelectronics industry. While important advances have been reported in SiN integrated photonics, there is a desire to improve the capability to accurately control the distribution of the electromagnetic field and the wavevectors of the propagating modes in a SiN platform. This has been successfully demonstrated in SiP by using SWG metamaterials, resulting in many integrated optical devices with unprecedented performance, yet no reports were previously made for SWG metamaterial

waveguides in SiN.

Here we propose and experimentally demonstrate SWG metamaterial waveguides on an SiN platform for the first time. Our SWG SiN waveguides have low propagation loss (~ 1.5 dB/cm) in the telecom C-band. At the same time, a large overlap ($>50\%$) of the Floquet-Bloch mode with the top cladding material (in this case, silicon dioxide (SiO_2)) is achieved, which is a promising property for applications in evanescent field sensing and light amplification. Furthermore, we use our metamaterial waveguide to demonstrate the first SWG-engineered ring resonator in the SiN platform. The SiO_2 -clad SiN SWG resonator has a measured internal quality factor of $\sim 2.11 \cdot 10^5$, comparable to conventional ring resonators in similar SiN platforms. Meanwhile, the same resonator with a water coating has a calculated bulk sensitivity of 0.33 RIU/RIU (~ 285 nm/RIU for 1540 nm wavelength) and measured loaded quality factor of 5200, which is competitive with equivalent SWG ring resonator sensors reported in the silicon-on-insulator (SOI) platform. We believe that these results represent an important advancement towards SWG metamaterial-engineered integrated photonic devices based on SiN waveguides for a wide range of applications leveraging established integrated photonics technology.

The contents of this chapter are mostly reprinted with open access permission from the publisher under the following citation:

Cameron M. Naraine, Jocelyn N. Westwood-Bachman, Cameron Horvath, Mirwais Aktary, Andrew P. Knights, Jens H. Schmid, Pavel Cheben, and Jonathan D. B. Bradley, “Subwavelength grating metamaterial waveguides and ring resonators on a silicon nitride platform,” *Laser & Photonics Reviews*, vol. 17, no. 2, p. 2200216, 2023. DOI: [10.1002/lpor.202200216](https://doi.org/10.1002/lpor.202200216).

The only section added to the thesis that was not in the original publication is the experimental results and corresponding discussion for the water-coated SiN SWG ring resonator. Section 4.1 introduces the background and role of SWG metamaterial structures in SiP, as well as the motivation to implement them in SiN waveguides. Section 4.2 explains the design process and fabrication methods used to produce SiN-based SWG metamaterial waveguide devices. Section 4.3 describes the characterization steps and presents the experimental results for the fabricated SiN SWG metamaterial waveguides and ring resonators. Finally, Section 4.4 summarizes the results and highlights the potential that SWG metamaterials have in SiN photonic integrated circuits (PICs) and their related applications.

Abstract

We propose and demonstrate SWG metamaterial waveguides and ring resonators on a SiN platform. The SWG waveguide is engineered such that a large overlap of 53% of the Floquet-Bloch mode with the top cladding material is achieved, demonstrating excellent potential for applications in evanescent field sensing and light amplification. The devices, which have critical dimensions greater than 100 nm, are fabricated using a commercial rapid turn-around SiN prototyping foundry process using electron beam lithography (EBL). Experimental characterization of the fabricated device reveals excellent ring resonator internal quality factor ($2.11 \cdot 10^5$) and low propagation loss (~ 1.5 dB/cm) in the C-band, a significant improvement of both parameters compared to Si-based SWG ring resonators. These results demonstrate the promising prospects of SWG metamaterial structures for SiN based PICs.

4.1 Introduction

SiP has become a leading integrated photonics technology by leveraging existing microelectronics manufacturing processes and infrastructure to produce compact, scalable, low-power, and cost-effective PICs [1; 2; 3]. This development has stimulated commercial and research interest, compelling many foundries to offer new services that deliver high-performance integrated optical components and circuits, including process design kits (PDKs) and multi-project wafer (MPW) runs [4; 5]. While SOI has been established as the dominant platform for SiP circuits, its high index contrast ($\Delta n \sim 2$) implies several functional drawbacks, including strict fabrication tolerances, strong polarization dependence, and significant scattering and coupling losses. Furthermore, its bandgap of 1.12 eV limits its application to wavelengths above ~ 1.1 μm . To circumvent these disadvantages, SiN has been developed as a versatile complementary material. SiN is a common material available in many SiP foundries and shares plenty of the same mature fabrication methods as SOI that enable nanoscale integrated optical devices with high integration density and compact footprints [6; 7]. Compared to SOI, SiN benefits from a moderate index contrast ($\Delta n \sim 0.5$) for design flexibility, low scattering losses, reduced birefringence and polarization dependent losses, transparency throughout the VIS and near-infrared (NIR) spectra, higher tolerance to fabrication variance, negligible two-photon absorption (TPA), and advantageous nonlinear optical properties [8; 9; 10]. These interesting features make SiN an attractive platform for applications such as evanescent field sensing and light amplification, where performance is enhanced by increased light-matter interaction with the cladding material [11; 12; 13; 14; 15; 16; 17; 18; 19; 20].

Since their first demonstration in Si waveguides, SWG metamaterials [21; 22] have become an essential tool in integrated photonics due to the design flexibility and precise lithographic control over the waveguide effective index and mode field distribution [23]. This has led to many on-chip devices for routing, coupling, filtering, switching, modulation, multiplexing, and management in polarization, anisotropy, and dispersion [24; 25]. SWG metamaterials were first proposed for on-chip sensors exploiting their increased mode overlap with the low index sensing environment surrounding the SWG waveguide core [26]. SWG-based ring resonator sensors reported higher sensitivities compared to the conventional devices [27], owing to the strong longitudinal field component within the gaps between the SWG segments that is not accessible in conventional strip or slot waveguides. SWG engineering has also been suggested to enhance gain in waveguide amplifiers and lasers based on optically active cladding materials [28].

Thus far, SWG metamaterial waveguides have been almost exclusively implemented in SOI [21; 22; 23; 24; 25]. While SWG ring resonators based in SOI have reported good sensitivity figures of merit, their demonstrated quality factors (Q) have been limited to the 10^4 range, which is quite low compared to SiN ring resonators. Here, we demonstrate SWG metamaterial waveguides and ring resonators on an SiN platform. For sensing applications, an SiO₂ cladding above the SiN waveguide would be typically implemented by a different material, depending on a specific application, e.g., water-based analyte for evanescent field sensing, or rare-earth (RE)-ion doped oxide for optical amplifiers. However, the operation would still rely on the same principle, i.e., modification of optical properties in the superstrate medium affecting the mode propagation constant, which can be controlled by optimizing the mode overlap with the superstrate. Leveraging SWG metamaterial engineering in the SiN platform allows enhancement of the overlap of the waveguide mode with the superstrate material due to the reduced waveguide effective index, and the mode localization within the SWG gaps. According to our 3D simulations, a 53% mode overlap with the oxide top cladding is achieved for our SiN SWG waveguides. SWG engineering in the SiN platform brings some drawbacks because of reduced effective index and possibly increased loss penalty due to substrate leakage and bend loss. We judiciously selected a design point optimizing the tradeoff between different parameters, including modal confinement in the region of interest (superstrate), substrate leakage and minimum bend radius. An internal Q of $2.11 \cdot 10^5$ at 1540 nm wavelength is measured in the fabricated SWG ring resonators, which is comparable to equivalent conventional SiN ring resonators fabricated on the same platform and a significant improvement compared to reported Si based SWG ring resonators. The same device using water as a superstrate medium is also demonstrated with a measured loaded

Q of 5200 at 1540 nm wavelength, thus validating its potential as a sensing device. These performances shows that the realization of SWG metamaterials holds significant promise for compact and efficient components and devices in SiN integrated photonics.

4.2 Design and fabrication

Fig. 4.1 shows a schematic of our SiN SWG metamaterial ring resonator. We designed our SWG metamaterial waveguides and ring resonators for the SiN platform offered by Applied Nanotools Inc. (ANT) [29]. Direct-write EBL was used to define the SWG waveguide structures, which have a critical feature size of ~ 100 nm. The platform comprises a 400-nm-thick low pressure chemical vapour deposition (LPCVD) SiN waveguide layer (refractive index $n \sim 2$) on a 4.5- μm SiO₂ buried oxide (BOX) with a 3- μm plasma enhanced chemical vapour deposition (PECVD) SiO₂ top cladding ($n \sim 1.47$). This SiN thickness is also widely available in other foundries, yields compact single mode waveguides with low propagation loss and moderate confinement around 1550 nm, and has minimal risk of stress-induced film cracking [9].

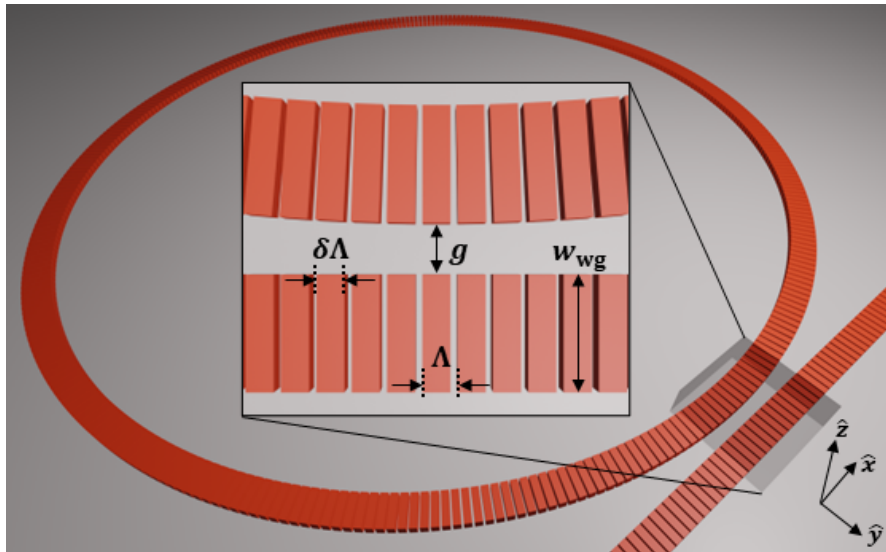


FIGURE 4.1: Schematic of SiN SWG metamaterial ring resonator. Inset: top view of coupling section between ring resonator and bus waveguide.

An analysis of SWG waveguides for the SiN platform was conducted using the DEVICE Suite from Ansys Lumerical [30]. We first used a 2D finite difference eigenmode (FDE) solver to calculate the mode properties of various SWG waveguides within the effective medium theory (EMT) approximation [23]. The SWG waveguide is modeled

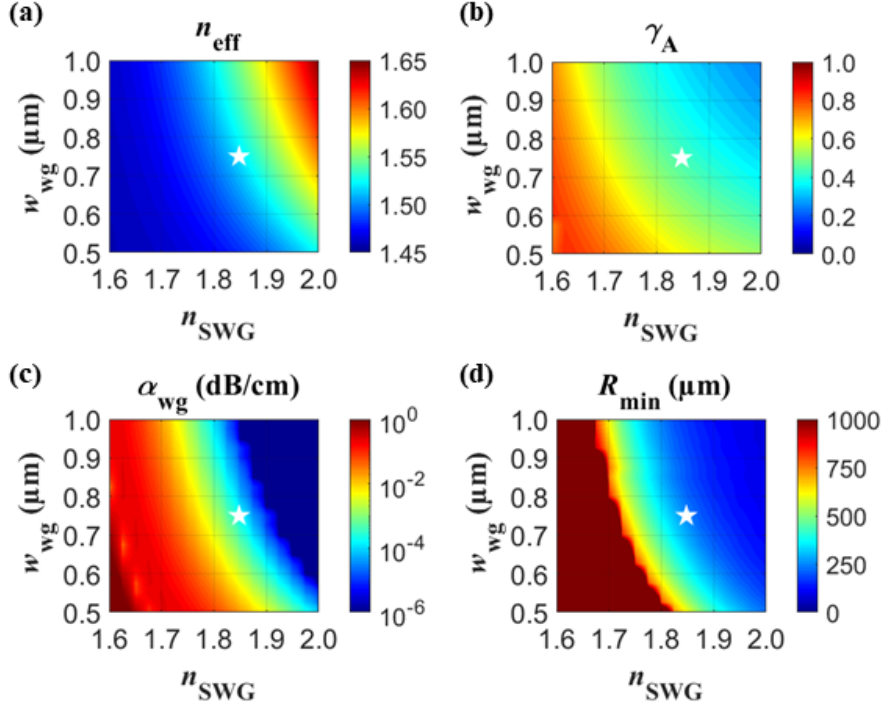


FIGURE 4.2: Simulated (a) mode effective index, (b) mode overlap with the upper cladding, (c) propagation loss, and (d) minimum bend radius for various TE-polarized SiN SWG metamaterial waveguides, using EMT and a 2D FDE solver.

as a conventional strip waveguide with a variable core index (n_{SWG}) that is dependent on the refractive indices of the constituent materials and the SWG duty cycle δ . We set the material refractive index values to match the ANT platform and varied the duty cycle between 0.25 and 1 in our calculations, where $\delta = 1$ is analogous to a conventional strip waveguide. Fig. 4.2 displays the 2D simulation results for transverse electric (TE)-polarized waveguides as a function of n_{SWG} and waveguide width (w_{wg}). We quantify the optical intensity overlap with the upper cladding, which we consider the active region, by calculating the electric field energy density factor (γ_{A}) using Eq. 1.3, where the integration domain extends over the 2D transverse cross-sectional area of the waveguide [31; 32]. The overlap is maximized when n_{SWG} and w_{wg} are reduced but a trade-off is observed between the overlap factor and increasing substrate leakage loss penalty as the mode effective index (n_{eff}) decreases and the mode expands deeper into the BOX layer, as shown in Fig. 4.2(c). The bend losses also increase significantly for low n_{eff} . We define the minimum bend radius (R_{min}) as the value for which the simulated radiation loss is <1 dB/cm and plot the results in Fig. 4.2(d) for various SWG structures calculated

using the bent waveguide eigenmode solver. We aim to maintain compact devices with bend radius <1 mm, so the saturated low n_{eff} region of Fig. 4.2(d) is associated with high bend radiation loss. We chose $w_{\text{wg}} = 0.75 \mu\text{m}$ and $n_{\text{SWG}} \sim 1.85$ (corresponding to $\delta = 0.7$) for our fabricated devices since this configuration offers compact, low-loss waveguide structures while maintaining a good overlap metric. The white stars throughout Fig. 4.2 mark the results of the simulated waveguide with these parameters, which exhibits $n_{\text{eff}} = 1.52$, $\gamma_{\text{A}} = 44\%$, $\alpha_{\text{wg}} \sim 0.001$ dB/cm, and $R_{\text{min}} = 250 \mu\text{m}$.

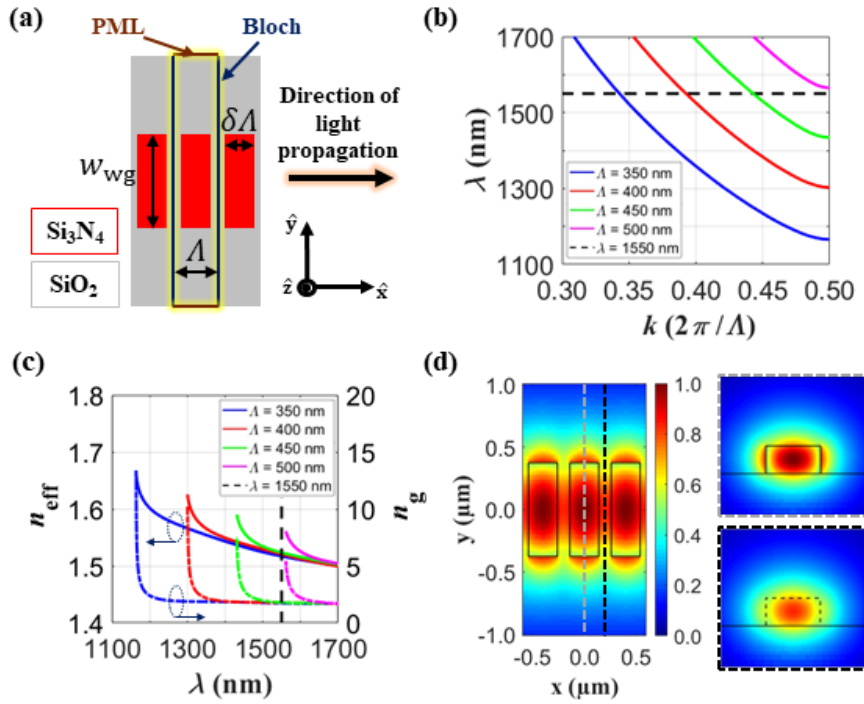


FIGURE 4.3: (a) Top view schematic of SWG-engineered SiN waveguide. 3D FDTD simulated (b) photonic bandstructures and (c) corresponding effective (solid lines) and group (dashed lines) indices of SWG devices with varying grating period Λ . Dashed black lines correspond to a wavelength (λ) of 1550 nm. (d) Floquet-Bloch mode propagating in the SWG SiN waveguide. Transverse mode distributions are shown across the SiN segment (top right) and within the gap between SiN segments (bottom right) for in-plane TE polarization.

We performed 3D finite-difference-time-domain (FDTD) simulations to accurately calculate the photonic bandstructure and corresponding Floquet-Bloch mode profiles of our SWG waveguide structure. The FDTD simulation setup and results are shown in Fig. 4.3. The simulation window consists of a single unit cell confined by Bloch and perfectly

matched layer (PML) boundary layers along the propagation axis and transverse regions, respectively. This emulates an infinitely periodic grating structure and significantly reduces the simulation time. Fig. 4.3(b) shows the calculated bandstructures for 750 nm waveguide width (w_{wg}), 0.7 SWG duty cycle (δ), and various SWG periods (Λ) plotted with respect to free space wavelength (λ). The dispersion relation shows that the first-order band in each series gradually flattens as the Brillouin zone boundary ($k = \pi/\Lambda$) is approached. This causes the effective (n_{eff}) and group (n_{g}) indices to rapidly increase, as observed in Fig. 4.3(c), before reaching the band edge wavelength where the photonic bandgap begins. Increasing Λ causes the band to significantly redshift, as expected. We selected a period of 400 nm to ensure our fabricated devices are subwavelength in the C-band and operate far from the photonic bandgap. For this architecture, at 1550 nm wavelength, $n_{\text{eff}} = 1.52$ and $n_{\text{g}} = 1.78$, which is in good agreement with the 2D simulation. Fig. 4.3(d) shows the Floquet-Bloch mode profile propagating through the SWG metamaterial waveguide. For the 3D simulation, the electric field energy density factor γ_{A} is re-evaluated by replacing the 2D transverse cross-section integration area by a volume corresponding to one grating period. Our 3D simulation yields a 53% mode intensity overlap with the upper cladding and SWG gap regions. This is about 20% higher compared to the 2D simulation result, mainly due to the inclusion of the electric field localized within the gaps of the SWG structure in the 3D simulation.

Our fabricated ring resonator is shown in Fig. 4.4. To couple light efficiently from a fiber to the bus waveguide on the chip, we designed an SWG edge coupler with 0.4 μm tip width and 100 μm length at the facet, adopting the general concept previously demonstrated in SOI [33]. We fabricated multiple SWG ring resonator circuits in the all-pass configuration with 400 μm ring radius and various coupling gaps between the ring and the bus waveguide to assess the coupling conditions. The fabricated chips underwent a deep trench etching process and were then diced into individual dies to facilitate fiber-chip edge coupling.

4.3 Optical characterization and analysis

The devices were characterized by coupling TE-polarized light from a 1510 nm – 1640 nm tunable laser on chip to the bus waveguide and off chip to an indium gallium arsenide (InGaAs) photodetector, using 2.5 μm spot size lensed fibers. Fig. 4.5 shows the insertion loss spectrum for an SWG ring resonator with a 2 μm gap. The inset displays resonances close to the critical coupling point near 1610 nm with a maximum extinction ratio (ER) of 14.2 dB. The coupling is stronger at longer wavelengths due to the enlarged mode size

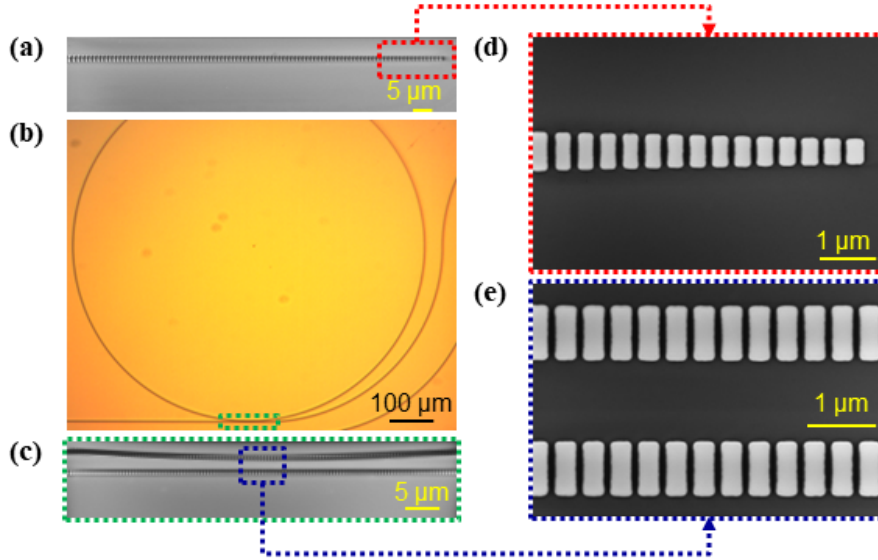


FIGURE 4.4: (a) Top view scanning electron microscope (SEM) image of SWG edge coupler. (b) Optical microscope image of fabricated SWG ring resonator. (c) Top view SEM image of coupling section of SWG ring resonator circuit with a 1.2 μm gap. (d, e) Detailed magnified views of (a) and (c), as marked.

and increased overlap between the bus and ring waveguide modes. As the wavelength decreases, the ER is reduced, and we observe under-coupling. The SWG waveguides and ring resonators are designed to support only the fundamental mode, so there are no higher order modes present. This is also confirmed in our experiment, as the zoomed in spectrum (inset of Fig. 4.5) does not show any higher-order mode resonance features and a resonance spectrum corresponding to the fundamental TE mode is observed. The experimental group index (n_g) is determined from the measured free spectral range (FSR), using the relation [34]:

$$n_g = \frac{\lambda^2}{FSR \cdot 2\pi R}, \quad (4.1)$$

where λ is the resonance wavelength and R is the resonator radius. For 1510 nm and 1640 nm wavelengths, $FSR = 0.51$ and 0.63 nm, yielding $n_g = 1.79$ and 1.70 , respectively, which is in good agreement with the 3D FDTD simulation.

We quantify the performance of our fabricated devices by fitting the resonances using coupled mode theory [35] and calculating the Q factors. The external (Q_e) and internal (Q_i) quality factors are associated with the coupling strength and resonator propagation

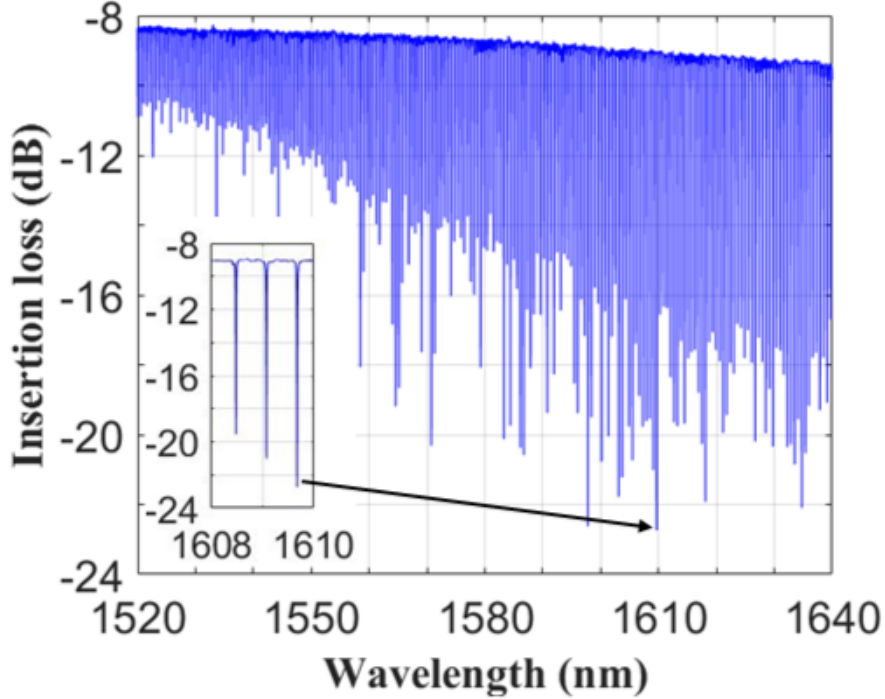


FIGURE 4.5: Measured transmission spectrum for SiN SWG ring resonator with 2 μm gap. Inset: Critically coupled resonances near 1610 nm wavelength with a maximum ER of ~ 14 dB.

loss, respectively. As these parameters decrease, their respective Q factors increase. The resulting loaded quality factor (Q_L) of a resonance is determined by Eq. 3.5 [36]. Fig. 4.6 shows measured resonances centered near 1540 nm wavelength of three SWG ring resonators with different coupling gaps. Each resonance is associated with a different coupling regime. The device with 1.2 μm gap is over-coupled ($Q_e < Q_i$), has a Q_L of $3 \cdot 10^4$, and displays a low ER of 2.9 dB. The device with 1.6 μm gap is critically coupled ($Q_e \sim Q_i$) as indicated by the large ER of 14.4 dB, which is equivalent to the maximum ER shown in Figure 4.5. This resonance exhibits a Q_L of $7.34 \cdot 10^4$. The device with a 2 μm gap is under-coupled ($Q_e > Q_i$). Resonators in this regime may feature split resonances caused by interaction between two counter-propagating modes. We included this effect in our fitting algorithm based on the analysis presented in [37] and report an average Q_L and Q_i of $1.56 \cdot 10^5$ and $2.11 \cdot 10^5$, respectively, between the two resonance peaks. The propagation loss (α) is calculated using Eq. 3.7 [38], which yields $\alpha = 1.48$ dB/cm for the SWG ring resonator. Conventional strip waveguide-based ring resonators with 250 μm radius were also fabricated on the same chip and underwent the same

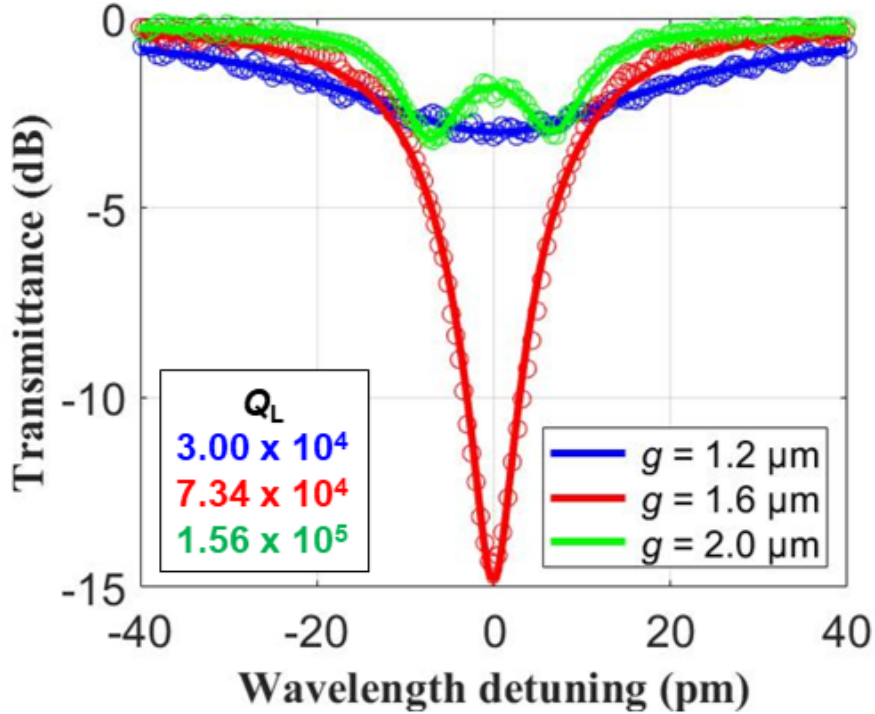


FIGURE 4.6: Fitted resonances near 1540 nm wavelength for over-coupled (blue), critically coupled (red) and under-coupled (green) SiN SWG ring resonators with 400 μm ring radius and varying gap sizes.

characterization process. A Q_i of $2.42 \cdot 10^5$ and n_g of 2 were measured in an under-coupled device near 1540 nm wavelength, corresponding to a propagation loss of 1.47 dB/cm. These results show that SWG ring resonators have comparable performance with conventional ring resonator devices in the same SiN platform. At the same time, our SWG SiN ring resonator exhibits a substantially higher Q compared to SWG Si ring resonators [39], albeit the structural parameters (ring radius, modal confinement, etc.) are different.

TABLE 4.1: Sensitivity calculations for water-coated SiN waveguides obtained from 3D FDTD simulations.

Waveguide type	δ	w_{wg} (μm)	S_b (RIU/RIU)	S_s (RIU/nm)
SWG	0.7	0.75	0.33	3.76×10^{-4}
Strip	1	0.75	0.26	2.59×10^{-4}

The main advantage of our SWG SiN waveguides and ring resonators is that, unlike

previously reported conventional SiN structures, they allow an additional degree of freedom to engineer the mode profile, which is important for optimization of mode overlap with the cladding material. To clarify this point, we carried out numerical investigations to directly compare performance of SWG and conventional SiN waveguides in terms of bulk and surface sensitivity [26], which are determined using the following respective equations:

$$S_b = \frac{\partial n_{\text{eff}}}{\partial n_{\text{clad}}}, \quad (4.2)$$

$$S_s = \frac{\partial n_{\text{eff}}}{\partial t}, \quad (4.3)$$

where n_{eff} is the mode effective index, n_{clad} is the top cladding refractive index, and t is the thickness of the adsorbed molecular layer on the surface of the waveguide. Specifically, we calculated S_b for SiN waveguides coated in water ($n = 1.32$), as well as S_s for water-coated SiN waveguides with a protein adlayer of refractive index $n = 1.45$ and thickness $t = 10$ nm. Table 4.1 summarizes the calculated sensitivities at a wavelength of 1550 nm, obtained by rigorous 3D FDTD simulations. Considering the same waveguide parameters as those reported above, we observed a substantial increase in both bulk and surface sensitivities in the SWG waveguide, which echoes the principles of reported SOI-based sensors that implement these different waveguide types [26].

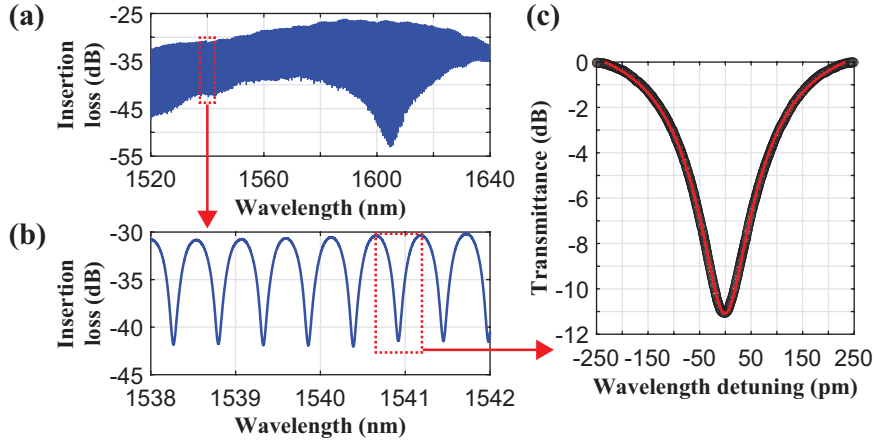


FIGURE 4.7: (a) Full measured transmission spectrum, (b) zoomed-in C-band spectrum, and (c) fitted resonance near 1540 nm wavelength for under-coupled SiN SWG ring resonator covered with water.

To demonstrate a viable SWG sensor waveguide on this SiN platform, additional measurements were performed on ring resonators without SiO₂ top cladding, and then with

a droplet of water covering the chip, thus emulating an air-clad and water-clad device, respectively. No resonances were observed for the air-clad ring resonator because the current geometry ($w_{\text{wg}} = 0.75 \mu\text{m}$ and $\delta = 0.7$), which was specifically selected to work with SiO_2 top cladding, does not provide enough mode confinement in the waveguide to overcome the strong modal asymmetry between the top and bottom claddings. The air cladding significantly lowers the mode effective index, so the mode is effectively pushed towards the BOX, thus inducing prohibitively high leakage losses. On the other hand, clear resonance features were measured when water was used as a superstrate medium, as shown in Fig. 4.7. The full transmission spectrum of the water-coated SWG ring resonator with a $0.8 \mu\text{m}$ coupling gap (Fig. 4.7(a)) shows critical coupling at 1605 nm wavelength with an ER of 26.5 dB . Based on the discussion of the results in Fig. 4.5, this places the C-band in the under-coupled regime. The same fitting procedure used for the resonances in Fig. 4.6 was performed on a resonance near 1540 nm wavelength (Fig. 4.7(c)) and revealed an Q_i and Q_L of 8400 and 5200 , respectively, which is comparable to many reported SOI-based SWG ring resonators using water as a superstrate medium [26; 27; 40; 41]. While these results demonstrate a working SiN SWG ring resonator in an environment that is commonly used for sensing applications, the Q factors are quite low. Because the current waveguide design is optimized to obtain high mode overlap with SiO_2 top cladding, the same device with a lower index cladding, such as air and water, suffers from lower effective index and greater leakage, which ultimately leads to higher loss and lower Q . This effect is amplified by the SWG metamaterials since the superstrate medium has a direct influence on the waveguide refractive index. The loss performance of these waveguides with lower index superstrate materials can be enhanced by increasing the waveguide width and/or the SWG duty ratio to boost the mode effective index and reduce substrate leakage. A comprehensive design procedure like the one described in Section 4.2 must be repeated to obtain the appropriate waveguide parameters that will optimize the SWG device performance for the specific material and application under investigation. Nevertheless, these results provide a reasonable margin for the refractive indices of the superstrate media of interest for applications in sensing and light amplification.

Resonances at different wavelengths shown in the transmission spectrum in Fig. 4.5 were also fitted and their Q factors calculated. These results are displayed in Fig. 4.8. The data points were averaged using a quadratic polynomial fit across the measured spectrum. The relationship between Q_i and Q_L is consistent with the discussion of the various coupling regimes. Near 1540 nm wavelength, the resonator is under-coupled since Q_L is equivalent to and limited by Q_i . As the coupling strength increases with the

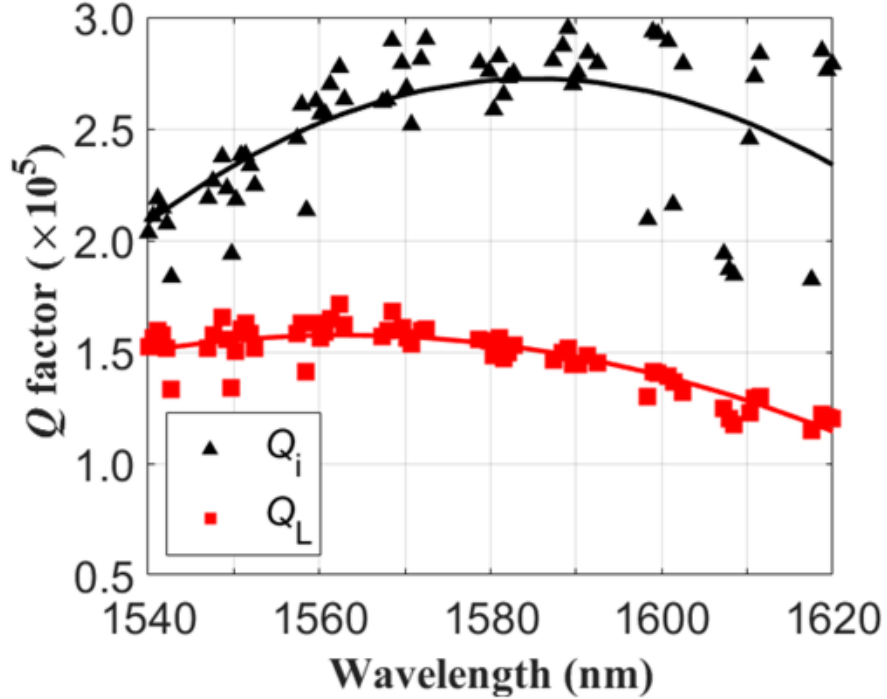


FIGURE 4.8: Measured internal (black triangles) and loaded (red squares) Q factors with the corresponding polynomial fitting curves for SWG ring resonator with 2 μm gap over the C- and L-bands.

wavelength, the values of Q_L and Q_i gradually diverge. Critical coupling is achieved at 1610 nm wavelength, where $Q_L \approx Q_i/2$, as expected from Fig. 4.5. Q_L beyond the L-band shows a continuous decrease due to persistent over-coupling. The intrinsic quality factor fitting curve peaks near 1587 nm wavelength with $Q_i = 2.72 \cdot 10^5$, corresponding to a propagation loss of 1.1 dB/cm. The quality factor may be enhanced by implementing a trapezoidal SWG geometry throughout the ring resonator and waveguide bends, as has been demonstrated for Si waveguides [39].

4.4 Conclusion

In conclusion, we have demonstrated SiN-based SWG metamaterial waveguides and microring resonators. A 53% mode overlap with the SiO_2 upper cladding material was calculated using 3D FDTD simulations. An internal quality factor $Q_i = 2.11 \cdot 10^5$ was measured near 1540 nm wavelength and a maximum fitted Q_i of $2.72 \cdot 10^5$ was determined at a wavelength of 1587 nm, corresponding to propagation losses of 1.48 and 1.1 dB/cm, respectively. This is comparable to other ring resonator devices reported on similar SiN

platforms and presents a significant improvement in performance compared to Si based SWG metamaterial ring resonators. Uncladded ring resonators were also measured in an aqueous environment, exhibiting an Q_i and Q_L of 8400 and 5200, respectively, near 1540 nm wavelength. This showcases the SWG device's capabilities as a waveguide sensor, as well as its flexibility in operating with different top cladding materials of varying refractive index. These SWG metamaterial engineered devices have great potential for the development of advanced PICs, particularly for light amplification and evanescent field sensing applications, where high mode overlap with the local environment surrounding the waveguide is important. Based on these results, we expect that exploration of SWG metamaterials for other SiN integrated photonic components and devices will be a fruitful new research direction in integrated photonics.

Bibliography

- [1] G. T. Reed, W. R. Headley, and C. E. Jason Png, "Silicon photonics: the early years," in *Optoelectronic Integration on Silicon II* (J. A. Kubby and G. E. Jabbour, eds.), vol. 5730, pp. 1–18, International Society for Optics and Photonics, SPIE, 2005.
- [2] R. A. Soref, "The past, present, and future of silicon photonics," *IEEE Journal of Selected Topics in Quantum Electronics*, vol. 12, no. 6, pp. 1678–1687, 2006.
- [3] D. Thomson, A. Zilkie, J. E. Bowers, T. Komljenovic, G. T. Reed, L. Vivien, D. Marris-Morini, E. Cassan, L. Viroth, J.-M. Fédéli, J.-M. Hartmann, J. H. Schmid, D.-X. Xu, F. Boeuf, P. O'Brien, G. Z. Mashanovich, and M. Nedeljkovic, "Roadmap on silicon photonics," *Journal of Optics*, vol. 18, no. 7, p. 073003, 2016.
- [4] L. Chrostowski, H. Shoman, M. Hammood, H. Yun, J. Jhoja, E. Luan, S. Lin, A. Mistry, D. Witt, N. A. F. Jaeger, S. Shekhar, H. Jayatilleka, P. Jean, S. B.-d. Villers, J. Cauchon, W. Shi, C. Horvath, J. N. Westwood-Bachman, K. Setzer, M. Aktary, N. S. Patrick, R. J. Bojko, A. Khavasi, X. Wang, T. Ferreira de Lima, A. N. Tait, P. R. Prucnal, D. E. Hagan, D. Stevanovic, and A. P. Knights, "Silicon photonic circuit design using rapid prototyping foundry process design kits," *IEEE Journal of Selected Topics in Quantum Electronics*, vol. 25, no. 5, pp. 1–26, 2019.
- [5] S. Y. Siew, B. Li, F. Gao, H. Y. Zheng, W. Zhang, P. Guo, S. W. Xie, A. Song, B. Dong, L. W. Luo, C. Li, X. Luo, and G.-Q. Lo, "Review of silicon photonics technology and platform development," *Journal of Lightwave Technology*, vol. 39, no. 13, pp. 4374–4389, 2021.

- [6] C. G. H. Roeloffzen, M. Hoekman, E. J. Klein, L. S. Wevers, R. B. Timens, D. Marchenko, D. Geskus, R. Dekker, A. Alippi, R. Grootjans, A. van Rees, R. M. Oldenbeuving, J. P. Epping, R. G. Heideman, K. Wörhoff, A. Leinse, D. Geuzebroek, E. Schreuder, P. W. L. van Dijk, I. Visscher, C. Taddei, Y. Fan, C. Taballione, Y. Liu, D. Marpaung, L. Zhuang, M. Benelajla, and K.-J. Boller, “Low-loss Si₃N₄ TriPleX optical waveguides: Technology and applications overview,” *IEEE Journal of Selected Topics in Quantum Electronics*, vol. 24, no. 4, pp. 1–21, 2018.
- [7] P. Muñoz, P. W. L. van Dijk, D. Geuzebroek, M. Geiselmann, C. Domínguez, A. Stassen, J. D. Doménech, M. Zervas, A. Leinse, C. G. H. Roeloffzen, B. Gargallo, R. Baños, J. Fernández, G. M. Cabanes, L. A. Bru, and D. Pastor, “Foundry developments toward silicon nitride photonics from visible to the mid-infrared,” *IEEE Journal of Selected Topics in Quantum Electronics*, vol. 25, no. 5, pp. 1–13, 2019.
- [8] R. Baets, A. Z. Subramanian, S. Clemmen, B. Kuyken, P. Bienstman, N. Le Thomas, G. Roelkens, D. Van Thourhout, P. Helin, and S. Severi, “Silicon photonics: Silicon nitride versus silicon-on-insulator,” in *2016 Optical Fiber Communications Conference and Exhibition (OFC)*, pp. 1–3, 2016.
- [9] P. Muñoz, G. Micó, L. A. Bru, D. Pastor, D. Pérez, J. D. Doménech, J. Fernández, R. Baños, B. Gargallo, R. Alemany, A. M. Sánchez, J. M. Cirera, R. Mas, and C. Domínguez, “Silicon nitride photonic integration platforms for visible, near-infrared and mid-infrared applications,” *Sensors*, vol. 17, no. 9, p. 2088, 2017.
- [10] J. F. Bauters, M. J. R. Heck, D. John, D. Dai, M.-C. Tien, J. S. Barton, A. Leinse, R. G. Heideman, D. J. Blumenthal, and J. E. Bowers, “Ultra-low-loss high-aspect-ratio Si₃N₄ waveguides,” *Optics Express*, vol. 19, no. 4, pp. 3163–3174, 2011.
- [11] M. Belt, T. Huffman, M. L. Davenport, W. Li, J. S. Barton, and D. J. Blumenthal, “Arrayed narrow linewidth erbium-doped waveguide-distributed feedback lasers on an ultra-low-loss silicon-nitride platform,” *Optics Letters*, vol. 38, no. 22, pp. 4825–4828, 2013.
- [12] Purnawirman, J. Sun, T. N. Adam, G. Leake, D. Coolbaugh, J. D. B. Bradley, E. S. Hosseini, and M. R. Watts, “C- and L-band erbium-doped waveguide lasers with wafer-scale silicon nitride cavities,” *Optics Letters*, vol. 38, no. 11, pp. 1760–1762, 2013.

- [13] N. Li, E. S. Magden, Z. Su, N. Singh, A. Ruocco, M. Xin, M. Byrd, P. T. Callahan, J. D. B. Bradley, C. Baiocco, D. Vermeulen, and M. R. Watts, “Broadband 2- μm emission on silicon chips: monolithically integrated Holmium lasers,” *Optics Express*, vol. 26, no. 3, pp. 2220–2230, 2018.
- [14] J. Rönn, W. Zhang, A. Autere, X. Leroux, L. Pakarinen, C. Alonso-Ramos, A. Säynätjoki, H. Lipsanen, L. Vivien, E. Cassan, and Z. Sun, “Ultra-high on-chip optical gain in erbium-based hybrid slot waveguides,” *Nature Communications*, vol. 10, p. 432, 2019.
- [15] N. Li, M. Xin, Z. Su, E. S. Magden, N. Singh, J. Notaros, E. Timurdogan, P. Purnawirman, J. D. B. Bradley, and M. R. Watts, “A silicon photonic data link with a monolithic erbium-doped laser,” *Scientific Reports*, vol. 10, p. 1114, 2020.
- [16] K. Mirabbas Kiani, H. C. Frankis, H. M. Mbonde, R. Mateman, A. Leinse, A. P. Knights, and J. D. B. Bradley, “Thulium-doped tellurium oxide waveguide amplifier with 7.6 dB net gain on a silicon nitride chip,” *Optics Letters*, vol. 44, no. 23, pp. 5788–5791, 2019.
- [17] H. C. Frankis, H. M. Mbonde, D. B. Bonneville, C. Zhang, R. Mateman, A. Leinse, and J. D. B. Bradley, “Erbium-doped TeO_2 -coated Si_3N_4 waveguide amplifiers with 5 dB net gain,” *Photonics Research*, vol. 8, no. 2, pp. 127–134, 2020.
- [18] K. Mirabbas Kiani, H. C. Frankis, R. Mateman, A. Leinse, A. P. Knights, and J. D. B. Bradley, “Thulium-doped tellurium oxide microring lasers integrated on a low-loss silicon nitride platform,” *Optical Materials Express*, vol. 11, no. 11, pp. 3656–3665, 2021.
- [19] R. Heideman, M. Hoekman, and E. Schreuder, “TriPleX-based integrated optical ring resonators for lab-on-a-chip and environmental detection,” *IEEE Journal of Selected Topics in Quantum Electronics*, vol. 18, no. 5, pp. 1583–1596, 2012.
- [20] G. A. J. Besselink, R. G. Heideman, E. Schreuder, L. S. Wevers, F. Falke, and H. H. Van den Vlekkert, “Performance of arrayed microring resonator sensors with the TriPleX platform,” *Journal of Biosensors and Bioelectronics*, vol. 7, no. 2, p. 1000209, 2016.
- [21] P. Cheben, D.-X. Xu, S. Janz, and A. Densmore, “Subwavelength waveguide grating for mode conversion and light coupling in integrated optics,” *Optics Express*, vol. 14, no. 11, pp. 4695–4702, 2006.

- [22] P. Cheben, P. J. Bock, J. H. Schmid, J. Lapointe, S. Janz, D.-X. Xu, A. Densmore, A. Delâge, B. Lamontagne, and T. J. Hall, “Refractive index engineering with subwavelength gratings for efficient microphotonic couplers and planar waveguide multiplexers,” *Optics Letters*, vol. 35, no. 15, pp. 2526–2528, 2010.
- [23] P. Cheben, R. Halir, J. H. Schmid, H. A. Atwater, and D. R. Smith, “Subwavelength integrated photonics,” *Nature*, vol. 560, pp. 565–572, 2018.
- [24] R. Halir, A. Ortega-Moñux, D. Benedikovic, G. Z. Mashanovich, J. G. Wangüemert-Pérez, J. H. Schmid, Í. Molina-Fernández, and P. Cheben, “Subwavelength-grating metamaterial structures for silicon photonic devices,” *Proceedings of the IEEE*, vol. 106, no. 12, pp. 2144–2157, 2018.
- [25] J. M. Luque-González, A. Sánchez-Postigo, A. Hadij-ElHouati, A. Ortega-Moñux, J. G. Wangüemert-Pérez, J. H. Schmid, P. Cheben, Í. Molina-Fernández, and R. Halir, “A review of silicon subwavelength gratings: building break-through devices with anisotropic metamaterials,” *Nanophotonics*, vol. 10, no. 11, pp. 2765–2797, 2021.
- [26] J. G. Wangüemert-Pérez, P. Cheben, A. Ortega-Moñux, C. Alonso-Ramos, D. Pérez-Galacho, R. Halir, Í. Molina-Fernández, D.-X. Xu, and J. H. Schmid, “Evanescent field waveguide sensing with subwavelength grating structures in silicon-on-insulator,” *Optics Letters*, vol. 39, no. 15, pp. 4442–4445, 2014.
- [27] J. G. Wangüemert-Pérez, A. Hadij-ElHouati, A. Sánchez-Postigo, J. Leuermann, D.-X. Xu, P. Cheben, A. Ortega-Moñux, R. Halir, and Í. Molina-Fernández, “Subwavelength structures for silicon photonics biosensing,” *Optics & Laser Technology*, vol. 109, pp. 437–448, 2019.
- [28] C. M. Naraine, J. W. Miller, H. C. Frankis, D. E. Hagan, P. Mascher, J. H. Schmid, P. Cheben, A. P. Knights, and J. D. B. Bradley, “Subwavelength grating metamaterial waveguides functionalized with tellurium oxide cladding,” *Optics Express*, vol. 28, no. 12, pp. 18538–18547, 2020.
- [29] “Silicon nitride resources, Applied Nanotools Inc., https://www.appliednt.com/nanosoi/sys/resources/rules_nitride/, (accessed: 01.07.2022).”
- [30] “Product overview, Ansys Lumerical, <https://www.lumerical.com/products/>, (accessed: 01.07.2022).”

- [31] J. T. Robinson, K. Preston, O. Painter, and M. Lipson, “First-principle derivation of gain in high-index-contrast waveguides,” *Optics Express*, vol. 16, no. 21, pp. 16659–16669, 2008.
- [32] K. Mirabbas Kiani, H. C. Frankis, C. M. Naraine, D. B. Bonneville, A. P. Knights, and J. D. B. Bradley, “Lasing in a hybrid rare-earth silicon microdisk,” *Laser & Photonics Reviews*, vol. 16, no. 1, p. 2100348, 2022.
- [33] P. Cheben, J. H. Schmid, S. Wang, D.-X. Xu, M. Vachon, S. Janz, J. Lapointe, Y. Painchaud, and M.-J. Picard, “Broadband polarization independent nanophotonic coupler for silicon waveguides with ultra-high efficiency,” *Optics Express*, vol. 23, no. 17, pp. 22553–22563, 2015.
- [34] K. Luke, Y. Okawachi, M. R. E. Lamont, A. L. Gaeta, and M. Lipson, “Broadband mid-infrared frequency comb generation in a Si₃N₄ microresonator,” *Optics Letters*, vol. 40, no. 21, pp. 4823–4826, 2015.
- [35] B. E. Little, S. T. Chu, H. A. Haus, J. Foresi, and J.-P. Laine, “Microring resonator channel dropping filters,” *Journal of Lightwave Technology*, vol. 15, no. 6, pp. 998–1005, 1997.
- [36] H. C. Frankis, K. Mirabbas Kiani, D. Su, R. Mateman, A. Leinse, and J. D. B. Bradley, “High-*Q* tellurium-oxide-coated silicon nitride microring resonators,” *Optics Letters*, vol. 44, no. 1, pp. 118–121, 2019.
- [37] M. Soltani, *Novel Integrated Silicon Nanophotonic Structures using Ultra-high Q Resonators*. PhD thesis, Georgia Institute of Technology, 2009.
- [38] P. Rabiei, W. H. Steier, C. Zhang, and L. R. Dalton, “Polymer micro-ring filters and modulators,” *Journal of Lightwave Technology*, vol. 20, no. 11, pp. 1968–1975, 2002.
- [39] Z. Wang, X. Xu, D. Fan, Y. Wang, and R. T. Chen, “High quality factor subwavelength grating waveguide micro-ring resonator based on trapezoidal silicon pillars,” *Optics Letters*, vol. 41, no. 14, pp. 3375–3378, 2016.
- [40] P. Cheben, J. H. Schmid, R. Halir, J. M. Luque-González, J. G. Wangüemert-Pérez, D. Melati, and C. Alonso-Ramos, “Recent advances in metamaterial integrated photonics,” *Advances in Optics and Photonics*, vol. 15, no. 4, pp. 1033–1105, 2023.

- [41] L. S. Puumala, S. M. Grist, K. Wickremasinghe, M. A. Al-Qadasi, S. J. Chowdhury, Y. Liu, M. Mitchell, L. Chrostowski, S. Shekhar, and K. C. Cheung, “An optimization framework for silicon photonic evanescent-field biosensors using sub-wavelength gratings,” *Biosensors*, vol. 12, no. 10, p. 840, 2022.

Chapter 5

Towards a subwavelength grating metamaterial waveguide amplifier: silicon nitride coated in atomic layer deposited alumina/erbium films

This chapter describes the design, fabrication, and characterization processes for a new type of silicon nitride (SiN) waveguide amplifier engineered using subwavelength grating (SWG) metamaterials and functionalized by erbium (Er)-doped aluminum oxide (Al_2O_3) thin films grown via atomic layer deposition (ALD). As silicon photonics (SiP) technology expands into application spaces such as high-speed optical communications, satellite communications, quantum computing, sensing, artificial intelligence and light detection and ranging (LiDAR), SiN is evolving in parallel as an outstanding complementary material to silicon (Si) for integrated photonics. With benefits such as complementary-metal-oxide-semiconductor (CMOS) manufacturing compatibility, superior fabrication tolerance, visible (VIS) to near-infrared (NIR) transparency, negligible two photon absorption (TPA), and ultralow waveguide loss, SiN has gained significant research attention as an integrated photonics platform for developing efficient on-chip light sources

and nonlinear optical devices. In particular, amplifiers and lasers grounded on SiN photonic integrated circuits (PICs) and incorporating post-process rare-earth (RE)-doped gain media have been thoroughly demonstrated, exhibiting advantages over their III-V counterparts such as high saturated output power, broadband gain, minor thermal drift, narrow intrinsic linewidth, and low noise and lasing threshold. Al_2O_3 is a well-established dielectric material for integrated optics with wide optical transparency, stable chemical and mechanical properties, and various deposition methods that are compatible as back-end-of-line (BEOL) CMOS processes. It serves as an excellent amorphous host for RE-ion dopants with a low thermo-optic coefficient and limited phonon energies. On SiN waveguides, the relatively high refractive index of RE-doped Al_2O_3 provides a moderate index contrast with the buried oxide (BOX) insulator for a compact footprint and allows for significant modal overlap with the RE ions in the cladding that leads to higher gain. Precise control over the wavevectors and field distribution of the propagating modes in such a device is important to obtain optimal performance. This has been successfully demonstrated by implementing SWG metamaterials in various SiP devices and in our recent publication on SiN waveguides. While unprecedented performance has been presented in many passive integrated optical devices, SWG metamaterial engineering was relatively absent from active integrated photonic devices, such as on-chip optical amplifiers and lasers.

Here, we propose and experimentally demonstrate signal enhancement in SWG metamaterial waveguides fabricated on a commercial SiN foundry platform and coated in an Er-doped Al_2O_3 cladding gain material. The waveguides are designed to have a large overlap ($>50\%$) between the Floquet-Bloch mode and the Er-doped Al_2O_3 gain medium, which is essential for light amplification applications and also beneficial for evanescent field sensing. The Er-doped Al_2O_3 material is grown inside a custom thermal atomic layer deposition (tALD) reactor by sequentially depositing monolayers of Al_2O_3 and erbium oxide (Er_2O_3) under self-limiting conditions for fine, pure, and highly uniform films that permeate the nanoscale spaces around the SiN gratings. Experimental characterization of our SiN SWG waveguides shows a low background propagation loss (~ 1.3 dB/cm) outside the Er absorption spectrum and an ~ 8.6 dB signal enhancement of 1533 nm wavelength light in a 0.64 cm long device subjected to 148 mW power from 1480 nm pump laser diodes. Compared to an equivalent wire waveguide fabricated on the same chip, the loss is equal, yet the signal enhancement is almost twofold due to the enhanced mode overlap factor with the gain material in the SWG waveguide. Internal net gain is not achieved, but methods for reducing the loss, such as re-design considerations and post-processing steps such as annealing, are discussed. We believe that

these results represent an important advancement for the development of SiN active devices assisted by SWG metamaterial engineering, which will service a wide range of applications leveraging the mature technology of integrated photonics.

The work presented in this chapter is part of a collaboration with the Emslie Group in the Department of Chemistry and Chemical Biology at McMaster University. The chapter contents comprise a manuscript in preparation by the authors and have been included in the thesis to showcase an experimental demonstration that represents the culmination of the concepts presented in all the previous thesis chapters. In particular, it combines the flexibility of SWG metamaterial-engineered SiN PICs with the power of high-index glass cladding materials doped with RE ions (primarily Er^{3+}) for the specific application of on-chip optical amplification. Section 5.1 introduces the background and motivation for the different subcomponents of our proposed amplifier, including SiN PICs, SWG metamaterial structures, and RE-based optical amplifiers and lasers. Section 5.2 reiterates the design process for developing waveguides with high mode overlap with the cladding gain material. Section 5.3 discloses the fabrication methods used to manufacture SiN-based SWG metamaterial waveguide devices and produce highly conformal Er-doped Al_2O_3 films using tALD. Section 5.4 describes the passive and active characterization steps and presents the experimental results for the fabricated SiN SWG metamaterial waveguides coated in the optically active hybrid $\text{Al}_2\text{O}_3/\text{Er}_2\text{O}_3$ films. Finally, Section 5.5 summarizes the chapter and emphasizes the potential of SWG metamaterials in SiN PICs for active and nonlinear optical applications.

Abstract

We propose and demonstrate SiN-based SWG metamaterial waveguides coated in hybrid $\text{Al}_2\text{O}_3/\text{Er}_2\text{O}_3$ thin films. The waveguides are designed to achieve up to 55% mode overlap between the Floquet-Bloch mode and the Er-doped top cladding material, which offers excellent potential for applications in light amplification and lasing. The waveguides are fabricated using a commercial SiN prototyping foundry process based on electron beam lithography (EBL) technology, enabling critical dimensions down to 100 nm. The cladding gain material is grown directly onto the SiN waveguides using a BEOL tALD process and periodic $\text{Al}_2\text{O}_3/\text{Er}_2\text{O}_3$ heterocycle approach, producing high purity thin films that uniformly fill the space around the grating segments where modal interaction is the greatest. Experimental characterization of the fabricated SWG devices reveals a background propagation loss as low as 1.3 dB/cm, which is comparable to wire waveguides fabricated on the same SiN platform and coated with the same gain medium. A

signal enhancement of ~ 8.6 dB at 1533 nm wavelength is demonstrated in a 0.64 cm long SWG waveguide when pumped by 1480 nm laser diodes with a total launched power of 148 mW. These results demonstrate an enhancement factor of ~ 3.8 dB over equivalent SiN wire waveguide test structures and illuminate the promise of SWG metamaterial waveguide structures for the next generation of active and nonlinear integrated photonic devices in SiN.

5.1 Introduction

SiP is an advanced modern technology driving the development of scalable, cost-effective, high-quality PICs due to its ability to leverage established microelectronics fabrication processes [1]. The promises and successes of SiP over recent decades have bred a healthy ecosystem among integrated device manufacturers, tech companies, academic institutions, and photonics startups and design houses, utilizing a fabless foundry model to inspire innovation of new integrated optical devices and microsystems [2; 3]. SiN is a complementary material for integrated optical devices that has developed in parallel to Si thanks to their shared mature fabrication methods [4; 5]. Unlike silicon-on-insulator (SOI), SiN has a moderate refractive index contrast with silicon dioxide (SiO_2 , $\Delta n \sim 0.5$) that relaxes susceptibility to fabrication error and reduces losses related to scattering, coupling, and birefringence [6]. Its large bandgap (~ 5 eV) enables optical transparency throughout the VIS and NIR spectra and produces negligible TPA losses that make it a beneficial core material for nonlinear optical devices [6]. Furthermore, foundries developing integrated photonic devices around the SiN material have varying structural arrangements, so the design parameters of SiN waveguides are much more flexible compared to standard SOI platforms [4; 7]. These benefits have made SiN an appealing material platform for applications such as free-space communications, biomedical and environmental sensing, imaging, spectroscopy, beam steering for LiDAR, quantum computing, and artificial intelligence [1; 2].

SWG metamaterials have become fundamental building blocks in integrated photonics because they offer greater design flexibility and unprecedented lithographic control over the electromagnetic field distribution throughout the chip [8]. Many silicon photonic components, such as waveguides, fiber-chip couplers, crossings, filters, switches, and multiplexers, have incorporated SWG metamaterials for improved device performance and capabilities such as ultrabroadband operation, low-loss response, and sophisticated management over polarization, anisotropy, and dispersion [9; 10; 11]. SWG metamaterial waveguides have lower effective index compared to their wire waveguide counterparts,

which results in relaxed modal confinement, a larger evanescent field, and enhanced interaction with the environment outside the waveguide core. This principle has been exploited in silicon photonic evanescent field sensors showcasing exceptional bulk and surface sensitivity metrics in a variety of sensing architectures and SWG waveguide topologies [11; 12; 13]. The same strategy can not only be applied to SWG sensors on other integrated photonic platforms [14; 15], but also to other applications that benefit from increased spatial mode distribution outside the waveguide, such as optical amplification [16]. We recently demonstrated SWG metamaterials ring resonators fabricated on a SiN foundry platform [17]. Compared to SOI, the implementation of SWG metamaterials in moderate index contrast SiN generates a larger mode overlap with the local environment surrounding the waveguide, which can lead to higher sensitivity in sensors and greater gain for optical amplifier and laser devices utilizing a cladding gain medium. This mode overlap can be further enhanced by replacing conventional top cladding materials, such as SiO₂, water, and air, with high refractive index ($n > 1.6$) glass materials [16].

Compact amplifiers and light sources are crucial components for compensating gain in optoelectronic integrated circuits and meeting power requirements for optical interconnects and in other SiP applications [2; 18]. Poor light emission directly in Si due to its indirect bandgap has been the greatest hurdle in making SiP the penultimate PIC platform [19; 20]. As a result, other methods for realizing light sources on silicon chips have been heavily investigated, including heterogeneous integration or epitaxial growth of III-V semiconductors, germanium (Ge) and Ge-tin alloys, stimulated Raman emission in Si, SiN-based parametric oscillators, and RE-doped thin films and gain media [21; 22; 23; 24; 25]. Among these, RE-doped materials have shown significant promise as gain media for advanced circuits on silicon with advantages such as high optical output power, low noise figures, strong thermal stability, narrow intrinsic linewidth, low lasing threshold, and broadband optical gain and lasing across various spectral regions [26; 27; 28]. A prime example of this is the recent demonstration of an ultralow-loss Er-doped Si₃N₄ waveguide amplifier enabled by high-energy ion implantation, which exhibited >145 mW on-chip output power and a measured noise figure of ~7 dB at a net gain of >20 dB [29]. To acquire gain in moderate or low confinement SiN waveguides (thickness $t_{\text{SiN}} < 0.4 \mu\text{m}$), RE-doped glasses are an appealing option due to their single-step, BEOL deposition process, which enables scalable, monolithic integration and a roadmap towards mass production of low-cost, high-volume on-chip light sources [27]. Al₂O₃ has been extensively explored for waveguiding and as an optically active material to monolithically integrate with silicon-based waveguides due to its

moderately high refractive index ($n \sim 1.65$, $\lambda = 1550$ nm), wide optical transparency, compatibility with RE ion dopants, low thermo-optic coefficient as a host medium, and strong chemical and mechanical stability [27; 30]. Various RE-doped Al_2O_3 amplifier and laser devices grown onto silicon chips and PICs using a reactive co-sputtering deposition have been extensively explored and demonstrated over the last two decades [31; 32; 33; 34; 35; 36; 37; 38; 39; 40; 41; 42; 43; 44]. Al_2O_3 grown via ALD is also of interest in this application space due to the self-limiting growth conditions of Al_2O_3 monolayers that produce pure films with excellent uniformity and low loss [45; 46; 47]. Er-doping can be incorporated into the ALD process by inserting Er cycles between the Al_2O_3 cycles to manufacture highly conformal gain media for on-chip amplifiers [48]. The resulting material is a hybrid $\text{Al}_2\text{O}_3/\text{Er}_2\text{O}_3$ thin film with atomic concentrations of the constituent materials that can be precisely controlled through the deposition parameters. ALD Er-doped Al_2O_3 has already been demonstrated as a gain medium in ridge waveguide amplifiers [48; 49] and hybrid SiN slot and strip waveguide amplifiers [50; 51]. Slot waveguides greatly benefit from the ALD growth process since the deposited material completely fills in the nanoscale gap between the SiN waveguide rails [52; 53]. This phenomenon can be exploited for SWG metamaterial waveguides requiring Al_2O_3 thin film claddings, which also feature nanovoid spaces between the waveguide grating segments.

Here, we discuss the design, fabrication, characterization, and results of SiN-based SWG metamaterial waveguides coated in ALD Al_2O_3 and hybrid $\text{Al}_2\text{O}_3/\text{Er}_2\text{O}_3$ thin films. Using photonic computer-aided design (CAD) simulation software tools from Ansys Lumerical, the waveguides are designed for maximum mode overlap with the cladding gain material (i.e., $\text{Al}_2\text{O}_3/\text{Er}_2\text{O}_3$) while maintaining reasonable footprint (i.e., bend radius) and mode effective index and area. The SiN waveguides are fabricated using a commercial SiN prototyping foundry process [54]. The ALD films are grown at a temperature of 250 °C in a custom-built ALD reactor using a tALD process that utilizes sequential pulses of de-ionized (DI) water and trimethylaluminium (TMA, i.e., AlMe_3) precursors for the Al_2O_3 films, and DI water and tris(methylcyclopentadienyl)erbium(III) ($(\text{CpMe})_3\text{Er}$) precursors for the Er_2O_3 layers within the $\text{Al}_2\text{O}_3/\text{Er}_2\text{O}_3$ films [55]. Measurements using a variable angle spectroscopic ellipsometer (VASE) and prism coupler system were performed on undoped and Er-doped Al_2O_3 planar waveguide samples deposited on Si and thermal SiO_2/Si substrates, respectively. The measured optical propagation loss in the undoped Al_2O_3 films range from 1.2 dB/cm ($\lambda = 518$ nm) to near lossless ($\lambda = 1550$ nm), and background losses as low as 0.25 dB/cm are reported in the 940-1000 nm wavelength range for the Er-doped Al_2O_3 films. The ALD Al_2O_3 -coated

SiN SWG metamaterial waveguides were characterized on an edge coupling lab setup and had a propagation loss of 2.5 ± 0.3 dB/cm and a coupling loss of 2.9 ± 0.1 dB/facet across the C- and L-bands via the cutback method [56]. Both strip/wire and SWG metamaterial waveguides coated in various hybrid ALD $\text{Al}_2\text{O}_3/\text{Er}_2\text{O}_3$ films exhibited background propagation losses as low as 1.3 dB/cm. The setup was later adjusted to incorporate two 1480 nm laser diodes as a bidirectional pump source so the $\text{Al}_2\text{O}_3/\text{Er}_2\text{O}_3$ -coated devices could be tested as waveguide amplifiers. Gain measurements showed maximum signal enhancements of 4.80 and 8.57 dB in wire and SWG metamaterial waveguides with the same waveguide length and $\text{Al}_2\text{O}_3/\text{Er}_2\text{O}_3$ films, respectively, highlighting the enhanced gain factor in the SWG waveguide caused by greater modal confinement with the gain material. However, similar background losses from Er absorption and waveguide scattering prevented internal net gain in all measured devices. Future steps include rapid-thermal annealing (RTA) of the waveguide samples to drive out excess organic contaminants leftover from precursor materials during deposition that can induce undesirable luminescence quenching and spontaneous emission. Other strategies for optimizing the waveguide design and film deposition process are also discussed. Expanding upon the works of other $\text{Al}_2\text{O}_3/\text{Er}_2\text{O}_3$ ALD on-chip amplifiers, these results show promise for monolithic integration of optically active ALD Al_2O_3 claddings on SiN waveguide optical amplifiers and lasers and provide many new avenues for exploring SWG metamaterials in integrated photonics waveguides.

5.2 Design

5.2.1 2D FDE simulations

A 2D finite difference eigenmode (FDE) solver was used to study the fundamental transverse electric (TE) mode profiles of various Al_2O_3 -clad SiN SWG metamaterial waveguide structures approximated using effective medium theory (EMT) [57]. Fig. 5.1(a) depicts a cross section of the simulated structure. A 400 nm SiN waveguide thickness (t_{wg}) and 4.5 μm SiO_2 BOX thickness (t_{BOX}) were predetermined by the foundry process [54]. The refractive indices of the relevant materials at 1550 nm wavelength are $n_{\text{SiN}} = 1.9974$ [54], $n_{\text{Al}_2\text{O}_3} = 1.637$ [47], $n_{\text{SiO}_2} = 1.444$ [10], and $n_{\text{Air}} = 1$. The variable parameters in the FDE simulations are the waveguide width (w_{wg}), SWG duty cycle (δ), and Al_2O_3 cladding thickness ($t_{\text{Al}_2\text{O}_3}$). w_{wg} and δ are adjustable within the SiN waveguide fabrication limits (i.e., the minimum feature size (MFS)) set by the foundry, which, in this case, is 120 nm. From EMT, δ and the refractive indices of the constituent materials of the SWG waveguide (i.e., $n_1 = n_{\text{SiN}}$ and $n_2 = n_{\text{Al}_2\text{O}_3}$) are responsible for determining

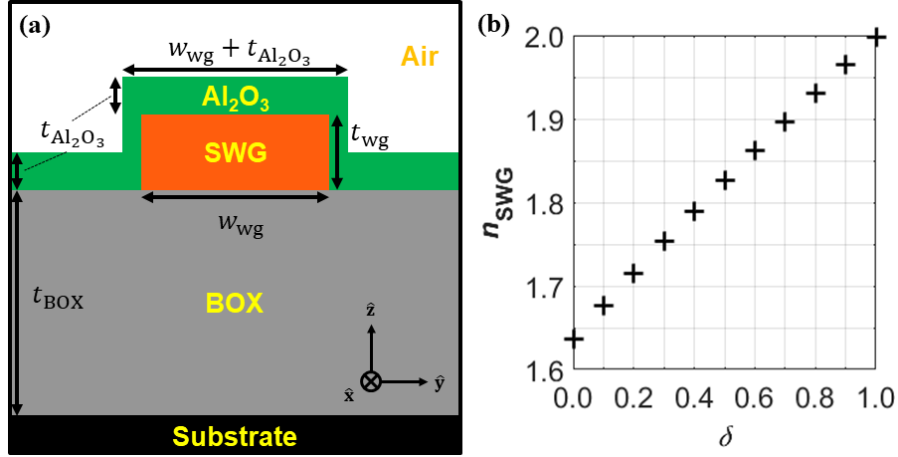


FIGURE 5.1: (a) Cross sectional diagram of FDE-simulated Al_2O_3 -coated SWG metamaterial waveguide approximated using EMT. (b) Approximated core refractive index of SWG waveguide with SiN core and Al_2O_3 cladding materials as a function of SWG duty cycle based on EMT calculation.

the SWG core refractive index (n_{SWG}). Fig. 5.1(b) summarizes the n_{SWG} values with respect to δ for these specific materials. The bounds of $t_{\text{Al}_2\text{O}_3}$ are determined by the limitations of the post-process ALD system. For our simulations, we chose 100 nm and 500 nm as the lower and upper limits for the Al_2O_3 cladding thickness, respectively. At least 100 nm is required to provide acceptable mode effective index and mode overlap factor results, and ALD film thicknesses above 500 nm become difficult to fabricate due to the excessive deposition time on the scale of days as well as imposed wear-and-tear that diminishes film quality and damages the ALD reactor. Explanation of the latter will be discussed in greater detail in Section 5.4.1.

Fig. 5.2 highlights the results of the FDE simulations using colour maps. Each row corresponds to a different result, including mode effective index (n_{eff}), group index (n_g), mode overlap with the Al_2O_3 cladding ($\gamma_{\text{Al}_2\text{O}_3}$), and mode confinement factor in the Al_2O_3 cladding ($\Gamma_{\text{Al}_2\text{O}_3}$), whereas each column represents a particular δ value for the SWG waveguide under investigation. For clarity, $\delta = 1$ is analogous to a conventional strip/wire waveguide. The colour maps exhibit the result value as a function of w_{wg} and $t_{\text{Al}_2\text{O}_3}$. w_{wg} values between 0.5 and 1.5 μm were simulated to account for large discrepancies in the core refractive index, depending on δ .

Two regions of each colour map are whited out. The bottom left region represents lossy modes with low n_{eff} (<1.47) suffering greatly from substrate leakage. The top

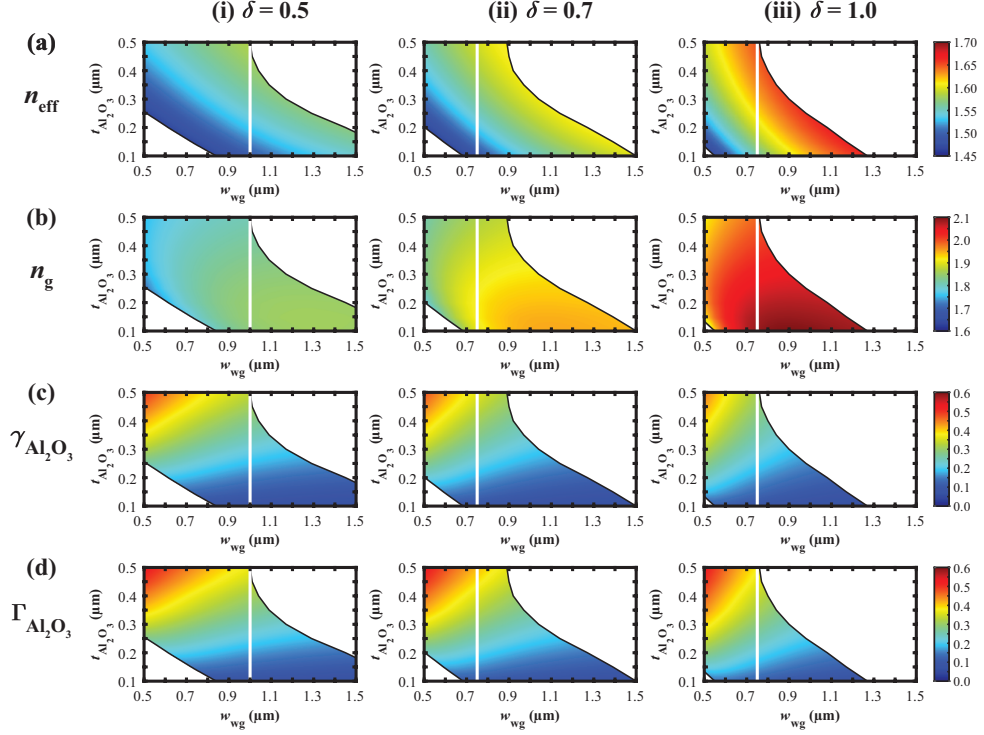


FIGURE 5.2: 2D FDE simulated (a) mode effective index (n_{eff}), (b) group index (n_g), (c) mode overlap with the Al_2O_3 cladding ($\gamma_{\text{Al}_2\text{O}_3}$), and (d) mode confinement factor in the Al_2O_3 cladding ($\Gamma_{\text{Al}_2\text{O}_3}$) for EMT-approximated SWG metamaterial waveguides with varying waveguide width (w_{wg}) and Al_2O_3 cladding thickness ($t_{\text{Al}_2\text{O}_3}$) and fixed duty cycles (δ) of (i) 0.5, (ii) 0.7, and (iii) 1.

right region features multimode waveguides outside the scope of this thesis. In the FDE simulation, a mode is supported by the waveguide if its effective index is greater than the slab mode effective index ($n_{\text{eff}}^{\text{slab}}$, i.e., simulated n_{eff} of the same structure in Fig. 5.1(a) but with no waveguide and no cladding ridge present). The boundary between the single mode and multimode waveguides is the single mode cutoff (SMC) condition, which indicates the w_{wg} value for each $t_{\text{Al}_2\text{O}_3}$ value where the first order TE mode (TE_{01}) effective index surpasses the $n_{\text{eff}}^{\text{slab}}$ threshold. Only waveguides in the coloured region between these two outer white regions are considered for our designs. The white vertical lines on the colour maps indicate the w_{wg} values that were selected for our designs. Specifically, $w_{\text{wg}} = 1 \mu\text{m}$ was used for SWG waveguides with $\delta = 0.5$ and $w_{\text{wg}} = 0.75 \mu\text{m}$ was used for the reference strip waveguide structures ($\delta = 1$). The chosen waveguides are single mode regardless of $t_{\text{Al}_2\text{O}_3}$. Their mode profiles with the

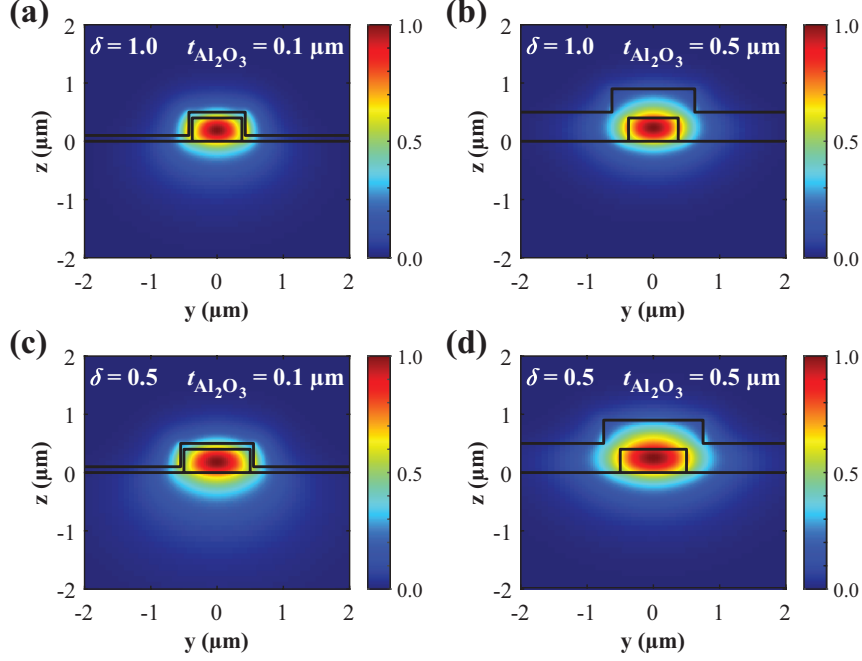


FIGURE 5.3: 2D FDE simulated TE mode profiles for selected strip waveguide with (a) 100 nm and (b) 500 nm Al_2O_3 cladding thickness, as well as selected SWG metamaterial waveguide with (c) 100 nm and (d) 500 nm Al_2O_3 cladding thickness. The core refractive index of the SWG waveguide with $\delta = 0.5$ is approximated using EMT.

minimum and maximum simulated $t_{\text{Al}_2\text{O}_3}$ values (i.e., 100 nm and 500 nm, respectively) are depicted in Fig. 5.3, and the simulation results are summarized in Table 5.1. Both waveguides with $t_{\text{Al}_2\text{O}_3} = 100$ nm are just above the n_{eff} cutoff (< 1.47) and have very low $\gamma_{\text{Al}_2\text{O}_3}$ metrics. This is because the thin cladding layer has such a small area that limits $\gamma_{\text{Al}_2\text{O}_3}$, and it does not provide much support for pulling the mode out of the BOX. This is more evident in the SWG waveguide, which has a much smaller n_{SWG} that makes it more susceptible to substrate leakage [58]. This prompts us to aim for a greater $t_{\text{Al}_2\text{O}_3}$ during fabrication, which will be discussed in more detail in Section 5.3. A lower n_{SWG} is also what generates greater $\gamma_{\text{Al}_2\text{O}_3}$ in SWG waveguides over conventional strip waveguides, particularly for higher $t_{\text{Al}_2\text{O}_3}$. However, for $t_{\text{Al}_2\text{O}_3} = 500$ nm, $\gamma_{\text{Al}_2\text{O}_3}$ is about the same between the two waveguide types. This is because the widths for each waveguide type were selected to push the single mode condition as far as possible. When w_{wg} is equivalent, the SWG waveguide has much greater mode overlap with the Al_2O_3 cladding (e.g., for $w_{\text{wg}} = 0.75$ μm , $\gamma_{\text{Al}_2\text{O}_3} = 0.4$ for the SWG waveguide while $\gamma_{\text{Al}_2\text{O}_3} =$

TABLE 5.1: 2D FDE simulation results for selected SiN-Al₂O₃ waveguides designs shown in Fig. 5.3.

Parameter / result	Waveguide type			
	Strip/wire		SWG*	
Waveguide width (μm)	0.75		1	
Duty cycle	1		0.5	
Al ₂ O ₃ thickness (μm)	0.1	0.5	0.1	0.5
Effective index	1.555	1.65	1.496	1.586
Group index	2.088	1.986	1.841	1.811
Al ₂ O ₃ mode overlap	0.095	0.316	0.077	0.337
Al ₂ O ₃ confinement factor	0.121	0.382	0.086	0.372

* EMT approximated.

0.316 for the strip waveguide). A 0.75 μm width for the SWG waveguide could have been used in the SWG waveguide design to achieve greater $\gamma_{\text{Al}_2\text{O}_3}$, but it also generates lower n_{eff} , thus increasing loss caused by substrate leakage and bend radiation. Because this is a novel waveguide device on an uncommon hybrid material platform, we opted for safe operating parameters that would produce realistic initial results that can be improved upon in a future design for a more specific application. It is also worth noting that these initial overlap values are just estimates based off EMT. Generally, 3D finite-difference-time-domain (FDTD) simulations reveal higher overlap values for SWG waveguides since the mode field in the gap between the gratings is considered in the overlap calculation performed on the Floquet-Bloch mode [17]. This will be disseminated in the next section.

5.2.2 3D FDTD simulations

A 3D FDTD solver was used to calculate the Floquet-Bloch modes, dispersion relations and corresponding effective and group indices of the SWG waveguides with parameters obtained from the FDE simulations. Because these simulations acquire optical information across a broad spectrum, it is imperative to consider the full dispersion profile for each material involved in the waveguide structure. Fig. 5.4 highlights the refractive and group indices for the low pressure chemical vapour deposition (LPCVD) SiN waveguide, the ALD Al₂O₃ cladding, and the SiO₂ BOX, which are imported into the FDTD model. The refractive index material data used for the Al₂O₃ cladding is obtained from the VASE measurements of film AE03 (see Section 5.4.1). The group index of each

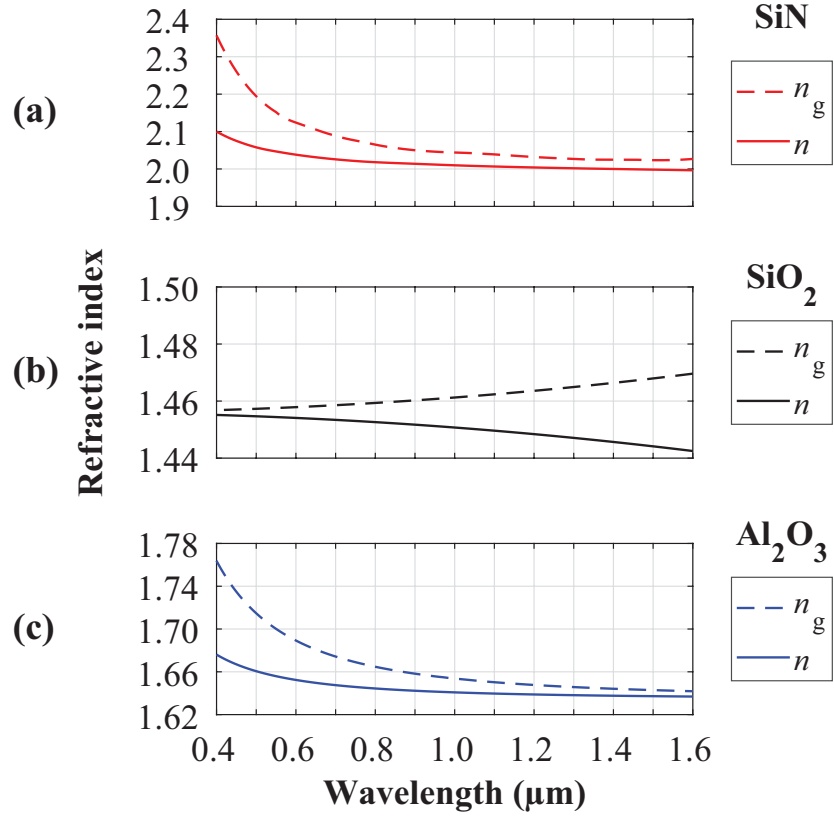


FIGURE 5.4: Refractive and group indices of (a) SiN, (b) SiO₂, and (c) Al₂O₃ materials used in FDTD simulations.

material is acquired using the following equation:

$$n_g(\lambda) = n(\lambda) - \lambda \frac{dn(\lambda)}{d\lambda}. \quad (5.1)$$

Fig. 5.5 shows a full 3D model of the structure simulated in FDTD. The simulation environment is fixed around a single unit grating cell with a length of Λ and Bloch boundary conditions along the propagation axis. This emulates an infinitely repeating 1-D photonic crystal, like the one shown in Fig. 5.5, by re-injecting the fields incident on the output boundary back into the simulation region via the input boundary. Perfectly matched layer (PML) boundaries are applied along the transverse edges of the simulation window to absorb and record evanescent fields that contribute to radiation loss. The same simulation setup, procedure and analysis described in [59] was used to obtain the

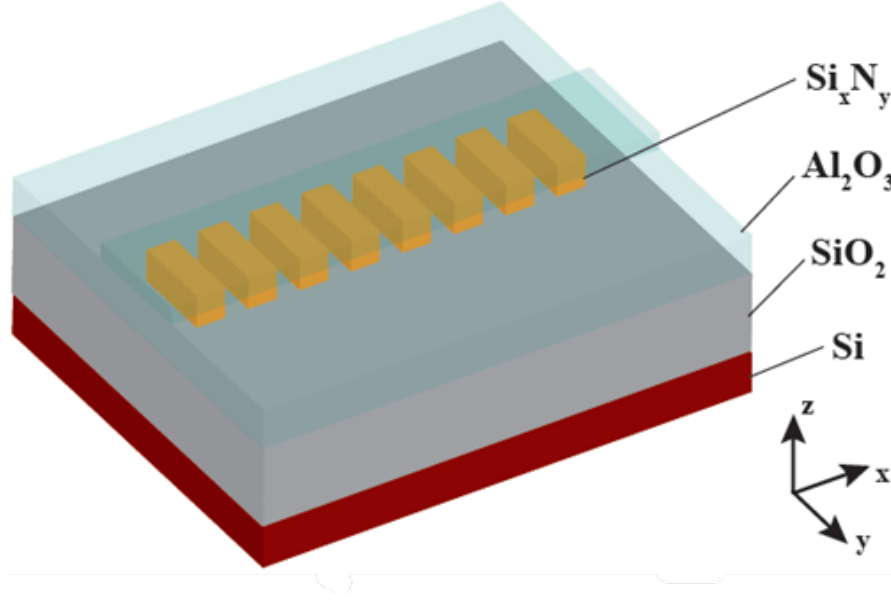


FIGURE 5.5: 3D model of Al_2O_3 -coated SiN SWG metamaterial waveguide structure simulated in FDTD.

first (lowest) order photonic band for our SWG metamaterial waveguides, which are plotted in Fig. 5.6(a). The SWG waveguide parameters collected from the 2D FDE simulation are used, along with two different grating periods ($\Lambda = 400$ nm and 440 nm) and three different Al_2O_3 cladding thicknesses ($t_{\text{Al}_2\text{O}_3} = 100$ nm, 300 nm, and 500 nm). The dispersion relations are expressed in terms of free space wavelength for better comparison with the corresponding effective and group index results (Fig. 5.6(b-c)) and the experimental results, which will be discussed in a later section. Effective and group indices are calculated such that:

$$n_{\text{eff}} = \frac{c}{v_p} = \frac{c}{\omega/k}, \quad (5.2)$$

$$n_g = \frac{c}{v_g} = \frac{c}{d\omega/dk}. \quad (5.3)$$

The dispersion relations reveal information about the operating regimes of the device and where they are located along the electromagnetic (EM) spectrum. Each band behaves like a regular homogeneous waveguide in the deep subwavelength regime where the slope is steeper. As k increases closer toward the band edge ($k = \pi/\Lambda$), the bands begin to flatten, causing a rapid decrease (increase) in the group velocity (index) that results in slow light behaviour [60; 61]. Wavelengths below the band edge wavelength ($\lambda_{\text{BE}} =$

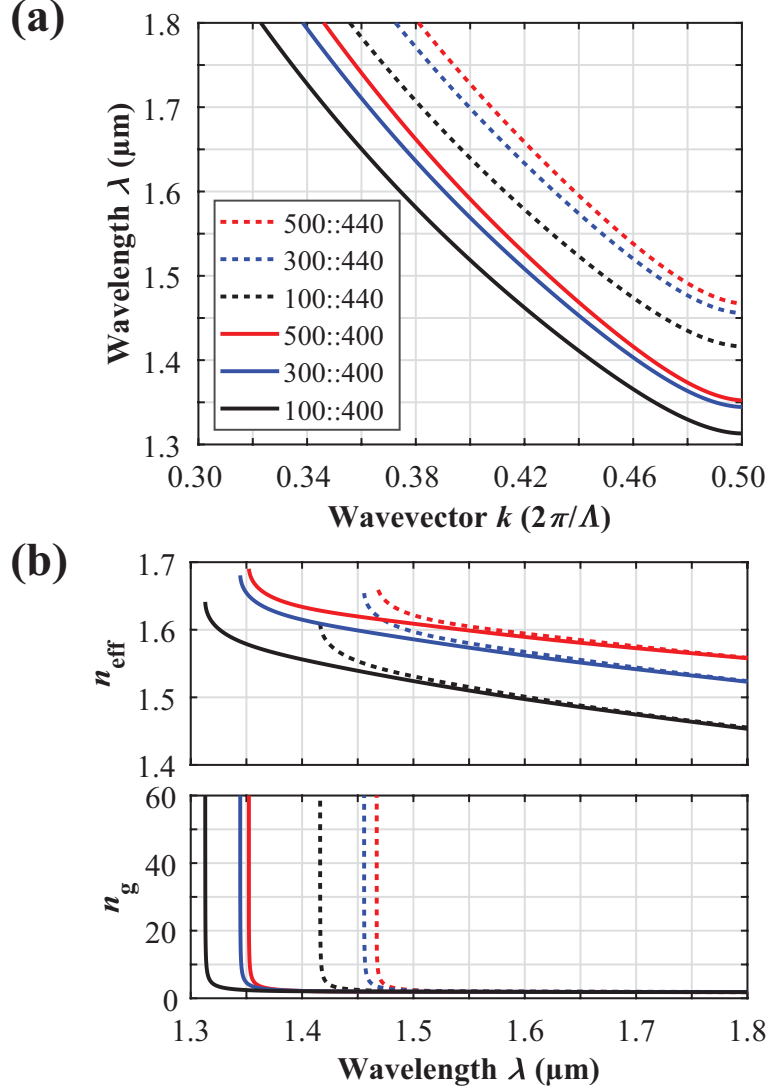


FIGURE 5.6: 3D FDTD simulated (a) dispersion relation and (b) corresponding effective (top) and group (bottom) refractive indices for Al_2O_3 -coated SiN SWG metamaterial waveguide structure. Legend values in (a) indicate Al_2O_3 cladding thickness ($t_{\text{Al}_2\text{O}_3}$) on left and grating period (Λ) on right, both in units of nm.

$\lambda(k = \pi/\Lambda)$) exist in the photonic bandgap, where the Bragg condition is fulfilled [8]. Light in this spectral regime recognize the discontinuities in the alternating media, which prohibit forward propagating modes. From Fig. 5.6(a), redshifting of λ_{BE} is observed as both Λ and $t_{\text{Al}_2\text{O}_3}$ increase. Changes in Λ cause a more significant shift in λ_{BE} due to their proportional relationship in the Bragg condition. $t_{\text{Al}_2\text{O}_3}$ only has a small effect on

increasing n_{eff} to cause changes in λ_{BE} . All simulated waveguides feature subwavelength operation at 1550 nm wavelength. $\Lambda = 400$ nm was selected for the primary waveguide design to enable deep subwavelength mode propagation across the C-band. $\Lambda = 440$ nm was selected for a secondary waveguide design focused on enabling slow light behaviour of the 1477 nm pump source wavelength used to excite Er^{3+} ions implanted in the Al_2O_3 film. This phenomenon enhances light-matter interaction, which can help improve gain metrics [62]. Fig. 5.6(a) shows that $\lambda_{\text{BE}} \sim 1467$ nm when $t_{\text{Al}_2\text{O}_3} = 500$ nm. Further testing and optimization could be performed to pinpoint the exact $t_{\text{Al}_2\text{O}_3}$ value required to place λ_{BE} on the 1477 nm pump source wavelength and calculate the slow light factor based on n_g . However, the slow light region is very hard to pinpoint due to its narrow bandwidth (e.g., a few nm where $n_g > 10$), the nm-scale uncertainty of the λ_{BE} calculation, and the high sensitivity to fabrication imperfections.

TABLE 5.2: 3D FDTD results for simulated Al_2O_3 -coated SiN SWG metamaterial waveguide structures.

$t_{\text{Al}_2\text{O}_3}$ (μm)	0.1	0.1	0.3	0.3	0.5	0.5
Λ (μm)	0.4	0.44	0.4	0.44	0.4	0.44
λ_{BE} (nm)	1313.15	1416.45	1344.66	1456.01	1352.55	1467.13
n_{eff}	1.51	1.515	1.574	1.58	1.599	1.605
n_g	1.923	1.974	1.946	2.007	1.904	1.974
$\gamma_{\text{Al}_2\text{O}_3}$	0.3	0.299	0.454	0.426	0.55	0.504
$\Gamma_{\text{Al}_2\text{O}_3}$	0.352	0.361	0.54	0.522	0.639	0.607
Fig 5.7	a)	b)	c)	d)	e)	f)

The Floquet-Bloch mode profiles of each FDTD simulated device at 1550 nm wavelength are illustrated in Fig. 5.7. Table 5.2 summarizes the results of all the FDTD simulation results, including the mode overlap with the Al_2O_3 cladding ($\gamma_{\text{Al}_2\text{O}_3}$) and the Al_2O_3 confinement factor ($\Gamma_{\text{Al}_2\text{O}_3}$), which are calculated such that [50]:

$$\Gamma_{\text{Al}_2\text{O}_3} = \frac{n_{\text{eff}}^g}{n_{\text{Al}_2\text{O}_3}^g} \gamma_{\text{Al}_2\text{O}_3} = \frac{n_{\text{eff}}^g}{n_{\text{Al}_2\text{O}_3}^g} \frac{\iiint_{\text{Al}_2\text{O}_3} n_{\text{Al}_2\text{O}_3} (2n_{\text{Al}_2\text{O}_3}^g - n_{\text{Al}_2\text{O}_3}) |\mathbf{E}|^2 dx dy dz}{\iint_{\infty} n (2n^g - n) |\mathbf{E}|^2 dx dy dz}, \quad (5.4)$$

where $n_{\text{Al}_2\text{O}_3}$ and n are the refractive index of the Al_2O_3 and the material located at the corresponding Cartesian coordinates, respectively, and n_{eff}^g , $n_{\text{Al}_2\text{O}_3}^g$, and n^g are the group indices of the effective waveguide mode, the Al_2O_3 material, and the material located at the corresponding Cartesian coordinates, respectively. This expression is an extension of Eq. 1.3 and Eq. 1.4, originally derived for high-index-contrast waveguides [63], but with consideration of the material dispersion, and treating Al_2O_3 as the active medium. The maximum overlap values obtained from the simulations were $\gamma_{\text{Al}_2\text{O}_3} = 0.550$ and

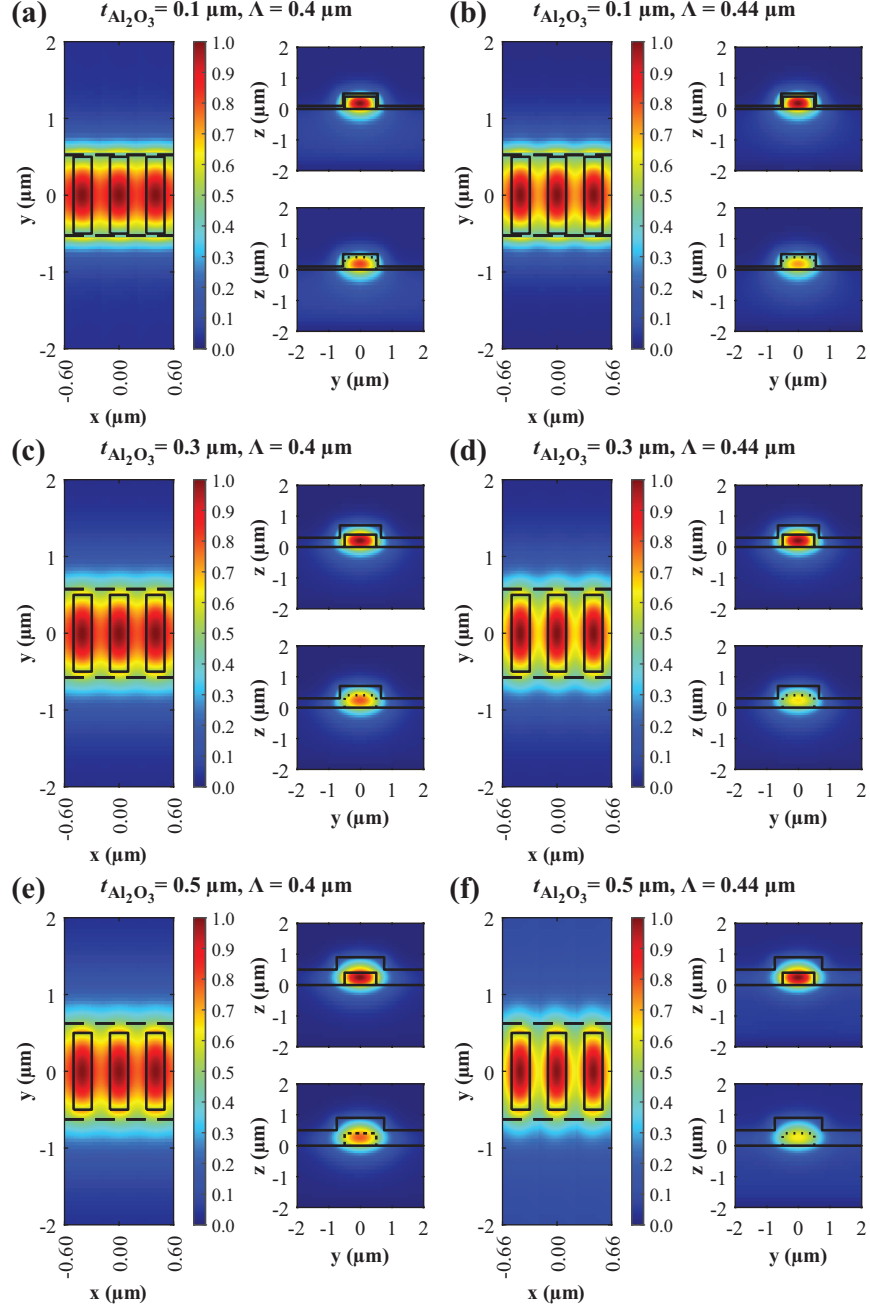


FIGURE 5.7: 3D FDTD simulated Floquet-Bloch mode propagation through the Al_2O_3 -coated SiN SWG metamaterial waveguide (left) and corresponding TE mode profiles across the SiN segments (top right) and within the gap between the SiN segments (bottom right) for waveguides with different simulated $t_{\text{Al}_2\text{O}_3}$ and Λ values.

$\Gamma_{\text{Al}_2\text{O}_3} = 0.639$ in the waveguide with $\Lambda = 400$ nm and $t_{\text{Al}_2\text{O}_3} = 500$ nm. Comparing the Floquet-Bloch mode profiles with the same $t_{\text{Al}_2\text{O}_3}$ but different Λ (e.g., Fig. 5.7(e-f)), the lower grating period increases the index homogenization effect through the waveguide, resulting in greater modal distribution across the gaps between the grating segments filled with Al_2O_3 cladding material. This reveals that $\gamma_{\text{Al}_2\text{O}_3}$ can be enhanced not only by increasing $t_{\text{Al}_2\text{O}_3}$, but also by decreasing Λ . This effect is less applicable for lower $t_{\text{Al}_2\text{O}_3}$ where the cladding does not fill the entire gap, such as $t_{\text{Al}_2\text{O}_3} = 100$ nm in Fig. 5.7(a-b), where $\gamma_{\text{Al}_2\text{O}_3}$ for each mode are almost identical. The mode overlap results are also much higher than those obtained from the 2D FDE simulation ($\gamma_{\text{Al}_2\text{O}_3} = 0.337$ and $\Gamma_{\text{Al}_2\text{O}_3} = 0.372$ for a waveguide with $t_{\text{Al}_2\text{O}_3} = 500$ nm), thanks to the inclusion of the mode field between the grating segments that is disregarded in the numerator of the 2D overlap integral calculation. This stresses the importance of 3D FDTD simulations for SWG metamaterial waveguides designed to optimize the mode overlap with the environment surrounding the core waveguide material.

5.3 Fabrication

5.3.1 SiN waveguides

Our SWG metamaterial waveguides were fabricated using the commercial SiN platform from Applied Nanotools Inc. (ANT) [54]. The platform features a 400 nm-thick LPCVD SiN device layer ($n \sim 2$) on a 4.5 μm -thick BOX. Direct-write EBL was used to etch out the waveguide structures with an MFS of ~ 120 nm. The fabrication process involves minimal risk of stress-induced film cracking and promises moderate confinement, single mode waveguides with losses in the NIR spectrum that are competitive with SiN devices produced by other integrated photonics foundries [7].

Fig. 5.8 shows the fabricated waveguides in a spiral topology, which were used to assess the propagation loss using the cutback method. To reduce the device footprint, the half-circle bends in the center section of the spiral design were composed of a wire waveguide with 0.75 μm width, which has a much lower minimum bend radius over the selected SWG waveguide design (from FDE simulation: 180 μm vs. 400 μm , respectively, for 1 μm Al_2O_3 cladding thickness and TE polarization). The smallest bend radii used in the spiral circuit are 250 μm and 515 μm for the chosen wire and SWG waveguides, respectively. This wire center section was connected to the rest of the SWG spiral using a 100- μm long SWG-wire mode transformer on each end. The wire bridge width, SWG segment width and grating period were linearly chirped through the mode

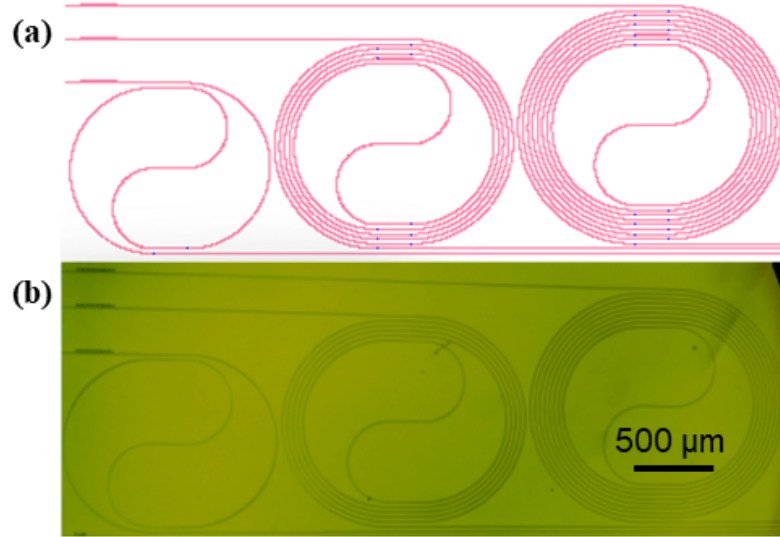


FIGURE 5.8: (a) Mask layout schematic and (b) corresponding optical microscope image of fabricated Al_2O_3 -coated SiN SWG meta-material waveguides in a spiral configuration with varying lengths.

transformer to alleviate unwanted Fabry-Perot resonances in the wavelength range of interest. A grating segment length ($\delta\Lambda$) was fixed at 150 nm through the transformer and a minimum grating period (Λ) of 300 nm was applied at the wire waveguide end of the transformer. The spiral was purposely elongated from a conventional Archimedean spiral to make room for the straight mode transformers without having any direct impact on the device performance. The chips were removed from the fabrication line prior to SiO_2 upper cladding deposition to allow for post-process deposition of our ALD Al_2O_3 and $\text{Al}_2\text{O}_3/\text{Er}_2\text{O}_3$ films directly onto the exposed waveguides.

5.3.2 ALD of undoped and Er-doped Al_2O_3 thin films

Our ALD thin films were grown using a tALD process (reactor shown in Fig. 5.9) that sequentially pulses liquid precursors into a vacuum chamber based on the material being deposited. Al_2O_3 monolayers were constructed from TMA and DI water precursors, while Er_2O_3 monolayers were assembled from $(\text{CpMe})_3\text{Er}$ and DI water precursors. The undoped Al_2O_3 films were grown layer by layer using the same deposition parameters (e.g., precursor pulse times, cycle purge time, etc.) until the desired thickness was achieved. On the other hand, the hybrid $\text{Al}_2\text{O}_3/\text{Er}_2\text{O}_3$ films used a X:Y ratio macrocycle technique, where X number of Al_2O_3 layers were grown, followed by Y number of Er_2O_3 layers [49; 64]. Each macrocycle, consisting of X + Y monocycles of their respective

materials, was repeated until the target thickness was reached. The Al_2O_3 and Er_2O_3 cycles each had their own fixed deposition parameters to accommodate the material being grown and the surface in which it grew on. For each of our hybrid $\text{Al}_2\text{O}_3/\text{Er}_2\text{O}_3$ films, 1 Er_2O_3 layer was grown per macrocycle (i.e., $Y = 1$). Therefore, Er_2O_3 was only grown onto pre-deposited Al_2O_3 , whereas Al_2O_3 layers could be grown on Al_2O_3 , Er_2O_3 , or the original substrate material, depending on the step in the overall deposition. Different surface chemistries have different effects on the film growth quality. These characteristics can be optimized but that study is outside the scope of this thesis.

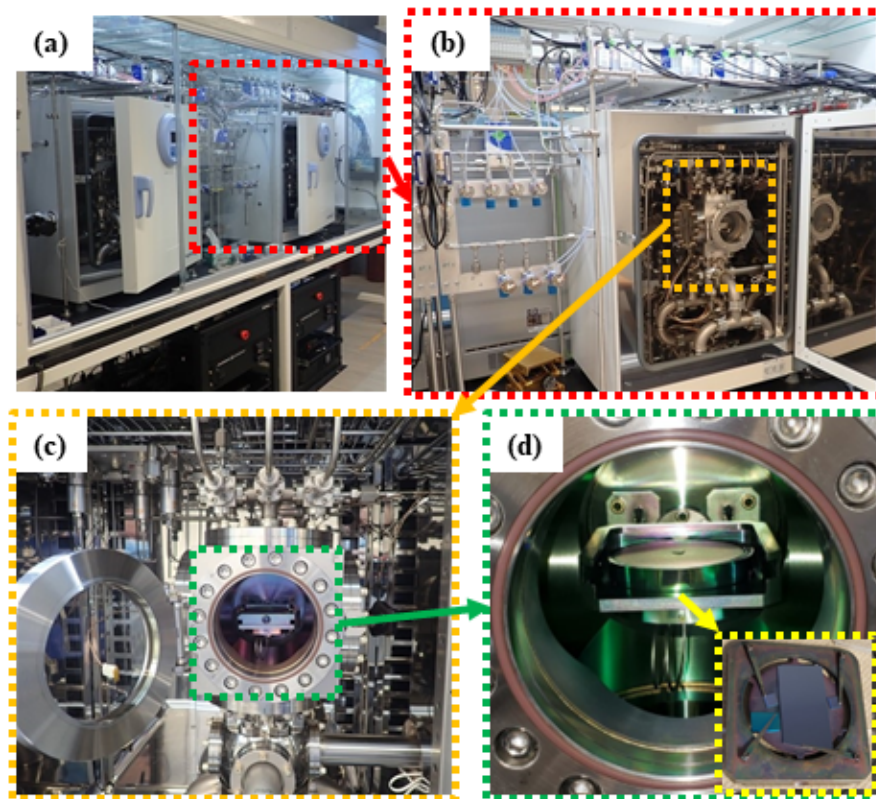


FIGURE 5.9: Custom tALD reactor. (a) 2 ALD reactors with corresponding electronics racks below them in a vented enclosure. (b) Right-side ALD reactor with reaction chamber, attachment points for RT bubblers, and MFCs for gas delivery shown. (c) Open ALD reaction chamber with heated substrate stage and 8 precursor inlets at the top of the reactor shown. (d) Zoomed in image of the reaction chamber. Inset shows inserted stage with clip-mounted waveguide chips and substrate samples receiving ALD films.

Both Al_2O_3 and $\text{Al}_2\text{O}_3/\text{Er}_2\text{O}_3$ films were deposited onto witness samples containing

Si and 6 μm -thick SiO_2/Si substrates, as well as fabricated chips with exposed SiN waveguides. The prepared samples underwent an O_2 plasma surface cleaning and activation process (Harrick Plasma PDC-32G Basic Plasma Cleaner) before being clip-mounted to the ALD chamber stage (see Fig. 5.9(d) inset). A process temperature of 250°C was used for all our ALD films since it provides sufficient thermal energy to promote surface reactions for reasonable self-limiting growth rates ($\sim 1.5 \text{ \AA}/\text{cycle}$) of Er_2O_3 films with relatively low impurity (i.e., H and C) concentrations [55]. It also avoids undesirable crystallinity in the predominantly amorphous Al_2O_3 film structure produced around 300°C [30], as well as detrimental thermal decomposition of the $(\text{CpMe})_3\text{Er}$ precursor that occurs beyond 350°C [55].

Various undoped Al_2O_3 films were deposited as calibration runs. The final run (code named “A06”) was deposited onto SiN chips with waveguides described in Section 5.2. This deposition featured a total of 5060 Al cycles. Afterwards, the Er_2O_3 film deposition process was calibrated and multiple hybrid $\text{Al}_2\text{O}_3/\text{Er}_2\text{O}_3$ films (code named “AE02–AE05”) were deposited around the same thickness but with different cycle ratios to obtain a variety of volumetric Er concentrations for assessment. The same pulse and purge times were used for each deposition. Both AlMe_3 and H_2O precursors had pulse times of 0.05 seconds in the Al_2O_3 deposition cycles, which featured a purge time of 60 seconds. When implemented, the Er_2O_3 cycles used $(\text{CpMe})_3\text{Er}$ and H_2O pulse times of 7 and 0.1 seconds, respectively, and a 180 second purge time. Table 5.3 summarizes any variable deposition parameters used for each of the $\text{Al}_2\text{O}_3/\text{Er}_2\text{O}_3$ ALD runs.

TABLE 5.3: Summary of variable parameters used for ALD $\text{Al}_2\text{O}_3/\text{Er}_2\text{O}_3$ film depositions.

Film code	AE02	AE03	AE04	AE05
# macrocycles	250	133	90	69
Al:Er cycle ratio	10:1	20:1	30:1	40:1

5.4 Characterization

5.4.1 Film characterization

All Al_2O_3 and hybrid $\text{Al}_2\text{O}_3/\text{Er}_2\text{O}_3$ films mentioned in Table 5.3 were characterized using a VASE (J. A. Woollam M-2000 VASE), accessed via the Centre for Emerging Device Technologies (CEDT), and a prism coupler system (Metricon 2010/M). These measurement apparatuses are depicted in Fig. 5.10. The VASE was used to extract

film thickness and material dispersion (i.e., refractive index) data across a 400–1700 nm wavelength range for each ALD film deposited on bare Si substrates. The prism coupler was primarily used to assess the optical propagation loss through the ALD film grown on thermal SiO₂/Si substrates.

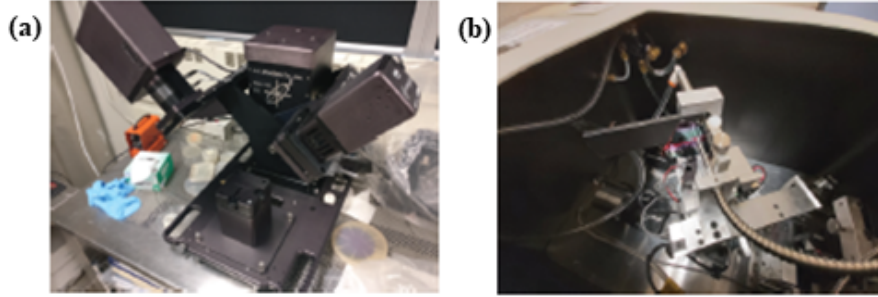


FIGURE 5.10: (a) J. A. Woollam M-2000 VASE and (b) Metricon 2010/M prism coupler system used for characterizing ALD Al₂O₃ and Al₂O₃/Er₂O₃ films.

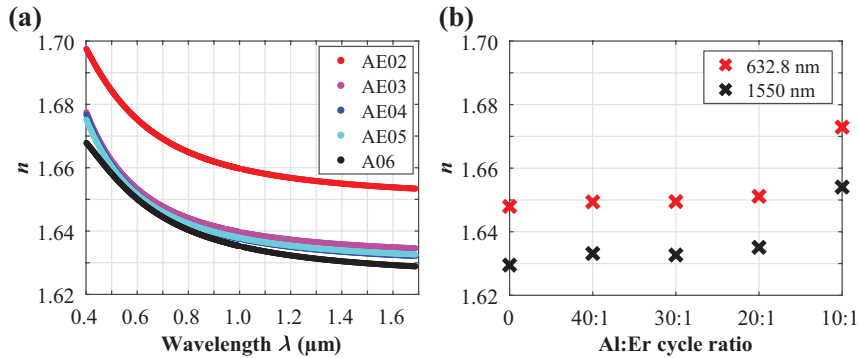


FIGURE 5.11: ALD Al₂O₃ (A) and Al₂O₃/Er₂O₃ (AE) film characterization results obtained from the VASE. Measured film refractive index (a) as a function of wavelength and (b) with respect to Al:Er cycle ratio for 632.8 nm and 1550 nm wavelengths.

The material refractive index results acquired from the VASE are shown in Fig. 5.11. The refractive index curves in Fig. 5.11(a) were obtained by fitting the measured VASE data with a model based on Cauchy’s transmission equations [65]. Fig. 5.11(b) shows the refractive indices at 632.8 nm (red) and 1550 nm (NIR) wavelengths for each film, which are compared with respect to Al:Er cycle ratio. The undoped Al₂O₃ A06 film (Al:Er cycle ratio = 0 in Fig. 5.11(b)) was the first to be grown onto waveguide chips. This film exhibited a measured thickness of 721.5 ± 2.32 nm and measured refractive indices of 1.648 and 1.630 at 632.8 and 1550 nm wavelengths, respectively. The targeted thickness

for this film was 500 nm. However, strange issues arose during the deposition that prevented self-limiting growth and promoted chemical vapour deposition (CVD)-type behaviour, leading to a greater thickness than expected. While the mode overlap with the Al₂O₃ cladding material in the resulting film would certainly increase compared to the targeted thickness, CVD-type film growth affects the film quality, especially around the nanoscale SiN grating structures. Consequences of these issues will be assessed in the discussion of the Metricon prism coupler results. The VASE results for the hybrid Al₂O₃/Er₂O₃ films are summarized at the top of Table 5.4 (under the “VASE” heading). The targeted thickness for each run was between 300-400 nm, which was achieved in all cases and with low uncertainty (e.g., within ± 5 nm). The dispersion profile of each film highlighted in Fig. 5.11(a) closely resembles those demonstrated in literature [66]. The AE02 film showed notably greater refractive index across the measured spectra due to the lower Al:Er cycle ratio promoting greater volumetric Er concentration in the film. The refractive index does not vary much between the other three films. It can be hypothesized that using the current ALD process, the low volume of Er³⁺ ions in films with Al:Er cycle ratios greater than 20:1 do not produce notable changes to the film refractive index. Al:Er cycle ratios less than 10:1 were not tested and could potentially reveal refractive indices greater than the AE02 film that would help boost the mode overlap with the ALD cladding material [49]. This can be optimized with further investigation while considering the increased Er concentration and its effect on absorption and photoluminescence properties.

TABLE 5.4: Summary of ALD Al₂O₃/Er₂O₃ film simulation and measurement results.

Film code	AE02	AE03	AE04	AE05
VASE				
t [nm]	305.5 ± 0.23	380.8 ± 3.65	390.6 ± 0.62	357.4 ± 0.37
n ($\lambda = 632.8$ nm)	1.673	1.65	1.649	1.65
n ($\lambda = 980$ nm)	1.66	1.64	1.638	1.638
n ($\lambda = 1550$ nm)	1.654	1.635	1.633	1.633
RSoft				
n_{eff} ($\lambda = 980$ nm)	1.488	1.503	1.504	1.493
Γ ($\lambda = 980$ nm)	0.539	0.647	0.659	0.603
Metricon				
N_{Er} [ions/cm ³]	13.63×10^{20}	5.27×10^{20}	5.8×10^{20}	3.4×10^{20}
N_{Er} [at. %]	1.51	0.58	0.64	0.38
α_{bg} [dB/cm]	0.6	0.4	3.32	5.34

The Metricon 2010/M prism coupler system was used to characterize the loss of TE polarized light in the Al₂O₃ and hybrid Al₂O₃/Er₂O₃ ALD films grown on thermal SiO₂ witness samples. The system is equipped with various laser sources so that the loss may be assessed at different wavelengths, including 518, 638, 847, 980, 1310 and 1550 nm. The latter three options are tunable wavelength sources that can be tuned within a reasonable bandwidth from the center wavelength. The A06 Al₂O₃ film was characterized at all wavelengths. Fig. 5.12 depicts the optimally coupled visible light streaks across the film sample as well as the measured loss results with respect to wavelength. Losses below 1.2 dB/cm were measured for all wavelengths, with 1550 nm being nearly lossless.

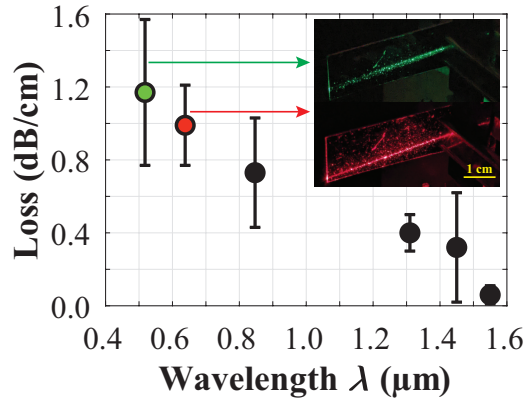


FIGURE 5.12: Measured A06 Al₂O₃ film loss with respect to wavelengths in the VIS and NIR spectra. Inset shows green (top) and red (bottom) light propagation through Al₂O₃ film during prism coupling measurements.

The two main loss mechanisms involved in the hybrid Al₂O₃/Er₂O₃ films are passive (or background) loss due to light scattering in the film or along the material boundary interfaces, and loss from active processes such as light absorption caused by Er³⁺ ions in the film, particularly around 980 nm wavelength and throughout the S-, C-, and L-bands. Prism coupling was used to experimentally determine the total Al₂O₃/Er₂O₃ film loss, which can be represented by the following relation [51; 67]:

$$\alpha_{\text{total}}(\lambda) = \alpha_{\text{bg}}(\lambda) + \alpha_{\text{Er}}(\lambda) = \alpha_{\text{bg}}(\lambda) + \sigma_{\text{Er}}(\lambda) \cdot \Gamma \cdot N_{\text{Er}} \cdot 10 \log_{10}(e), \quad (5.5)$$

where $\alpha_{\text{bg}}(\lambda)$ and $\alpha_{\text{Er}}(\lambda)$ are the wavelength-dependent background losses of the film unrelated and related to Er absorption, respectively, $\sigma_{\text{Er}}(\lambda)$ is the Er absorption cross section, Γ is the confinement factor in the film layer, N_{Er} is the Er³⁺ ion dopant concentration, and $10 \log_{10}(e)$ is a log scale (dB) conversion term. By performing a linear

regression fit over the measured total film loss data with respect to $\sigma_{\text{Er}}(\lambda)$, we can experimentally determine N_{Er} (slope) and $\alpha_{\text{bg}}(\lambda)$ (y-intercept) for the film.

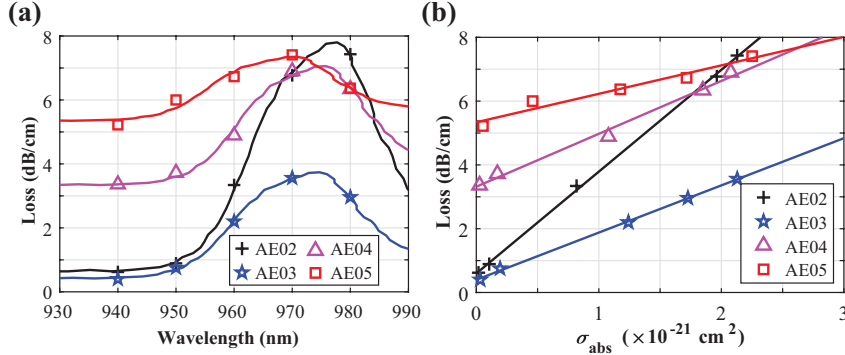


FIGURE 5.13: ALD $\text{Al}_2\text{O}_3/\text{Er}_2\text{O}_3$ (AE) film characterization results from Metricon prism coupler. (a) Measured film loss with respect to wavelength (points) and corresponding absorption cross section data from literature (lines). (b) Measured film loss with respect to absorption cross section (points) with linear regression fit over data used to extrapolate film background loss and Er ion concentration (lines).

The hybrid $\text{Al}_2\text{O}_3/\text{Er}_2\text{O}_3$ films grown (AE02-AE05) were within the 300-400 nm thickness range. However, a finite element method (FEM) solver (Synopsys RSoft FemSIM) determined that an Al_2O_3 planar film with the A06 dispersion profile from Fig. 5.11(a) atop a 6 μm -thick SiO_2/Si substrate must have a thickness > 500 nm to guide light at 1550 nm wavelength. Thicknesses below this suffer from low confinement factor in the film and significant substrate leakage losses that greatly reduce the accuracy of the prism coupling loss measurements. Therefore, light within the 930-980 nm wavelength range was used to characterize the loss and Er absorption properties of the films. Absorption cross sections were assumed based on a study of another Er^{3+} -doped aluminate glass host with a peak absorption cross section of $2.26 \times 10^{-21} \text{ cm}^2$ near 978 nm wavelength [68]. The confinement factors were calculated using RSoft FemSIM by modeling a 1-D planar waveguide featuring the refractive index data determined by the VASE measurements shown in Fig. 5.11. The simulation results for each film at 980 nm wavelength are summarized in the middle of Table 5.4 (under the ‘‘RSoft’’ heading). Fig. 5.13 shows the results from the prism coupling measurements, while the bottom of Table 5.4 (under the ‘‘Metricon’’ heading) summarizes the results of the linear regression fittings in Fig. 5.13(b). The atomic % concentration values in Table 5.4 are calculated

from the absolute concentration such that [49]:

$$N_{\text{Er}}[\text{at. \%}] = \frac{N_{\text{Er}} [\text{ions/cm}^3]}{9.02 \times 10^{20} \text{ ions/cm}^3}. \quad (5.6)$$

Most of the Er concentrations in our ALD films are much lower than those reported in literature demonstrating $\text{Al}_2\text{O}_3/\text{Er}_2\text{O}_3$ waveguide amplifiers [49; 50; 51]. However, our waveguides are much longer (e.g., cm scale, rather than mm- or μm -scale) and better suited for achieving greater overall net gain with small signal gain. This requires lower Er concentrations and lower injected pump powers to avoid fast saturation of the pump source. SWG waveguides also have greater overlap with the gain medium than strip and slot waveguides and therefore greater sensitivity to these saturation effects. Lower Er concentrations also alleviate potential Er quenching issues that are a common gain deterrent in Er-based waveguide amplifiers and lasers [69].

The best background losses of 0.6 and 0.4 dB/cm are exhibited in films AE02 and AE03, respectively, which provide promising results for active gain media on our SiN waveguide amplifiers. These two films have absolute Er concentrations of 13.63×10^{20} and 5.27×10^{20} ions/cm³. AE02 is comparable to the other ALD $\text{Al}_2\text{O}_3/\text{Er}_2\text{O}_3$ films reported in literature and may possess better gain characteristics in shorter waveguide devices, while AE03 is more promising for our longer waveguides. It is surprising that the Er concentration in AE03 is lower than that of AE04, considering its lower Al:Er cycle ratio. However, a small software malfunction occurred during the deposition of film AE04 where the timing of the different valve openings was perturbed. This may have alleviated self-limiting growth conditions, which would help explain the greater thickness compared to all the other films, as well as the higher background loss over AE02 and AE03. Films AE04 and AE05 have notably higher background losses of 3.32 and 5.34 dB/cm, respectively. Beyond the malfunction of AE04 deposition, it is suspected that the high loss for these two films was caused by an issue called flaking. Past tests in our ALD reactor have shown that multiple consecutive depositions generate a buildup of excess material onto the surrounding chamber walls. After many runs, the leftover material in the chamber begins to break off in small chunks or flakes during depositions and becomes a contaminant in the growth of new films. These impurities severely diminish the quality of new films, interrupt important deposition conditions such as self-limiting growth, and can even cause damage to fine structures such as optical waveguides. The flaking issue is accentuated when depositing thick (hundreds of nm) Al_2O_3 films over long periods of time (days), such as ours, and becomes worse during later depositions when the problem is left unattended. To solve the flaking issue, the ALD reactor must be

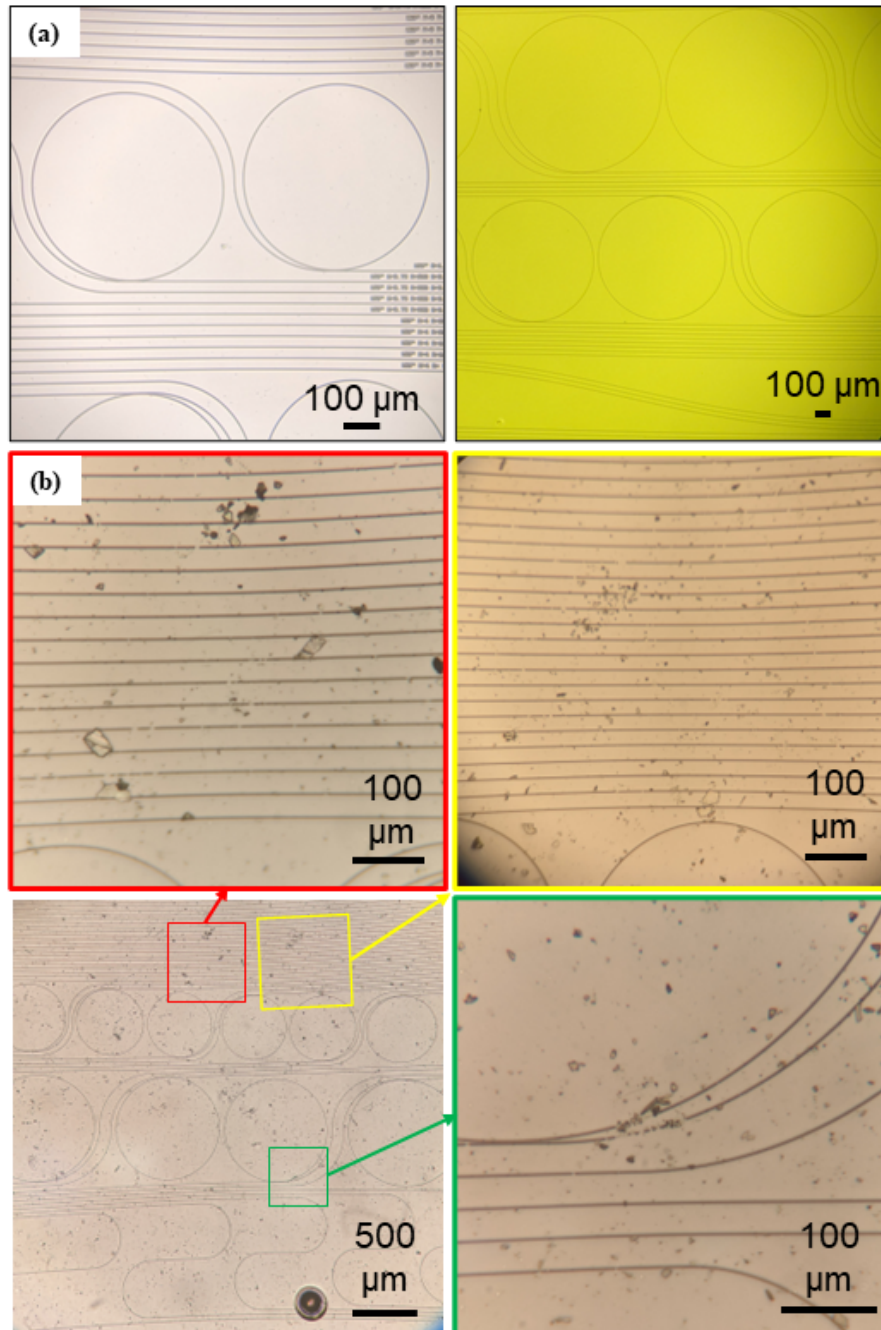


FIGURE 5.14: Optical microscope images of (a) normal SiN waveguides and (b) SiN waveguides damaged by flaking during the deposition of ALD $\text{Al}_2\text{O}_3/\text{Er}_2\text{O}_3$ film AE05.

disassembled, and the chamber must be bead blasted carefully and completely. However,

doing so requires complete recalibration of the system after cleaning. This will change the deposition parameters for optimal film growth and eliminate consistency of the film samples grown before and after the chamber cleaning, so we opted not to clean the system until all films were deposited. Because AE04 and AE05 were deposited last, it is suspected that this issue was the prime culprit for the high background loss in the two films. Waveguide chips included in the AE05 deposition suffered heavy damage and became unmeasurable in the waveguide characterization process. Fig. 5.14(b) shows images of waveguides under an optical microscope, highlighting the irreversible damage of the flaking that occurs during ALD.

Overall, the film characterization results from the Metricon are predicted to have high uncertainty since the absorption cross section was assumed from another study rather than being measured directly for each of our respective films. This will cause reasonable uncertainty in the calculated Er concentrations for each measured film. Future steps will involve spectroscopic measurements of each film sample to obtain the appropriate absorption and emission cross sections so that a more accurate calculation of the Er concentration and film background loss can be obtained. Alternatively, other film characterization methods, such as Rutherford backscattering spectrometry (RBS), can be performed on the film samples to directly measure and calculate the Er concentration.

5.4.2 Al₂O₃-coated waveguide characterization

The fabricated waveguide devices coated in ALD undoped Al₂O₃ underwent passive characterization on a fiber-chip edge coupling setup. The optical signal path begins from a 1510-1640 nm tunable laser source (Agilent 8168A Lightwave Measurement System), where light is emitted through optical fiber and tuned to TE polarization using manual polarization paddles. The light is coupled onto and off the chip via 2.5 μm spot size lensed fibers and is collected by an indium gallium arsenide (InGaAs) photodetector at the end of the signal path. Once fiber-chip coupling is optimized, a MATLAB script is used to sweep the laser wavelength and plot the collected optical power at the detector. The acquisition is performed for multiple SWG metamaterial waveguide spirals, like those shown in Fig. 5.8. The results for waveguides coated in ALD Al₂O₃ film A06 are plotted in Fig. 5.15. The transmission spectra in Fig. 5.15(a) show the measured insertion loss, which only includes loss related to light propagation through the SWG waveguide and light coupling between fiber and chip. Each waveguide has a different length, as indicated by the legend. The insertion loss for each device is collected at specific wavelengths and plotted with respect to SWG waveguide length in Fig. 5.15(b). A linear regression fit is performed over each data series to reveal the propagation loss

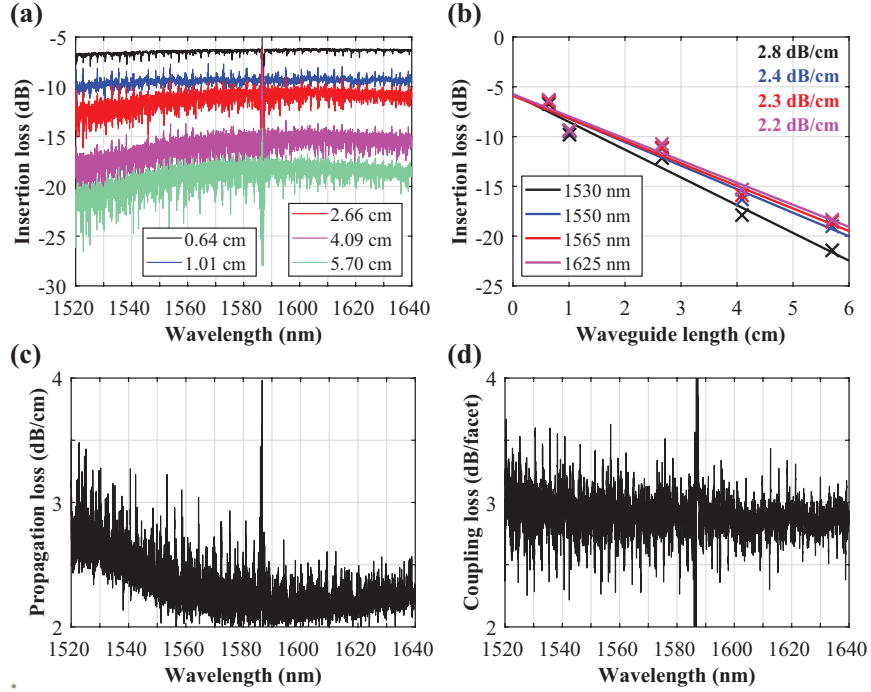


FIGURE 5.15: Passive measurement results for fabricated Al_2O_3 -coated SiN SWG metamaterial waveguides. (a) Measured TE-polarized transmission spectra of spiral waveguides with varying length. (b) Measured and fitted insertion loss with respect to SWG waveguide length for various wavelengths across the C- and L-bands. Calculated (c) propagation and (d) coupling loss across all measured wavelengths using linear regression fitting technique from (b).

(slope) and coupling loss (y-intercept) of the general waveguide structure. The Al_2O_3 -coated SiN SWG metamaterial waveguide reveals propagation losses of 2.8, 2.4, 2.3, and 2.2 dB/cm for 1530, 1550, 1565, and 1625 nm wavelengths, respectively. This method can be applied over all wavelengths and plotted with respect to propagation and coupling loss, as illustrated in Fig. 5.15(c-d). A strange transmission distortion is observed across all waveguides near 1587 nm wavelength. Such artifacts have been reported in measured transmission spectra of silicon SWG waveguides for TE polarization due to fabrication glitches with interconnecting wire waveguides [70]. It is possible that such an error occurred in the fabrication of the SWG-wire mode transformers in our spirals. Disregarding this anomaly, the fiber-chip coupling loss for this specific waveguide structure is 2.9 ± 0.1 dB/facet across all measured wavelengths. Higher propagation loss around 3 dB/cm is reported near 1520 nm, which likely corresponds to light absorption

from hydrogen impurities in both the SiN waveguide (in the form of N-H and Si-H bonds [71]) and the Al₂O₃ film (in the form of O-H bonds [31; 47]). Meanwhile, the best measured propagation loss is ~ 2 dB/cm, which is comparable to the reported background loss of similar SiN strip waveguides coated in hybrid ALD Al₂O₃/Er₂O₃ [51].

5.4.3 Al₂O₃/Er₂O₃-coated waveguide characterization

Waveguides coated in hybrid Al₂O₃/Er₂O₃ films underwent the same passive characterization described above to obtain the background propagation loss through the waveguide under investigation. 1650 nm wavelength is assumed to have negligible absorption losses from the presence of Er ions in the ALD film, so the propagation loss at this wavelength acquired via the cutback method is used to classify the passive waveguide background loss.

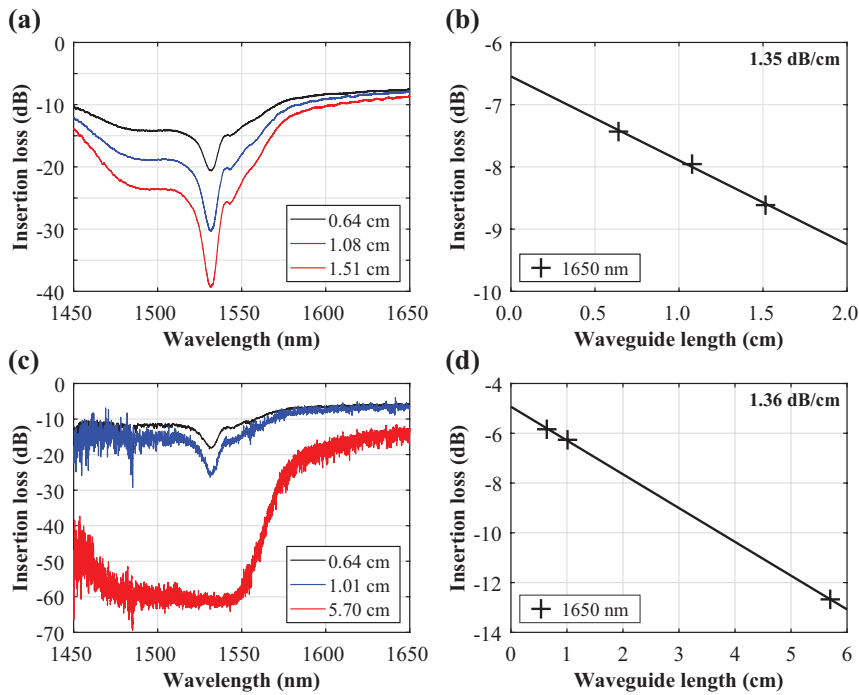


FIGURE 5.16: Passive cutback measurement results for fabricated SiN waveguides coated in hybrid Al₂O₃/Er₂O₃ ALD films. (a) Measured TE-polarized transmission spectra and (b) fitted insertion loss at 1650 nm wavelength as a function of waveguide length for SiN wire waveguides coated in film AE02. (c) Measured TE-polarized transmission spectra and (d) fitted insertion loss at 1650 nm wavelength as a function of waveguide length for SWG meta-material waveguides coated in film AE03.

Fig. 5.16 shows the passive measurement results acquired for wire and SWG metamaterial waveguides coated in the hybrid $\text{Al}_2\text{O}_3/\text{Er}_2\text{O}_3$ ALD films AE02 and AE03, respectively. The transmission spectra of both waveguide types highlight significant loss within the Er absorption region, peaking near 1533 nm wavelength. The absorption loss, which we consider the difference between the measured minimum and maximum insertion loss (around 1533 nm and 1650 nm wavelengths, respectively), increases with waveguide length since it is proportional to the interaction time and length between the light propagating through the waveguide and the Er ions in the film cladding. At 1650 nm wavelength, the measured propagation and fiber-chip coupling losses are 1.35 dB/cm and 3.27 dB/facet, respectively, for the wire waveguides coated in ALD film AE02, and 1.36 dB/cm and 2.47 dB/facet, respectively, for the SWG waveguides coated in ALD film AE03. These waveguides share a very similar background loss that is significantly lower than the loss in the undoped Al_2O_3 -clad SWG waveguides reported in Fig. 5.15. It is noted that the coupling loss in the SWG waveguides, which use SWG metamaterial-engineered edge couplers, is 0.8 dB/facet lower than the wire waveguides, which use conventional inverse nanotaper edge couplers. The use of SWG edge couplers for lower coupling loss and enhancing broadband behaviour is well-known and has been previously demonstrated in SOI [14; 72]. These results show that the same principle also applies to SiN waveguides and that SWG edge couplers can be leveraged to enhance the on-chip pump power, which helps to achieve higher gain. Table 5.5 highlights the background propagation and fiber-chip coupling losses measured for SiN waveguides coated in other hybrid $\text{Al}_2\text{O}_3/\text{Er}_2\text{O}_3$ films using the same procedure as described above. Each one shows a higher background propagation loss compared to the waveguides illustrated in Fig. 5.16 but they maintain propagation losses <3 dB/cm and coupling losses <3 dB/facet. The exception is the SWG waveguide coated in AE02, which did not have enough reliable data points to perform an accurate loss calculation. A known coupling loss from another SWG waveguide structure (e.g., AE03) was assumed to determine the best and worst case losses from these measured test structures. As a result, the losses for this particular waveguide are reported as a range with a large uncertainty rather than a single value.

Fig. 5.17 highlights the process for determining the effective absorption and emission cross sections using passive waveguide measurements. In Fig. 5.17(a), the raw transmission spectra of the 0.64 cm-long wire and SWG metamaterial waveguides mentioned in Fig. 5.16 are displayed in bold red. The spectra are broken down with respect to their different loss components. The tunable laser source had a launched signal power of 0 dB for all wavelengths. Loss related to light propagation through the optical setup

TABLE 5.5: Summary of passive cutback measurement results for Al₂O₃/Er₂O₃-coated SiN waveguides.

ALD film, chip code	WG type	Measured lengths [cm]	α_{bg} [dB/cm]	α_{coup} [dB/facet]
AE02, 12UR*	Wire	[0.64, 1.08, 1.51]	1.35	3.27
AE02, 15UR [!]	SWG	[1.01, 4.09]	7.10–7.64	2.87–4.10
AE03, 15LL	Wire	[0.64, 1.08, 1.95]	2.91	2.11
AE03, 15LL*	SWG	[0.64, 1.01, 5.70]	1.36	2.47
AE04, 12UL	Wire	[1.08, 1.51, 1.95]	2.46	1.97
AE04, 13UR	SWG	[0.64, 1.01, 2.66, 5.70]	2.36	2.77

* shown in Fig. 5.16.

[!] assumed coupling loss from AE03 SWG sample data.

unrelated to the chip are highlighted in black. They are wavelength dependent, with a minimum and maximum transmission loss of -3.18 dB and -2.65 dB at wavelengths of 1650 nm and 1521 nm, respectively. The background loss was calculated from the propagation loss extracted from the cutback measurement results, such as those shown in Fig. 5.16, and the waveguide length. This results in background losses of 0.86 dB and 0.87 dB for wire and SWG waveguides in Fig. 5.17, respectively. The fiber-chip coupling loss is the difference between the measured transmission and the sum of the background and fiber losses at a wavelength of 1650 nm, where Er absorption losses are considered negligible. This reveals coupling losses of 6.58 dB for the wire waveguide, which is in good agreement with the coupling loss obtained from the cutback measurement (6.545 dB). For simplicity, both the fiber-chip coupling and background loss are assumed to be constant across the measured spectrum. The remaining loss is related to Er absorption and is plotted by itself in Fig. 5.17(b) (i.e., the red line minus the yellow line). The measured Er absorption loss of a given waveguide device (α_{Er}) can be used to back calculate the effective absorption cross section (σ_{abs}) using the following relation [73]:

$$\sigma_{\text{abs}}(\lambda) = \frac{\alpha_{\text{Er}}(\lambda)}{\Gamma \cdot N_{\text{Er}} \cdot l \cdot 10 \log_{10}(e)}, \quad (5.7)$$

where Γ is the confinement factor in the Al₂O₃/Er₂O₃ film layer, N_{Er} is the Er³⁺ ion dopant concentration, and l is the waveguide length, which is 0.64 cm in this case. N_{Er} is known from the Metricon film measurement results summarized in Table 5.4. Meanwhile, Γ is calculated using 2D FDE and 3D FDTD simulations for the wire and SWG metamaterial waveguides, respectively. To acquire the effective emission cross section (σ_{em}), a generalized version of McCumber theory [74] applied to the transitions

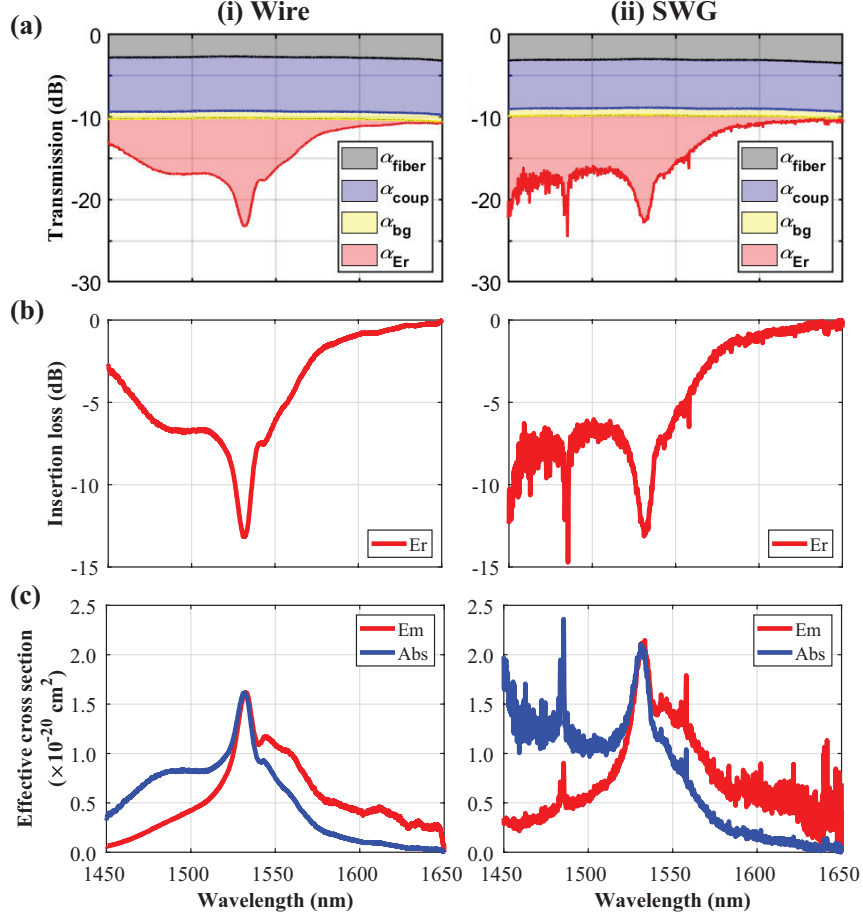


FIGURE 5.17: (a) Measured transmission for a 0.64 cm-long SiN (i) wire waveguide coated in film AE02 and (ii) SWG metamaterial waveguide coated in film AE03, broken down into loss contributions from optical fiber transmission (α_{fiber}), fiber-chip coupling (α_{coup}), background loss in the coated SiN waveguide (α_{bg}), and Er absorption (α_{Er}). (b) Isolated Er absorption loss. (c) Calculated effective absorption and emission cross sections based on Eq. 5.7 and 5.8, respectively.

between the ground and first excited states of Er^{3+} -doped glasses was used such that [75]:

$$\sigma_{\text{em}}(\lambda) = \sigma_{\text{abs}}(\lambda) \exp\left(\frac{\epsilon - h\nu}{kT}\right), \quad (5.8)$$

where ϵ is the temperature-dependent excitation energy, $\nu = c/\lambda$ is the independent photon frequency variable, h is Planck's constant, k is Boltzmann's constant, and T is temperature. The absorption and emission cross section for this SiN wire waveguide,

calculated with an assumed room temperature of 300K and mean energy at 1532 nm wavelength, are displayed in Fig. 5.17(c). In general, the shape of the emission spectrum agrees well with results from other reported ALD Al₂O₃/Er₂O₃ works [50]. The peak effective cross sections near 1532 nm wavelength are determined to be 1.6×10^{-20} cm² and 2.1×10^{-20} cm² for the waveguides with AE02 and AE03 claddings, respectively. Even with the greater Γ value from the SWG waveguide (0.43 versus 0.22 in the wire waveguide), the increased effective cross section in the AE03 film arises from its significantly lower N_{Er} value (5.27×10^{20} ions/cm³, versus 13.63×10^{20} ions/cm³ in the AE02 film).

Active characterization (hereon referred to as “gain measurements”) of the SiN waveguides coated in hybrid Al₂O₃/Er₂O₃ ALD films were performed using the optical lab setup described in [76]. The core signal path between the tunable laser source and the output photodetector remained the same, except with a 25 dB optical attenuator added after the polarization paddles for the signal source. This had to be done to significantly reduce the launched signal power into the chip since the tunable laser source has a minimum output power of 1 mW, which is not small enough to measure small signal gain. Two 1470 nm pump laser diodes were appended to the setup using fused fiber optic 1480/1550 wavelength division multiplexers (WDMs) on each side of the chip. This allowed the pump and signal sources to simultaneously enter and exit the chip on the same fiber. Furthermore, the two pump diodes enabled both single- and double-side pump operation from either side or both sides of the chip. Each source was equipped with its own set of polarization paddles and optimized for TE polarization. A 1500 nm edgepass filter was applied on the output side of the signal source path to alleviate any remaining residual pump light following the WDM as well as amplified spontaneous emission (ASE) noise reaching the detector.

Gain measurements were carried out by performing multiple sweep acquisitions of the coupled device under test. First, a baseline reference was collected by measuring the power response of the device with only the signal source activated (i.e., both pump diodes are inactive). Next, multiple data acquisitions were performed with both the signal and forward pump sources activated (backward pump is still inactive). The applied current of the forward pump diode was gradually increased for each subsequent measurement. Finally, a few more acquisitions were performed with the forward pump diode fixed at the maximum current from the previous measurement and the backward pump diode activated with a gradually increasing current on each recorded sweep. Between each acquisition run, the wavelength-independent ASE response was recorded by reading the

photodetector output with the relevant pump source(s) active and the signal source disabled. This was subtracted from the acquired data in the gain analysis to eliminate any amplification effects from spontaneous emission that do not contribute to actual optical amplification of the signal.

Fig. 5.18 shows the gain measurement results for the 0.64 cm-long SiN waveguides illustrated in Fig. 5.17. Fig. 5.18(a) shows the raw insertion loss spectrum of the unpumped waveguide device under test plotted with the pumped waveguide spectra at different launched pump powers, which increases as the spectrum colour changes from blue to red. All measurements had ~ 3 μW signal power entering the chip, which was obtained using 0 dB output power from the tunable laser source (Keysight N7778C, option 216) and a 25 dB optical attenuator between the signal polarization paddles and front-side WDM. Generally, the transmitted power across the measured gain region (i.e., 1520-1570 nm) increases with the launched pump power, as expected. The signal enhancement (SE) and internal net gain (g_{net}) are defined such that [67; 77]:

$$SE(\lambda, P)[dB] = 10 \log_{10} \left(\frac{P_{\text{pumped}}(\lambda, P)[\text{mW}] - P_{\text{ASE}}(P)[\text{mW}]}{P_{\text{unpumped}}(\lambda)[\text{mW}]} \right), \quad (5.9)$$

$$g_{\text{net}}(\lambda, P)[dB] = SE(\lambda, P)[dB] - \alpha_{\text{Er}}(\lambda)[dB] - \alpha_{\text{bg}}(\lambda)[dB] \quad (5.10)$$

where $P_{\text{unpumped}}(\lambda)$ is the measured power of the unpumped waveguide device, $P_{\text{pumped}}(\lambda, P)$ is the measured power of the pumped waveguide device with launched pump power P , and $P_{\text{ASE}}(P)$ is the measured ASE running through the optical setup with launched pump power P . All powers were measured in linear units (mW) and then converted to logarithmic units (dB) in the signal enhancement calculation. The internal net gain is simply the signal enhancement with the primary on-chip losses subtracted: Er absorption loss (α_{Er}) and background waveguide propagation loss (α_{bg}). To demonstrate a working on-chip optical amplifier, the measured insertion loss must supersede these losses when pumped (i.e., internal net gain must be positive). The top dotted line in Fig. 5.18(a) represents this power threshold for achieving internal net gain. The dotted line below it is the Er loss threshold, which does not consider the background loss. These values are derived for each measured device using the same procedure that produced Fig. 5.17(a). Fig. 5.18(b) reveals maximum measured signal enhancements of 4.8 dB and 5.0 dB at 1533 nm wavelength for the wire and SWG waveguides, respectively. Comparing these two waveguides, which have similar background and Er absorption losses, we observe slightly higher signal enhancement in the SWG waveguide over the wire waveguide. The main difference is the reduced coupling loss in the SWG waveguide, which enables greater

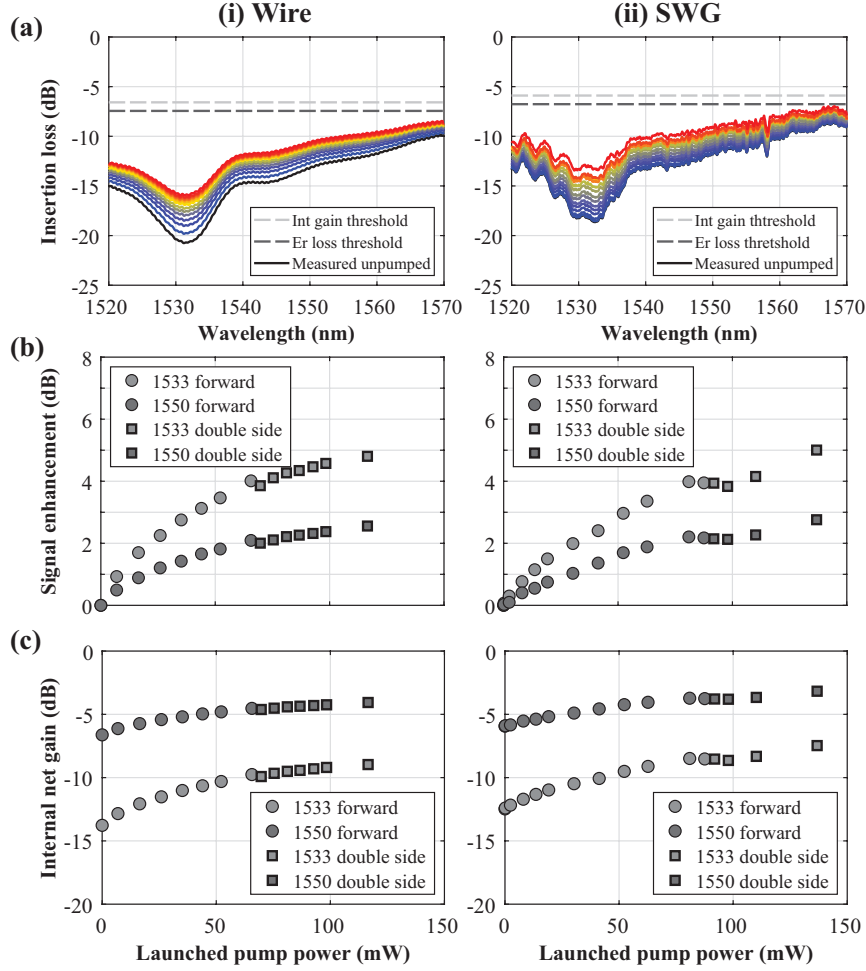


FIGURE 5.18: Gain measurements for the fabricated 0.64 cm-long SiN (i) wire waveguide coated in film AE02 and (ii) SWG meta-material waveguide coated in film AE03. (a) Measured insertion loss across the spectral gain region of interest (1520–1570 nm) for unpumped (black) and pumped (coloured) waveguides. Colour of spectra changes from blue to red as the launched pump power increases. Dotted lines represent power thresholds for surpassing Er absorption loss (dark grey) and achieving internal net gain (light grey). Corresponding measured (b) signal enhancement and (c) internal net gain with respect to launched pump power for 1533 nm (light grey) and 1550 nm (dark grey) wavelengths.

launched pump power into the waveguide (e.g., 137 mW in the SWG waveguide versus 116 mW in the wire waveguide). This is an additional benefit for implementing SWG edge couplers in waveguide amplifier designs for better performance. It is also worth

noting that the AE03 film surrounding the SWG waveguide has a significantly lower Er dopant concentration than the AE02 film coating on the wire waveguide. If the same film deposited on the wire waveguide was applied to this equivalent SWG waveguide, it offers even greater potential for increasing the signal enhancement.

TABLE 5.6: Gain measurement results for Al₂O₃/Er₂O₃-coated SiN waveguides.

Film, chip code	WG type	L_{wg} [cm]	α_{coup} [dB/facet]	α_{bg} [dB]	α_{Er} [dB]	LPP* [mW]	SE_{max} [dB]		$g_{net,max}$ [dB]	
							1533 nm	1550 nm	1533 nm	1550 nm
AE02, 15UR [!]	Wire [§]	0.64	3.29	0.86	13.17	65.6 (F)	4.01	2.09	-9.76	-4.53
						116 (D)	4.80	2.56	-8.97	-4.06
AE02, 12UR	Wire	1.08	3.22	1.46	22.35	38.8 (F)	3.90	2.14	-19.65	-9.51
						60 (D)	4.90	2.66	-18.65	-8.99
AE02, 12UR	Wire	1.51	3.34	2.05	33.34	37.8 (F)	4.38	2.15	-28.30	-13.97
						58.4 (D)	5.46	2.88	-27.22	-13.24
AE02, 15UR	SWG	0.64	0.68	4.54	24.57	95.2 (F)	5.44	2.42	-24.55	-13.52
						186 (D)	8.57	4.21	-21.42	-11.73
AE03, 15LL	Wire	0.64	2.30	1.86	7.57	115 (F)	1.74	0.91	-7.52	-4.52
						210 (D)	2.60	1.44	-6.66	-3.99
AE03, 15LL	SWG [§]	0.64	2.95	0.87	13.13	81 (F)	3.99	2.21	-8.49	-3.73
						137 (D)	5.00	2.76	-7.47	-3.17
AE03, 15LL	SWG	1.01	2.03	1.37	20.80	100 (F)	3.84	2.04	-16.02	-8.04
						156 (D)	5.28	2.89	-14.58	-7.19
AE04, 12UL	Wire	1.08	1.93	2.65	9.58	111 (F)	2.19	1.24	-11.42	-6.46
						154 (D)	2.49	1.44	-11.11	-6.26
AE04, 13UR	SWG	0.64	3.00	1.51	9.21	86.6 (F)	2.46	0.94	-8.29	-4.35
						121 (D)	2.32	0.95	-8.43	-4.34
AE04, 13UR	SWG	1.01	2.41	2.38	14.08	71 (F)	3.20	1.56	-14.31	-7.98
						155 (D)	4.21	2.14	-13.30	-7.40

* LPP = launched pump power, (F) = forward pump only, (D) = double-side pump.

[!] Used background loss data from another chip.

[§] Sample corresponding to results shown in Fig. 5.17 and Fig. 5.18.

Table 5.6 provides a summary of the gain measurements performed on various devices across multiple chips coated in different hybrid Al₂O₃/Er₂O₃ ALD films. The greatest measured signal enhancement in all the waveguides was 8.57 dB at 1533 nm wavelength in the AE02-coated SWG waveguide with 0.64 cm length. Compared to the wire waveguide in Fig. 5.18, which has the same waveguide length and Al₂O₃/Er₂O₃ gain medium, while there is some discrepancy between the launched pump powers (116

mW vs. 186 mW), the results show that the SWG waveguide is superior to a wire waveguide by a reasonable margin with respect to signal enhancement. This is mainly due to the increased confinement factor with the gain material in the SWG waveguide that is essential for boosting the amplification factor. The drawback of this SWG waveguide is the loss, where the background loss is 4.54 dB and the peak Er absorption loss is 24.57 dB due to the waveguide's larger mode overlap with the high N_{Er} gain material. This severely limits the maximum internal net gain to -21.42 dB in the SWG waveguide. Future designs should consider ways to balance the various waveguide losses with the overlap factor, such as larger duty cycle (≥ 0.7) and/or reduced grating period. The latter will enhance the homogenization effect of the effective waveguide medium, thus increasing the overlap with the gain material in the voids between the gratings. Finally, there should also be more consideration for the optimization between the waveguide length and Er concentration.

While promising signal enhancement was observed, none of the waveguides exhibited positive internal net gain. The insertion loss spectra for each measured device mimic the pattern shown in Fig. 5.18(a), where the power is boosted, but inversion near the Er emission peak does not occur. This is evidence that there is a lack of active Er ions in the ALD films that contribute to stimulated emission. The prime culprit of this may possibly be attributed to a fast-quenching process, which commonly arises from fast static energy transfer upconversion (ETU) in ion pairs and clusters or the presence of impurities within the host material [69]. Our ALD films are likely susceptible to both, given the larger Er concentrations used in our study compared to other works [26], as well as reasonable levels of leftover organic precursor material remaining in the deposited film [47; 55]. The latter, specifically hydrogen, also contributes significant undesired absorption loss to the gain region of interest [31; 47]. Annealing is a common solution to addressing both these issues by driving out excess organic contaminants and reactivating Er ions in the gain material [77; 78; 79]. This is the next step for these devices. While finding the proper environment for these films and devices requires careful investigation, it is noted that annealing above 600°C increases the luminescence in Er-doped Al_2O_3 ALD films [30; 64]. Furthermore, temperatures above 800°C should be avoided to alleviate phase formation of polycrystalline $\gamma\text{-Al}_2\text{O}_3$, which produces qualities that are undesirable for our target application [30; 79].

5.5 Conclusion

In conclusion, we have presented work towards developing SiN waveguide amplifiers engineered using SWG metamaterials. The waveguides were fabricated using a commercial SiN prototyping foundry process leveraging EBL for producing subwavelength feature sizes. Al₂O₃/Er₂O₃ films were grown in a custom-built ALD reactor utilizing a tALD process for highly uniform and conformal films that effectively fill the nanovoids between the SiN waveguide features. Low loss (<1 dB/cm) was realized in films with different Er ion concentrations. Passive waveguide losses down to 1.3 dB/cm were measured for both wire and SWG metamaterial waveguides coated in the hybrid Al₂O₃/Er₂O₃ ALD thin film. Using a 1470 nm wavelength pump diode source, a maximum signal enhancement of 8.57 dB was exhibited at a peak wavelength of 1533 nm in the SiN SWG waveguide device, compared to an equivalent wire waveguide device with 4.8 dB signal enhancement. However, overwhelming losses from Er absorption and sidewall scattering hampered the possibility of acquiring positive internal net gain in all measured devices. In addition, the lack of population inversion observed in the gain spectra raises the suspicion that significant luminescence quenching limited the overall net gain. Annealing of the presented devices is required to drive out excess hydrogen- and carbon-based impurities from the ALD film and restore optically active Er ions in the devices required for net gain. Further design considerations, such as duty cycle and grating period re-evaluation and optimization between the waveguide length and Er concentration in the film, may also assist in boosting gain metrics in future iterations of the waveguide. These results show promise towards demonstrating a new type of Er-based SiN waveguide amplifier and provide a basis for another core component in integrated photonics incorporating SWG metamaterials, which are valuable assets for establishing SiN PICs as essential tools in various photonic applications.

Bibliography

- [1] D. Thomson, A. Zilkie, J. E. Bowers, T. Komljenovic, G. T. Reed, L. Vivien, D. Marris-Morini, E. Cassan, L. Viot, J.-M. Fédéli, J.-M. Hartmann, J. H. Schmid, D.-X. Xu, F. Boeuf, P. O'Brien, G. Z. Mashanovich, and M. Nedeljkovic, "Roadmap on silicon photonics," *Journal of Optics*, vol. 18, no. 7, p. 073003, 2016.
- [2] S. Y. Siew, B. Li, F. Gao, H. Y. Zheng, W. Zhang, P. Guo, S. W. Xie, A. Song, B. Dong, L. W. Luo, C. Li, X. Luo, and G.-Q. Lo, "Review of silicon photonics

- technology and platform development,” *Journal of Lightwave Technology*, vol. 39, no. 13, pp. 4374–4389, 2021.
- [3] M. U. Khan, Y. Xing, Y. Ye, and W. Bogaerts, “Photonic integrated circuit design in a foundry+fabless ecosystem,” *IEEE Journal of Selected Topics in Quantum Electronics*, vol. 25, no. 5, pp. 1–14, 2019.
- [4] P. Muñoz, G. Micó, L. A. Bru, D. Pastor, D. Pérez, J. D. Doménech, J. Fernández, R. Baños, B. Gargallo, R. Alemany, A. M. Sánchez, J. M. Cirera, R. Mas, and C. Domínguez, “Silicon nitride photonic integration platforms for visible, near-infrared and mid-infrared applications,” *Sensors*, vol. 17, no. 9, p. 2088, 2017.
- [5] C. Xiang, W. Jin, and J. E. Bowers, “Silicon nitride passive and active photonic integrated circuits: trends and prospects,” *Photonics Research*, vol. 10, no. 6, pp. A82–A96, 2022.
- [6] R. Baets, A. Z. Subramanian, S. Clemmen, B. Kuyken, P. Bienstman, N. Le Thomas, G. Roelkens, D. Van Thourhout, P. Helin, and S. Severi, “Silicon photonics: Silicon nitride versus silicon-on-insulator,” in *2016 Optical Fiber Communications Conference and Exhibition (OFC)*, pp. 1–3, 2016.
- [7] P. Muñoz, P. W. L. van Dijk, D. Geuzebroek, M. Geiselmann, C. Domínguez, A. Stassen, J. D. Doménech, M. Zervas, A. Leinse, C. G. H. Roeloffzen, B. Gargallo, R. Baños, J. Fernández, G. M. Cabanes, L. A. Bru, and D. Pastor, “Foundry developments toward silicon nitride photonics from visible to the mid-infrared,” *IEEE Journal of Selected Topics in Quantum Electronics*, vol. 25, no. 5, pp. 1–13, 2019.
- [8] P. Cheben, R. Halir, J. H. Schmid, H. A. Atwater, and D. R. Smith, “Subwavelength integrated photonics,” *Nature*, vol. 560, pp. 565–572, 2018.
- [9] R. Halir, A. Ortega-Moñux, D. Benedikovic, G. Z. Mashanovich, J. G. Wangüemert-Pérez, J. H. Schmid, Í. Molina-Fernández, and P. Cheben, “Subwavelength-grating metamaterial structures for silicon photonic devices,” *Proceedings of the IEEE*, vol. 106, no. 12, pp. 2144–2157, 2018.
- [10] J. M. Luque-González, A. Sánchez-Postigo, A. Hadij-ElHouati, A. Ortega-Moñux, J. G. Wangüemert-Pérez, J. H. Schmid, P. Cheben, Í. Molina-Fernández, and R. Halir, “A review of silicon subwavelength gratings: building break-through devices with anisotropic metamaterials,” *Nanophotonics*, vol. 10, no. 11, pp. 2765–2797, 2021.

- [11] P. Cheben, J. H. Schmid, R. Halir, J. M. Luque-González, J. G. Wangüemert-Pérez, D. Melati, and C. Alonso-Ramos, “Recent advances in metamaterial integrated photonics,” *Advances in Optics and Photonics*, vol. 15, no. 4, pp. 1033–1105, 2023.
- [12] J. G. Wangüemert-Pérez, P. Cheben, A. Ortega-Moñux, C. Alonso-Ramos, D. Pérez-Galacho, R. Halir, Í. Molina-Fernández, D.-X. Xu, and J. H. Schmid, “Evanescent field waveguide sensing with subwavelength grating structures in silicon-on-insulator,” *Optics Letters*, vol. 39, no. 15, pp. 4442–4445, 2014.
- [13] J. G. Wangüemert-Pérez, A. Hadij-ElHouati, A. Sánchez-Postigo, J. Leuermann, D.-X. Xu, P. Cheben, A. Ortega-Moñux, R. Halir, and Í. Molina-Fernández, “Subwavelength structures for silicon photonics biosensing,” *Optics & Laser Technology*, vol. 109, pp. 437–448, 2019.
- [14] P. Cheben, D.-X. Xu, S. Janz, and A. Densmore, “Subwavelength waveguide grating for mode conversion and light coupling in integrated optics,” *Optics Express*, vol. 14, no. 11, pp. 4695–4702, 2006.
- [15] L. Puts, X. Leijtens, P. Cheben, J. Schmid, S. Reniers, and D. Melati, “Anti-reflection subwavelength gratings for InP-based waveguide facets,” *Optics Letters*, vol. 46, no. 15, pp. 3701–3704, 2021.
- [16] C. M. Naraine, J. W. Miller, H. C. Frankis, D. E. Hagan, P. Mascher, J. H. Schmid, P. Cheben, A. P. Knights, and J. D. B. Bradley, “Subwavelength grating metamaterial waveguides functionalized with tellurium oxide cladding,” *Optics Express*, vol. 28, no. 12, pp. 18538–18547, 2020.
- [17] C. M. Naraine, J. N. Westwood-Bachman, C. Horvath, M. Aktary, A. P. Knights, J. H. Schmid, P. Cheben, and J. D. B. Bradley, “Subwavelength grating metamaterial waveguides and ring resonators on a silicon nitride platform,” *Laser & Photonics Reviews*, vol. 17, no. 2, p. 2200216, 2023.
- [18] R. A. Soref, “Silicon-based optoelectronics,” *Proceedings of the IEEE*, vol. 81, no. 12, pp. 1687–1706, 1993.
- [19] M. Lipson, “Guiding, modulating, and emitting light on silicon—Challenges and opportunities,” *Journal of Lightwave Technology*, vol. 23, no. 12, pp. 4222–4238, 2005.
- [20] B. Jalali and S. Fathpour, “Silicon photonics,” *Journal of Lightwave Technology*, vol. 24, no. 12, pp. 4600–4615, 2006.

- [21] D. Liang and J. E. Bowers, “Recent progress in lasers on silicon,” *Nature Photonics*, vol. 4, no. 8, pp. 511–517, 2010.
- [22] Z. Fang, Q. Y. Chen, and C. Z. Zhao, “A review of recent progress in lasers on silicon,” *Optics & Laser Technology*, vol. 46, pp. 103–110, 2013.
- [23] Z. Zhou, B. Yin, and J. Michel, “On-chip light sources for silicon photonics,” *Light: Science Applications*, vol. 4, no. 11, p. e358, 2015.
- [24] Y. Han, H. Park, J. Bowers, and K. M. Lau, “Recent advances in light sources on silicon,” *Advances in Optics and Photonics*, vol. 14, no. 3, pp. 404–454, 2022.
- [25] B. Wang, P. Zhou, and X. Wang, “Recent progress in on-chip erbium-based light sources,” *Applied Sciences*, vol. 12, no. 22, p. 11712, 2022.
- [26] J. D. B. Bradley and M. Pollnau, “Erbium-doped integrated waveguide amplifiers and lasers,” *Laser & Photonics Reviews*, vol. 5, no. 3, pp. 368–403, 2011.
- [27] N. Li, M. Xin, Z. Su, E. S. Magden, N. Singh, J. Notaros, E. Timurdogan, P. Purnawirman, J. D. B. Bradley, and M. R. Watts, “A silicon photonic data link with a monolithic erbium-doped laser,” *Scientific Reports*, vol. 10, p. 1114, 2020.
- [28] K. Mirabbas Kiani, H. C. Frankis, C. M. Naraine, D. B. Bonneville, A. P. Knights, and J. D. B. Bradley, “Lasing in a hybrid rare-earth silicon microdisk,” *Laser & Photonics Reviews*, vol. 16, no. 1, p. 2100348, 2022.
- [29] Y. Liu, Z. Qiu, X. Ji, A. Lukashchuk, J. He, J. Riemensberger, M. Hafermann, R. N. Wang, J. Liu, C. Ronning, and T. J. Kippenberg, “A photonic integrated circuit-based erbium-doped amplifier,” *Science*, vol. 376, no. 6599, pp. 1309–1313, 2022.
- [30] W. A. P. M. Hendriks, L. Chang, C. I. van Emmerik, J. Mu, M. de Goede, M. Dijkstra, and S. M. Garcia-Blanco, “Rare-earth ion doped Al_2O_3 for active integrated photonics,” *Advances in Physics: X*, vol. 6, no. 1, p. 1833753, 2020.
- [31] K. Wörhoff, J. D. B. Bradley, F. Ay, D. Geskus, T. P. Blauwendraat, and M. Pollnau, “Reliable low-cost fabrication of low-loss $\text{Al}_2\text{O}_3:\text{Er}^{3+}$ waveguides with 5.4-dB optical gain,” *IEEE Journal of Quantum Electronics*, vol. 45, no. 5, pp. 454–461, 2009.
- [32] L. Agazzi, J. D. B. Bradley, M. Dijkstra, F. Ay, G. Roelkens, R. Baets, K. Wörhoff, and M. Pollnau, “Monolithic integration of erbium-doped amplifiers with silicon-on-insulator waveguides,” *Optics Express*, vol. 18, no. 26, pp. 27703–27711, 2010.

- [33] M. Belt, T. Huffman, M. L. Davenport, W. Li, J. S. Barton, and D. J. Blumenthal, “Arrayed narrow linewidth erbium-doped waveguide-distributed feedback lasers on an ultra-low-loss silicon-nitride platform,” *Optics Letters*, vol. 38, no. 22, pp. 4825–4828, 2013.
- [34] M. Belt and D. J. Blumenthal, “Erbium-doped waveguide DBR and DFB laser arrays integrated within an ultra-low-loss Si₃N₄ platform,” *Optics Express*, vol. 22, no. 9, pp. 10655–10660, 2014.
- [35] S. A. Vázquez-Córdova, M. Dijkstra, E. H. Bernhardt, F. Ay, K. Wörhoff, J. L. Herek, S. M. García-Blanco, and M. Pollnau, “Erbium-doped spiral amplifiers with 20 dB of net gain on silicon,” *Optics Express*, vol. 22, no. 21, pp. 25993–26004, 2014.
- [36] Purnawirman, J. Sun, T. N. Adam, G. Leake, D. Coolbaugh, J. D. B. Bradley, E. S. Hosseini, and M. R. Watts, “C- and L-band erbium-doped waveguide lasers with wafer-scale silicon nitride cavities,” *Optics Letters*, vol. 38, no. 11, pp. 1760–1762, 2013.
- [37] E. S. Hosseini, Purnawirman, J. D. B. Bradley, J. Sun, G. Leake, T. N. Adam, D. D. Coolbaugh, and M. R. Watts, “CMOS-compatible 75 mW erbium-doped distributed feedback laser,” *Optics Letters*, vol. 39, no. 11, pp. 3106–3109, 2014.
- [38] J. D. B. Bradley, E. S. Hosseini, Purnawirman, Z. Su, T. N. Adam, G. Leake, D. Coolbaugh, and M. R. Watts, “Monolithic erbium- and ytterbium-doped microring lasers on silicon chips,” *Optics Express*, vol. 22, no. 10, pp. 12226–12237, 2014.
- [39] Z. Su, N. Li, E. S. Magden, M. Byrd, Purnawirman, T. N. Adam, G. Leake, D. Coolbaugh, J. D. B. Bradley, and M. R. Watts, “Ultra-compact and low-threshold thulium microcavity laser monolithically integrated on silicon,” *Optics Letters*, vol. 41, no. 24, pp. 5708–5711, 2016.
- [40] E. S. Magden, N. Li, Purnawirman, J. D. B. Bradley, N. Singh, A. Ruocco, G. S. Petrich, G. Leake, D. D. Coolbaugh, E. P. Ippen, M. R. Watts, and L. A. Kolodziejski, “Monolithically-integrated distributed feedback laser compatible with CMOS processing,” *Optics Express*, vol. 25, no. 15, pp. 18058–18065, 2017.
- [41] Z. Su, N. Li, H. C. Frankis, E. S. Magden, T. N. Adam, G. Leake, D. Coolbaugh, J. D. B. Bradley, and M. R. Watts, “High-*Q*-factor Al₂O₃ micro-trench cavities integrated with silicon nitride waveguides on silicon,” *Optics Express*, vol. 26, no. 9, pp. 11161–11170, 2018.

- [42] N. Li, E. S. Magden, Z. Su, N. Singh, A. Ruocco, M. Xin, M. Byrd, P. T. Callahan, J. D. B. Bradley, C. Baiocco, D. Vermeulen, and M. R. Watts, “Broadband 2- μm emission on silicon chips: monolithically integrated Holmium lasers,” *Optics Express*, vol. 26, no. 3, pp. 2220–2230, 2018.
- [43] M. Pollnau and J. D. B. Bradley, “Optically pumped rare-earth-doped Al_2O_3 distributed-feedback lasers on silicon [Invited],” *Optics Express*, vol. 26, no. 18, pp. 24164–24189, 2018.
- [44] D. B. Bonneville, C. E. Osornio-Martinez, M. Dijkstra, and S. M. García-Blanco, “High on-chip gain spiral $\text{Al}_2\text{O}_3:\text{Er}^{3+}$ waveguide amplifiers,” *Optics Express*, vol. 32, no. 9, pp. 15527–15536, 2024.
- [45] P. Kumar, M. K. Wiedmann, C. H. Winter, and I. Avrutsky, “Optical properties of Al_2O_3 thin films grown by atomic layer deposition,” *Applied Optics*, vol. 48, no. 28, pp. 5407–5412, 2009.
- [46] M. M. Aslan, N. A. Webster, C. L. Byard, M. B. Pereira, C. M. Hayes, R. S. Wiederkehr, and S. B. Mendes, “Low-loss optical waveguides for the near ultra-violet and visible spectral regions with Al_2O_3 thin films from atomic layer deposition,” *Thin Solid Films*, vol. 518, no. 17, pp. 4935–4940, 2010.
- [47] M. Demirtaş, C. Odacı, N. K. Perkgöz, C. Sevik, and F. Ay, “Low loss atomic layer deposited Al_2O_3 waveguides for applications in on-chip optical amplifiers,” *IEEE Journal of Selected Topics in Quantum Electronics*, vol. 24, no. 4, pp. 1–8, 2018.
- [48] K. Solehmainen, M. Kapulainen, P. Heimala, and K. Polamo, “Erbium-doped waveguides fabricated with atomic layer deposition method,” *IEEE Photonics Technology Letters*, vol. 16, no. 1, pp. 194–196, 2004.
- [49] M. Demirtaş and F. Ay, “High-gain $\text{Er}^{3+}:\text{Al}_2\text{O}_3$ on-chip waveguide amplifiers,” *IEEE Journal of Selected Topics in Quantum Electronics*, vol. 26, no. 5, pp. 1–8, 2020.
- [50] J. Rönn, W. Zhang, A. Autere, X. Leroux, L. Pakarinen, C. Alonso-Ramos, A. Säynätjoki, H. Lipsanen, L. Vivien, E. Cassan, and Z. Sun, “Ultra-high on-chip optical gain in erbium-based hybrid slot waveguides,” *Nature Communications*, vol. 10, p. 432, 2019.
- [51] J. Rönn, J. Zhang, W. Zhang, Z. Tu, A. Matikainen, X. Leroux, E. Durán-Valdeiglesias, N. Vulliet, F. Boeuf, C. Alonso-Ramos, H. Lipsanen, L. Vivien,

- Z. Sun, and E. Cassan, “Erbium-doped hybrid waveguide amplifiers with net optical gain on a fully industrial 300 mm silicon nitride photonic platform,” *Optics Express*, vol. 28, no. 19, pp. 27919–27926, 2020.
- [52] A. Säynätjoki, L. Karvonen, T. Alasaarela, X. Tu, T. Y. Liow, M. Hiltunen, A. Teronen, G. Q. Lo, and S. Honkanen, “Low-loss silicon slot waveguides and couplers fabricated with optical lithography and atomic layer deposition,” *Optics Express*, vol. 19, no. 27, pp. 26275–26282, 2011.
- [53] L. Karvonen, A. Saynatjoki, Y. Chen, X. Tu, T.-Y. Liow, J. Hiltunen, M. Hiltunen, G.-Q. Lo, and S. Honkanen, “Low-loss multiple-slot waveguides fabricated by optical lithography and atomic layer deposition,” *IEEE Photonics Technology Letters*, vol. 24, no. 22, pp. 2074–2076, 2012.
- [54] C. Horvath, J. N. Westwood-Bachman, K. Setzer, C. M. Naraine, H. M. Mbonde, B. L. Segat Frare, J. D. B. Bradley, and M. Aktary, “Prototyping of silicon nitride photonic integrated circuits using electron beam lithography,” in *2022 Photonics North (PN)*, pp. 1–1, 2022.
- [55] J. Päiväsaari, J. Niinistö, K. Arstila, K. Kukli, M. Putkonen, and L. Niinistö, “High growth rate of erbium oxide thin films in atomic layer deposition from $(\text{CpMe})_3\text{Er}$ and water precursors,” *Chemical Vapor Deposition*, vol. 11, no. 10, pp. 415–419, 2005.
- [56] C. M. Naraine, B. Hashemi, N. A. Hoffman, J. S. Price, A. P. Knights, D. J. H. Emslie, J. H. Schmid, P. Cheben, and J. D. B. Bradley, “Silicon nitride subwavelength grating metamaterial waveguides functionalized with atomic layer deposited Al_2O_3 cladding,” in *2023 Photonics North (PN)*, pp. 1–1, 2023.
- [57] S. M. Rytov, “Electromagnetic properties of a finely stratified medium,” *Soviet Physics JETP*, vol. 2, no. 3, pp. 466–475, 1956.
- [58] J. D. Sarmiento-Merenguel, A. Ortega-Moñux, J.-M. Fédéli, J. G. Wangüemert-Pérez, C. Alonso-Ramos, E. Durán-Valdeiglesias, P. Cheben, Í. Molina-Fernández, and R. Halir, “Controlling leakage losses in subwavelength grating silicon metamaterial waveguides,” *Optics Letters*, vol. 41, no. 15, pp. 3443–3446, 2016.
- [59] L. S. Puumala, S. M. Grist, K. Wickremasinghe, M. A. Al-Qadasi, S. J. Chowdhury, Y. Liu, M. Mitchell, L. Chrostowski, S. Shekhar, and K. C. Cheung, “An optimization framework for silicon photonic evanescent-field biosensors using sub-wavelength gratings,” *Biosensors*, vol. 12, no. 10, p. 840, 2022.

- [60] Y. A. Vlasov, M. O’Boyle, H. F. Hamann, and S. J. McNab, “Active control of slow light on a chip with photonic crystal waveguides,” *Nature*, vol. 438, no. 7064, pp. 65–69, 2005.
- [61] P. Jean, A. Gervais, S. LaRochelle, and W. Shi, “Slow light in subwavelength grating waveguides,” *IEEE Journal of Selected Topics in Quantum Electronics*, vol. 26, no. 2, pp. 1–8, 2020.
- [62] S. Ek, P. Lunnemann, Y. Chen, E. Semenova, K. Yvind, and J. Mork, “Slow-light-enhanced gain in active photonic crystal waveguides,” *Nature Communications*, vol. 5, no. 1, p. 5039, 2014.
- [63] J. T. Robinson, K. Preston, O. Painter, and M. Lipson, “First-principle derivation of gain in high-index-contrast waveguides,” *Optics Express*, vol. 16, no. 21, pp. 16659–16669, 2008.
- [64] J. Rönn, L. Karvonen, C. Kauppinen, A. P. Perros, N. Peyghambarian, H. Lipsanen, A. Säynätjoki, and Z. Sun, “Atomic layer engineering of Er-ion distribution in highly doped Er:Al₂O₃ for photoluminescence enhancement,” *ACS Photonics*, vol. 3, no. 11, pp. 2040–2048, 2016.
- [65] H. M. Mbonde, H. C. Frankis, and J. D. B. Bradley, “Enhanced nonlinearity and engineered anomalous dispersion in TeO₂-coated Si₃N₄ waveguides,” *IEEE Photonics Journal*, vol. 12, no. 2, pp. 1–10, 2020.
- [66] M. Demirtaş, A. Özden, E. Açıkbay, and F. Ay, “Extensive mode mapping and novel polarization filter design for ald grown Al₂O₃ ridge waveguides,” *Optical and Quantum Electronics*, vol. 48, no. 7, p. 357, 2016.
- [67] H. C. Frankis, *Low-loss TeO₂ devices integrated on Si and Si₃N₄ photonic circuit platforms*. PhD thesis, McMaster University, 2021.
- [68] R. Weber, J. A. Tangeman, P. C. Nordine, R. N. Scheunemann, K. J. Hieria, and C. S. Ray, “Rare earth–aluminum oxide glasses for optical applications,” *Journal of Non-Crystalline Solids*, vol. 345–346, pp. 359–365, 2004. Physics of Non-Crystalline Solids 10.
- [69] L. Agazzi, *Spectroscopic excitation and quenching processes in rare-earth-ion-doped Al₂O₃ and their impact on amplifier and laser performance*. PhD thesis, University of Twente, 2012.

- [70] C. Pérez-Armenta, A. Ortega-Moñux, J. Manuel Luque-González, R. Halir, J. Schmid, P. Cheben, Í. Molina-Fernández, and J. Gonzalo Wangüemert-Pérez, “Polarization insensitive metamaterial engineered multimode interference coupler in a 220 nm silicon-on-insulator platform,” *Optics & Laser Technology*, vol. 164, p. 109493, 2023.
- [71] R. M. de Ridder, K. Wörhoff, A. Driessen, P. V. Lambeck, and H. Albers, “Silicon oxynitride planar waveguiding structures for application in optical communication,” *IEEE Journal of Selected Topics in Quantum Electronics*, vol. 4, no. 6, pp. 930–937, 1998.
- [72] P. Cheben, J. H. Schmid, S. Wang, D.-X. Xu, M. Vachon, S. Janz, J. Lapointe, Y. Painchaud, and M.-J. Picard, “Broadband polarization independent nanophotonic coupler for silicon waveguides with ultra-high efficiency,” *Optics Express*, vol. 23, no. 17, pp. 22553–22563, 2015.
- [73] J. D. B. Bradley, L. Agazzi, D. Geskus, F. Ay, K. Wörhoff, and M. Pollnau, “Gain bandwidth of 80 nm and 2 dB/cm peak gain in $\text{Al}_2\text{O}_3:\text{Er}^{3+}$ optical amplifiers on silicon,” *Journal of the Optical Society of America B*, vol. 27, no. 2, pp. 187–196, 2010.
- [74] D. E. McCumber, “Einstein relations connecting broadband emission and absorption spectra,” *Physical Review*, vol. 136, pp. A954–A957, 1964.
- [75] W. J. Miniscalco and R. S. Quimby, “General procedure for the analysis of Er^{3+} cross sections,” *Optics Letters*, vol. 16, no. 4, pp. 258–260, 1991.
- [76] H. C. Frankis, H. M. Mbonde, D. B. Bonneville, C. Zhang, R. Mateman, A. Leinse, and J. D. B. Bradley, “Erbium-doped TeO_2 -coated Si_3N_4 waveguide amplifiers with 5 dB net gain,” *Photonics Research*, vol. 8, no. 2, pp. 127–134, 2020.
- [77] C. Wang, J. Song, Z. Ao, S. Yang, Y. Li, X. Li, N. Zhu, Q. Chen, and Z. Li, “High-gain waveguide amplifiers in $\text{Ge}_{25}\text{Sb}_{10}\text{S}_{65}$ photonics heterogeneous integration with erbium-doped Al_2O_3 thin films,” *Laser & Photonics Reviews*, vol. 18, no. 3, p. 2300893, 2024.
- [78] F. S. Hickernell, “Post-deposition annealing of zinc oxide films,” in *1981 Ultrasonics Symposium*, pp. 489–492, 1981.
- [79] G. N. West, W. Loh, D. Kharas, C. Sorace-Agaskar, K. K. Mehta, J. Sage, J. Chiverini, and R. J. Ram, “Low-loss integrated photonics for the blue and ultraviolet regime,” *APL Photonics*, vol. 4, no. 2, p. 026101, 2019.

Chapter 6

Conclusion

6.1 Summary

This thesis focused on exploring and developing subwavelength grating (SWG) metamaterials in different material systems to realize novel integrated photonic devices with unique passive properties and advanced functionalities for applications including sensing and light amplification.

In Chapter 2, tellurium oxide (TeO_2) thin films deposited using reactive magnetron sputtering were demonstrated as a top cladding material for SWG metamaterial waveguides fabricated on standard silicon-on-insulator (SOI) foundry platforms. SWG waveguides with a 100 nm-thick TeO_2 coating exhibited a propagation loss of 1.0 ± 0.1 dB/mm, which was better than the 1.5 ± 0.1 dB/mm propagation loss expressed by equivalent SWG waveguides embedded in the standard foundry silicon dioxide (SiO_2) cladding. Studies of new silicon (Si)- TeO_2 waveguide designs revealed that up to 86% mode overlap with the TeO_2 material could be achieved in SWG waveguide structures with a 400 nm-thick TeO_2 cladding. Mode transformer components that smoothly transition between conventional wires and SWG metamaterial waveguides were fabricated with ~ 400 nm TeO_2 film thickness and demonstrated only 0.12 ± 0.02 dB loss over a length of 50 μm . Fishbone SWG (FB-SWG) waveguides are currently being fabricated and are expected to help increase robustness to fabrication error and decrease waveguide propagation and radiation loss while maintaining reasonable mode overlap with the TeO_2 material. The TeO_2 cladding and SWG metamaterial waveguides compliment each other well. While

the high refractive index of the TeO_2 reduces mode leakage into the substrate, the loosely confined Floquet-Bloch mode supported by the SWG waveguide experiences increased light interaction with the TeO_2 medium. This is beneficial for enhancing gain in a waveguide amplifier integrating the TeO_2 as a host glass for rare-earth (RE) ions, as well as for leveraging the advantageous material properties of the TeO_2 for enhanced nonlinear optical processes in Si waveguides.

In Chapter 3, a foundry process for rapid prototyping silicon nitride (SiN) photonic integrated circuits (PICs) was presented. The platform comprises a 400 nm-thick SiN device layer and uses direct-write electron beam lithography (EBL) technology for writing and patterning waveguides that can have feature sizes as low as 100 nm, which is essential for fabricating metamaterial structures. Moderate confinement waveguides fabricated on the platform showed propagation losses between 0.6 and 1.3 dB/cm across the O-band and between 0.4 and 1.8 dB/cm across the S-, C- and L-bands for transverse electric (TE) and transverse magnetic (TM) polarizations. This demonstrates single mode operation across multiple spectral regions of interest with losses that are competitive with other commercially available SiN integrated photonics foundry platforms. Other important integrated photonic components, including fiber-chip grating and edge couplers, 3 dB multimode interference (MMI) power splitters, and all-pass ring resonators, were demonstrated at 1.31 and/or 1.55 μm wavelengths. All presented components have been compiled into a process design kit (PDK), which is available through the NanoSOI Design Center operated by Applied Nanotools Inc. (ANT) and being continually updated.

In Chapter 4, the first demonstrations of SWG metamaterial-engineered SiN waveguides and ring resonators were presented. The devices were fabricated using the prototyping SiN foundry process described in Chapter 3, which leverages direct-write EBL technology for patterning feature sizes necessary for SWG metamaterial structures. The fabricated SiN SWG metamaterial waveguides and ring resonators exhibited propagation losses of ~ 1.5 dB/cm and internal quality factors (Q_i) near $\sim 2.11 \cdot 10^5$ in the C-band, respectively, which are comparable to equivalent conventional SiN waveguides and competitive with SOI SWG ring resonators. These SWG devices possess a large mode overlap of 53% with the SiO_2 upper cladding material and a bulk sensitivity of 0.33 RIU/RIU (~ 285 nm/RIU for 1540 nm wavelength) when coated in water, which emphasizes their potential for applications in evanescent field sensing and light amplification. Sensing functionality was experimentally demonstrated by applying a water coating directly onto an exposed SWG SiN ring resonator, which displayed a loaded quality factor (Q_L) of 5200. This metric is proportionate with equivalent SWG ring resonator

sensors reported in the SOI platform and highlights the prospects of SWG metamaterial engineering in SiN photonic devices and other potential material platforms in integrated optics.

In Chapter 5, work towards a waveguide amplifier engineered using SWG metamaterials was presented. The SWG waveguide amplifier was situated on SiN using the rapid prototyping foundry process detailed in Chapter 3. The gain medium, composed of a hybrid alumina-erbium ($\text{Al}_2\text{O}_3/\text{Er}_2\text{O}_3$) thin film upper cladding, was grown directly onto the SiN waveguides using a thermal atomic layer deposition (tALD) process, where monolayers of aluminum oxide (Al_2O_3) and erbium oxide (Er_2O_3) were sequentially grown under self-limiting conditions, producing a high quality, uniform film over the fine SiN grating features. A low propagation loss of ~ 1.3 dB/cm was realized in the fabricated devices by performing passive cutback measurements on SWG waveguide spiral test structures. Gain measurements done on a 0.64 cm-long SWG metamaterial waveguide coated in a ~ 300 nm-thick $\text{Al}_2\text{O}_3/\text{Er}_2\text{O}_3$ cladding gain medium revealed up to 8.6 dB power enhancement of the 1533 nm signal source when exposed to ~ 148 mW of 1480 nm launched pump power. However, overwhelming losses, primarily caused by strong erbium (Er) absorption, prohibited internal net gain. Nevertheless, thanks to the increased light-matter interaction with the gain medium, the observed signal enhancement in the SWG waveguide almost doubles the performance shown in an equivalent wire waveguide (~ 4.8 dB). This demonstration provides promise for using SWG metamaterials to generate light in Si-based PICs and potential for improving the performance of other active integrated photonic devices.

6.2 Future work

Each demonstration presented in this thesis has already undergone or is subject to future work. Improvements to current devices and suggestions for exploring other related projects will be discussed below and individually by chapter.

While the first iteration of TeO_2 -clad SOI SWG metamaterial waveguides showed superior propagation loss over their SiO_2 -clad counterparts, the loss is still high compared to other SWG waveguides demonstrated on the SOI platform. The first SWG waveguides, coated in an SU-8 polymer, possessed losses as low as 2.1 dB/cm in the C-band. SWG metamaterial waveguides utilizing high-index TeO_2 cladding should match this in order to be considered competitive with standard complementary-metal-oxide-semiconductor (CMOS) materials. This first demonstrated waveguide featured a very

thin TeO₂ film (~100 nm), so very little modal interaction occurred with the TeO₂ medium. Furthermore, the expanded SWG mode experienced greater interaction with the TeO₂-air boundary above the waveguide, which produced additional unwanted scattering loss. The cladding volume around the waveguide may be easily expanded by increasing the cladding thickness, which requires no additional fabrication steps. However, because of how the TeO₂ film nucleates to itself as it grows over time in the sputtering chamber, goblet-shaped clumps form over adjacent gratings without filling in the gaps between them, leaving behind air pockets that absorb most of the Floquet-Bloch mode energy and severely diminish the device performance. Careful study of the TeO₂ film growth with increasing thickness would help provide details to optimize an SWG design where air pocket formation is limited. Different SWG metamaterial topologies may also be explored. FB-SWG metamaterial waveguides feature a thin Si wire bridging together adjoining grating segments, which still leverage the index homogenization principles that SWGs are known for. These structures offer increased robustness to the fragile gratings so that the nanostructures remain in tact during the initial waveguide fabrication and the post-process TeO₂ deposition. The thin Si wire also pre-fills some of the gap space between the grating, which helps to alleviate the air pocket issue. Fabrication of a follow-up design based on fishbone-style SWG waveguides (i.e., “Design #3” described in Chapter 2) has already begun. The fabricated chips will receive TeO₂ films via sputtering upon arrival and then undergo characterization to assess propagation and coupling loss. Other interesting SWG topologies to explore for the Si-TeO₂ platform include tilted or bricked SWGs, which have been considerably investigated in the SOI platform in other studies. Another interesting research avenue for this project is the testing of different high-index oxide cladding materials for these SOI SWG waveguides. The Al₂O₃ and Al₂O₃/Er₂O₃ thin films grown by atomic layer deposition (ALD) described in Chapter 5 may be applied as a top cladding. The sequential layer-by-layer growth process of ALD would produce highly conformal films for the SWGs and eliminate the formation of any air pockets between the gratings. While the refractive index of Al₂O₃ is not as large as TeO₂, it is still moderately high compared to conventional cladding materials, so the waveguide can be designed to have a relatively high mode overlap with the Al₂O₃ material.

The moderate confinement SiN waveguide platform offered by ANT that is presented in Chapter 3 is continually being updated. The SiN material exhibited significantly higher loss near 1520 nm in both the film and waveguide measurements, which is likely caused by Si-H and N-H bonds in the film leftover from the chemical vapour deposition (CVD) procedure. Preliminary prism coupling measurements have already been

performed on a wafer sample featuring a SiN film layer that underwent post-deposition annealing at 1100°C. The results, which could not be prepared in time for the thesis but will appear in the corresponding publication, show reduced loss in the noted H absorption region, indicating that the annealing is fixing the issue. Re-designs of the tested waveguide structures reported in the chapter will be re-fabricated, annealed, and characterized so that the losses in the PDK may be updated to reflect optimal values and keep up with other foundry competitors. As discussed in the chapter, the edge couplers and ring resonators underwent the most development. The optimal edge coupler tip widths have been reported for 1.31 and 1.55 μm under both TE and TM polarization. However, the coupler length may still be fine tuned. Pinpointing the 1310 nm critical coupling point for the ring resonators will require one more design layout. On the other hand, the grating couplers and MMI power splitters require much more optimization. The performance of these components is sub-optimal compared to those reported by other foundries and research groups. Furthermore, the demonstrations for these components were only performed at 1.55 μm for TE polarization. Therefore, each one must undergo further rounds of design (at least 2 or 3) to realize high-performance PDK building blocks. Beyond this, other components commonly featured in foundry PDKs are queued for investigation, including MMI combiners, directional couplers, interferometers, and Bragg gratings. With SiN, there is the opportunity to explore other operating wavelength ranges of interest for different applications, such as the 2 μm window for medical diagnostics, environmental sensing, and expanding optical telecommunications. Furthermore, near-infrared (NIR) wavelengths $\sim 0.9 \mu\text{m}$ are of interest for light detection and ranging (LiDAR) and quantum computing applications. However, single mode operation with this SiN thickness becomes strained at these wavelengths, and even more so down towards the visible (VIS) spectrum. Therefore, exploring thinner SiN waveguide layers ($\sim 150\text{-}200 \text{ nm}$) is an exciting endeavour. Work on this with ANT is already underway.

The SiN SWG metamaterial waveguides and ring resonators presented in this thesis are the first domino to fall when it comes to implementing SWG metamaterials and realizing their impact in SiN PICs. Similar to the trajectory of SWG metamaterial incorporation in SOI, SWG metamaterials can be used to improve the performance and functionality of various components that are essential for integrated photonics. For starters, SWG metamaterials help modify the electromagnetic field distribution in fiber-chip edge and grating couplers to better match the overlap between the fiber mode and the chip interface. SWG metamaterials have also been used in many on-chip couplers and multiplexers (e.g., directional couplers, Y-splitters, interferometers, MMI couplers, etc.) to inhibit ultrabroadband operation, reduce polarization dependability, and lower

loss overall. Such benefits will certainly prompt many foundries, researchers, and chip makers to adopt SWG metamaterials in their devices over time. Different metamaterial topologies explored in SOI may also be exploited in SiN, including tilted and bricked SWGs, for finer control over anisotropy and dispersion directly in the waveguide layer. SiN also opens a broad range of wavelengths, and therefore applications, outside of Si's transparency window (i.e., $<1.1 \mu\text{m}$). However, though the lower refractive index of SiN provides some room for leveraging lower subwavelength periods over Si, exploiting subwavelength operation at wavelengths under $1 \mu\text{m}$ mainly depends on the allowed critical dimensions of the fabrication technology. Investigation on this is a pivotal step for determining what is possible for SWG metamaterials in VIS and short wave NIR applications in SiN.

Although significant signal enhancement was demonstrated in the hybrid SiN- $\text{Al}_2\text{O}_3/\text{Er}_2\text{O}_3$ SWG metamaterial waveguide, internal net gain was not shown. Instead, gain was prohibited by many losses within the system. The main loss comes from strong Er absorption in the gain region, which is associated with the high Er concentration in the ALD films. Much work can be undertaken here to optimize the device and the processes used to produce it. The first step is re-assessing the deposition process itself and considering system maintenance. There are many ways to adjust the process layer stack. Our $\text{Al}_2\text{O}_3/\text{Er}_2\text{O}_3$ films only used a single Er_2O_3 monolayer per macrocycle. It would be interesting to study $\text{Al}_2\text{O}_3/\text{Er}_2\text{O}_3$ films with multiple stacked Er_2O_3 layers within a macrocycle and observe the effects on the signal enhancement. The flaking issue also poses a big problem for continual use of the ALD reactor. Precise planning of the depositions and the studies being performed for each sample is required to avoid unwanted contamination and damage caused by flaking. Cleaning of the chamber should be scheduled accordingly to achieve the best quality films while avoiding unnecessary maintenance delays. The next is re-considering the film deposition properties for the waveguide in question. There is an optimal point between the waveguide length and the Er concentration where the highest amount of gain is exhibited across the device before saturation begins to occur. This can be found using a rate equation model. However, an accurate model requires full spectroscopic details of the Er ions involved in the system. Various spectroscopic measurements must be performed to acquire this information, including absorption/emission cross sections, luminescent lifetimes, ion quenching, and energy transfer upconversion (ETU). Once obtained, the rate equation model will have better accuracy, generate a greater understanding of the current gain results, and help guide future devices to be investigated. For the devices already presented in the thesis, further examination is needed to potentially achieve net gain. The samples can undergo

post-process steps like annealing to drive out excess hydrogen contaminants that possess strong absorption characteristics in the gain region. This will help reduce loss. Furthermore, annealing reduces quenching and restores properties for bolstering stimulated emission in Er ions throughout the film, which are needed for leveraging the large mode overlap enabled by the SWG waveguide and achieving higher gain. Following annealing, gain measurements should be redone and compared to the presented initial results. Spectroscopic measurements of the annealed samples will also reveal many details about the effects of annealing on both the ALD films and the SiN waveguides. Overall, there are many pathways to explore and there is promise for net gain in these SWG metamaterial waveguide amplifiers. An interesting alternative pathway for this project is testing other RE ions. Many RE ions have been incorporated into sputtered Al_2O_3 films for integrated photonic waveguide amplifiers and lasers operating in various regions of the NIR spectrum. However, none (except for Er) have been reported in ALD Al_2O_3 . For this endeavour, extensive research of proper precursor materials is required and careful testing of ALD process parameters must be considered.